Study on effects of an isolated elliptical terrain (Jeju Island) on rainfall enhancement in a moist environment

(湿潤環境場における楕円形孤立峰(済州島)の降雨強化に対する地形効果に関する研究)

Keunok LEE

(李 根玉)

A dissertation for the degree of Doctor of Science
Department of Earth and Environmental Sciences,
Graduate School of Environmental studies,
Nagoya University

(名古屋大学大学院 環境学研究科 地球環境科学専攻 学位論文 博士(理学))

2013

Abstract

Jeju Island, southern part of Korea has frequently suffered from flooding and landslides due to orographically–intensified rainfall systems during the rainy season. The island is an isolated terrain with an elliptical–shaped mountain extending east–to–west (width 35 km, length 78 km, height 1.95 km). During the rainy season (June to mid–July) when a stationary front is located off the northern shore of the island, a moist environment and ambient southwesterly winds are well predominant around the island. In last 10 years (2003–2012), when the southwesterly wind prevails in low altitudes during June and July, the maximum rainfall amount of 3,805 mm was recorded locally on the northern slope of the mountain showing the relatively large rainfall (> 700 mm) on the northern and eastern side of the island, while rainfall less than 700 mm was accumulated on the western and southern sides of the island; the large regional–rainfall distinction was apparent on a mountainous region with a small horizontal scale. This study aims to reveal the effects of an isolated elliptical–shaped terrain on the flow modification and the related enhancement of rainfall system, especially on the northern side of the terrain, in a moist environment by both of data analyses and numerical simulations.

Two intense rainfall systems occurred on 30 June 2006 and 6 July 2007 were selected to identify the orographic effect of an elliptically–shaped terrain on rainfall enhancement. Both of the selected rainfall systems moved eastward and passed over the northern side of the island, showing the system enhancement on the northern side of the island. Four–dimensional structures of reflectivity and wind of convective cell within both systems were analyzed using S–band dual–Doppler radar dataset and a non–hydrostatic numerical model, Cloud Resolving Storm Simulator (CReSS). Comparison of the enhancement mechanisms of two systems reveals that first, moist environment and the southwesterlies at low altitudes are the favourable condition for the system enhancement, and secondly the isolated elliptical–shaped terrain of Jeju Island induces a horizontal rerouting of relatively–weak low–level southwesterly winds, generating a local updraft region on

the northwestern lateral side of the island; in result, rainfall enhances on the lateral side of the island. Sensitivity experiments reveals that (a) 30.6 % of rainfall amount is induced by the steep topography of Jeju Island, and (b) concentrated moisture in low altitudes works for increasing rainfall; a reduction in the low–level RH of 2 % results in a 20.8 % reduction in rainfall amount.

Comparison of the two systems also shows some differences on the system evolution. In order to clarify the key parameter to induce the differences, a series of idealized experiments using CReSS were conducted. One key parameter is the arrival location of the eastward–moving system on the island. When the system travels off the northwestern shore of the island, further intensified system arrives on the island. As the distance between the system and terrain decreased, the southwesterlies blowing parallel to the coastline accelerates in the space between the system and terrain; thus updraft is locally generated. Subsequently, abundant vapour over sea surface is supplied to interior of the convective cell; thus warm rain process is mainly important to the system enhancement on the northwestern part of the island. Another key parameter is revealed to be intensity of low–level southwesterlies. Fairly weak southwesterly wind (Fr = 0.2) at low altitudes allows enhancement of the system on the lee side of the island by generating the convergence of a relatively weak go–around northwesterly from the northern island and a relatively strong moist southwesterly from the southern island, thus producing a relatively long–lived rainfall system is resulted. With the strong southwesterly wind over the southeastern slope, the moist air is supplied to interior of the system to above the melting layer; thus both warm and cold rain processes are important in enhancing the convective cell on the eastern side of the island. As the low–level southwesterly winds strengthen at low altitudes (Fr » 0.2), a dry descending air mass intensified on the northeastern downwind side, which actively and rapidly dissipates rainfall system, resulting in a relatively short–lived rainfall system.

In this study, the effect of an elliptically–shaped terrain (Jeju Island) on the enhancement of rainfall system in a moist environment is revealed. The results imply us two meteorological

elements for improving rainfall forecast over the mountainous region in a moist environment; first, predominant moist southwesterly wind has potential to bring out intense rainfall on the lateral (northern) side of the island, besides secondly, the fairly–weak southwesterly wind has potential to induce intense rainfall, also on the lee (eastern) side of the island. Furthermore, in the identical environment, if the eastward–moving pre–existing rainfall system passes off the northwestern shore of the terrain, the system has potential to bring further intense rainfall on the lateral (northern) side of the terrain. These results suggest us key meteorological elements for rainfall enhancement which are applicable to a terrain with further complicated topographic feature in a moist environment so that it can help to improve the rainfall forecast over the mountainous region.

Contents

1. Introduction

1.1. Mesoscale convective system in moist environment

The humid subtropical region is generally characterized by high annual precipitation, high humidity for all season, and high temperature in summer season (Kottek et al., 2006; Trewartha and Horn, 1980). East Asia in latitude from 25°N to 35°N, such as southern China and western Japan including southern Korea, is generally categorized into the humid subtropical region (gray-shaded region of Fig. 1.1). More than 50 % of the annual precipitation in the humid subtropical region can be explained by heavy rainfall more than 50 mm per day (Ninomiya and Mizuno, 1987; Ninomiya, 2001). Changma/Baiu/Meiyu season from June to mid–July is one of the major peak seasons of high precipitation (Ninomiya and Mizuno, 1987). Changma/Baiu/Meiyu front is characterized by a weak temperature contrast, but is accompanied by a large moisture contrast in south–north (Akiyama, 1975). In theses synoptic-scale features, it is well recognized that there is a hierarchy of disturbances in the stationary frontal region: mesoscale convective system (MCS).

A MCS is generally defined as a cloud system that occurs in connection with an ensemble of thunderstorms and produces a contiguous precipitation area of ~100 km or more in horizontal scale in at least on dimension (Houze, 1993). In recent years, MCS, which has a wide range of horizontal scales, is often subdivided into meso-α-scale convective system (MαCS) and meso-β-scale convective system (MβCS) on the basis on the horizontal scale of the contiguous precipitation area following the classification of Orlanski (1975) (e.g., Ninomiya and Akiyama, 1992; Moteki et al., 2004a and 2004b). The MαCS corresponds to weather systems such as frontal systems and hurricanes having horizontal scales of 200–2000 km and temporal scales of 1 day to 1 weak (Cotton and Anthes, 1989). The MβCS corresponds to such systems as squall lines, cloud clusters, rainbands, organized multicell thunderstorms with a stratiform region, and supercell thunderstorm region, having horizontal scales of 20–200 km and temporal scales of 1 hour to 1 day (Cotton and

Anthes, 1989).

In the Changma/Baiu/Meiyu frontal region, the existence of multi-scale hierarchical structures of the precipitation system (Fig. 1.2) were reported by Ninomiya and Akiyama (1992) and Moteki et al. (2004a). MβCSs are often embedded in MαCS in the Changma/Baiu/Meiyu frontal region (Fig. 1.2a–b). An MβCS consists of several convective cells (meso-γ-scale of ~10 km) enclosed by a weak precipitation region (Fig. 1.2c), which is recognized as a stratiform region associated with the convective cells or as some part of MαCS. The MβCS and the convective cells are major causes of heavy rainfall (Ninomiya and Mizuno, 1987) and are the important fundamental fragment of precipitation system.

The formed MβCSs travels on a warm and moist environment, and the convective cells within the system are enhanced by several causes such as low–level jet (LLJ) feeding warm and moist air into the system (Maddox, 1983; Schmidt and Cotton, 1989; Raymond and Jiang, 1990; Olsson, 1994; Pandya and Durran, 1996; Yamada et al., 2003; Geng et al., 2009), cold pool generation supplying moist and unstable air into the updrafts (Byers and Braham, 1949; Kane et al., 1987; Johnson et al., 1989), daytime unstable boundary layer in metropolitan area (Bernardet and Cotton, 1998; Chun and Baik, 1994; Baik and Chun, 1997), condition with sufficiently high convective available potential energy (CAPE) (Tripoli and Cotton, 1989b; Geng et al., 2004), and locally–generated updraft in the vicinity of mountainous region (Grossman and Durran, 1984; Tripoli and Cotton, 1989a and 1989b; Lin et al., 2001; Lin, 2007; Houze, 2012). These causes which mentioned above have common fact in generation of low–level updrafts which can supply warm and moist air into the MβCS.

1) The LLJ is an important factor in the transformation of an MCS from a system dominated by upright convection to one dominated by slantwise ascending and descending motions. By the slantwise ascending air, low–level moisture and energy enter into the system (Olsson, 1994; Johnson et al., 1999). 2) In the behind of the system in the moist boundary layer, cold pool

generated by evaporating and melting precipitation from cumulonimbi during mature and dissipating stages of the system. The cold pool develops the slantwise ascending air, and is able to continually retrigger deep convective cells (Fritsch and Forbes, 2001). Besides of the dynamical causes (e.g., moist LLJ and generation of cold pool) to intensify the MβCS and the inner convective cells, thermal causes (e.g., heated boundary layer and significant amount of CAPE) are also noteworthy factor. 3) The MβCS intensifies when it travelses over an environment of sufficient warm air at low altitudes, where the convective instability is high; consequently, the convective instability works at increasing vertical motion within the system. Jirak and Cotton (2007) mentioned that MCS typically develop in more unstable environments of high level of instability parameter (e.g. CAPE). 4) One of the profound causes for intensifying MβCS is orographically-generated updraft in vicinity of the terrain; moist air-flow is affected by orographic lifting and blocking that may modify and trigger MβCS in the vicinity. The sophisticated structure and triggering for the enhancement of convective cells within an MβCS are revealed to be different over distinct geographic locations (e.g., Chen and Chang, 1980; Kato, 1985; Ninomiya and Muraki, 1986), as the location and intensity of the local updraft/downdraft is widely varied depends on size and shape of the topography and the surrounding environment (Houze, 2012). Furthermore, as East Asia is composed by complex mountainous regions, the terrain effects on the MβCS enhancement must not be oversimplified. In the next section, a review of studies on orographic effect on the MβCS enhancement will be shown.

1.2. Review of studies on orographic effect

In order to understand the orographic effect on the MβCS enhancement, previous studies (e.g., theoretical, observational, and numerical experimental approaches) have examined factors such as low-level convergence, wind blocking (measured by Froude number, Fr), ambient wind direction and speed, steepness of the topography (measure by aspect ratio, β), and latent heating and cooling

processes induced by various terrain morphologies (Smolarkeiwicz and Rotunno, 1989; Li et al., 1997; Lin et al., 2001; Chiao and Lin, 2003; Jiang, 2003; Petersen et al., 2003; Reeves and Lin, 2007; Xu et al., 2012). Many theoretical studies have investigated the orographic effect on dynamical fields around the various shape and size of terrain (e.g., circular–shaped mountain, elliptical-shaped mountain, elongated mountain ranges, and hill) in a dry environment. These studies establish our understanding of general concept for orographic effect on flow dynamics, and its potential to trigger the enhancement of MCS in the vicinity of terrain (Smolarkiewicz and Rotunno, 1990; Petersen et al., 2005).

Based on the results of theoretical approaches, studies based on field observational data have been accomplished to extend our understanding, and to improve prediction of rainfall over regions adjacent to mountain ranges assessing the impact of terrain on precipitation distribution and intensity (Li et al., 1997; Kanada et al., 2000; Yoshizaki et al., 2000; Bousquet and Smull, 2003; Rotunno and Ferretti, 2003). The observational approaches offer a unique opportunity to explore orographic effect on evolution of MβCS: detailed 3–dimensional spatial and temporal structures and evolutions of convective cells within the system. However, because of the complexity and ruggedness of the terrain, mountainous areas are generally poorly instrumented. As the complementary tool of observational instruments, numerical modeling appears to address the problem of severe orographic effect on MCS. By numerical approaches, the impact of several causes and environmental conditions which was mentioned as influential factors to trigger the MCS enhancement has been revealed (Rotunno and Ferretti, 2001; Lin et al., 2002; Kirshbaum et al., 2007). The previous studies by each approach will be introduced in next section.

1.2.1. Orographic effect on flow dynamics (theoretical approach)

Many theoretical studies have investigated the interaction between dry atmospheric flows and topography by numerical experiments, showing the critical values of Froude number (*Fr*) which

diagnose the practicable wind patterns (Miles and Huppert, 1969; Smith, 1980; Smolarkiewicz et al., 1988; Lin and Wang, 1996; Olafsson, 2000). To measure the degree of wind blocking by terrain, *Fr* is widely used, which is proportional to the square root of the ratio of kinetic energy of the upstream parcel to the energy required to lift the fluid element over a terrain, is a dimensionless parameter calculated as follows:

$$Fr=U_0/Nh \qquad (1)$$

where U_0 is the averaged wind speed under the height of the terrain, N is the Brunt–Väisälä frequency, and h is the central height of the mountain. By previous studies (e.g., Smolarkiewicz and Rotunno, 1989 and 1990; Smith and Gronas, 1993; Lin and Wang, 1996; Olafsson and Bougeault, 1996; Jiang, 2003; Petersen et al., 2005), it has been known that in a high–*Fr* regime ($Fr > 1$, see Fig. 1.3a–c), the strong and unblocked low–level flow is forced to ascend up the mountain slope, generating descending air in lee side of the mountain which are intensified by gravity wave. Compared to the flow modification in a high–*Fr* regime, in a low–*Fr* regime ($Fr < 0.6$, Fig. 1.3d–f), the flow passing adjacent to a terrain is modified further complicatedly, and the shape of terrain plays further important role in determining the pattern of flow modification. The flow modification by an obstacle has been studied by changing the degree of *Fr* in various terrains of size and shape. To measure the terrain shape, aspect ratio of β parameter has been widely used, which is calculated by ratio of the mountain width perpendicular to the flow direction divided by the width in the flow direction.

Smolarkiewicz and Rotunno (1989, 1990) investigated the flow pattern modified by a circular–shaped obstacle ($\beta = 1$; Fig. 1.3b and e). According to their result, when *Fr* is low ($Fr < 0.6$), with a horizontal rerouting of the low–level flow in regions of high terrain, flow stagnation and the deceleration are characterized; a zone of flow reversal is generated on the windward side of the obstacle. Consequently, an arc–shaped convergence zone by the horizontal–rerouting flow at

low altitudes and the flow reversal from the upslope of the terrain was characterized adjacent to the western coastal region. The horizontally–rerouted low–level wind combined off the eastern shore, generating lee–vortices on the lee side of the mountain which are closely associated with gravity wave.

Smolarkiewicz and Rotunno (1990) showed the distinct flow pattern modified by elliptical shaped–terrain with longer length along stream (β = 0.5; Fig. 1.3d): further gentle upslope of terrain. In a low *Fr* regime, absence of the flow reversal on the upslope was resulted; the horizontal rerouting of the low-level flow converged with ambient flow to lateral edges of the obstacle. The horizontally–split low–level flows at windward side were combined in lee side, generating a reversal flow toward the obstacle; lee vortices results over the lee side of the terrain.

Even same terrain shape in ellipse, terrain effect on the flow modification was shown differently depending on the elongated direction toward ambient flow direction. An elliptical–shaped terrain (β = 4; Fig. 1.3f), but with shorter length along stream modified the surrounding flow, inducing an elongated convergence zone of the horizontal rerouting flow and the flow reversal from upslope along the western long edge of the obstacle. Off the shore of the lee side, the relatively–large scaled lee–vortices is resulted.

As mentioned above, the size and shape of mountain controls the flow distributions around the terrain. Furthermore even same elliptic shape of terrain, different location of wind convergence was resulted in identical wind direction (westerly wind); terrain–generated convergence on the southern and northern lateral sides of the elliptically-shaped terrain extending west-east (β = 0.5, Fig. 1.3d), whereas the convergence on the western side of the elliptically-shaped terrain extending south to north (β = 4, Fig. 1.3f). When a moist airflow enters a mountainous area, the flow is modified by orographic lifting and blocking; it is directly linked to the enhancement/dissipation of MCS passing around the mountainous region. The detailed terrain effect on the MCS evolution will be shown in the next section.

1.2.2. Orographic effect on MCS (Observational and modeling approaches)

The distribution of precipitation adjacent to a terrain of a given height and topographic shape is determined by a combination of the dynamical behavior of a fluid flow encountering a terrain barrier, microphysics of particle growth, and the thermodynamics of moist air. The influence of terrain on the MCS enhancement has been revealed by field observation and numerical experiments (Hobbs et al., 1975; Lin et al., 2005; Rotunno and Ferretti, 2003; Yuter, 2003; Houze and Median, 2005; Galewsky and Sobel, 2005; Woods et al., 2005; Rowe, 2011; Houze, 2012). These studies showed that the enhancement mechanisms of MCS approaching and traversing a certain mountain area are patterned in principle by prevailing wind direction and speed, spatial moist distribution and the additional causes. Although the prediction of rainfall over regions adjacent to mountain ranges assessing the impact of orography on precipitation distribution and intensity is remained as one of the most significant challenges (Jiang, 2003; Lin, 2007; Xu et al., 2012).

As mentioned in section 1.1, Changma/Baiu/Meiyu front accompanied by a large moisture contrast in south–north (Ninomiya and Akiyama, 1974; Akiyama, 1978), hence it is well recognized that there is a hierarchy of disturbances: MCS. Furthermore, as diverse features of topographies are situated in East Asia: Taiwan's central mountain region (CMR; height 4 km, width 120 km, length 320 km extending southwest–northeast), Yaku–shima Island in southern Kyushu, Japan (height 2 km, radius 15 km) and mountain crests in western Kyushu, Japan (height 500 m), the sophisticated structure and triggering for the system enhancement are revealed to be different over distinct geographic locations (Li et al., 1997; Kanada et al., 2000; Yoshizaki et al., 2000; Chiao and Lin, 2003; Kato et al., 2003; Kato, 2005; Wang et al., 2005; Yu et al., 2007).

When southerly–southwesterly winds are predominant on the southern side of the Baiu front, orographically–enhanced MβCS in line shape frequently occur over the western part (Koshikijima and Nagasaki area) of Kyushu Island (Yoshizaki et al., 2000; Kato, 2005). The mountain crests are

500–600 m and not high. On 26 June 1997, generated line–shaped MβCS moved northeastward with low–level southwesterly wind (10 m s^{-1}) and southwesterly wind (15–25 m s^{-1}) between 900 hPa and 500 hPa, and enhanced over the terrain in deep. Related to the system enhancement, they revealed the important role of upslope forcing due to mountains in triggering convection. Kato (2005) investigated the favourable conditions for the maintenance of the MβCS by statistical analyses; the southwesterly low–level wind field persists for longer than 12 hours, and that the wind speed at an 850 hPa level is between 5 m s^{-1} and 25 m s^{-1}.

Wang et al. (2005) analyzed radar observations and the results of numerical experiments to investigate the effect of elliptic–shaped topography in CMR terrain on MCS enhancements in a moist environment of Meiyu season. Their results indicated that a predominant westerly wind toward the western CMR was blocked by high terrain, changing the westerly wind to a southwesterly wind that blew parallel to the elongated terrain. Under this configuration, a line-shaped MβCS oriented southwest–northeast slowly approached the northwest CMR from the nearby ocean. The convective cell within the southern part of the system was subsequently significantly enhanced by additional convergence due to terrain blocking, resulting in heavy rainfall (nearly 200 mm in 2 hr) along the northwestern coast of Taiwan. The similar enhanced MCS was reported by Li et al. (1997); the heaviest rainfall occurred along the northwestern coast (windward side) of CMR terrain, with the maximum rainfall of 107 mm for 2 hours on 25 June 1987, related to the low–level convergence caused by orographically–modified airflow. A preexisting MβCS moved eastward heading for the northwestern CMR from off the northwestern ocean with westerly wind. The high terrain of CMR modified the westerly to southwesterly wind, concentrating the low–level moist air in between the system and terrain. Therefore, the prevailing low–level westerly–southwesterly wind toward the CMR terrain in a moist environment is revealed to be a proper condition to trigger the enhancement of a pre-existing MCS on the northwestern upslope of CMR terrain.

Similar to the CMR terrain of Taiwan, Jeju Island of Korea has an isolated topography with an elliptically–shaped mountain, and the southwesterly monsoonal flow prevails in low altitudes during Changma season. Despite these similarities between the two domains, some differences are also apparent; Jeju Island has smaller horizontal scale with lower mountain peak height (width 35 km, length 78 km, height 2 km; Fig. 1.4) than the CMR terrain (width 120 km, length 320 km, height 4 km). Around the relatively–large and high elliptic mountainous region of the CMR terrain, many previous studies (Kuo and Chen, 1990; Chen, 1992; Lin, 1993; Chiao and Lin, 2003; Wang et al., 2005; Yu et al., 2007) have been revealed that the eastward–moving MCS significantly enhanced on the western slope of the CMR terrain with moist southwesterly low–level wind; thus, the large amount of rainfall has been recorded on the western side of the CMR terrain. Around the relatively–small elliptic mountainous region of Jeju Island, the distinct rainfall distribution to the CMR terrain was shown when southwesterly monsoonal flow prevailed. The detailed rainfall distribution will be shown in next section.

Furthermore, the enhanced MCS is frequently blocked in the windward side of CMR terrain, and dissipated gradually. The MCS evolution in the lee side of the elliptical terrain of CMR terrain is still poorly understood. In order to understand the enhancement mechanism of MCS on the lee side, further studies by the analysis of observational data and results of the numerical simulations are required to be done in a domain having a simple isolated terrain with elliptical shape such as Jeju Island.

1.3. Research area

The Jeju Island, southern part of Korea (Fig. 1.4) has frequently suffered from flooding and landslides due to orographically–intensified rainfall systems with a moist environment during the rainy season (June to mid–July). Jeju Island is suitable site for studying orographic enhancement of MCS, as the island is an isolated feature with a simple elliptically-shaped topography of small

horizontal scale (extending east to west; width 35 km, length 78 km, height 1.95 km; Fig. 1.4). Accompanying with the Changma front, the generated MCS has frequently intensified in the vicinities of the island, but the enhancement mechanism has not been revealed yet. In addition, the Korea Meteorological Administration (KMA) operates two S-band Doppler radars at the east and west of Jeju Island, collecting data of reflectivity and Doppler velocity at 10-min intervals.

To investigate the climatological rainfall distribution over the island during June to July for 10 years (from 2003 to 2012), the surface station data collected by KMA on Jeju Island at 1-min intervals at 22 sites (locations of symbols in Fig. 1.5) are used. During the period, the surface rainfall amount over 1.0 mm per hour is considered and then classified into 8 categories according to the hourly surface wind direction (westerly, southwesterly, southerly, southeasterly, easterly, northeasterly, northerly, and northeasterly wind). The classified rainfall amount for each wind category was accumulated during June to July for the 10 years, and the result is shown in Fig. 1.5. The location of rain gauge having the accumulated rainfall less than 1000 mm is shown by white circles, and the size of each circle is weighted to show the relative rainfall amount. The location of the surface rain gauge having the accumulated rainfall less than 2000 mm and 3000 mm, and larger than 3000 mm is depicted as stars colored by light blue, blue, and violet, respectively.

The maximum accumulated rainfall amount (3804.5 mm) was shown in the northern slope of the island with the southwesterly surface wind (violet star in Fig. 1.5b). Simultaneously, the relatively large amount of rainfall accumulated on the northern side of the island and southeastern slope of the mountain. As shown in Fig. 1.5b–d, when the surface wind was southwesterly, southerly and southeasterly during the period, the intense rainfall larger than 2000 mm was accumulated on the northern side of the island. In contrast, with the surface northwesterly and northerly winds (Fig. 1.5e–f), the relatively small rainfall amount less than 700 mm was accumulated on the island. The distinguished rainfall distribution depends on the surface wind direction during June–July across the island implies us the terrain effect of an isolated elliptical–

shaped island on the rainfall distribution over the terrain. However, the terrain effect of the island on the regional rainfall distribution which is strongly associated with MCS enhancement/ dissipation on the island has not been revealed yet. Thus this study aims to reveal the terrain effect of an isolated elliptical–shaped terrain (Jeju Island) on the rainfall enhancement in the vicinities, especially on the northern lateral side and eastern lee side of terrain by both observational and numerical experimental approaches.

In order to achieve the aims, observations and numerical simulations that are sophisticated enough to reveal the fine dynamic and thermodynamic structure of MβCS and the inner convective cells in a moist environment are needed to be conducted. Fortunately, in Jeju Island, fine–scale data can be obtained from two S–band Doppler radars installed in the east and west points of the island (Seongsan (SSN) and Gosan (GSN), open circles in Fig. 1.4b). On 30 June 2006 and 6 July 2007, an elongated intense MβCS, which were accompanied with Changma front, passed over the northern side of the island, and the two cases were successfully observed by the Doppler radars, and are successfully reproduced by a Cloud Resolving Storm Simulator (CReSS; Tsuboki and Sakakibara, 2002) with high resolution of 0.5 and 1.0-km.

A description of the observational data and numerical experiment using CReSS used for the present analysis is presented in Section 2. The analyses result of an MβCS occurred on 30 June 2006 is presented in Section 3. The Section 3 includes the synoptic situation (Section 3.1), the evolution of the convective cell within the system investigated by single–Doppler radar analysis and surface data (Section 3.2), results of sensitivity numerical experiment to reveal the effect of terrain and low–level moisture on the system enhancement (Section 3.3), and brief summary of a case on 30 June 2006 with a conceptual model (Section 3.4). The analyses result of an MβCS occurred on 6 July 2007 is presented in Section 4. The Section 4 consists of environmental description of the system (Section 4.1), 3–dimensional structure investigated by dual–Doppler radar analysis (Section 4.2), and the microphysical structure associated with enhancement of

convective cells within the MβCS revealed by CReSS (Section 4.3). Section 5 describes the results of idealized numerical experiment to reveal the terrain effect of Jeju Island on flow dynamics (Section 5.1) and on the rainfall enhancement (Section 5.2). Section 6 includes a discussion about effects of an isolated elliptic terrain on flow dynamics (Section 6.1) and an isolated elliptic terrain on rainfall enhancement (Section 6.2). The conclusion of the enhancement mechanism of rainfall system applicable to an elliptical–shaped terrain in a moist environment is presented in Section 7.

2. Data and analysis method

Observational data in this study were used to understand the rainfall distribution and the detailed structure and evolution of convective cells within MCS traversing over Jeju Island. The fine spatial and temporal resolution of three–dimensional information achieved these aims. In this study, the range of radar reflectivity stronger than 45 dBZ is referred to as the "convective cell". This region corresponds to the range with intense rainfall. The details of the observational setting are described in the following section.

2.1. Observational data for the case of 30 June 2006

2.1.1. Description of Doppler radar data

Single S–band Doppler radar operated by KMA is located at GSN. The Doppler radar (Fig. 2.1), covering a radius of 250 km (Nyquist velocity of 63.17 $m s^{-1}$) around Jeju Island, records sets of volume scans of reflectivity and Doppler velocity (radius 120 km) every 10 min. The sampling resolution of the radar data is 500 m in the radial direction and 1.0° in the azimuthal direction. Each volume scan consists of 15 elevation angles (0.5°, 0.6°, 0.8°, 1.0°, 1.5°, 2.0°, 2.5°, 3.5°, 4.5°, 6.0°, 7.8°, 10.5°, 13.7°, 18.1° and 24.0°), although the volume scans obtained before 1330 local standard time (LST; = UTC + 9 hr) on June 30 consisted of 13 elevation angles (0.5°, 0.6°, 1.5°, 2.5°, 3.5°, 4.5°, 5.5°, 6.5°, 7.5°, 8.5°, 10.0°, 12.0°, 15.0° and 19.5°).

The Doppler radar data were interpolated in a Cartesian coordinate system with a 1-km horizontal grid and a 0.5-km vertical grid interval (3D Constant Altitude Plane Position Indicators (CAPPI) dataset). For the interpolation, the location of the bin data was shifted to take the advection into account (Gal–Chen, 1982) assuming a westerly of 10 $m s^{-1}$ system movement, and a Cressman–type weighting function was used to increase the radius of influence as the distance

from the radar increased. The horizontal and vertical effective radius of influence was fixed to 1.5 and 1.0 km, respectively (Cressman, 1959).

2.1.2. VVP method for wind retrieval using single Doppler radar

To determine the horizontal wind field, we used a simplified Velocity Volume Processing (VVP) method (Waldteufel and Corbin, 1979; Doviak and Zrnic, 1984; Tatehira and Suzuki, 1994) that can directly calculated the horizontal component of wind within a volume based on the spatial wind-velocity distribution in the radial direction.

The wind components are derived from the radial velocity at the measurement point (γ, θ, φ). A spherical earth coordinate system is used with x and y as arc distances from the radar along two orthogonal great circle paths. The earth's radius vector, drawn through the measurement location, defines the vertical axis along which z measures the height above the surface. The earth is assumed to have an effective radius a_e due to the mean vertical gradients of the refractive index. If $r \ll a_e$, then the coordinates x, y, and z are related to the radar coordinates r, azimuth angle θ, and elevation angle Φ, as follows:

$$\theta' = \theta + \tan^{-1}[r\cos\theta/(a_e + r\sin\theta)]$$

$$x = r\cos\theta'\sin\Phi$$

$$y = r\cos\theta'\cos\Phi$$

$$z = (a_e^2 + r^2 + 2ra_e\sin\theta)^{1/2} + a_e \qquad (2)$$

The radial velocity Vr is the projection of **v** onto **r**, the vector from the radar to the point (γ, θ, Φ):

$$Vr = v \bullet (\hat{\imath}\cos\theta'\sin\Phi + \hat{\jmath}\cos\theta'\cos\Phi + \hat{k}\sin\theta'), \qquad (3)$$

where, ***i, j,*** and ***k*** are unit vectors at **r** in the x, y, and z directions, respectively. Substituting the first-order expansion and the relations for x and y from equation (2) into equation (3), we obtain

$$Vr\ (\gamma,\theta,\Phi)=u_0\ sin\theta cos\Phi + v_0\ cos\theta sin\Phi \qquad (4)$$

where u_0 is the x-component of velocity and v_0 is the y-component of velocity. The vector wind at γ, θ, and Φ is assumed to be well represented by a first-order (linear) Taylor series in a given region, and wind components can be obtained using the following equation-(1) (Doviak and Zrnic, 1984; Tatehira and Suzuki, 1994; Waldteufel and Corbin, 1979). Using the Plane Position Indicators (PPI) data for 0.5° elevation, we conducted the horizontal wind components, u_0 and v_0.

2.1.3. Surface observation and sounding data

To determine the horizontal distribution of rainfall amount over Jeju Island on 30 June 2006, we used rain gauge data collected by KMA at 1-min intervals at 19 sites are located in the island (dots in Fig. 1.5b).

System environment was evaluated using data of upper-air sounding of temperature, wind and humidity at GSN (same site as GSN radar, Fig. 1.5b) of the KMA. For the case of 30 June 2006, sounding data launched at 0900 LST on 30 June 2006 was used. Based on the upper–air sounding data, we calculated several environmental parameters, including precipitable water (PW) at the low-levels from surface to 700 hPa and mid-levels from 700 to 400 hPa, surface relative humidity (RH), and the level of free convection (LFC). *Fr* was calculated using averaged wind velocity below mountain peak (altitude 2 km) obtained from upper-air sounding data.

2.2. Observational data for the case of 6 July 2007

2.2.1. Description of dual–Doppler radar data

As shown in Fig. 2.2, two S–band Doppler radar are operated by KMA on Jeju Island, one at GSN (west) and the other at SSN (east). The distance between the two radar stations is 65 km. The dual–

Doppler radars, which each cover a radius of 250 km (Nyquist velocity of 63.17 $m s^{-1}$) and together cover all of Jeju Island, record volume scans of reflectivity and Doppler velocity (radius 120 km) every 10 min. The two Doppler radars have identical specifications, with sampling resolutions of 500 m in the radial direction and 1.0° in the azimuthal direction. Each volume scan consists of 15 elevation angles (0.5°, 0.6°, 0.8°, 1.0°, 1.5°, 2.0°, 2.5°, 3.5°, 4.5°, 6.0°, 7.8°, 10.5°, 13.7°, 18.1° and 24.0°).

The dual–Doppler radar data are interpolated into a Cartesian system with vertical grid intervals of 0.25 km and horizontal grid intervals of 1.0 km (CAPPI dataset). A Cressman-type weighting function is used for the interpolation with the fixed horizontal and vertical effective radius of influence of 1.5 and 1.0 km, respectively (Cressman, 1959). The moving direction and speed of the precipitation system are reflected in CAPPI dataset for gaining the system-relative wind field (Gal–Chen, 1982); the system moving direction of eastward and speed of 10 $m s^{-1}$ were considered for conducting CAPPI dataset.

2.2.2. Variational method for wind retrieval using dual-Doppler radars

The three Cartesian components of wind are calculated within the dashed circles, except in the intersection area specified in Fig. 2.2 (intersection angle 35°). The dual-Doppler analysis with the three-dimensional variational method introduced by Gao et al. (1999) is used to calculate the distribution of wind velocity. The method, based on a three-dimensional variational approach, permits the use of various constraints through the definition a cost function. Shimizu and Maesaka (2006) modified the original method of Gao et al. (1999) to apply rigid wall condition at top and bottom boundary and evaluated the accuracy of the wind estimated by the method. In this study, the variational method which modified by Shimizu and Maesaka (2006) is used; the boundary condition is specified as $w = 0$ $m s^{-1}$ at z = 0.5 km and the precipitation system top. The observed radar reflectivity at the top of the system was sufficiently weak (less than 15 dBZ) to assume 0 $m s^{-1}$

vertical velocity.

The parameter settings are identical to those used by Gao et al. (1999): $\lambda_o = 1$, $\lambda_d = 1.0 \times 10^5$, $\lambda_{us} = \lambda_{vs} = \lambda_{uw} = 5.0 \times 10^3$, and $\lambda_b = 0$. The calculation error in the vertical velocity is large at upper levels because of signal noise. To account for this uncertainty, airflows are shown only below 6 km above sea level (ASL) and the description of the airflow structure focuses only on the lower and middle levels of the precipitation system.

2.2.3. Surface observation and sounding data

To determine the horizontal distribution of rainfall amount over Jeju Island on 6 July 2007, we used rain gauge data collected by KMA at 1-min intervals at 17 sites are located in the island (dots in Fig. 1.5b).

System environment was evaluated using data of upper-air sounding of temperature, wind and humidity at GSN (same site of GSN radar, Fig. 1.5b) of KMA. Sounding data at 2100 LST on 6 July 2007 was used. Based on the upper–air sounding data, we calculated several environmental parameters, including precipitable water (PW) at the low-levels from surface to 700 hPa and mid-levels from 700 to 400 hPa, surface relative humidity (RH), and the level of free convection (LFC). *Fr* was calculated using averaged wind velocity obtained from upper-air sounding data.

2.3. Model description

2.3.1. Cloud Resolving Storm Simulator

In order to clarify the enhancement mechanism of the orographically induced localized intense precipitation system, and to investigate how the topography and low-level moist condition contributed to the system, we performed numerical simulations using CReSS with 500 m resolution.

CReSS is a three-dimensional non-hydrostatic model developed by Hydrospheric Atmospheric Research Center (HyARC) of Nagoya University, Japan (Tsuboki and Sakakibara, 2002). This model employs fully compressible, non-hydrostatic dynamics, and is designed to realistically simulate mesoscale systems at high resolution using explicit cloud microphysics (see Table 2.1 for a detailed description of the model). The Cartesian coordinate (x, y) in the horizontal and a terrain-following curvilinear coordinate (ζ) in the vertical directions are used, such that

$$\zeta(x,y,z) = z_t[z - z_s(x,y)] / z_t - z_s(x,y) \,, \qquad (5)$$

where z_t and z_s are model heights at the top and surface, respectively. With this coordinate system, the equations for 3-dimensional momentum, pressure, and potential temperature (θ) are formulated as described in detail by Tsuboki and Sakakibara (2002). The equation set includes all types of waves, such as Rossby waves, acoustic waves, and gravity waves. Final variables predicted are 3-dimensional wind components (u, v, and w) and pressure and potential temperature perturbations (p' and θ') from the mean state, which is in hydrostatic equilibrium at the starting time of model integration.

The CReSS model includes a bulk cold rain parameterization and a 1.5-order closure with a turbulent kinematic energy prediction (Tsuboki and Sakakibara, 2001). The prognostic variables in microphysics are the mixing ratios of water vapour (q_v), cloud water (q_c), rain (q_r), cloud ice (q_i), snow (q_s), and graupel (q_g), and the number concentrations of cloud ice (N_i), snow (N_s), and graupel (N_g). The microphysics in CReSS is based on Lin et al. (1983), Cotton et al. (1986), Murakami (1990), Ikawa and Saito (1991), and Murakami et al. (1994). Two moment cold rain scheme is available in CReSS. That is, microphysical processes of CReSS include three basic categories of processes in both liquid water and ice phase: (1) phase nucleation, (2) growth or evaporation by diffusion, and (3) inter-particle collection.

For numerical computation in CReSS, the Arakawa-C staggering grid and the Lorenz grid are used for discretization in the horizontal and vertical, respectively. To improve computational efficiency, a mode-splitting technique (Klemp and Wilhelmson, 1978) is adopted to integrate acoustic mode terms (and gravity mode by option) using a smaller time step $\Delta\tau$, and terms of all other modes using a larger time step Δt. The leapfrog scheme with the Asselin time filter (Asselin, 1972) is used for time stepping, while the Crank-Nicolson scheme can be used to solve p' and w implicitly in the vertical for small $\Delta\tau$ by option. Computational mixing is used to remove grid-scale noise. For parallel computing, data exchange between individual processing elements is performed by the Massage Passing Interface (MPI).

The surface fluxes of momentum and energy and surface radiation processes (Kondo, 1976; Louis et al., 1981; Segami et al., 1989) are included with a 1-dimensional heat diffusion model in the underground layer for ground temperature prediction. The sea surface temperature at initial time is calculated from the dataset of NEAR-GOOS Regional Real Time Data Base, which is provided by Japan Meteorological Agency (JMA). The landuse data is used from the dataset of Global Land Cover Characteristics Data Base, which is provided by U. S. Geological Survey.

2.3.2. Model setting for case on 30 June 2006

Initial and lateral boundary conditions to the numerical simulations were provided by outputs of the Japan Meteorological Agency meso-scale model (JMA-MSM). The JMA-MSM contains a horizontal resolution of 5 km with 253 × 241 grid points and 16 vertical σ levels. The domain of the CReSS simulation is shown in Fig. 2.3 (the smallest inner domain). It was forward-integrated in time using the JMA-MSM output data at 1200 LST on 30 June 2006 as initial data. For the simulation, the horizontal grid size was 500 m and the vertical grid contained 85 levels with variable grid intervals (Δz = 50 m near the surface and 290 m at the top level, at 12.7 km). The horizontal domain had 600 × 600 grid points, with a time step of Δt = 1 s.

We performed three numerical simulations to investigate the influence of orographic effects and a moist environment on localized strong precipitation. First, for the control simulation (CNTL), we ran CReSS with a full physical model containing topography. Second, we ran an experiment without considering terrain (NOTR), in which topography throughout the model domain was assigned the elevation of sea level. Third, we performed low-level RH-controlled numerical experiments in which RH from the surface to 700 hPa in all regions within the initial JMA-MSM output data, since the relatively high RH (~95%) was concentrated below 700 hPa at 1200 LST on 30 June 2006 (not shown). In the sensitivity experiments, RH value was reduced by 10% (experiment D10), 5% (experiment D05), or 2% (experiment D02); other conditions were the same as in the CNTL experiment.

2.3.3. Model setting for case on 6 July 2007

We used output of the JMA-MSM for the initial and lateral boundary conditions of the numerical simulations. The JMA-MSM has a horizontal resolution of 5 km with 253 × 241 grid points and 16 vertical σ levels. The domain of the CReSS simulation is shown in Fig. 2.3 (the biggest inner domain), and it was forward-integrated in time using the JMA-MSM output data from 2100 LST on 5 July 2007 as the initial data. In this study, ST indicates the simulation time following initial time. During the simulation, the horizontal grid size was 1.0 km, and the vertical grid contained 41 levels with variable grid intervals (Δz = 150 m near the surface and 340 m at the top level, at 9.5 km). The horizontal domain had 850 × 740 grid points, with a time step of Δt = 3.75 s.

We performed two numerical simulations to investigate the influence of the terrain on Jeju Island. First, for the control simulation (CNTL), we ran CReSS with a full physical model containing topography. Second, we ran an experiment that did not incorporate the island's terrain (NOTR), in which the topography of Jeju Island was assigned an elevation of 10 m; other conditions were the same as in the CNTL experiment.

To allow a comparison with the radar reflectivity data, we estimated the reflectivity from the predicted 3D mixing ratios of rain water (q_r), snow (q_s), and graupel (q_g), based on Murakami (1990). The range of the estimated reflectivity greater than 50 dBZ is referred to as the convective cell. This range corresponds to the region of intense rainfall.

2.4. Idealized numerical experiment

2.4.1. Design for experiment

The model setup for this study was as follows. The CReSS domain in the present study was set to 31.0°N–35.2°N, 124.0°E–128.5°E (an intermediate domain in Fig. 2.3) with a 1.0-km horizontal grid size. A total of 69 levels were used in the vertical dimension, spaced at 150 m from the surface to 10.3 km; the total number of grid points was 400 × 400 × 69. The USGS GTOPO30 dataset with a horizontal grid spacing of approximately 1-km (http://www1.gsi.go.jp/geowww/globalmapgsi/gtopo30/gtopo30.html) was used for depicting the terrain of Jeju Island. The elliptically shaped Jeju Island spans 126.17°E–126.95°E (width, 78 km) and 33.19°N–33.56°N (length, 35 km). An isolated mountain (Mt. Halla; height, 1950 m) is located in the centre of the island. The CReSS domain was defined so that Jeju Island is located at the centre of the domain (Fig. 2.3). The lower and upper boundary conditions were set as rigid walls. A wave-radiating boundary condition with a constant phase speed (fastest gravity wave speed, 37.5 $m s^{-1}$) and an advection speed was applied at all four lateral boundaries. Each experiment was integrated for 3 hr using the bulk cold–rain microphysics with time steps of 3.75 s (large) and 1.25 s (small) with output every 5 min.

2.4.2. Design of initialization for experiment

Considering the environmental conditions of system occurred on 30 June 2006 and 6 July 2007, the initial flow field in the present study was initialized using a pseudo-sounding derived analytically

from the following parameters: air temperature (T), relative humidity (RH), and horizontal wind (*u* and *v*). In both of the cases, temperature in the range of 296–301 K and relative humidity in the range of 88–90% were observed at the surface. The environments were horizontally homogeneous at the start of the simulations. The maximum T and RH were set to 299 K and 90%, respectively, at the surface and were gradually decreased to 259 K and 50% at a height of 8.0 km, respectively (N = 0.011 s^{-1}). The basic-state T and RH used at each level of the model are shown in Table 2.2. To reproduce the warm and moist environment at low altitudes, the surface T was set to 299 K and the lapse rate at heights of < 3 km was set to the moist adiabatic lapse rate for stable air conditions (N = 0.011 s^{-1}). The RH was set to 90% at heights < 2 km, and gradually decreased with altitude.

In warm and moist environmental condition, southwesterly winds are dominant at low altitudes, and they are gradually redirected to westerly above 2 km, with a gradual increase in wind speed. Considering the wind distribution for two cases on 30 June 2006 and 6 July 2007, three categories of Froude number (*Fr*) were designed: 0.2, 0.4, and 0.55; the detailed wind distributions are shown in Fig. 2.4. From the surface to a height of 2 km, the wind speed is designed to gently increase with height, and is then set as constant above 2 km: 15 m s^{-1} at heights of 2.5–4.5 km and 20 m s^{-1} at heights of 5–8 km. The southwesterly wind is designed to be gently redirected westerly above a height of 2 km, which can bring the rainfall system to the eastern (lee) side of the island.

The rainfall system was initiated with an elongated warm bubble having a maximum potential temperature perturbation of 2 K. The bubble had horizontal and vertical radii of 10 km and 22.5 km, respectively, over which the perturbation decreased to zero. The bubble was centred at a height of 2 km above the ground surface. Control parameters in the present study were wind speed at low altitudes (measured by *Fr*) and the initial location of the bubble (B_{IL}); these parameters are summarized in Table 2.3. For B_{IL}, two case were considered: a bubble off the western shore (BW; 33.35°N, 125.85°E), and a bubble off the northwestern shore (BNW; 33.45°N, 125.85°E) of the island, separated by approximately 10 km (cross symbols in Fig. 1.5a). Experiments without the

warm bubble (no bubble, NB) were performed for the three *Fr* values to understand the terrain effect of the elliptically shaped steep topography of Jeju Island on dynamic fields.

3. Enhancement mechanism of 30 June 2006 precipitation system

3.1. Environmental description

Figure 3.1 shows a surface weather map of East Asia at 0900 LST on 30 June 2006, revealing a stationary front (the Changma/Baiu/Meiyu front) located around Jeju Island. Table 3.1 lists the environmental parameters obtained from an upper-air sounding performed at GSN several hours before the precipitation system developed. A near-saturated layer (surface RH, 92%) was observed from the surface to 700 hPa, with relatively high PW (44.9 $kg\,m^{-2}$); hence near 70 % of the moisture content was concentrated at low-levels, and the average wind speed was around 11 $m\,s^{-1}$ (Fig. 3.2). In contrast, relatively low PW (17.8 $kg\,m^{-2}$) occurred at the mid–levels (700–400 hPa), where relatively strong westerly winds (23.3 $m\,s^{-1}$) was observed. The lifting condensation level (LCL) was high (951 hPa) and surface RH was 92%. The convective available potential energy (CAPE) was calculated to be 33.2 $J\,kg^{-1}$, since the air was almost saturated from the surface under the stationary front and temperature slopes are generally close to the moist adiabatic curve. *Fr* was calculated to be 0.55, indicating that the airflow was unlikely to override the mountain and that it would be affected by the triggering of lee-side convection due to the influence of Mt. Halla (Yoshizaki et al., 2000).

Figure 3.3 shows the surface accumulated rainfall recorded by 19 rain gauges located adjacent to Jeju Island from 1320 to 1500 LST on 30 June 2006. More than 80 mm (maximum 84 mm) of accumulated rainfall was recorded on the northwestern side of Mt. Halla, making this the heaviest rainfall event of 2006. Low rainfall (≤ 20 mm) was recorded on the western and northeastern sides of the island. Although the island is small in size (width 78 km and length 35 km), we observed distinct geographic variations in rainfall amount, with heavy rainfall (> 80 mm in 100 min) recorded on the northwestern side of the island.

3.2. Observation results

To determine the enhancement mechanism of the precipitation system observed over Jeju Island on 30 June 2006, we analyzed the reflectivity and wind distribution of the system using GSN radar data, focusing on its enhancement stage and movement direction. The system was observed by GSN radar from 1230 to 1450 LST on 30 June 2006, as it passed from the western to eastern sides of the island.

Figure 3.4 shows the horizontal reflectivity distribution at 2 km ASL and the low-level wind distribution from 1300 to 1440 LST. At 1300 and 1310 LST (Fig. 3.4a and b, respectively), the convective cell (region with reflectivity greater than 45 dBZ) within the precipitation system was located approximately 40 km west offshore of the island. At these times, low-level wind blew mainly from the west at a velocity of around 10 $m s^{-1}$, although a region of wind convergence was observed northwest of the island. This low-level convergence can be explained by the confluence of northwesterly and southwesterly winds and the occurrence of strong winds (> 10 $m s^{-1}$). As shown in Fig. 3.4c (at 1320 LST), the convective cell moved toward the east, being located approximately 20 km west of the island. VVP calculations revealed southwesterly wind (10 $m s^{-1}$) associated with the convergence region located northwest of the island, corresponding to the southwesterly wind (10 $m s^{-1}$) at around 1,000 hPa observed by upper-air sounding at GSN (Fig. 3.2). From 1330 to 1350 LST (Fig. 3.4d–e), the eastward-moving convective cell moved from the offshore region west of the island to the northwest of the island; in addition, the convective cell over the northwestern island increased in size from 1330 to 1350 LST. At 1400 and 1410 LST, the enlarged area of high reflectivity was identified on the north of the island (Fig. 3.4f–g). At 1420 LST (Fig. 3.4h), when the convective cell was located around the northeastern side of the island, the reflectivity intensity of the convective cell dissipated. At 1430 LST (Fig. 3.4i), the dissipated convective cell was located northeast of the island and a convective cell was barely discernible

within the precipitation system. A further-dissipated horizontal area of convective cell was observed northeast of the island at 1440 LST (Fig. 3.4j).

The enhancement and dissipation process of the convective cell is evident not only in the area of the convective cell, but also in the echo-top height. Figure 3.5 shows vertical cross-sections of reflectivity along the line **A**–**A′** (see Fig. 3.4i) from 1320 to 1430 LST on 30 June 2006, and along the line **B–B′** (see Fig. 3.4j) for 1440 LST on the same day. Before 1330 LST (Fig. 3.5a–b), the height and maximum horizontal width of the convective cell (region with reflectivity greater than 45 dBZ) were ~2.3 km ASL and 6.5 km, respectively, and the maximum width was found near the surface. At 1350 LST (Fig. 3.5c), the height and maximum width had increased to 5.5 km ASL and 11.5 km, respectively, and the maximum width was found above 2.9 km ASL. From 1320 to 1350 LST, we observed large increases in the height and horizontal width of the convective cell, associated with the convective cell moving onshore (Fig. 3.4c–e). The height of the convective cell increased to 6.8 km ASL at 1420 and 1430 LST (Fig. 3.5f–g), and the height of 39 dBZ was observed at around 8.4 km ASL. At 1420 LST, the maximum width of the convective cell increased to 16 km at around 2.7 km ASL. At 1440 LST (Fig. 3.5h), when the convective cell was located northeast of the island (Fig. 3.4j), the height of the convective cell decreased to approximately 6.2 km ASL and the height of 39 dBZ decreased to 6.8 km ASL. At this time, the maximum width of the convective cell had decreased to 6.5 km, and it located above 2.2 km ASL.

The observation data reveal that on 30 June 2006, localized heavy rainfall (> 80 mm) occurred on the northwestern side of Jeju Island due to moist environmental conditions (low LCL of 951 hPa and relatively high average RH of 90% from the surface to 700 hPa) (Table 3.1). Although the precipitation system passed over the topography with easterly movement, the convective cell with reflectivity greater than 45 dBZ within the precipitation system passed northeastward (Fig. 3.4d–f) around the central mountain, probably affected by the high terrain with relatively low *Fr* (0.55). Corresponding to the passage of the convective cell, the precipitation system showed a marked

enhancement on the northwestern lateral side (in this study, the term 'lateral side' refers to the sides of the mountain other than the lee-side and windward side) of Mt. Halla and a subsequent dissipation of reflectivity intensity on the northeastern (downwind) side (Fig. 3.4). Associated with enhancement of the convective cell, the region of low-level wind convergence (7×10^{-4} s^{-1}), which was probably induced by orographic blocking, was observed continuously from 1300 to 1430 LST (Fig. 3.4a–i) northwest of the island. After passing over the low-level convergence region, the convective cell started to dissipate in intensity (both horizontally and vertically) over the lee-side of the island (Figs. 3.4 and 3.5). This time evolution of the convective cell corresponds well with the distribution of rainfall amount recorded by rain gauges (Fig. 3.3). The convective cell caused localized heavy rainfall (> 80 mm) on the northwestern lateral side of the island (Fig. 3.3), where the convective cell was enhanced (Fig. 3.4d–e), whereas relatively low rainfall (≤ 30 mm) occurred on the windward side and lee-side of the island (Fig. 3.3), where the enhanced convective cell dissipated (Fig. 3.4h–j).

3.3. Numerical results

To investigate how the topography and low-level moist environment contributed to the development of localized heavy precipitation on the northwestern lateral side of Jeju Island, we conducted numerical experiments using CReSS with a resolution of 500 m. We compared the precipitation system simulated by the control run (CNTL) with that observed by GSN radar. Based on the CNTL experiment, with some modifications, we conducted a series of experiments to assess the sensitivity of the precipitation system to topography (NOTR) and low-level moisture (D10, D05, and D02). In this study, ST is the simulation time from the initiation of the experiment.

Figure 3.6 shows the horizontal reflectivity and wind distributions at a height of 2,085 m, as simulated by CNTL. We then compared the simulated reflectivity distribution with the reflectivity distribution observed at 2 km ASL by GSN radar (Fig. 3.4). Figure 3.7 shows the horizontal wind

distribution at a height of 50 m, as simulated by CNTL; this distribution was then compared with the low-level wind distribution observed by GSN radar (Fig. 3.4). As shown in Fig. 3.6a, the convective cell (area with estimated reflectivity greater than 45 dBZ) within the precipitation system approached the western side of the island at 0050 ST. At the same time, low-level wind blew around the mountain and a southwesterly wind blew near the western side of the island (Fig. 3.7a), where the convective cell was located (Fig. 3.6a). Associated with the go-around wind (Fig. 3.7a), the model produced low-level wind convergence ($\geq 1.6 \times 10^{-3}\ s^{-1}$) over the northwestern island; the south-southwesterly wind and low-level convergence region over the northwestern island are in good agreement with those observed at 1320 LST (Fig. 3.4c). The convective cell was apparent over the northwestern island at 0140 ST (Fig. 3.6c), with an enlargement of the horizontal extent of the convective cell compared with the previous time step (Fig. 3.6b). This enlarged convective cell corresponds to that observed from 1330 to 1350 LST (Fig. 3.6d–e). As shown in Fig. 3.7c, the low-level convergence region remained over the northwestern side of the island, in a similar position to that at 0050 ST. The horizontal extent of the reflectivity convective cell is larger at 0205 ST than at 0140 ST (Fig. 3.6c–d), and high reflectivity intensity (> 47 dBZ) is predicted over the northwestern island (Fig. 3.6d). Between 0050 ST and 0205 ST (Fig. 3.6a–d), the convective cell increased in horizontal extent and passed over the low-level convergence region located over the western and northwestern island. This simulated convective cell and the convergence region induced by the central mountain are in good agreement with the features observed from 1300 to 1410 LST (Fig. 3.4a–g). The enhanced convective cell moved over the northern slope of the Mt. Halla at 0230 ST, with high reflectivity intensity (> 47 dBZ) over the northwestern side of the island (Fig. 3.6e). After 0255 ST (Fig. 3.6f), the convective cell started to shrink in horizontal extent, as it passed over the low-level convergence region on the lee-side of the topography. The convective cell was almost non-existent over the topography at 0320 ST (Fig. 3.6g), and it moved away from the northeastern island at 0345 ST (Fig. 3.6h). Simulated

reflectivity patterns are partly different from those observed in terms of oriented direction of the high reflectivity region over the island (Figs. 3.4 and 3.6). Although there are some disparities between observation and simulation, the following essential characteristics of the observed convective system are well reproduced by the 1km-CReSS simulation: 1) deflected low-level wind at northwestern island (Figs. 3.4 and 3.7) and 2) enhancement and subsequent dissipation of the convection at northwest and northeast of the island, respectively (Figs. 3.4 and 3.6). Therefore, we propose that the simulated convective system at 0205 ST (Fig. 3.6d) corresponds to the convection observed at 1350 LST (Fig. 3.6e) for the purpose of understanding enhancement mechanism of the convective cell within a precipitation system.

Figure 3.8 shows the low-level RH region at 50 m ASL. At 0050 ST (Fig. 3.8a), when the convective cell was located over the western island (Fig. 3.6a), a region of relatively high RH (~95%) covered the entire island except for the northeastern side (RH ≤ 84%). At 0140 ST (Fig. 3.8c), a moist region (RH ~95%) covered most of Jeju Island, with a relatively dry region (RH ≤ 84%) remaining over the northeastern side of the island. Between 0050 and 0205 ST, the convective cell passed over the region of relatively high RH over the northwestern island, where it showed enhanced reflectivity. After 0255 ST, the convective cell (Fig. 3.6f) moved over the region of relatively low RH on the northeastern lee-side of the island (Fig. 3.8f–h). The area of northeastern island, where the convective cell dissipated, is in good agreement with the region of relatively low RH.

Corresponding to the reflectivity distribution obtained from radar data (Fig. 3.4), the enhancement and dissipation of the convective cell were simulated over the northwestern and northeastern sides of Jeju Island, respectively, producing the simulated distribution of total accumulated rainfall shown in Fig. 3.9, which is in good agreement with the accumulated rainfall distribution recorded by rain gauges (Fig. 3.3). As shown in Fig. 3.9, the area with total accumulated rainfall exceeding 40 mm defines an elongate region aligned WSW–ENE with areas

of total rainfall amount larger than 70 mm (maximum 72 mm) occurring over the northwestern island. In contrast to the high rainfall amount on the northwestern side, relatively low accumulated rainfall (< 30 mm) was simulated on the northeastern side of the island.

The CNTL experiment simulated concentrated heavy rainfall (≥ 70 mm) over the northwestern island. The simulated precipitation system passed over Jeju Island from west to east, whereas the convective cell (range with reflectivity exceeding 45 dBZ) within the precipitation system moved northeastward (Fig. 3.6) and the accumulated rainfall amount, which defined an elongate region aligned WSW–ENE, showed marked enhancement and dissipation over the northwestern lateral side and northeastern downwind side of the island, respectively (Fig. 3.9). Associated with enhancement of the convective cell (Fig. 3.6a–e), the model simulated go-around wind, and a region of low-level convergence (1.6×10^{-3} s^{-1}) due to orographic blocking, and high RH (~95%) over the northwestern island (Figs. 3.7 and 3.8). In contrast, dissipation of the convective cell (Fig. 3.6f–h) was associated with a region of relatively low RH (≤ 88%) over the downwind side of the island (Fig. 3.8). These enhancement and dissipation processes determined the regional rainfall distribution. The region in which the precipitation system was enhanced (Fig. 3.6a–e) was marked by intensively localized heavy rainfall amounts exceeding 70 mm (maximum 72 mm) (Fig. 3.9). In contrast, the region in which the precipitation system dissipated (Fig. 3.6f–h) was characterized by relatively low rainfall amounts of around 30 mm (Fig. 3.9). The simulated distribution of accumulated rainfall amount is in good agreement with the surface rainfall distribution recorded by rain gauges (Fig. 3.3). The distributions of the go-around wind and low-level convergence region induced by orographic blocking, as well as the low-level RH which caused the regional rainfall, were probably controlled by the location of Mt. Halla. To clarify the sensitivity of these distributions to topography and to investigate the contribution of topography to the localized heavy precipitation observed over Jeju Island, we conducted sensitivity experiments based on the CNTL experiment.

3.3.1. Sensitivity experiments investigating orographic effects

We compared the low-level RH and low-level wind convergence simulated in NOTR (in which terrain was not considered) with that simulated in CNTL. Figure 3.10 shows the distributions of the simulated (NOTR) low-level horizontal wind and RH at a height of 50 m. In the NOTR simulation, the precipitation system occurred west of Jeju Island at 0050 ST, subsequently moving over the island, as in CNTL (data not shown). The wind direction was southwesterly near Jeju Island (Fig. 3.10a), and it blew over Mt. Halla. From 0050 to 0345 ST, no south-southwesterly winds and no low-level convergence was simulated around the northwestern and lee-side of the island associated with the distribution of straightforward wind (Fig. 3.10a–h). Homogeneous distribution of the low-level RH (> 92%) was simulated over the island. The local low-level convergences were continuously scarcely distributed on the northwestern and lee side of the island until 0255 ST; homogeneous low-level RH was also continuously present until 0255 ST. At 0320 ST, relatively low RH (< 92%) was simulated over the western and northwestern sides of the island at the time that the precipitation system started to move away from the island.

Figure 3.11 shows the distribution of the difference in total accumulated rainfall amount between the CNTL and NOTR simulations (CNTL minus NOTR). Red (blue) areas indicate greater rainfall amount in CNTL (NOTR) than in NOTR (CNTR). Positive anomalies are seen over the northwestern and southern island. The maximum positive anomaly (> 22 mm) is located over the northwestern lateral side of the island, induced by orographic blocking. The proportion of terrain-produced rainfall amount calculated by subtracting the NOTR amount from the CNTL amount, against the rainfall amount produced by CNTL, is 30.6%. NOTR produced a greater rainfall amount than CNTL over the northeastern and southeastern island. The maximum negative anomaly (18 mm) is seen over the northeastern island, where no orographic blocking occurred. Without the influence of orographic blocking, the area of high rainfall amount moved over the eastern island,

reflecting advection of the precipitation system. The effect of orographic blocking generated maximum positive and negative anomalies over the northwestern and northeastern island, respectively, thereby determining the regional rainfall distribution shown in Fig. 3.9.

Figure 3.12a and b shows the low-level potential temperatures (PT) simulated by CNTL and NOTR, respectively, at 0230 ST, when the convective cell was enhanced in the CNTL experiment. In CNTL (Fig. 3.12a), the region of relatively high PT (≥ 297.5 K) was distributed over the northeastern side of the island, and the region with PT ≤ 296 K occurred over the northwestern side, representing a difference in PT of about 2 K between the two areas. At this time, the location of relatively low RH over the northeastern slope (Fig. 3.8e) coincided with the area of relatively high PT shown in Fig. 3.12a. In the NOTR experiment (Fig. 3.12b), PT increased with decreasing latitude. PT over the northwestern lateral side of the island (≤ 296 K) was similar to that in CNTL, whereas NOTR predicted no regional PT over the northeastern (downwind) side of the island (Fig. 3.12b).

The CNTL experiment predicted terrain–induced horizontally–rerouted wind surrounding the island, whereas NOTR predicted straight–forward wind. In the CNTL case, the go-around wind was associated with the regional low–level convergence (1.6×10^{-3} s^{-1}), relatively high RH (≥ 92%), and low PT (≤ 296 K) over the northwestern side of the island, and relatively low RH (≤ 92%) and high PT (≥ 297.5 K) over the northeastern down-wind side of the island. Simultaneously with the terrain–induced horizontally–rerouted wind, a part of the low–level southwesterly wind seems to go along the mountain slope. Consequently, adiabatic warming due to descending air causes an increase in PT on the downwind side of the island. In fact, we confirmed descending air motion (w, –0.5 m s^{-1}) in the high-PT region (data not shown). An additional experiment performed without considering condensation also showed this high-PT region over the downwind side of the island (data not shown). Therefore, the region of relatively–low RH over the northeastern slope of Mt. Halla is considered to have been induced by topography.

In contrast, the NOTR experiment did not simulate the horizontally–rerouted wind and the associated region of low–level convergence. The CNTL (NOTR) experiment predicted go–around (straightforward) wind and an associated region of the low–level convergence on the northwestern side of the island (region of no convergence), a low RH on the northeastern side of the island (homogeneous RH), and a high PT on the downwind side of the mountain (homogeneous PT). The horizontally–rerouted wind and the associated low-level convergence due to orographic blocking, in combination with the moist environment, produced heavy rainfall on the northwestern slope of the island in CNTL (Fig. 3.9), where a positive anomaly (maximum 22 mm) was distinguished (Fig. 3.11). The dry descending air (w, –0.5 $\mathrm{m\,s^{-1}}$), and orographic blocking combined to produce relatively low rainfall (≤ 30 mm) over the northeastern island in CNTL (Fig. 3.9), where a negative anomaly (maximum 18 mm) was apparent (Fig. 3.11). Although the topography in the present study is of small horizontal scale, the relatively high central mountain controlled the regional distribution of rainfall amount via its influence on the terrain-induced regional distribution of low-level wind, associated convergence, RH, and PT.

3.3.2. Sensitivity of rainfall to the low-level environment

The 30 June 2006 precipitation event occurred during the rainy season under a moist environment with a near-saturated low layer, low value of LCL (951 hPa), and high RH (92%). To investigate how the moist environment contributed to the heavily localized rainfall on the northwestern slope of the island, we compared the results of the D10, D05, and D02 simulations with the CNTL experiment. The D10, D05, and D02 experiments were assigned RH values of 10%, 5%, and 2% less than those within the initial JMA-MSM output data for all regions, respectively, from the surface to 700 hPa. Other conditions were the same as in the CNTL experiment.

To investigate the influence of low-level RH conditions, Fig. 3.13 shows the distributions of the difference in accumulated rainfall between CNTL and each of D02, D05, and D10 (calculated

as CNTL minus each of D02, D05, and D10 experiment). Black contours indicate the topography of Jeju Island, blue shading indicates greater accumulated rainfall amount in CNTL, and gray shading indicates greater rainfall in the RH-sensitivity experiments. The comparison between CNTL and D10 (Fig. 3.13a) reveals an elongate positive anomaly that trends WSW–ENE across Jeju Island, showing the high positive anomalies (over 30 mm; maximum 35 mm) on the western and northwestern sides of the island. The accumulated rainfall amount was reduced by 48.6% when the simulation employed a low-level RH reduced by 10%. The D05 simulation produced more rainfall than that in D10 (Fig. 3.13b). The comparison between D05 and CNTL (Fig. 3.13b) yielded a similar horizontal distribution to that in Fig. 3.13a, with the maximum positive anomaly (27 mm) located in the region where the precipitation had moved toward the island. The experiment produced 37.5% less rainfall than that predicted in CNTL. Figure 3.13c shows the difference in total accumulated rainfall amount between CNTL and D02. Compared with Fig. 3.13a and b, the area in which CNTL rainfall dominated is reduced in size, and the maximum difference in rainfall amount between the two simulations is 15 mm. Rainfall in D02 is reduced by 20.8% compared with that in CNTL.

The results of the numerical experiments are summarized as follows. Orographic blocking and associated horizontally–rerouted wind, low-level convergence, and moist environment in low altitudes combined to intensify the convective cell. Furthermore, the go-around wind caused by orographic blocking modified the movement direction of the enhanced convective cell from eastward to northeastward within the eastward-moving precipitation system. The dissipation of rainfall amount was caused by descending air (w, –0.5 $\mathrm{m\,s^{-1}}$) and a relatively dry region ($\leq$ 92 %) over the downwind side of the central mountain, which were generated by partly go–over southwesterly wind. These enhancement and dissipation processes controlled the regional rainfall distribution over Jeju Island, with heavy rainfall ($\geq$ 70 mm) being concentrated on the northwestern slope of the island. The small but steep topographic features of Jeju Island modified the intensity

and location of the convective cell within a precipitation system, forcing the region of enhanced convective to move northeastward and bringing heavy rainfall to the northwestern island. The sensitivity experiments performed for low-level RH revealed that rainfall amount was highly sensitive to the degree of the moisture in low-levels; increased moisture in the low–level environment induced heavier rainfall and enhanced convection. A reduction in the low–level RH of just 2 % resulted in a 20.8 % reduction in rainfall amount.

3.4. Summary

More than 80 mm of rainfall amount was recorded on the northwestern lateral side of Jeju Island (width 35 km, length 78 km, height 1.95 km) between 1320 and 1500 LST on 30 June 2006. To reveal the enhancement mechanism of the convective cell within a precipitation system (hereafter, it is called as 06P), we analyzed observational data and performed numerical experiments using CReSS with a resolution of 500 m. A schematic illustration of this process is shown in Fig. 3.14. Table 3.2 summarized the environmental conditions and characteristics of 06P. A near-saturated layer (RH 92 %) was observed from the surface to 700 hPa, with relatively high PW (44.9 $kg\,m^{-1}$); hence near 70 % of the moisture content was concentrated at low levels.

The enhancement process of a convective cell (region with reflectivity greater then 45 dBZ) within 06P, which were occurred in a warm and moist environment, analyzed using S-band Doppler radar dataset and results of CNTL experiment. Between 1320 and 1500 LST, 06P moved eastward from west to east with predominant westerly in mid levels. The inner convective cell (blue shaded area in Fig. 3.14) approached to the western side of the island with predominant southwesterly wind in low levels (10 $m\,s^{-1}$; *Fr* of 0.55), and moved northeastward. During the passage, the convective cell showed a marked enhancement and subsequent dissipation over the northwestern lateral side and lee-side of the island, respectively. Associated with enhancement of the convective cell, we observed a region of stationary low-level wind convergence (7×10^{-4} s^{-1},

red shaded area in Fig. 3.14) of the predominant southwesterly wind with the south–southwesterly wind on the northwestern side of the island. As the convective cell passed over the region of low-level convergence, it intensified both horizontally and vertically. Once the convective cell reached the lee side of the central mountain, it started to dissipate both horizontally and vertically. In terms of the dissipation of convection over the lee side of the island, a descending air (w, –0.5 m s^{-1}; gray shading area in Fig. 3.14) and a relatively dry region (RH < 88 %) were simulated over the northeastern island.

Comparison of CNTL and NOTR (in which terrain was not considered) revealed that an isolated small but steep central mountain modified the ambient wind (producing a go-around distribution) and the associated low-level convergence region over the northwestern slope of the island. Corresponding to the enhanced convective cell, we found go-around wind, and an associated region of low-level convergence (1.6×10^{-3} s^{-1}) due to orographic blocking, and a moist environment (RH > 92 %) over the northwestern island. Associated with the relatively low RH (≤ 88 %), we found descending air (w, –0.5 m s^{-1}) due to orographic blocking, and dissipation of the convective cell on the northeastern island. The terrain-induced region of low-level convergence (red shaded area in Fig. 3.14) resulted in enhanced convective cell and the formation of horizontally–rerouted low–level wind due to the influence of orographic blocking on the northeastward passage of enhanced convection. The dissipation of convective cell was caused by descending air (gray shaded area in Fig. 3.14) on the downwind side of the mountain, as revealed by the low surface RH. The small but steep topography modified the intensity and location of the intense rainfall.

The dissipation of convective cell was caused by descending air on the downwind side of the mountain, as revealed by the low surface RH. The small but steep topography modified the intensity and location of the intense rainfall. A comparison of the CNTL and RH-controlled experiments revealed that the low-level moist environment during the rainy season contributed to

the development of convective cell. The increased moisture in the low-level environment induced heavier rainfall and enhanced convection. A reduction in the low-level RH of 2 % resulted in a 20.8 % reduction in rainfall amount.

The enhancement mechanism of a convective cell within a 06P that formed in a moist environment over an isolated small but steep topography is summarized as below, based on both observation data and numerical simulations.

1) The occurrence of an orographically-induced convergence region (7×10^{-4} s^{-1}) and a dry descending air induced by an isolated small, narrow, but steep mountain with moderate *Fr* (0.55) combined to intensify the convective cell over the northwestern island and subsequently dissipate the system over the northeastern island, thereby controlling the localized rainfall distribution over Jeju Island.
2) The NOTR experiment produced no orographically-generated mountain-blocking wind, no associated low-level convergence, and no regional RH distribution; consequently, no regional rainfall distribution was produced over Jeju Island.
3) The development of intense precipitation systems over Jeju Island is especially sensitive to the occurrence of a sufficiently moist low-level environment during the rainy season, which can lead to increased rainfall over the small, narrow, but high topographic features.

4. Enhancement mechanism of 6 July 2007 precipitation system

4.1. Environmental description

On 6 July 2007, an elongated intense precipitation system passed through the observation area of the dual-Doppler radars between 0000 and 0130 LST. Figure 4.1 shows a surface weather map over East Asia at 0300 LST on 6 July. A stationary front was located slightly north of Jeju Island. The horizontal distribution of RH at 950 hPa (Fig. 4.2a) shows that a band-shaped moist region (RH > 94%) covered the southern Korean peninsula at 0000 LST on 6 July 2007. The winds at 950 hPa near Jeju Island were southwesterly and relatively weak (5 $m s^{-1}$). At 700 hPa (Fig. 4.2b), the RH over the island was high (> 94 %) and the winds were westerly and relatively strong (20 $m s^{-1}$).

Table 4.1 lists the environmental parameters obtained from an upper–air sounding launched at GSN a few hours prior to the approach of the precipitation system. A near-saturated layer of air (RH ~94%) was observed near the surface, with high PW (41.7 $kg m^{-2}$) from the surface to 700 hPa. Approximately 65% of the moisture content concentrated in low levels. The lifting condensation level (LCL) was located at 922.9 hPa. By contrast, the PW at mid levels (700–400 hPa) was relatively low (19.8 $kg m^{-2}$). *Fr* was calculated to be 0.2 under these relatively moist low-level conditions at Jeju Island, indicating that the airflow was unlikely to pass over the mountain (Yoshizaki et al., 2000).

In this moist environment in low altitudes, an elongated intense precipitation system passed through the observation area, delivering a relatively high rainfall amount (25 mm over 1.5 h) on the northern lateral side of the mountain on 6 July 2007 (Fig. 4.3). Simultaneously, the maximum accumulated rainfall (35 mm) associated with this system was recorded on the northeastern part of the island.

4.2. Result of dual–Doppler radar analysis

4.2.1. The enhancement of convective cells

The horizontal distributions of reflectivity at 2 km ASL are shown for every 10 minutes between 0000 and 0130 LST in Fig. 4.4. At 0000 LST (Fig. 4.4a), the convective cell (radar reflectivity > 45 dBZ) of the precipitation system was located approximately 20 km from the northwestern shore of the island. The convective cell intensified as it approached the northwestern shore of the island during 0010–0030 LST (Fig. 4.4b–d), then moved eastward during 0040–0050 LST (Fig. 4.4e–f), passing around the northern part of the island and continuing to intensify. The precipitation system was located over the northeastern part of the island at 0100 LST (Fig. 4.4g), while the enhanced convective cell persisted over the northern coast (20–30 km north of GSN). By contrast, the convective cell off the northern coast of the island (30–50 km north of GSN) was relatively weak by this time. The convective cell moved to the eastern slope of the island (10–25 km north of GSN) and re-intensified during 0110–0120 LST (Fig. 4.4h–i), while the convective cell off the northeastern coast of the island (30–50 km north of GSN) weakened even further. By 0130 LST (Fig. 4.4j), the convective cell was located off the eastern shore of the island and relatively weak.

To show the horizontal evolution of the convective cell depending on the relative location to Jeju Island, four analysis domains were selected within a 40 km × 10 km area north of GSN that includes the convective cell. These domains are referred to as **N1** (10–20 km north of GSN over mountainous area), **N2** (20–30 km north of GSN over the northern coast), **N3** (30–40 km north of GSN just off the northern coast), and **N4** (40–50 km north of GSN over open sea). These analysis domains are shifted at the same speed as the system (~10 $m\,s^{-1}$) while it moves through the area. The domain boundaries are depicted in Fig. 4.4b, d, f, and h. Figure 4.5 shows the time variation of the horizontal area of the convective cell at 2 km ASL for every 10 minutes between 2350 LST on 5 July and 0140 LST on 6 July 2007. To better understand the evolution of the system, the system passage can be divided into three stages based on its location relative to the mountain: approaching

stage (0000–0030 LST), lateral-side stage (0040–0050 LST), and lee-side stage (0100–0130 LST). The area of the convective cell in the **N1** domain was less than 10 km^2 during the approaching and lateral-side stages (Fig. 4.5, thick solid line). This area expanded to approximately 60 km^2 during the lee-side stage, when the convective cell moved to the eastern part of Jeju Island, but decreased again after 0130 LST. The area of the convective cell in the **N2** domain consistently enlarged (near 60 km^2) during the approaching and lateral-side stages, with a maximum area of approximately 65 km^2 at 0100 LST (Fig. 4.5, thick dashed line). This area decreased sharply during the lee-side stage, to approximately 20 km^2. The area of the convective cell in the **N3** domain expanded gradually during the approaching stage to a maximum of approximately 40 km^2, before decreasing gently during the lateral-side stage (Fig. 4.5, thin dotted line). Similarly, the convective cell in the **N4** domain expanded gradually during the approaching stage to a maximum of approximately 30 km^2 before decreasing sharply during the lateral-side stage (Fig. 4.5, thin solid line). During the lee-side stage, the areas of the convective cells within **N3** and **N4** were negligible.

The convective cell within this elongated precipitation system evolved differently in each analysis domain (**N1**–**N4**) as the system developed relative to the island (approaching stage, lateral-side stage, and lee-side stage). In particular, the convective cell in **N2** underwent a sharp enhancement near the northwestern coast of the island during the approaching stage. During the lee-side stage, a similar sharp enhancement of the convective cell in **N1** occurred on the eastern slope of the island. By contrast, the convective cells in **N3** and **N4** expanded gradually during the approaching stage, and then dissipated during the lateral-side and lee-side stages after passing around northern part of the island. To reveal the enhancement mechanisms of this precipitation system, the detailed structures and evolutions of the significantly enhanced convective cells in **N2** during the approaching stage and in **N1** during the lee-side stage are examined in detail and contrasted with the structure and evolutions of the less-enhanced convective cells in **N3** and **N4**. This analysis is accomplished using the 3-dimensional reflectivity and wind structure from dual-

Doppler radar data.

4.2.2. The 3–Dimensional structure of the convective cells

The detailed structure of the evolution of the convective cell is analyzed for each of the three stages of precipitation system development using dual-Doppler radar data.

4.2.2.1. Approaching stage (0000–0030 LST)

The horizontal evolution of the convective cell between 0000 and 0030 LST is shown as a sequence of the horizontal distribution of reflectivity at 2 km ASL in Fig. 4.6a–d. Each panel of Fig. 4.6 shows an area of 40 km × 45 km, the location of which is shifted approximately 10 km eastward every 10 minutes. The horizontal axis indicates the distance east of the GSN radar, and the vertical axis indicates the distance north of the GSN radar. As shown in Fig. 4.5, the convective cell strengthened during the approaching stage in all four regions (**N1**–**N4**). Between 0010 and 0030 LST (Fig. 4.6b–d), as the convective cell strengthened, the relatively strong westerly winds (18 m s^{-1}) prevailed at the western side and relatively weak southwesterly winds (9 m s^{-1}) prevailed at the eastern side of the elongated precipitation system at 2 km ASL (Fig. 4.6f–h). Simultaneously, an elongated updraft region (oriented southwest-to-northeast) became obvious on the west side of the precipitation system (Fig. 4.6j–k, dark shading). At 0010 LST (Fig. 4.6f), southwesterly winds (13 m s^{-1}) prevailed in the southern part of the system, from 7 km west to 3 km east and 5 to 12 km north of GSN. As the system approached the northwestern coast of the island at 0020 LST (Fig. 4.6g), these southwesterly winds accelerated to approximately 20 m s^{-1}. This acceleration induced an updraft region between the southern part of the precipitation system and the northwestern coast of the island, around 5 km east and 15 km north of GSN (Fig. 4.6k). At 0030 LST, this updraft region was located 15 km east and 15 km north of GSN (Fig. 4.6l). Relatively weak southwesterly

winds (12 m s^{-1}) appeared at the northwestern side of the island at 0030 LST (Fig. 4.6h), while the precipitation system continued to be characterized by relatively strong westerly winds on its western side and relatively weak southwesterly winds on its eastern side. The winds associated with the precipitation system were of similar direction at 4 km ASL between 0010 and 0030 LST (Fig. 4.6n–p), with westerly winds (13 m s^{-1}) on the western side and southwesterly winds (11 m s^{-1}) on the eastern side. Westerly winds (13 m s^{-1}) also prevailed at 4 km ASL to the south of the system during 0010–0020 LST (Fig. 4.6n–o), in contrast to the accelerated southwesterlies at 2 km ASL (Fig. 4.6f–g). This configuration persisted over the northwestern side of the island through 0030 LST (Fig. 4.6p), with westerly winds (13 m s^{-1}) at 4 km ASL overlying weak southwesterly winds (12 m s^{-1}) at 2 km ASL (Fig. 4.6h).

Several vertical cross-sections have been selected from the regions depicted in Fig. 4.6c–d to illustrate the vertical structure of the updraft region and accelerated southwesterly winds that were generated off the northwestern coast of the island, to the south of the precipitation system. Figure 4.7 shows vertical cross-sections of radar reflectivity and wind along the transect lines a–a', b–b', c–c', d–d', and e–e' at 0020 LST. The transect lines a–a', b–b', and c–c' were selected from around the **N2** analysis domain because they are oriented parallel to the horizontal axis of Fig. 4.6c, near the **N2** analysis domain. Along the a–a' transect, the convective cell had a maximum height of 6.5 km ASL and a maximum width of 6 km (Fig. 4.7a). A region of paired updrafts (dark shading) and the downdrafts (light shading) was located near this convective cell, extending from 1 to 6 km ASL at 10–20 km. The thick downward arrow on the horizontal axis of Fig. 4.7a indicates the Jeju Island coastline. Another updraft region is apparent to the east of this coastline, between the convective cell and the island. This updraft region extended from 1.5 to 6 km ASL at 20–30 km, with reflectivity in excess of 35 dBZ up to 6 km ASL. Along the b–b' transect (Fig. 4.7b), located 5 km north of the a–a' transect, the convective cell is tilted in the vertical from lower–west to upper–east (15–25 km). This vertically tilted convective cell extended from the surface to 4 km ASL with a

maximum width of 7 km. A region of paired updrafts and downdrafts is apparent along this transect at 10–20 km, including an area of intense updrafts (stronger than 4 m s^{-1}) between 2 and 4 km ASL. An additional updraft region can be identified above 3 km ASL to the east of the downdraft region (20–30 km in Fig. 4.7b). Along the c–c' transect (Fig. 4.7c), the convective cell extended from the surface to 6 km ASL with a maximum width of 10 km. The updraft region can be found adjacent to the convective cell, from 1.5 to 6 km ASL, and the downdraft region can be found below 5 km ASL to the east of the updraft region. The additional updraft region identified to the east of the downdraft along the a–a' and b–b' transects (Fig. 4.7a–b) is not apparent along the c–c' transect (Fig. 4.7c). The updrafts between the convective cell and the island were generated locally by the convergence of the strong westerly wind and the enhanced southwesterly wind.

The vertical transects d–d' and e–e' (Fig. 4.7d–e) are oriented parallel to the enhanced southwesterly wind. As shown in Fig. 4.6c, the d–d' transect is located at the center of the southern edge of the precipitation system, while the e–e' transect is located off the northwestern shore of the island. Along the d–d' transect (Fig. 4.7d), the convective cell extended from the surface to 6 km ASL over a relatively wide horizontal range (5–35 km). An updraft region was located adjacent to the convective cell (10–20 km) from 3 to 6 km ASL, with a downdraft region below. The convective cell was relatively small along the e–e' transect (Fig. 4.7e), in the region of accelerated southwesterly winds (Fig. 4.6g) and updraft region (Fig. 4.6k), extending only from 2 to 4.5 km ASL. A relatively wide updraft region is apparent along this transect at 10–28 km. This updraft region tilted from lower–southwest to upper–northeast, and extended from 1.5 to 6 km ASL.

Figure 4.8 shows vertical cross-sections of reflectivity and wind at 0030 LST along the f–f', g–g', h–h', and i–i' transect lines (Fig. 4.6d). The f–f', g–g', and h–h' transect lines are oriented parallel to the horizontal axis of Fig. 4.6d and spaced at 5 km intervals. Along the f–f' transect (Fig. 4.8f), the convective cell extended from 1.5 to 6 km ASL with a maximum width of 6 km. A related updraft region was located to the west of the convective cell. The height of this updraft region

extended from 1 to 6 km ASL, and included areas of intense updrafts (stronger than 4 $m s^{-1}$) above 2 km ASL. Another updraft region that extended from 1.5 to 6 km ASL is apparent to the east of the Jeju Island coastline (indicated by thick downward arrow), in a similar location (east of the downdrafts) to the additional updraft region identified along the a–a' transect (Fig. 4.7a). Reflectivity in excess of 40 dBZ extended to 5 km ASL in this updraft region. Along the g–g' transect (Fig. 4.8g), the convective cell extended from 1 to 5.5 km ASL over the 17–25 km range, with a maximum width of 4 km. A relatively wide updraft region (17 km maximum width) can be identified above 2.5 km ASL adjacent to the convective cell, with intense updrafts at 3–4 km ASL. Along the h–h' transect (Fig. 4.8h), the convective cell extended from 1.5 to 7 km ASL. A relatively narrow updraft region was located above 3 km ASL to the west of the convective cell, in the range of 20–25 km. Downdrafts were predominant below 4 km ASL inside of the convective cell.

The vertical cross-section i–i' is oriented parallel to the southwesterly wind as shown in Fig. 4.6d, with the same cross-section angle as the d–d' and e–e' transects (Fig. 4.6c). The updraft region along the i–i' transect (Fig. 4.8i), was relatively wider (20 km) including intensive updrafts, than those identified along the d–d' and e–e' transects (Fig. 4.7d–e). This updraft region extended from 1 to 6 km ASL over the 15–20 km range (Fig. 4.8i), with intense updrafts above 2 km ASL. A relatively tall convective cell (1.5 to 6 km ASL) was located to the northeast of the updraft region at 22–27 km, and included another region of intense updrafts above 4.5 km ASL.

4.2.2.2. Lateral-side stage (0040–0050 LST)

The convective cell near the northern coast of the island (**N2**) retained its area during the lateral-side stage, while the areas of the offshore convective cells (**N3** and **N4**) gradually dissipated (see Fig. 4.5). Detailed horizontal distributions of reflectivity and wind during 0040–0050 LST are shown in Fig. 4.9.

The consistency of the area of the retained convective cell in **N2** (Figs. 4.5 and 4.9a–b) can be explained by convergence of westerly winds (8 m s^{-1}) at the western edge of the convective cell and southwesterly winds (10 m s^{-1}) over the northwestern slope of the island. At 2 km ASL, this convergence is consistently located 10–30 km east and 10–25 km north of GSN (Fig. 4.9c–d). This horizontal wind distribution induced an updraft region over the northern part of the island (Fig. 4.9e–f). At 4 km ASL (Fig. 4.9g–h), the winds over the northwestern slope of the island were predominantly westerly. The convective cells in **N3** and **N4** gradually dissipated off the northern shore of the island (Figs. 4.5 and 4.9a–b). Westerly (15 m s^{-1}) and southwesterly (10 m s^{-1}) winds appeared at the western and eastern edges of the convective cell, respectively (Fig. 4.9c–d), and the area of the updraft region at 2 km ASL gradually decreased (Fig. 4.9e–f). At 0050 LST, the winds in the convective cell were predominantly westerly (15 m s^{-1}; Fig. 4.9d).

Several vertical cross-sections are used to examine the convective cell over the northern part of the island during the lateral-side stage in further detail. The locations of the transect lines are indicated in Fig. 4.9a–b. Figure 4.10 shows vertical cross-sections of reflectivity and wind along the a–a', b–b', c–c', d–d', and e–e' transect lines at 0040 LST. The a–a' to d–d' transects are oriented parallel to the Jeju Island coastline and spaced at 5 km intervals from the northern slope of the island to the sea off the northern shore. No convective cell is discernable along the a–a' transect (Fig. 4.10a), although an updraft region that extended from 1 to 6 km ASL is apparent over a relatively wide horizontal range (10–35 km). Intense updrafts (stronger than 4 m s^{-1}) occurred between 2 and 5 km ASL at 16–19 km, over the northwestern slope of the island where southwesterly winds were predominant (Fig. 4.9c). At the northeast of the intense updraft region (19–24 km), the height of 40 dBZ was 6 km ASL. These southwesterly winds converged with the predominant westerly winds along the b–b' transect (Figs. 4.9c and 4.10b). Along this transect, the convective cell extended from the surface to 7 km ASL with a maximum width of 14 km. A region of intense updraft region was located in the 17–23 km range (Fig. 4.10b). A relatively tall

convective cell (up to 7 km ASL) was located near the northeastern edge of this intense updraft region. Updrafts along the c–c' transect (Fig. 4.10c) were relatively weak. The convective cell along this transect had a maximum height of 6 km ASL and a maximum width of 7 km. Along the d–d' transect, off the northern shore of the island (Fig. 4.10d), the updraft region was even weaker and convective cell only reached to 3.5 km ASL.

The e–e' transect line is located near the coastline and oriented parallel to the direction of precipitation system movement. Along the e–e' transect (Fig. 4.10e), the convective cell extended from the surface to 5.5 km ASL with a maximum width of 8.5 km, and was slightly tilted from lower–west to upper–east. The Jeju Island coastline is indicated by a thick downward arrow on the horizontal axis of Fig. 4.10e. In the e–e' transect, the westerly and southwesterly winds converged in the offshore area between the coastline and the point located 15 km from point ‘e’ in Fig. 4.10e, inducing a region of intense updrafts at 2–4 km ASL. The convective cell east of these intense updrafts extended to 5.5 km ASL. Reflectivity in this convective cell exceeded 35 dBZ up to 7 km ASL. Downdrafts were predominant off the northwestern shore of the island, in the 7–15 km range (Fig. 4.10e).

Figure 4.11 shows vertical cross-sections of reflectivity and wind along the f–f', g–g', and h–h' transect lines at 0050 LST (Fig. 4.9b). The f–f' to h–h' transects in Fig. 4.11 are oriented parallel to the coastline of the island and spaced at 5 km intervals from the northern slope of the island to the sea off the northern shore. Along the f–f' transect (Fig. 4.11f), where southwesterly winds were predominant (Fig. 4.9d), the convective cell extended from 1 to 4.5 km ASL with a maximum width of 5 km. A related updraft region is apparent at 10–25 km, with intense updrafts from 2 to 6 km ASL (Fig. 4.11f). By contrast, the convective cells along the g–g' and h–h' transects (5 and 10 km north of the f–f' transect, respectively) contained enlarged downdraft regions and relatively small updraft regions (Fig. 4.11g–h).

On the basis of Figs. 4.10 and 4.11, the intense updraft region over the northern slope of the

island was induced locally by convergence of the predominant westerly and local southwesterly winds over the northwestern slope of the island. This convergence ensured that the convective cell in **N2** retained its area as it passed over the northern slope of the island.

4.2.2.3. Lee-side stage (0100–0130 LST)

During the lee–side stage, the area of the convective cell in **N1** expanded significantly, whereas that of the convective cell in **N2** was reduced (see Fig. 4.5). Figure 4.12 shows the detailed horizontal evolutions of reflectivity and wind in the vicinity of the convective cell. At 0100 LST (Fig. 4.12a), the precipitation system is located over the northeastern part of the island and moving eastward. The area of the convective cell at 2 km ASL in **N2** was roughly unchanged from that in the lateral-side stage at this point (Fig. 4.5). Westerly (12 $m s^{-1}$) and southwesterly (13 $m s^{-1}$) winds were observed approximately 35 km east and 25 km north of GSN (Fig. 4.12e). The convergence of these winds induced an updraft region on the western side of the convective cell (Fig. 4.12h) in **N2**. Relatively strong southwesterly (16 $m s^{-1}$) and weak westerly (5 $m s^{-1}$) winds were observed to the east of the convective cell, 50 km east and 25 km north of GSN (Fig. 4.12e). Related updrafts occurred in a region 45–63 km east and 18–22 km north of GSN, ahead of the eastward-moving precipitation system (Fig. 4.12h). Strong southwesterly winds were also observed at 4 km ASL over the updraft region (Fig. 4.12k).

During 0100–0110 LST, the convective cell moved with the predominant westerly wind to the eastern slope of the island, passing over the region of preexisting updrafts (Fig. 4.12a–b). At 0110 LST, the convective cell in **N1** (Fig. 4.4h) extended horizontally to the southwest (Fig. 4.12b). The updraft region at 2 km ASL was consistently located over the eastern part of the island adjacent to the convective cell, 45–63 km east and 18–22 km north of GSN (Fig. 4.12i). Strong southwesterly (20 $m s^{-1}$) and weak westerly (6 $m s^{-1}$) winds were consistently observed in the vicinity of this updraft region (Fig. 4.12f). Off the northeastern shore of the island (**N3** and **N4**), the winds were

westerly (15 m s^{-1}) during this period at both 2 km and 4 km ASL (Figs. 4.12e–f and 4.12k–l). These steady westerly winds contributed to the further dissolution of the convective cell off the northeastern shore of the island (Fig. 4.12b), as shown in Fig. 4.5.

The convective cell in **N1** retained its intensity as it approached the eastern coastal area of the island at 0120 LST, whereas the intensity of the convective cell in **N2** was relatively weak (Figs. 4.5 and 4.12c). During 0110–0120 LST, the convective cell in **N1** passed over the preexisting updraft region on the eastern slope of the island (see Fig. 4.12i), preserving the convective cell as it entered the eastern coastal area of the island at 0120 LST. At this time, the winds over the eastern coast of the island were southwesterly at 10 m s^{-1} (Fig. 4.12g). This horizontal wind distribution weakened the updraft region (Fig. 4.12j). The winds at 4 km ASL over the eastern part of the island (Fig. 4.12m) were westerly and nearly homogeneous (12 m s^{-1}). At 0130 LST, the convective cell was located off the eastern shore of the island and was relatively reduced in size and intensity (Fig. 4.12d).

Several vertical cross-sections are used to examine the vertical structure of the convective cell, the relatively strong southwesterly wind, and the preexisting updraft region in further detail. The locations of these transect lines are indicated in Fig. 4.12a–c. Figure 4.13 shows the vertical sections of reflectivity and wind along the a–a', b–b', c–c', and d–d' transect lines at 0100 LST (Fig. 4.12a). Transects a–a' and b–b' are oriented perpendicular to the convective cell and spaced 5 km apart. Along the a–a' transect (Fig. 4.13a), an upright convective cell extended from 0.5 to 5.5 km ASL with a maximum width of 6 km. Two updraft regions were located below 2.5 km ASL and above 4.5 km ASL at 13–18 km along the transect (Fig. 4.13a). The preexisting updraft region shown in Fig. 4.12h was located to the southeast of the convective cell. This updraft region extended from 1 to 6 km ASL with a maximum width of 14 km, and included an area of intense updrafts (stronger than 4 m s^{-1}) above 2.5 km ASL. The maximum height of 40 dBZ reflectivity exceeded 6 km ASL in the intense updraft region. At this time, the downdraft region was located on

the northwestern side of the convective cell (0–15 km). Along the b–b' transect (Fig. 4.13b), 5 km north of the a–a' transect, the convective cell extended from 1 to 5 km ASL with a maximum width of 8 km. Downdrafts occurred below 5.5 km ASL, while updrafts occurred above 3 km ASL over the land area. The intense updraft region identified along a–a' (Fig. 4.13a) is not apparent along b–b'.

The c–c' transect (Fig. 4.13c) is oriented parallel to the Jeju Island coastline (Fig. 4.12a). As with the b–b' section, the convective cell extended from 1 to 4.5 km ASL, with downdrafts prevalent below 5 km ASL. Along the d–d' transect (Fig. 4.13d), which is oriented parallel to the strong southwesterly wind and located over the eastern slope of the island (Fig. 4.13a), a concentrated narrow updraft region extended from 1 to 6 km ASL approximately 7–17 km along the transect. This updraft region contained an area of intense updrafts and a thin convective cell (1.5 km wide) that extended from 2.5 to 3.5 km ASL. The updraft region was only localized ahead of the eastward-moving convective cell over the eastern slope of the island at 1 km ASL and higher.

Selected vertical distributions of reflectivity and wind fields at 0110 LST are presented in Fig. 4.14. The a–a', b–b', and c–c' transects are oriented parallel to the horizontal axis of Fig. 4.12b and spaced at 5 km interval from the eastern slope to the northeastern coastal area of the island. Along the a–a' transect (Fig. 4.14a), the convective cell was tilted from lower–west to upper–east, and extended from the surface to 7.5 km ASL at 10–20 km along the transect. Updrafts were predominant within the convective cell, including two regions of intense updrafts (the darkest shading). One intense updraft region was located above 2 km ASL, at the west side of the convective cell near 8–15 km. Another intense updraft region was located above 3.5 km ASL near 15–25 km, and included a relatively tall convective cell that extended up to 7.5 km ASL. Along the b–b' transect (Fig. 4.14b), 5 km north of a–a', the convective cell was dominated by downdrafts. A narrow updraft region was located at 8–10 km along the transect with a vertical extent from 1 to 3.5 km ASL. To the east of this narrow updraft region, the convective cell extended from the surface to

6 km ASL with a maximum width of 7 km. To the east of this convective cell, another updraft region was located at 20–32 km above 2 km ASL, including a short convective cell between 2 and 4 km ASL. The maximum height of 40 dBZ reflectivity in this updraft region was 5.5 km ASL. Along the c–c' transect (Fig. 4.14c), 5 km north of b–b', the convective cell was even further diminished. This convective cell extended from 2 to 4 km ASL with maximum width of 4 km, and was dominated by downdrafts. The updraft region was very small, and is barely discernable in Fig. 4.14c.

The d–d' transect (Fig. 4.14d) is oriented parallel to the strong southwesterly wind and passes through the center of the convective cell. The convective cell was horizontally extensive along this transect, with a maximum width of 20 km. A relatively short convective cell (1 to 3 km ASL) was located at 0–10 km, over the eastern slope of the island. Updrafts were prevalent in this region above 2 km ASL, including an area of intense updrafts between 3 and 4 km ASL. This updraft region extended upward and northeastward, with another area of intense updrafts above 5.5 km ASL at 12–13 km. A relatively tall convective cell (6 km ASL) was located adjacent to this area of intense updrafts. Another narrow updraft was located in 4–6 km ASL at 20 km, coincident with another peak in the height of the convective cell (6 km ASL). Downdrafts were prevalent below 6 km ASL in the convective cell at 10–17 km (Fig. 4.14d). The e–e' transect (Fig. 4.14e) is oriented perpendicular to the convective cell. Downdrafts dominated the convective cell below 6 km ASL along the e–e' transect. A relatively wide updraft region (15 km) was located above 2 km ASL to the southeast of the convective cell.

Figures 4.13 and 4.14 indicated that the convective cell strengthened significantly as it passed over the preexisting intense updraft region on the eastern slope of the island. Figure 4.15 shows vertical cross-sections along the a–a', b–b', c–c', and d–d' transect lines at 0120 LST, when the convective cell moved to the eastern coastal area of the island. The locations of the transect lines are indicated in Fig. 4.12c. The a–a', b–b', and c–c' transects are oriented parallel to the Jeju Island

coastline and spaced at 5 km intervals. Along the a–a' transect (Fig. 4.15a), updrafts were prevalent above 2 km ASL between 15 and 20 km. This region included an area of intense updrafts located above 3.5 km ASL over the land area. Convective cell was located above 4.5 km ASL adjacent to the intense updrafts. The intense updraft and convective cells identified along the a–a' transect are not discernable along the b–b' and c–c' vertical sections (Fig. 4.15b–c; 5 and 10 km north of a–a', respectively). The d–d' transect is oriented parallel to the southwesterly wind along the eastern slope of the island (Fig. 4.12c). Along the d–d' transect (Fig. 4.15d), the convective cell extended from the surface to 2 km ASL with a downdraft region above it. Another convective cell extended from 4 to 5 km ASL (14–16 km). A related updraft region that included intense updrafts was located above 3.5 km ASL to the southwest of the convective cell (5–15km).

During the lee-side stage, the convective cell was significantly enhanced by local conditions on the eastern slope of the island. By contrast, the convective cell that passed off the northeastern shore of the island weakened and dissipated. The significant enhancement of the convective cell on the eastern slope was driven by the convergence of relatively weak westerly winds (6 $m\,s^{-1}$) on the northeastern slope and strong southwesterly winds on the eastern slope of the island. These winds were consistent throughout the lee-side stage, and induced a localized updraft region over the eastern slope of the island. By contrast, the convective cells over the northeastern coastal area and off the northeastern shore were characterized by downdrafts and homogeneous westerly winds of 13 $m\,s^{-1}$.

4.2.3. Summary

An elongated precipitation system strengthened significantly on the northern lateral and lee sides of an isolated mountain on Jeju Island on 6 July 2007 (hereafter, it is called as 07P). At 0300 LST, a stationary front (the Changma/Baiu/Meiyu front) was located slightly north of the island. Figure 4.16 shows the time–height cross section of maximum reflectivity in the analysis domains of **N1**,

N2, **N3**, and **N4**. Table 4.2 summarized the environmental conditions and characteristics of the 07P. Figure 4.17 shows the schematic illustration of the evolutions of the convective cells within the system.

A near–saturated layer of air (RH 90 %, Table 4.2) was observed near the surface with relatively high PW (41.7 kg m^{-2}) from the surface to 700 hPa; near 65 % of the moisture content concentrated in the low levels with weak southwesterly winds (around 5 m s^{-1}; *Fr* of 0.2). In the warm and moist environment, the 07P moved eastward and passed over the northern side of the island, showing two–times enhancement of the convective cell within the elongated 07P (Table 4.2); (1) in the approaching stage off the northwestern shore of the island, and (2) in the lee–side stage on the eastern side of the island.

4.2.3.1. Approaching stage

During the approaching stage, the convective cell (region with reflectivity greater than 45 dBZ) of the precipitation system intensified significantly in the northwestern coastal area of the island (Fig. 4.16a). This intensification was evident in the expansion of the area of the convective region at 2 km ASL from 10 to 60 km^2, and is shown in further detail in Fig. 4.16 as a time–height cross–section of maximum reflectivity. The heights of reflectivity in excess of 44 dBZ increased gradually from 0000 to 0020 LST in the **N2** (Fig. 4.16c; coast), **N3** (Fig. 4.16b; offshore), and **N4** (Fig. 4.16a; open sea) analysis domains. In **N2**, reflectivity in excess of 40 dBZ was observed up to 8 km ASL, and the area of reflectivity greater than 48 dBZ extended from the surface to 6 km ASL (Fig. 4.16c).

During this stage, relatively strong westerly winds (18 m s^{-2}) prevailed at the western side and relatively weak southwesterly winds (9 m s^{-2}) prevailed at the eastern side of the elongated 07P at 2 km ASL; an updraft region was then identified in the western side within the elongated system (longer hatched area in Fig. 4.17a). As the system approached the island from the northwest, the

distance between the southern part of 07P and the terrain decreased. In the space between the system and terrain on the sea, the accelerated southwesterly winds and the related regional updrafts were observed: another updraft region was identified (shorter hatched area in Fig. 4.17a). Related to the updraft, the strong enhancement of the convective region in **N2** (Figs. 4.5, 4.6b–c, and 4.16c) was driven by a localized updraft region (Fig. 4.6j–k; short hatched area in Fig. 4.17a) located between the southern part of the precipitation system and the island.

4.2.3.2. Lateral side stage

Following its intensification in the northwestern coastal area of the island, the convective cell maintained its intensity as it moved along the northern lateral side of the island (Fig. 4.17b). The horizontal area of the convective cell was consistently 60–65 km^2 at 2 km ASL; the height of reflectivity in excess of 48 dBZ was approximately 6 km ASL during the lateral–side stage (Fig. 4.16c). When the convective cell located on the northern lateral side of the island, the terrain–induced southwesterly winds with a relatively low *Fr* of 0.2 was observed on the northern part of the island (gray shaded arrow in Fig. 4.16b). Simultaneously, an updraft region (hatched region in Fig. 4.17b) was apparent on the northern side of the island, where the terrain–induced southwesterly wind converged with predominant westerly wind.

4.2.3.3. Lee side stage

Subsequently, the convective cell moved to the lee-side of the island, where it again intensified significantly (Fig. 4.17c). The area of the convective cell at 2 km ASL on the eastern side of the island increased significantly from 15 to 55 km^2. This significant enhancement of the convective cell is shown in Fig. 4.16d and illustrated schematically in Fig. 4.17c. The height of 40 dBZ reflectivity increased to 7.5 km ASL and that of strong reflectivity (48 dBZ) increased to 4 km ASL

(Fig. 4.16d). When the convective cell intensified, weak westerly wind from the northern lateral side of the island and relatively strong southwesterly from the southeastern slope of the island converged, generating a local updraft region over the lee-side of the island, consistently (hatched region in Fig. 4.17c). Subsequently, enhancement of the convective cell occurred as it passed over these locally generated updrafts. The part of the system passing off the northeastern shore showed the gradual decrease (Figs. 4.5, 4.12, and 4.16a–b).

The eastward–moving precipitation system of 6 July 2007 was enhanced locally and significantly on the lateral and lee sides of Jeju Island by orographically generated updrafts. This enhancement took place under the prevailing moist environment during the rainy season with ambient west-southwesterly winds observed in low altitudes. The analysis results of 07P stated in chapter 4.2 are summarized below.

1) A preexisting elongated precipitation system (oriented southwest–northeast) and an isolated elliptical mountain on Jeju Island (oriented west–east) induced accelerated southwesterly winds, convergence, and localized updrafts off the northwestern shore of the island as the system approached. Moist atmospheric conditions at low altitudes during the rainy season and the localized updraft between the system and the island combined to cause a dramatic enhancement in the southern part of the precipitation system.
2) The isolated elliptically-shaped terrain of Jeju Island played a role in modifying the low-level wind with a low *Fr* of 0.2. The horizontal rerouting of the wind at low altitudes by the terrain worked in concert with low-level moist air during the rainy season, resulting in further enhancement of the convective region as the system passed over the northwestern part of the island.
3) The terrain-modified low-level winds provided a plentiful supply of moist air into the enhanced convective region as the precipitation system passed around the northern part of the island. These environmental conditions acted to maintain the intensity of the convective region.

4) Relatively strong southwesterly wind coming over the southeastern slope of the island (height less than 500 m) generated a stationary local updraft over the eastern part of the island. The convergence of the relatively strong and moist southwesterly winds with the prevailing westerly winds caused the convective region to again intensify significantly as it passed over the lee-side of the island.

4.3. Numerical results

To develop an improved understanding of the microphysical structure of the atmosphere during such enhanced convective cells in the approaching and lee side stages, a CReSS with a high resolution (1 km) was conducted. CReSS successfully reproduced the enhancements of convective cells within the system that was observed by dual-Doppler radar on 6 July 2007. The simulation results allowed us to investigate the microphysical structures associated with the enhancements of convective cells that occurred off the northwestern shore and lee side of the isolated elliptical-shaped terrain of Jeju Island, with a focus on the distinctive properties of the two periods. To allow a comparison with the radar reflectivity data, we estimated the reflectivity from the predicted 3D mixing ratios of rain water (q_r), snow (q_s), and graupel (q_g), based on Murakami (1990). The range of the estimated reflectivity greater than 50 dBZ is referred to as the convective cell. In this study, ST is the simulation time from the initiation of the experiment.

4.3.1. Simulated enhancement of convective cells

The horizontal distributions of relative humidity (RH) and the mixing ratio of water vapour (q_v) at 0020 ST on 6 July 2007 from the CNTL simulation are shown in Fig. 4.18a. The RH distribution at a height of 407 m indicates two moist regions (RH over 96%) located on the northern and southeastern slopes of the island before the system approached the island. With the prevailing

southwesterly wind at low altitudes, a relatively low q_v of less than 16 g kg^{-1} was apparent on the northeastern side of the island. In the NOTR run (Fig. 4.18b), the local moist region that was found on the southeastern side of the island was hardly distributed. RH was shown to be high (> 96%) on the north of the island, and relatively low (< 88%) over the south, and q_v increased with decreasing latitude.

The eastward-moving precipitation system passed the northern side of the island and showed two periods of enhancement of its convective cells close to the islands with mountainous terrain (Fig. 4.17). As shown in Fig. 4.19, two regions of accumulated rainfall greater than 45 mm (deep gray shading with thin contours) were also generated by CReSS off the northwestern shore and on the northeastern side of the island. The simulated precipitation system by CReSS is compared with the rainfall distribution recorded by 17 surface rain gauges. As the rain gauges are installed on the ground surface, the comparison is restricted on the surface. On the northern coast of the island where rainfall amount of 24 mm in 1.5 hours recorded by rain gauge (dots), the simulated rainfall is in the range of 15–25 mm in 2.5 hours (the lightest gray shading). Simultaneously, on the northeastern coast of the island where the rainfall amount of 34.5 mm observed (dot), the simulated rainfall is in the range of 35–45 mm. In addition, the rainfall distribution conducted by CReSS implies the enhancement of the eastward–moving precipitation system. In the range of 33.4–33.6°N and 125.9–126.5°E, the gradual increase of the accumulated rainfall amount is depicted in west–east direction; subsequently the maximum accumulated rainfall amount larger than 55 mm is resulted off the northern shore of the island (33.5–33.6°N, 126.3–126.6°E). Simultaneously, in the range of 33.4–33.6°N and 126.7–126.9°E, the gradual increase of the accumulated rainfall amount is characterized in west–east direction, as well as in southwest–northeast direction. With this rainfall distribution, the large amount of accumulated rainfall over 45 mm is shown in northeastern coast of the island. The realistically reproduced the enhancements of convective cells off the

northwestern and eastern sides of the island on 6 July 2007 are detailed below, and divided into two stages: the approaching stage and the lee-side stage.

4.3.1.1. The approaching stage

Figure 4.20 shows the horizontal distributions of estimated reflectivity, horizontal wind, and convergence at 10-minute intervals between 0030 and 0110 ST, and includes a sequence of the horizontal distribution of the estimated reflectivity (contouring from 40 dBZ at an interval of 5 dBZ, light shading between 40 and 45 dBZ, and dark shading between 50 and 55 dBZ) at a height of 1.9 km. Regions with maximum convergences weaker (cross) and greater (circle) than 3×10^{-3} s^{-1} below a height of 1 km are also indicated, and the gray thick and thin solid lines in each panel mark the coast and topography of Jeju Island, respectively. Each panel of Fig. 4.20 shows an area of 0.45°N × 0.85°E, the location of which was shifted approximately 10 km eastward every 10 minutes, following the system movement. At 0030 ST, the area with reflectivity over 45 dBZ was located approximately 20 km from the northwestern shore of the island (Fig. 4.20a). A southwesterly wind of 10 m s^{-1} prevailed around the island at a height of 595 m. Between 0030 and 0050 ST (Fig. 4.20a–c), as the precipitation system approached the northwestern shore of the island, the convective cell (reflectivity >50 dBZ) interior of the system enlarged horizontally. At 0050 ST (Fig. 4.20c), the relatively strong southwesterly wind of 12 m s^{-1} was blowing between the system and the island (33.25°N–33.35°N, 126.0°E–126.3°E). The related low-level convergence of less than 3×10^{-3} s^{-1} was identified in the area between 33.3–33.45°N and 126.0–126.3°E, but this was not well simulated by the NOTR experiment (not shown). In between 0050 and 0100 ST (Fig. 4.20c–d), the regions of reflectivity stronger than 40 and 45 dBZ extended toward the southwest, where the convergence zone was located onshore at 0050 ST (Fig. 4.20c). At 0100 ST (Fig. 4.20d), the convective cell was situated near the northwestern coast of the island. In a region between 33.3°N–33.4°N and 126.06°E–126.3°E, the low-level convergence of less than 3×10^{-3} s^{-1} was

continuously apparent, with a relatively strong southwesterly of 12 m s^{-1}. Simultaneously, localized low-level convergence (< 3 × 10^{-3} s^{-1}) developed in the region bounded by 33.47°N–33.53°N and 126.2°E–126.4°E, off the northwestern shore of the island. As the convective cell moved further eastwards, and passed over the local low-level convergence between the system and the island, the relatively intensified convective cell developed at 0110 ST (Fig. 4.20e). At the same time, the regions of reflectivity stronger than 40 and 45 dBZ extended horizontally toward the southwest.

To show the horizontal evolution of the convective cell at a height of 1919 m, during the approaching stage, an analysis area (domain **A)** was selected within a 60 × 40 km^2 area (Fig. 4.20d), which includes the reflectivity region exceeding 45 dBZ. The analysis domain was shifted at the same speed as the system (ca. 10 m s^{-1}) as it moved through the area. Figure 4.21 indicates the time variation of the horizontal area of the convective cell (solid line), and also the range with reflectivity over 45 dBZ (dashed line) at a height of 1.9 km during the approaching stage (0020–0110 ST). During this period, the area of the convective cell within domain **A** expanded gradually from 23 to 88 km^2. Simultaneously, the horizontal area with reflectivity stronger than 45 dBZ enlarged from 178 to 345 km^2. Figure 4.22a shows a vertical profile of the enhanced horizontal area of the convective cell from 0030 to 0100 ST within domain **A**, and the horizontal enlargement of the convective cell during this period was significant near the surface where it exceeded 40 km^2, and an areal enlargement of over 10 km^2 was apparent from the surface up to an altitude of 2.6 km. Figure 4.22b shows a vertical profile of the difference in the horizontal areas with reflectivity over 45 dBZ (thin solid line) and 50 dBZ (thick solid line) between the CNTL and NOTR experiments (CNTL minus NOTR) at 0100 ST, when the enhanced convective cell was located close to the northwestern coast of the island. As shown in Fig. 4.22b, the positive anomalies of the convective cell (thick solid line) were identified from the surface to the 1.5 km level. In addition, the positive anomalies larger than 10 km^2 of the reflectivity region over 45 dBZ (thin solid line) were concentrated below 1.5 km. The positive anomalies exceeding 5 km^2 with reflectivity over 45 dBZ

extended up to an altitude of 3 km.

Related to the enhancement of the convective cell during the approaching stage, the evolution of the updraft (w) is shown in Fig. 4.23a. Vertical profiles of the maximum updraft at 0030 ST, 0100 ST, and the difference between them (0100 ST minus 0030 ST) within domain **A** are indicated by the dashed line, thin solid line, and thick solid line, respectively. The maximum updraft was less than 0.5 m s^{-1} below 1 km at 0030 ST. Within 30 minutes, the updraft had doubled to 1 m s^{-1} below a height of 1 km, as the convective cell approached the northwestern coast of the island (Fig. 4.20a–d). The profiles of temperature (T, black solid line), dew point temperature (TD, dashed line), and relative humidity (RH, gray solid line) at the point of maximum updraft at 0100 ST are shown in Fig. 4.23b. The surface temperature was 23°C, and the temperature remained above 20°C to a height of 0.8 km. An almost saturated layer was apparent from the surface to the 1 km level, where the updraft had doubled and RH was high (99%). The updraft gradually increased up to a height of 4.6 km (Fig. 4.23a), and reached a maximum of 7.8 m s^{-1}. Corresponding to the updraft profile at 0100 ST, the positive updraft anomaly between 0030 ST and 0100 ST attained a maximum of 2.3 m s^{-1} at a height of 4.6 km. Above 4.6 km, the positive updraft anomalies decreased gradually. Temperature decreased gradually with height, and had fallen to 0°C at 4.9 km.

4.3.1.2. The lee–side stage

Figure 4.24 shows the horizontal distributions of estimated reflectivity, horizontal wind, and convergence at intervals of 10 minutes between 0130 and 0210 ST; the thick gray solid line indicates the coastline of Jeju Island. At 0130 ST (Fig. 4.24a), the convective cell was located on the northern side of the island within domain **B** (rectangle in Fig. 4.24). Adjacent to the convective cell, a relatively weak westerly wind of 5 m s^{-1} blew along the northern side of the island. At the same time, convergence (gray cross) below 1 km on the eastern side of the island, driven by the relatively weak northwesterly (6 m s^{-1}) from the north, converged with the relatively strong

southwesterly (11 $m\,s^{-1}$) from the southeastern slope of the island (at elevations below 500 m), where a region of high RH (> 96%) was identified (Fig. 4.18a). Between 0140 and 0200 ST (Fig. 4.24b–d), the convective cell within domain **B** moved from the northern to the northeastern side of the island, passing on the stationary local convergence at low altitudes on the eastern slope. Consequently, at 0200 ST (Fig. 4.24d), a further horizontally enlarged convective cell was apparent on the northeastern side of the island. At 0210 ST (Fig. 4.24e), the relatively weakened convective cell was shown close to the east coast of the island.

Figure 4.25 shows the horizontal development of the convective cell within domain **B** at a height of 1919 m, and at intervals of 10 minutes, between 0130 ST and 0220 ST. The horizontal extent of the convective cell at 0130 ST was less than 5 km^2. As the convective cell passed to the northeast of the island (Fig. 4.24a–c), its horizontal area gradually increased, to reach a maximum of 18 km^2 on the eastern side of the island where the stationary convergence was identified (Fig. 4.24d). At 0210 ST, when the convective cell moved to the eastern coast of the island (Fig. 4.24e), the area of the convective cell decreased dramatically to less than 10 km^2 (Fig. 4.25). The vertical profile of the enhanced horizontal area of the convective cell from 0140 to 0200 ST within domain **B** (Fig. 4.24) is shown in Fig. 4.26a. The enlargement of the horizontal area of the convective cell to over 10 km^2 was apparent between heights of 0.7 to 3.3 km. Figure 4.26b shows the vertical profile of the difference in the horizontal area with reflectivity over 45 (thin solid line) and 50 dBZ (thick solid line) between the CNTL and NOTR simulations (CNTL minus NOTR) at 0200 ST when the horizontally enlarged convective cell was located on the northeastern slope of the island (Fig. 4.24d). The positive anomalies of the convective cell (thick solid line) were concentrated between 3 and 4.5 km in height. The positive anomalies in the area with reflectivity over 45 dBZ developed in two zones at heights of 1.5–3.5 km and 4.7–5.4 km.

Related to the enhancement of the convective cell during the lee-side stage, the evolution of the updraft (w) is shown in Fig. 4.27a. Vertical profiles of the maximum updraft at 0140 ST, 0200

ST, and the difference between them (0200 ST minus 0140 ST) within domain **B** are shown by a thin dashed line, thin solid line, and thick solid line, respectively. At 0200 ST, the updraft stronger than 1 $m\,s^{-1}$ was located above 1 km level. The profiles of temperature (T, black solid line), dew point temperature (TD, dashed line), and relative humidity (RH, gray solid line) at the point of maximum updraft at 0200 ST are shown in Fig. 4.27b. The temperature of 21°C, and RH of between 95 % and 99 %, below 1 km were relatively low compared with those recorded during the approaching stage (Fig. 4.23b). Temperature decreased gradually with height, and had fallen to 0°C at 4.9 km. The updraft gradually increased above a height of 1 km (Fig. 4.27a), and the maximum updraft (> 6 $m\,s^{-1}$) was distributed up to a height of 5.9 km. The updraft reached a maximum intensity of 6.5 $m\,s^{-1}$ at a height of 5.4 km. Corresponding to the updraft profile at 0200 ST, the positive updraft anomalies during the lee-side stage were located above a height of 1 km, and the positive anomalies greater than 1 $m\,s^{-1}$ were located between heights of 2.8 and 6 km.

4.3.2. Microphysical structure associated with enhancements of convective cells

In this section, we consider the evolution of the hydrometeors and microphysical processes during the enhancement of convective cells in the approaching and lee-side stages.

4.3.2.1. Structure of hydrometeors

Vertical profiles of the mixing ratios (q_v, q_c, q_r, q_g, and q_s) of hydrometeors (vapour, cloud water, rain water, graupel, and snow) during the approaching (solid lines) and lee-side stages (dashed lines) are shown in Fig. 4.28. Profiles of each mixing ratio at 0100 ST, and the increased mixing ratio from 0030 to 0100 ST of the approaching stage are depicted by thin and thick solid lines, respectively. At 0100 ST, the convective cell was enhanced off the northwestern shore of the island by convergences caused by the strong southwesterly wind blowing between the convective cell and

the island (Fig. 4.20d). At 0030 ST, before the enhancement, the convective cell was located 20 km from the northwestern shore of the island (Fig. 4.20a). Profiles of each mixing ratio at 0200 ST, and the increased mixing ratio from 0140 to 0200 ST of the lee-side stage are shown in Fig. 4.28 by dashed thin and thick lines, respectively. At 0200 ST, the convective cell was enhanced on the lee side by a stationary local convergence region that developed as a result of the convergence of the weak northwesterly wind from the north of the island with the relatively strong southwesterly wind from its southeastern slope (Fig. 4.24d). At 0140 ST, the convective cell had not yet reached the local convergence on the lee side (Fig. 4.24b).

As shown in Fig. 4.28a, the q_v below a height of 0.8 km at 0100 and 0200 ST was 17.5 g kg^{-1} and 16.5 g kg^{-1}, respectively. Above 0.8 km, q_v decreased gradually with increasing altitude at both times. As shown in Fig. 4.28b, a q_c of over 0.2 g kg^{-1} had developed above 0.4 km at 0100 ST, and above 1.5 km at 0200 ST. The q_c gradually increased up to a height of 4.1 km during both stages, and was then maintained up to 5 km at around 15 g kg^{-1} and 12 g kg^{-1} during the approaching and lee-side stages, respectively. The increase of q_c during the approaching and lee-side stages reached its maximum value at heights of 3 km and 3.6 km, respectively. During the lee-side stage, an increase in q_c of less than 5 g kg^{-1} was typical above 5.5 km. At 0100 ST (Fig. 4.28c), q_r increased from 3.3 g kg^{-1} to 4.9 g kg^{-1} in a layer extending from the surface up to 3 km, but then decreased gradually above 3 km. The related increase of q_r during the approaching stage of over 1 g kg^{-1} occurred between heights of 1 and 4 km (thick solid line). At 0200 ST, q_r increased from 2.5 to 4 g kg^{-1} between the surface and 3.6 km, and then decreased slowly above 4 km. During the lee-side stage (thick dashed line), q_r increased by over 1 g kg^{-1} in a zone between 3 and 5.6 km, which is higher than seen during the approaching stage. As shown in Fig. 4.28d, at 0100 ST, q_g was over 0.5 g kg^{-1} above 4.2 km, and over 2.0 g kg^{-1} above 5.4 km. At 0200 ST, q_g increased gradually from 0.5 to 2.5 g kg^{-1} between 4.2 and 6.1 km. The increased q_g during the lee-side stage was significant between 3.8 and 6.1 km, showing a maximum increase at 6.1 km. The profiles of q_s are shown in

Fig. 4.28e. At 0100 ST, q_s of over 0.001 g kg^{-1} had developed above 5.4 km height. During the approaching stage, an increase in q_s of less than 0.25 × 10^{-3} g kg^{-1} developed between 5.4 and 6 km. At 0200 ST, a q_s larger than 1.0 × 10^{-3} g kg^{-1} was seen above 5.6 km, but there was no increase in q_s during the lee-side stage.

4.3.2.2. Structure of microphysical process

Vertical profiles of the rates of increase of the microphysical processes during the approaching and lee-side stages are shown in Fig. 4.29a and b, respectively. The rate of increase of vapour deposition to cloud water (VD_{VC}) is indicated by the dotted line, of the conversion from cloud water to rain water (CN_{CR}) by the dashed line, and of the collection of cloud water to rain water (CL_{CR}) by the solid line. Fig. 4.29c contains the vertical profiles of the rates of snow melting to rain water (ML_{SR}, black lines) and graupel melting to rain water (ML_{GR}, gray lines) at 0030 ST (thin line) and 0100 ST (thick line) during the approaching stage. Fig. 4.29d contains the vertical profiles of the rates of snow melting to rain water (ML_{SR}, black lines) and graupel melting to rain water (ML_{GR}, gray lines) at 0140 ST (thin line) and 0200 ST (thick line) during the lee-side stage.

The increase of VD_{VC} during the approaching stage was evident from a height of 75 m (dotted line, Fig. 4.29a). The increase rate gradually increased to a height of 4.3 km, and the maximum increase rate was 0.017 × 10^{-3} s^{-1}. Above 4.5 km, a gradual decrease in VD_{VC} was identified. During the lee-side stage (dotted line, Fig. 4.29b), the increase of VD_{VC} was evident from a height of 1 km. Compared with that during the approaching stage, a large increase in VD_{VC} occurred between heights of 1 and 2 km during the lee-side stage. The increase rate of VD_{VC} increased gradually between 2 to 6 km, and the maximum increase rate of 0.015 × 10^{-3} s^{-1} was at 6.1 km. The increase rate of CN_{CR} during the approaching stage (dashed line, Fig. 4.29a) had two peak heights at 3 and 5 km. Similarly, the increase rate of CN_{CR} during the lee-side stage showed two peak heights (dashed line in Fig. 4.29b), but at the higher altitudes of 3.5 and 6 km. The increase of

CL_{CR} during the approaching stage (solid line, Fig. 4.29a) was apparent above 1.5 km, and reached a maximum at 4.3 km of 0.014×10^{-3} s^{-1}. During the lee-side stage (solid line, Fig. 4.29b), the increase in CL_{CR} became evident above 1.9 km, and the maximum increase rate of 0.015×10^{-3} s^{-1} occurred at a relatively high altitude of 5.6 km.

The rate of increase of ML_{GR} increased in the period from 0030 to 0100 ST during the approaching stage, and most significantly between the heights of 4.1 and 4.8 km (gray lines, Fig. 4.29c). Between 0140 and 0200 ST during the lee-side stage (gray lines, Fig. 4.29d), the rate of increase of ML_{GR} was greatest between 3.6 and 4.6 km in altitude, but decreased between 4.6 and 5.1 km. During the lee-side stage, ML_{SR} decreased significantly between 4.3 and 5.1 km (black lines, Fig. 4.29d). The increase and decrease rates of ML_{SR} are shown at heights of 5.1 and 4.8 km, respectively, between 0030 ST and 0100 ST, by the black lines in Fig. 4.29c.

4.3.3. Summary

As discussed in sections of 4.3.1 and 4.3.2, the enhancement of the convective cells associated with the precipitation system that passed off the northwestern shore and lee side of Jeju Island on 6 July 2007 (07P), showed related enhancement of the updraft and hydrometeors. The distinguishing features of the updraft, hydrometeors, and microphysical processes within the enhanced convective cells during the two stages are discussed in this section. In Fig. 4.30, the heights of the positive anomalies of the convective cells, updraft, hydrometeors (q_c, q_r, q_g, q_s, and $-q_s$) and microphysical processes (VD_{VC}, CN_{CR}, CL_{CR}, ML_{GR}, ML_{SR}, and $-ML_{SR}$) during the approaching (0030–0100 ST) and lee-side (0140–0200 ST) stages are summarized. **A** and **L** on the horizontal axes of Fig. 4.30 indicate the approaching stage and the lee-side stage, respectively. The cross on each bar indicates the height of the maximum anomaly for each parameter. A dotted line indicates the height of the 0°C level. Figure 4.31 shows the schematic diagrams of the two enhancements of convective cells, and the hydrometeors during the approaching stage and lee–side stage are illustrated.

4.3.3.1. Approaching stage microphysical structure

During the approaching stage, the convective cell (defined as the portion with an estimated reflectivity greater than 50 dBZ) intensified significantly over the northwestern coastal area of the island. This intensification was evident in the expansion of the horizontal area of the convective cell at a height of 1.9 km, and the increased positive anomaly of its vertical profile (Figs. 4.21 and 4.22a).

During this period, the positive anomaly of the convective cell was significant from the surface up to 4.2 km, with the maximum value occurring at the surface (Figs. 4.30 and 4.31a). Corresponding to the updraft off the northwestern shore of the island, the positive updraft anomalies during the approaching stage were seen below 1.5 km (Figs. 4.23a and 4.30, and gray arrow in Fig. 4.31a). With the positive anomaly of updraft, the difference in the horizontal area of the convective cell at 0100 ST between the CNTL and NOTR experiments was concentrated below 1.5 km (Fig. 4.22b).

With the positive anomalies of the convective cell and updraft developing at relatively low altitudes off the northwestern shore of the island, a high vapour mixing ratio (17.5 g kg^{-1}) localized below 0.8 km (Fig. 4.28a). With the high q_v at low altitudes, a positive VD_{VC} anomaly was apparent from the surface up to 6 km, and the maximum anomaly was at 4.5 km (Fig. 4.30). Consequently, a positive q_c anomaly developed between the surface and a height of 5.3 km (dark gray circles in Fig. 4.31a), with the maximum anomaly at 2.7 km (Fig. 4.30), while the melting layer was located at 4.9 km. With the large increase of q_c, the microphysical processes of CN_{CR} and CL_{CR} showed positive anomalies, but mainly below the melting layer, showing a maximum at 3.1 km and 4.3 km, respectively (Fig. 4.30). Consequently, the positive q_r anomalies were concentrated in a zone between 1 and 4.2 km in height (gray ellipses in Fig. 4.31a). The positive updraft anomalies persisted to a height of 5.8 km, with the maximum at 4.5 km. In between the heights of 1.5 and 5.2

km, the increase in the melting of graupel to form rain water was significant (Fig. 4.30 and symbols of white diamonds in Fig. 4.31a).

4.3.3.2. Lee-side stage microphysical structure

During the lee-side stage, the convective cell intensified significantly on the eastern slope of the island, where the terrain-modified go-around northwesterly wind from the north converged with the relatively strong and moist southwesterly wind on the southeastern slope. The intensification was evident in the expansion of the horizontal area of the convective cell at a height of 1.9 km, and the increased positive anomaly of its vertical profile (Figs 4.25 and 4.26a).

During this period, the positive anomaly of the convective cell was significant between heights of 1 and 3.8 km, with the maximum at 2.8 km (Figs. 4.30 and 31b). Toward the enhanced convective cell, the relatively weak northeasterly wind from the northern side of the island converged with moist southwesterly (RH > 96%) from the southeastern slope (elevation < 500 m). Dual-Doppler radar analyses identified this moist southwesterly upslope wind as a critical element in the generation of the local moist updraft that caused the enhancement of the convective cell on the lee side. With regard to the upslope wind in this study (gray arrow in Fig. 4.31b), the positive anomalies of the updraft were identified between heights of 1 and 6.3 km, and the maximum was at 5.5 km, which is above the melting layer.

Compared to NW offshore of the island, relatively–less amount of maximum vapour mixing ratio (16.5 g kg^{-1}) was shown below 1 km height, however related to the positive updraft anomalies at the higher altitudes than seen in the approaching stage (Figs. 4.28 and 4.30) are the positive q_c anomalies evident above 2 km (dark gray circles in Fig. 4.31b). With this q_c distribution, the microphysical processes from q_c to q_r of CN_{CR} and CL_{CR} developed the positive anomalies above 1.5 km (Fig. 4.30). In particular, the maximum anomalies of the CL_{CR} were identified at 5.3 km, which is above the melting layer. Consequently, the positive q_r anomalies were concentrated

between heights of 3.1 and 5.6 km (Fig. 4.30 and gray ellipses in Fig. 4.31b). Above 5.6 km, a continuous increase in updraft was seen during the lee-side stage. Related to this increasing updraft, positive q_g anomalies are apparent in the height range 3.8–6.0 km, with the maximum at 6 km (Fig. 4.30 and symbols of white diamonds in Fig. 4.31b). In between the heights of 4.9 and 6 km, the melting rate of graupel was hardly distributed, and this suggests the growth of graupel above the melting layer. In addition, a decrease in snow and increase in cloud water occurred in this layer (Fig. 4.30).

The analysis results stated in chapter 4.3 are summarized below.

1) A local updraft region by the accelerated southwesterly wind between the system and the coastal line of the northwestern island was simulated in CNTL experiment as shown in the result of dual–Doppler radar analysis (Section 4.2.2.1); no accelerated southwesterly wind and no local updraft region were apparent in the NOTR (in which terrain was not considered). With the terrain–induced local updraft from the sea surface, most of the hydrometeors increased from the surface to the region below the melting layer (4.9 km) during the approaching stge. Related to the increased hydrometeors, the microphysical processes of vapour deposition (vapour to cloud water), cloud collection (cloud water to rain water), and conversion (from cloud water to rain water) were increased mainly below the melting layer.
2) On the lee (eastern) side of the island, a convergence region which can explain by the weak westerly wind from the northern side of the island and relatively strong southwesterly wind on the southeastern slope of the island was consistently apparent. A local high-RH (> 96 %) was shown on the southeastern slope where the strong southwesterly wind blew; NOTR hardly conducted the local RH region. With the local convergence by moist southwesterly upslope wind (elevation < 500 m) with terrain–modified weak westerly wind, the evolutions of hydrometeors and the related microphysical process within the enhanced convective cell on the lee (eastern) side of the island were significant from in 1–6 km height, exceeding the melting layer.

5. Orographic effect of Jeju Island

5.1. Terrain effect on flow dynamics

The terrain effect of the elliptically shaped and topographically steep Jeju Island on dynamic fields around the island was investigated using three idealized numerical experiments (NB runs, without a bubble). The surface environment was identical in all experiments, having a surface RH of 90% and a temperature of 299 K; *Fr* was designed to be 0.2, 0.4, and 0.55 for the NB2, NB4, and NB5 runs, respectively (Table 2.3). No rainfall was generated in these runs.

5.1.1 Horizontal patterns

Horizontal distributions of horizontal wind, RH, convergence, and downdraft at low altitudes in the NB2, NB4, and NB5 runs are shown in Fig. 5.1. In each panel, the coastline and topography of Jeju Island are depicted by solid and dashed lines, respectively. The plates in the left panel of Fig. 5.1 show horizontal wind vectors and RH (gray scale with thin contours; contour interval, 2 %, starting at 88 %) at a height of 500 m for the NB2, NB4, and NB5 runs. Details of the horizontal distributions of the maximum convergence (symbols) below 1 km and the downdraft (contour intervals of 0.2 $m\,s^{-1}$ from 0.3 $m\,s^{-1}$) at a height of 500 m are shown in Fig. 5.1b, d, and f, respectively.

Figure 5.1a shows a prevailing southwesterly wind (7 $m\,s^{-1}$) off the southwestern shore of the island at a height of 500 m in the NB2 run. Relatively weakened southwesterly winds of 5 $m\,s^{-1}$ are distributed on the western slope of the island. The southwesterly wind splits into south–southwesterly and westerly winds on the northwestern and southwestern sides of the island, respectively (Fig. 5.1b); simultaneously, a high-RH (> 88%) region develops in an arc shape surrounding the terrain (Fig. 5.1a) and convergences greater than 0.5×10^{-3} s^{-1} (cross symbols, Fig. 5.1b) develops on the northwestern side of the island below 1 km. Subsequently, the rerouted

south–southwesterly wind on the northwestern side arrives on the northeastern side of the island as a weak westerly (6 $m s^{-1}$), converging with the relatively strong southwesterly (12 $m s^{-1}$) from the southern island. As a consequence, a convergence develops on the eastern side of the island (Fig. 5.1b, eastern side of 126.6°E). Downdrafts (contours, Fig. 5.1b) are barely detected on the lee side of the terrain.

The horizontally rerouted low-level winds, the related local convergences, and the arc-shaped high-RH region which are identified in the NB2 run are similarly apparent in the results of the NB4 run (Fig. 5.1c–d). Compared to the results of NB2 run, relatively strong southwesterly winds (8 m s^{-1}) are dominant around the island (Fig. 5.1c). The southwesterly wind redirects to the south–southwesterly on the northwestern slope of the island at a height of 500 m, generating a local convergence of greater than 0.5×10^{-3} s^{-1} (cross, Fig. 5.1d). On the eastern slope of the island (to the east of 126.6°E, Fig. 5.1d), the westerly (5 m s^{-1}) and southwesterly (11 m s^{-1}) winds converges, with a maximum convergence greater than 1.0×10^{-3} s^{-1} (open circles). At the same time, downdrafts (contours, Fig. 5.1d) stronger than –0.3 $m s^{-1}$ are identified below 1 km on the eastern slope of the island.

In the NB5 run, relatively strong southwesterly wind (13 $m s^{-1}$) prevails toward the western part of the island (Fig. 5.1e), generating convergences greater than 0.5×10^{-3} s^{-1} on both the northwestern (cross symbols in Fig. 5.1f) and southwestern sides of the island. Corresponding to the relatively strong southwesterly winds, the arc-shaped RH region (RH > 90%) expands horizontally (Fig. 5.1e), as compared with that found in the NB2 and NB4 runs (Fig. 5.1a and c). High RH (>94%) is distributed on the western slope of the island and relatively strong downdrafts (>–0.8 $m s^{-1}$) are apparent on the eastern slope of the island (to the east of 126.6°E) below 1 km (contours, Fig. 5.1f). Simultaneously, convergences greater than 1.0×10^{-3} s^{-1} (open circles, Fig. 5.1f) develop on the eastern side of the island.

5.1.2. Vertical patterns

A vertical southwest–northeast cross-section (**A**–**B**) was selected from the region depicted in Fig. 5.1a, c, and e to illustrate the vertical structure of vertical winds and RH across the mountain on Jeju Island. The **A**–**B** transect is oriented parallel to the dominant low-altitude southwesterly wind. In Fig. 5.2, the plates in the left column show the vertical distribution of updrafts (red shade) and downdrafts (blue shade) for NB2, NB4, and NB5 runs; the plates in the right column show corresponding vertical distributions of RH (shade), updrafts (solid contour lines) and downdrafts (dashed contour lines).

Along the **A**–**B** transect in the NB2 run (Fig. 5.2a), a relatively weak updraft of 0.5 $m\,s^{-1}$ is apparent on the southwestern slope of the island, in the region of the relatively weakened southwesterly wind (Fig. 5.1a–b). The related RH distribution is shown in Fig. 5.2b. A region of high RH (> 90%) is concentrated at low altitudes on the southwestern slope of the island. The altitudes of the high-RH region at the 10 km, 20 km, 30 km, and 40 km from point **A** are 0.9 km, 1.1 km, 1.2 km, and 1.9 km, respectively (Fig. 5.2b). A paired downdraft (blue shade) and updraft (red shade) region is located on the northeastern slope (Fig. 5.2a). At 50 km from point **A**, a thick downward arrow on the horizontal axis of each panel of Fig. 5.2 is present, and a black circle on the **A**–**B** line is depicted in Fig. 5.1. As shown in Fig. 5.2a, a region of relatively intense updraft (>2 $m\,s^{-1}$) is localized at 50–60 km along the transect on the northeastern slopes below altitudes of 2 km, at the location of convergence of the westerly and the southwesterly winds at low altitudes (Fig. 5.1a–b). The related high RH (>85%) is identified below altitudes of 2 km at 55–60 km along the transect (Fig. 5.2b).

In the NB4 run (Fig. 5.2c), a relatively weak updraft of 0.5 $m\,s^{-1}$ is distributed on the southwestern upslope, but relatively extends in the vertical direction as compared with that found in NB2 (Fig. 5.2a). The altitudes of the high-RH region (> 90%) at the 10 km, 20 km, 30 km, and 40 km from point **A** are 1.0 km, 1.3 km, 1.9 km, and 2.1 km, respectively (Fig. 5.2d); the region is

relatively extended in the vertical direction as compared with that in the NB2 run (Fig. 5.2b). On the crest, the downdraft is relatively intensified (–3.0 $m\,s^{-1}$) and it extends to the northeastern slope of the island. Two pairs of updraft–downdraft regions develop on the northeastern downstream (Fig. 5.2c–d). At low altitudes, relatively strong updrafts (1.5 $m\,s^{-1}$) and the relatively high RH region (> 85%) are located at 55–65 km and 60–70 km, respectively (Fig. 5.2c–d).

Further strengthening of updrafts is observed on the southwestern slope in the NB5 run (Fig. 5.2e). An updraft stronger than 1 $m\,s^{-1}$ is identified at 1–2 km heights at 35–45 km along the transect. The altitudes of the high-RH (> 90%) region at 10 km, 20 km, 30 km, and 40 km from point **A** are extended to 1.0 km, 2.1 km, 2.1 km, and 2.5 km, respectively (Fig. 5.2f). Simultaneously, the relatively high RH (> 95%) region is distributed at heights of 1.5–2.2 km at 35–45 km. Related to the intensified updrafts on the southwestern slope, a relatively intense downdraft of –3.5 $m\,s^{-1}$ develops and propagates further to northeast downstream, breaking the updraft region at around 60 km. Intense updrafts (2 $m\,s^{-1}$) are concentrated at low altitudes at 60–70 km. Similarly to the patterns in the NB2 and NB4 runs (Fig. 5.2b and d), a relatively high RH (> 85%) region is localized on the northeastern side of the island, but farther to the northeast, downstream (63–75 km, Fig. 5.2f).

5.2. Terrain effect on rainfall system

Terrain-generating local updrafts/downdrafts are one of the major factors in the evolution of rainfall systems in mountainous regions. This section focuses on the effects of terrain-induced flow fields (specifically, the three types of horizontal and vertical flow fields; see Section 5.1) on the evolution of a rainfall system (e.g., intensity variations and duration). Furthermore, to understand how the landing location of the system on the terrain affects the system's evolution as its approaches the terrain, two categories of system-passage regimes were investigated: BNW and BW (Fig. 1.5a and Table 2.3). In this study, ST is the simulation time from the initiation of the

experiment, and the q_r region is the area over which the mixing ratio of rain water (q_r) is >1 g kg^{-1}; the q_r region corresponds to the region of predicted rainfall.

5.2.1. BNW experiments

Three experiments with varying flow regimes were conducted in which the initial warm bubble was located off the northwestern shore of the island (BNW2, BNW4, and BNW5). The distributions of accumulated rainfall in each experiment are shown in Fig. 5.3.

In BNW2 (Fig. 5.3a), regions with accumulated rainfall greater than 15 mm over 3.5 hr are located on the northern and the eastern sides of the island. Among the three runs, the most intense rainfall accumulation (53 mm) in the broadest rainfall region (126.08°E–127.5°E) is in the BNW2 run. In the 4th quadrant domain of Fig. 5.3a (33.4°N–33.6°N, 126.0°E–126.7°E), two regions of intense rainfall (>30 mm) occur off the northwestern and northern sides of the island. In BNW4 (Fig. 5.3b), the maximum accumulated rainfall of 37 mm occurs off the northwestern shore, with the intense rainfall (>30 mm) off the northwestern shore and near the northern coast of the island. In BNW5 (Fig. 5.3c), the maximum accumulated rainfall (31 mm) is distributed off the northern shore of the island. Relatively narrow regions of rainfall (>15 mm) occur in BNW4 in the region 126.12°E–126.65°E and in BNW5 in the region 126.16°E–126.63°E, as compared with those shown in BNW2 (Fig. 5.3a). In Fig. 5.4a, the maximum rainfall accumulated rainfall in 5-min intervals from the initial state of simulation is depicted by solid, dashed, and dotted lines for the BNW2, BNW4, and BNW5 runs, respectively. The locations with the maximum rainfall at each 5-min interval are depicted by circles, rectangles, and stars for the BNW2, BNW4, and BNW5 runs, respectively (see Fig. 5.4b). The gray shading of the symbols indicates the time period, and is changed every 25 min from 0025 to 0225 ST. During the periods 0025–0045 ST and 0115–0135 ST, the symbols are shaded light and dark gray, respectively. During the period 0205–0225 ST, the symbols are shaded black. The size of each symbol in Fig. 5.4b is weighted to represent the

maximum accumulated rainfall. To understand the evolution of the system in detail, the horizontal distributions of updrafts (w) and the mixing ratios of rain water (q_r) are represented in Figs. 5.5, 5.6, and 5.7 for BNW2, BNW4, and BNW5, respectively. Updrafts at a height of 500 m are contoured by solid lines (contour interval, 0.2 m s^{-1}, starting at 0.3 m s^{-1}). Values of q_r > 1 g kg^{-1} at a height of 2 km are shaded and contoured at intervals of 3 g kg^{-1}. A thick gray line represents the coastline and thin gray lines represent the topography (contour interval, 200 m) of Jeju Island (Figs. 5.5, 5.6, and 5.7).

In BNW2, rainfall begins off the northwestern shore of the island after 25 min ST (Fig. 5.4a). A q_r region is located off the northwestern shore of the island from 0035 to 0050 ST (Fig. 5.5a–d); the horizontal distributions of q_r and updrafts are shown every 5 min. The horizontal distributions of q_r and updrafts are shown every 10 min during the passage of the q_r region on the northwestern island from 0055 to 0125 ST (Fig. 5.5e–h) and over the northeastern island from 0140 to 0210 ST (Fig. 5.5i–l). As shown in Fig. 6a, an elongated q_r region (oriented south–north) with a maximum q_r = 7 g kg^{-1} is located along longitude 126.15°E at 0035 ST. Updrafts of 0.9 and 1.7 m s^{-1} are located to the east and west of the q_r region, respectively, at the 500 m height. The thick gray contour in Fig. 5.5a indicates the coastline of Jeju Island. During the period 0035–0050 ST (Fig. 5.5a–d), the q_r region approaches near to the island. At 0040 ST (Fig. 5.5b), two regions of updrafts with velocities > 0.5 m s^{-1} occur in the eastern (33.44°N–33.52°N) and southern (33.41°N) parts of the q_r region. At 0045 ST (Fig. 5.5c), the updraft in the southern part of the q_r region intensifies to velocities over 0.9 m s^{-1} between the q_r region and the island. Subsequently, the updraft in the eastern part of the q_r region is hardly distributed at the 500 m height by 0050 ST (Fig. 5.5d); in contrast, the updraft between the q_r region and the island intensifies during this time, exceeding 1.1 m s^{-1}. At the same time, two regions with high q_r (> 4 g kg^{-1}) are apparent in the southern (33.44°N) and northern (33.47°N–33.52°N) parts of the q_r region. During the period 0050–0105 ST (Fig. 5.5d–f), the q_r region moves on the northwestern island and the updraft intensifies (1.3 m s^{-1}) in the southern part

of the q_r region. During the period 0100–0105 ST, the location of maximum rainfall shifts from offshore to the northwestern coast of the island (Fig. 5.4b). At 0105 ST (Fig. 5.5f), in the region 126.25°E–126.3°E, updrafts stronger than 0.7 ms^{-1} are distributed between the q_r region and the northwestern coast of the island. During the period 0110–0115 ST (Fig. 5.4b), the location of maximum rainfall shifts to offshore the northwestern side of the island. At 0115 ST (Fig. 5.5g), two regions of high q_r (>4 $g\,kg^{-1}$) develop on the northwestern and southeastern sides of the coastline (the thick gray solid line shows the coastline); in the southern part of the northwestern region, further intensification of updrafts to velocities >1.3 ms^{-1} are shown. Simultaneously, an elongated area of updrafts >0.3 ms^{-1} occurs in the region 126.3°E–126.43°E on the northwestern side of the island, at the location where terrain-generated convergences are concentrated at low altitudes in the NB2 run (Fig. 5.1b). During the period 0115–0125 ST, the q_r region migrates to the northern side of the island (Fig. 5.5g–h), maintaining the maximum rainfall intensity of about 12 mm/5 min (Fig. 5.4a). A continuous updraft of >1.1 ms^{-1} is distributed across the southern part of the q_r region. At 0140 ST (Fig. 5.5i), a q_r > 7 g kg^{-1} is apparent on the northern side of the island, and the maximum rainfall intensity is 19 mm/5 min (Fig. 5.4a). An intense elongated updraft (>1.1 ms^{-1}) related to the intense q_r develops on the northern side of the island (Fig. 5.5i). At 0145 ST (Fig. 5.4a–b), the maximum rainfall intensity of 20.1 mm/5 min is observed on the northern side of the island. At 0150 ST (Fig. 5.5j), a relatively intense updraft region (>1.1 ms^{-1}) is continuously present on the northern side of the island (126.55°E). During the period 0150–0210 ST (Fig. 5.5j–l), the q_r region migrates to the northeastern side of the island, and the maximum rainfall intensity decreases from 18 mm/5 min to 10 mm/5 min (Fig. 5.4a). At the same time, the low-level updraft gradually intensifies ahead of the q_r region (Fig. 5.5j–l). Subsequently, during the period 0210–0235 ST (Fig. 5.4a–b), the maximum rainfall intensity increases to 12 mm/5 min on the eastern side of the island. When the system migrates off the eastern shore of the island starting at 0240 ST (Fig. 5.4b), the maximum rainfall intensity decreases to 10 mm/5 min. Thus, the duration of the maximum rainfall

intensity exceeding 5 mm/5 min in BNW2 is 150 min, which is the longest life-time of rainfall among the experiments in this study.

In the BNW4 run (dashed line in Fig. 5.4a, rectangles in Figs. 5.4b and 5.6), the rainfall system passes closed to the northern coast of the island with relatively strong southwesterly winds (8 m s^{-1}). In Fig. 5.6, the horizontal distributions of q_r and updrafts are shown at intervals of 5 min during the passage of the q_r region off the northwestern shore of the island from 0035 ST to 0050 ST (Fig. 5.6a–d), and at intervals of 10 min during its passage along the northern coast from 0100 ST to 0130 ST (Fig. 5.6e–h). At 0035 ST (Fig. 5.6a), an elongated q_r region (oriented south–north, maximum q_r = 8 g kg^{-1}) is located along longitude 126.18°E. During the period 0035–0045 ST (Fig. 5.6a–c), the q_r region moves eastward. Simultaneously, updrafts on the eastern side of the q_r region gradually extends to the southern side of the q_r region. At 0050 ST (Fig. 5.6d), in the q_r region locates off the northwestern shore of the island (126.23°E–126.36°E), the maximum rainfall intensity is 13 mm/5 min along longitude of 126.28°E (Fig. 5.4). Due to the relatively strong southwesterly winds at low altitudes, a relatively intensified updraft region (maximum of 2.1 m s^{-1}) develops on the southwestern side (126.25°E) of the eastward-moving q_r region (Fig. 5.6d). During the period 0050–0110 ST (Fig. 5.6d–f), as the q_r region approaches closer to the northern side of the island, a relatively high q_r region (q_r > 4 g kg^{-1}) simultaneously develops adjacent to the northern coast of the island. At 0100 ST, the related updraft intensifies to 2 m s^{-1} along 126.28°E–126.35°E, between the q_r region and the island (Fig. 5.6e); the updraft is continuously develops in the northwestern coastal region until 0110 ST (Fig. 5.6f), but with a relatively weakened intensity to 0.7 m s^{-1}. Simultaneously, on the northern slope, another updraft develops at low altitudes along latitude 33.46°N; by 0120 ST, the updraft region has intensified and is elongated along the northern side of the island (Fig. 5.6g–h). During the period 0120–0135 ST (Fig. 5.4), maximum rainfall intensities gradually increase from 13.5 to 16.9 mm/5 min adjacent to the northern coast of the island. Subsequently, the q_r region moves to the northeastern side of the island and rapidly

dissipates (not shown). Therefore, in the BNW4 run, rainfall intensities >5 mm/5 min last for 80 min.

In the BNW5 run (dotted line in Fig. 5.4a, stars in Figs. 5.4b and 5.7), the rainfall system passes offshore the northern end of the island with relatively strong southwesterly winds (13 $m\,s^{-1}$) at low altitudes. In Fig. 5.7, the horizontal distributions of q_r and updraft velocities are shown at intervals of 5 min during the passage of the q_r region along offshore of the northwestern end of the island from 0035 to 0050 ST (Fig. 5.7a–d), and at intervals of 10 min during its passage along offshore of the northern end of the island from 0100 to 0130 ST (Fig. 5.7e–h). At 0035 ST (Fig. 5.7a), an elongated q_r region (oriented south–north, maximum q_r = 8 $g\,kg^{-1}$) is located along 126.2°E with an updraft velocity of 0.5 $m\,s^{-1}$ on the eastern side. During the period 0040–0045 ST (Fig. 5.7b–c), updrafts in the southern part of the q_r region gradually intensify when the q_r region is located offshore of the northwestern end of the island. At 0050 ST (Fig. 5.7d), further-intensified updrafts (1.7 $m\,s^{-1}$) are distributed between the q_r region and the island (126.22°E–126.33°E). Consequently, at 0055 ST (Fig. 5.4a–b), the accumulated rainfall reaches a 5-min maximum of 17.7 mm offshore of the northwestern end of the island (33.56°N, 126.3°E). At 0100 ST (Fig. 5.7e), the region with updrafts stronger than 0.5 $m\,s^{-1}$ (maximum updraft, 1.5 $m\,s^{-1}$) located between the q_r region and the island becomes horizontally enlarged. Subsequently, at 0110 ST, relatively intensified q_r values >7 g kg^{-1} are apparent offshore of the northern end of the island along 126.45°E (Fig. 5.7f). During the period 0110–0120 ST (Fig. 5.7f–g), updrafts greater than 0.5 $m\,s^{-1}$ are present on the northern side of the island, distant from the q_r region. At 0030 ST (Fig. 5.7h), a relatively weakened q_r region is identified offshore of the northeastern end of the island. After 0120 ST (Fig. 5.4), the maximum rainfall intensity rapidly decreases as the q_r region passes offshore of the northeastern end of the island. The duration of rainfall intensities greater than 5 mm/5 min is continuous for 75 min in the BNW5 run, representing the shortest duration of rainfall among the experiments.

5.2.2. BW experiments

Three experiments (BW2, BW4, and BW5) were initiated with a warm bubble located off the western shore of Jeju Island at 33.35°N, 125.85°E, located 0.1° south of the BNW runs (Table 2.3, Fig. 1.5a). The distributions of the accumulated rainfalls in the BW runs are shown in Fig. 5.8.

In the BW2 run (Fig. 5.8a), the accumulated rainfall greater than 15 mm over 3.5 hr is distributed across the central island in the range 33.35°N–33.45°N, 126.08°E–126.88°E. The maximum rainfall of 60 mm is located near the mountain crest. In the region of 33.3°N–33.5°N, 126.0°E–126.6°E (Fig. 5.8a), intense rainfall (>30 mm) occurs on the western side of the island (126.2°E–126.32°E) and on the mountain crest. In the BW4 run, rainfall is more pronounced on the northern side of the island (33.38°N–33.48°N, 126.13°E–126.7°E) (Fig. 5.8b), than is predicted in the BW2 run, showing a maximum accumulation of 44 mm on the northwestern slope of the island. In the BW5 run (Fig. 5.8c), a region of rainfall accumulation >15 mm is located in the region 33.4°N–33.53°N, 126.16°E–126.66°E, with a maximum rainfall of 42 mm on the northern slope of the island. The time variation of the maximum rainfall at 5-min increments is depicted in Fig. 5.9a by solid, broken, and dotted lines for the BW2, BW4, and BW5 runs, respectively. The locations of maximum rainfall are depicted by a circle, rectangle, and star for the BW2, BW4, and BW5 runs, respectively (Fig. 5.9b); the size of each symbol is weighted to depict the maximum accumulated rainfall. The horizontal distributions of updrafts at a height of 500 m and the mixing ratios of rain water (q_r) at a height of 2 km are illustrated in Figs. 5.10, 5.11, and 5.12 for the BW2, BW4, and BW5 runs, respectively. As the rainfall system passes at relatively high altitudes in the BW2 and BW4 runs, the updrafts (dotted contour lines with intervals of 2 m s^{-1}, from 4 m s^{-1}) at a height of 2 km are also illustrated.

As shown in Fig. 5.9a, rainfall develops in all three runs starting at 25 min from the initial state. In the BW2 run, multiple locations of maximum rainfall are distributed across the island

(circles, Fig. 5.9b). The horizontal distributions of q_r and updrafts are shown at increments of 5 min during passage of the q_r region near the western coast of the island from 0035 to 0050 ST (Fig. 5.10a–d), and at increments of 20 min during its passage over the mountain crest from 0100 to 0200 ST (Fig. 5.10e–h). As shown in Fig. 5.10a, an elongated q_r region (oriented south–north, maximum q_r = 8 g kg^{-1}) is located close to the island along longitude 126.15°E at 0035 ST. Updrafts of 0.9 m s^{-1} and 1.7 m s^{-1} (solid contour lines, Fig. 5.10a) are distributed to the east and west of the q_r region at the 500-m height. At 0040 to 0050 ST (Fig. 5.10b–d), the q_r region lands on the northwestern side of the island in an area of moist and weak southwesterly winds prevailing at low altitudes in the NB2 run (Fig. 5.1b). The related updraft region (>0.5 m s^{-1}; solid contours, Fig. 5.10c) is elongated on the northwestern side of the island in the region of 33.31°N–33.45°N at 0045 ST. At 0050 ST (Fig. 5.10d), intense q_r values >4 g kg^{-1} are distributed on the western side and the northwestern coast of the island. The relatively intense updrafts are apparent on the western side of the island (solid contours, Fig. 5.10d), in a region of moist southwesterlies (Fig. 5.1a). At 0100 ST, intensified q_r (7 g kg^{-1}) is apparent on the western upslope with relatively intense low-level updrafts (0.9 m s^{-1}; solid contours, Fig. 5.10e). The q_r region simultaneously is distributed in a relatively large range of 126.24°E–126.4°E, 33.34–33.45°N, on the northwestern side of the island. Then, at 0105 ST (Fig. 5.9a–b), the location of maximum rainfall shifts to the western slope of the island along latitude 33.36°N. During the period 0110–0145 ST (Fig. 5.9b), the locations of maximum rainfall intensities are distributed on the western slope (around 15 mm/5 min) (Fig. 5.9a) in a region of high RH (>90%) and relatively weak updrafts (Fig. 5.2a–b). Simultaneously, continuous updrafts stronger than 6 m s^{-1} (dotted contours) are distributed at a height of 2 km in the south of the q_r region (Fig. 5.10f–g). At 0150 ST (Fig. 5.9a), a maximum rainfall intensity of 19.2 mm/5 min occurs on the crest of the mountain (Fig. 5.9b). Until 0220 ST (Fig. 5.9a), the maximum rainfall intensity of approximately 15 mm/5 min is distributed on the southeastern slope (Fig. 5.9), in a region of prevailing southwesterly winds with high RH (>94%) (Fig. 5.1a). As the system

migrated to the eastern coast of the island, rainfall intensities decrease dramatically (Fig. 5.9). Thus, the duration of rainfall with intensities >5 mm/5 min is 130 min in the BW2 run.

In the BW4 run, with southwesterly winds of 8 $m\,s^{-1}$, the rainfall system passes on the northwestern slope of the island (rectangles, Fig. 5.9b). Figure 5.11 shows the horizontal distributions of q_r and updrafts at 5-min intervals during the passage of the q_r region near the northwestern coast of the island from 0035 to 0050 ST (Fig. 5.11a–d), and at 20-min intervals during its passage on the northern side of the island from 0110 to 0150 ST (Fig. 5.11e–g). At 0035 ST (Fig. 5.11a), the q_r region is located along longitude 126.18°E. During the period 0035–0050 ST (Fig. 5.11a–d), the q_r region moves to the northwestern side of the island, with updrafts forming ahead of the q_r region. At 0050 ST (Fig. 5.11d), the q_r region is apparent on the northwestern island in the region 126.25°E–126.37°E, including intense q_r (>7 g kg^{-1}). Ahead of the eastward-moving q_r region, in the area of terrain-modified moist south–southwesterly winds (Fig. 5.1c), an updraft of 0.5 m s^{-1} is distributed at a height of 500 m. During the period 0050–0130 ST (Fig. 5.9b), the regions with maximum rainfall are on the northwestern island, where terrain-induced updrafts are concentrated at low altitudes (Fig. 5.1d). Simultaneously, the maximum rainfall intensity gradually increases from 13 to 18 mm/5 min (Fig. 5.9a). At 0130 ST (Fig. 5.9), with the maximum intensity of 18.6 mm/5 min occurring on the northern slope of the island near the point 33.44°N, 126.5°E. During the period 0130–0150 ST (Fig. 5.11f–g), the q_r region moves further east to the area of dry descending air (Fig. 5.1c–d). Subsequently, the q_r intensity decreases to 5 g kg^{-1}, without passing the intense low-level updraft of 1.7 $m\,s^{-1}$ on the northern side of the island in the region 126.52°E–126.65°E (Fig. 5.11f). As a consequence, the maximum rainfall intensity decreases dramatically after 0140 ST (Fig. 5.9). Thus, in the BW4 run, a rainfall intensity greater than 5 mm/5 min is maintained for 90 min.

Similar to what is observed in run BNW2 (circles, Fig. 5.4b), the rainfall system in BW5 passes on the northern side of the island (stars, Fig. 5.9b), but with relatively strong winds (13 $m\,s^{-1}$).

Figure 5.12 shows the horizontal distributions of q_r and updrafts at increments of 5 min during the passage of the q_r region near the northwestern coast of the island from 0030 to 0050 ST (Fig. 5.12a–e), and at increments of 5 min during its passage on the northern side of the island from 0100 to 0120 ST (Fig. 5.12f–h). During the period 0030–0050 ST (Fig. 5.12a–e), the q_r region lands on the northwestern side of the island, with an updraft developing ahead of the q_r region. During the period 0045–0050ST (Fig. 5.12d–e), a relatively intense updraft exceeding 0.7 $\mathrm{m\,s^{-1}}$ is identified in the southern part of the q_r region, where the terrain-modified south–southwesterly winds converges with the southwesterly winds (Fig. 5.1e–f). As shown in Fig. 5.9b, from 0050 to 0100 ST, the locations of maximum rainfall intensities are distributed along the northwestern coastal region of the island, where intensities are >15 mm/5 min (Fig. 5.9a). During the period 0100–0110 ST (Fig. 5.12f–g), the q_r intensifies to >9 $\mathrm{g\,kg^{-1}}$ on the northern side of the island, and a low-level intense updraft of >1.3 $\mathrm{m\,s^{-1}}$ develops in the southern part of the q_r region (126.35°E – 126.48°E). At 0120 ST (Fig. 5.9a), maximum rainfall intensities of 19.2 mm/5 min occur on the northern slope of the island (33.48°N, 126.5°E) (Fig. 5.9b) at the point of local convergence at low altitudes (Fig. 5.1f). At 0130 ST (not shown), the q_r region located on the northeastern side of the island is dominant at low altitudes, in a region of low RH and downdrafts (Fig. 5.1e–f), showing the dissipation in q_r intensity. As a consequence, the rainfall system diminishes rapidly from 0130 ST as it passes on the northeastern slope (Fig. 5.9a–b). Therefore, the duration of maximum rainfall intensities greater than 5 mm/5 min is 70 min in the BW5 run.

5.3. Summary

In the present study, a series of idealized experiments using CReSS revealed the terrain effects of the isolated elliptically shaped terrain of Jeju Island on the evolution of a pre-existing rainfall system, namely, rainfall enhancement on the northwestern and lee sides of the island. Comparisons of the parameters of experimental simulations are in Tables 5.1 and 5.2. Table 5.1 compares

experiments in which an initial bubble is absent from the simulation (NB2, NB4, and NB5); C_{west} and C_{east} (10^{-3} s^{-1}) are the maximum intensities of the convergence on the island to the west and the east, respectively, of longitude 126.6°E; D_{east} ($m\,s^{-1}$) is the maximum intensity of the downdraft on the island to the east of longitude 126.6°E. Table 5.2 compares experiments which were initiated with a warm bubble present off the western shore and off the northwestern shore (i.e., the BW and BNW runs); P_{max} (mm/5 min) is the maximum rainfall intensity; L_{pmax} (°N, °E) is the location of P_{max}; A_{west} and A_{east} (km^2) represent the horizontal area of accumulated rainfall exceeding 20 mm to the west and east, respectively, of longitude 126.6°E; D_{rain} (min) is the duration of rainfall intensities exceeding 5 mm/5 min; and OC_{west} and OC_{east} represent whether the rainfall system passes over the convergence zone on the western and eastern sides, respectively, of longitude 126.6°E. Figure 5.13 is a schematic illustration of the effects of terrain (Jeju Island) on the modification of prevailing winds, and the related formation of updrafts and downdrafts.

5.3.1. The 4th quadrant side of Jeju Island

The experiments in which an initial bubble is absent from the simulation (NB2, NB4 and NB5; *Fr* ≤0.55) modify horizontally–rerouted southwesterly wind surrounding the isolated elliptical–shaped terrain; the low–level southwesterly to south–southwesterly wind on the northwesten side of the terrain (darkly shaded arrow in Fig. 5.13). With the rerouted low–level wind, an arc–shaped region with high RH (88 %) is apparent on the western side of the island. The enhancement of rainfall prior to their arrival on a terrain was identified in the results of BNW runs but not in the results of BW runs. The rainfall systems in BNW2 and BNW4 runs passed off the northwestern shore of the island, while the rainfall systems in BW2 and BW4 runs passed off the western shore of the island. Both rainfall systems in BNW2 and BNW4 runs approach the northern side of the island and rainfall enhancement occurred on the northwestern shore of the island. As the distance between a rainfall and the island decreased, low–level southwesterly winds became concentrated in the region

between the rainfall system and the island, resulting in local updraft (Figs. 5.5 and 5.6, updraft #2 in Fig. 5.13). As the rainfall system moved on the local updraft, gradual–intensified rainfall was resulted (Figs. 5.4, 5.5, and 5.6). The rainfall systems in BW2 and BW4 runs travel off the western shore of the island, showing intensified updraft between the rainfall system and the island.

In the BNW2 run, the enhanced rainfall system subsequently arrived on the northern side of the island at the local updraft region (updraft #1, hatched region in Fig. 5.13). As the result, rainfall intensities on the northern side of the island (P_{max} of 20.1 mm/ 5 min, Table 5.2) were greater than those predicted in any of the other experiments. As shown in Table 5.1, the maximum intensity of convergence in low altitudes was calculated to be 0.6 and 0.7 for NB2, and NB4 and NB5 run, respectively. The conducted rainfall system conducted in BNW2, BW4, and BW5 runs in which passes on the terrain–induced convergence region on the lateral side of the island shows a high maximum rainfall intensity (P_{max}) of 20.1 mm, 18.6 mm, and 19.6 mm in 5 min on the northern side of the island (L_{pmax}), respectively (Table 5.2). The relatively large amount of P_{max} was apparent in the rainfall system passing on the local updraft #1 than in which the rainfall is not passing on (e.g., BNW2 than BW2, BW4 than BNW, and BW5 then BNW5). Simultaneously, the relatively wide horizontal area of accumulated rainfall exceeding 20 mm to the west of longitude 126.6°E (A_{west}) was calculated to be 150 km^2, 160 km^2, and 138 km^2 in BNW2, BW4, and BW5 run, respectively (Table 5.2).

5.3.2. The 1st quadrant side of Jeju Island

On the lee (eastern) side of the terrain, the distribution of updraft and downdraft was differently shown depending on the intensity of *Fr*, in the range of 0.2 to 0.55. The experiments in which an initial bubble is absent from the simulation (NB2, NB4 and NB5) with relatively low *Fr* ($\leq$ 0.55) generate an updraft (updraft #3 in Fig. 5.13) that is generated by convergence of the horizontally–rerouted northwesterlies from the northern island with the moist southwesterly upslope wind from

the southern island. In NB2 (*Fr* = 0.2), the maximum convergence of 0.9×10^{-3} s^{-1} (Ceast, Table 5.1) generates on the east of longitude 126.6 °E with the weak downdraft of –0.3 $m s^{-1}$. Further strengthened downdraft (white region closed by a black line in Fig. 5.13) was apparent in low altitudes on the eastern side of the island in NB4 and NB5 run to be –0.6 $m\ s^{-1}$ and –0.8 $m\ s^{-1}$. Related to the different intensity of downdraft on the lee side (D_{east}, Table 5.1), different horizontal area of rainfall (A_{east}) was shown; wide region of 173 km^2 in BNW2, but narrow region of 12 km^2 and 8 km^2 in BW4 and BW5 run, respectively.

In the *Fr* range of 0.2–0.55, the isolated elliptical–shaped terrain induces the horizontally–rerouted southwesterly wind in low altitudes, generating the local wind convergence on the northwestern lateral side of the island, in the maximum intensities of 0.6×10^{-3} s^{-1} to 0.7×10^{-3} s^{-1}. Consequently, the rainfall system (BNW2, BW4, and BW5 runs) which is passing on the local convergence enhances on the northwestern side and then shows the intense rainfall on the northern side of the island. The rainfall system in BNW2 passes on the lee side of the island subsequently it intensified due to the local updraft (updraft #3) with no descending air; thus the duration of rainfall intensities exceeding 5 mm/5 min (Drain) was recorded as the longest one to be 150 min in BNW2. The rainfall system in BW4 and BW5 runs dissipates on the lee side due to the intensified descending air; short Drain in BW4 and BW5 was resulted to be 90 min and 70 min, respectively. The results of a series of idealized experiment (chapter 5) are summarized below.

1) A steep mountain (height, 2 km) on the elliptically shaped island (width, 35km; length, 78 km) modified the low-level southwesterly winds ($Fr \leq 0.55$), which flows around the terrain and generated two regions of moist updraft, on the northern lateral and the lee sides of the terrain.
2) As the eastward-moving pre-existing rainfall system approached the northwestern shore of the island, the distance between the system and terrain decreases. In that space, the southwesterly winds at low altitudes, which are blowing in parallel to the coastline of the elliptically shaped island (oriented east–west) are accelerated, generating a local updraft region on shore. The

related enhancement of a pre-existing rainfall system shows in advance of its arrival on the terrain.

3) Fairly weak southwesterly winds at low altitudes (Fr = 0.2) drive rainfall enhancement on the lee side of the island, where a local updraft region and the absence of dry descending air are co–existing conditions. As the southwesterly winds at low altitudes accelerate (Fr = 0.4 and 0.55), the low–level wind partly goes over the mountain. As a consequence, dry descending air which contributes to rapid rainfall dissipation strengthens on the northeastern downwind side of the terrain, which results in a relatively short life-time of the system.

6. Discussion

By both of observational and numerical experimental approaches, the effects of an isolated elliptical–shaped terrain of Jeju Island on the flow modification and enhancement of rainfall system area are investigated in this study. The similar and dissimilar features of two selected cases (06P and 07P) are compared and discussed with the results of idealized experiment and the previous studies to understand the effect of an isolated elliptical terrain of Jeju Island on flow dynamics in section 6.1, and the enhancement of pre–existing rainfall system in section 6.2.

Table 6.1 summarized the environmental conditions and evolutionary characteristics of 06P and 07P (combined table of Tables 3.2 and 4.2). Figure 6.1 shows the schematic diagram of stream line modified by terrain, (a)–(f) show the flow modification by terrain which were revealed by previous studies (same as shown in Fig. 1.3), and (g)–(h) show the flow modification (blue solid lines) by an elliptical shaped terrain (Jeju Island; black solid line) with southwesterly wind ($\beta = 0.8$) in (g) an environment with a low Fr (0.2), and (h) a moderate Fr (≤ 0.55). Figure 6.2 shows the schematic diagram of effect of an isolated elliptical shaped terrain on the distribution of moisture content and evolution of rainfall system in the vicinities of the terrain. The horizontal distribution of terrain–induced moisture contents (shading) and the wind at low altitudes (white arrows) are shown in Fig. 6.2a. In Fig. 6.2b, 6.2c, and 6.2d1–d2, the terrain–induced rainfall enhancement (high reflectivity region in vertical cross–section), the related low–level wind (dark–shaded arrow), and updraft (light–shaded upward arrow) showed off the northwestern shore, on the northern shore, and the lee side of the terrain, respectively.

6.1. Effect of an isolated elliptic terrain on flow dynamics

6.1.1. The lateral side of terrain

In this section, effect of an isolated elliptical terrain (Jeju Island) on flow dynamics, especially on the northern lateral side of the terrain is discussed by the results of observational analysis for two case studies (06P and 07P; sections of 3.2 and 4.2), those numerical experiments (sections of 3.3 and 4.3), a series of idealized numerical experiments (section 5.1), and the previous studies on terrain effect.

On 30 June 2006, the southwesterly wind of 10 $m\,s^{-1}$ prevails at low altitudes with moderate *Fr* of 0.55 (Table 6.1a). The control run (CNTL), which includes full model physics and actual topography, simulated terrain–modified horizontally–rerouted wind at low altitudes: the modified southwesterly to the south–southwesterly on the northwestern side of the island (Figs. 6.1h and 6.2a). Consequently, the associated region of low–level convergence with a moist air (RH > 92 %) was revealed on the northwestern side of the island (Figs. 3.7 and 3.8, and darkly shaded region in Fig. 6.2a). The NOTR run (in which terrain was not considered) conducted no horizontally–rerouted low–level wind and no regional RH distribution (Fig. 3.10). The modification of the low–level southwesterly wind and the related local convergence were similarly identified on the northwestern side of the island on 6 July 2007 by dual–Doppler radar analysis.

On 6 July 2007, the relatively–weak southwesterly wind of 5 $m\,s^{-1}$ was dominant at low altitudes with low *Fr* of 0.2 (Table. 6.1b). The detailed 3D structure of wind retrieved by dual–Doppler radar analysis identified the horizontal rerouting of the wind at low altitudes by the terrain; a region of wind convergence was locally apparent on the northern side of the island (Figs. 4.9e–f, 6.1g and 6.2a). With a good agreement to observational results, the control run (CNTL) simulated the terrain–modified wind convergence and the localized high RH region at low altitudes on the lateral side of the island (Figs. 4.18a and 4.20).

Both on 30 June 2006 and 6 July 2007, the southwesterly wind prevailed at low altitudes, but the *Fr* was dissimilar: *Fr* = 0.55 for 06P, and *Fr* = 0.2 for 07P (Table 6.1a–b). In a range of *Fr* from 0.2 to 0.55, a series of idealized experiment was conducted (Table 2.3). The experiments with *Fr* in range of 0.2–0.55 showed in common that an isolated mountain (height, 2 km) on the elliptically shaped island (width, 35 km; length, 78 km) generates the separation of low–level southwesterly on the western side of the island into south–southwesterly and westerly winds on the northwestern and southwestern sides of the island, respectively; simultaneously, a high–RH (> 88 %) region develops in an arc shape surrounding the terrain and convergences greater than 0.6×10^{-3} s^{-1} developed on the northwestern side of the island below 1 km ASL (Figs. 5.1 and 6.2a).

Based on the observational and numerical experiment analysis in this study, we found that an isolated elliptical terrain of Jeju Island generates the horizontal rerouting of southwesterly wind at low altitude (Figs. 6.1g–h and 6.2a) in an environment of relatively low *Fr* (≤ 0.55) and β of 0.8. With the relatively low β, the low–level wind blowing toward the gentle slope of the island generates the absence of the deceleration and stagnation of wind on the western slope of terrain; in turn, no convergence of the horizontally–rerouted wind and the wind reverse is generated on the western coast line of terrain. The absence of wind stagnation seems to allow the horizontally–rerouted south–southwesterly wind to be converged with dominant southwesterly wind on the lateral side of the terrain. Smolarkiewicz and Rotunno (1990) reported the similar wind distributions around an elliptical–shaped terrain with a low *Fr* and low β of 0.5 (Fig. 6.1d); that are the no wind stagnation on the windward upslope, horizontal rerouting of ambient low–level wind, and concentrated wind in the lateral side of the terrain. Even in low *Fr*, if the β become large to be 4 (Fig. 6.1f), the low–level wind is decelerated and stagnated on the windward slope, generating an elongated convergence region along the coastal line with approaching low–level wind. This suggests the important role of both intensities of *Fr* and β in the modification of low–level wind and the location of convergence around an elliptical–shaped terrain.

The horizontal scale of Jeju Island is relatively small (width, 35 km; length, 78 km), though its effect on wind modification at low altitudes on the lateral side of the island was similarly shown in those occurred in the terrain with relatively large horizontal scale (Petersen et al., 2005). The comparison with the previous studies (Smolarkiewicz and Rotunno, 1990; Petersen et al., 2005) who investigated the effect of an elliptical–shaped terrain with large horizontal size on the flow dynamics, the low–level wind blowing toward the terrain with $\beta \leq 0.8$ and the relatively–low Fr seem to be a favourable condition to generate the wind convergence on the lateral side of the terrain. In the environment of $\beta = 0.8$ and the relatively low $Fr < 0.55$, an elliptical–shaped terrain (Jeju Island) thus generates the horizontal rerouting of the low–level southwesterly wind and the moist convergence zone on the lateral side, which are favourable conditions for triggering rainfall enhancement (Fig. 6.2a).

6.1.2. The lee side of terrain

In this section, effect of an isolated elliptical terrain (Jeju Island) on flow dynamics, especially on the lee (eastern) side of the terrain is discussed. Despite of the similar wind distribution (horizontal rerouting of southwesterly wind and convergence at low altitudes) of two cases (06P and 07P) on the lateral side of the island, the distinguished wind distributions were characterized on the lee side with dissimilar degree of Fr: (1) $Fr = 0.55$ for 06P, and (2) $Fr = 0.2$ for 07P (Table 6.1). Theoretically, for large Fr ($Fr > 1$), the flow tends to induce a vertically propagating wave over an obstacle; a low Fr ($Fr \leq 0.5$), on the other hand, tends to induce intense clouds and a nearly horizontal detour of the flow around the obstacle (Smolarkeiwicz et al, 1988; Smolarkeiwicz and Rotunno, 1989, 1990; Yoshizaki et al., 2000).

On 30 June 2006 (06P; Table 6.1a and Fig. 6.1h), the terrain of Jeju Island with relatively strong southwesterly wind at low altitudes ($Fr = 0.55$) generates both horizontal and vertical rerouting of flows over the island. Under the condition, a portion of the wind passed over the

mountain, generating a downdraft region over the northeastern part of the island. Where the descending air (–0.5 ms^{-1}) was identified, high potential temperature was apparent (Fig. 3.12) which implies the adiabatic warming of the descending air mass on the downwind slope. These downdrafts play a role to cut off the low–level moist air provided by a portion of horizontally–rerouted winds (Fig. 3.8).

On 6 July 2007 (07P; Table 6.1b and Fig. 6.1g), the relatively–weak southwesterly wind of 5 ms^{-1} was dominant in low altitudes (*Fr*=0.2). Consequtnly, the horizontally–rerouted southwesterly wind arrived on the lee (eastern) side of the island; the downdraft was absent on the northeastern side of the island. The horizontally–rerouted weak westerly over the northern side of the island converged with relatively strong southwesterly wind over the southeastern slope of the island; in turn, a region of stationary convergence was localized on the lee side of the island. With the southwesterly wind from the southern island, moist air can supply onto the lee side of the island (Figs. 4.12e–f, 4.12h–i, 4.18a, and Fig. 6.2a).

A series of idealized experiment in a range of *Fr* in 0.2–0.55 conducts the distinguished wind distribution on the lee side of the island (Figs. 5.1, 5.2, and 5.13). As shown in 07P, in a moist environment with low *Fr* (0.2) the horizontally–rerouted south–southwesterly wind on the northwestern side of the island arrives on the northeastern side of the island as a weak westerly (6 ms^{-1}), converging with the relatively strong southwesterly (12 ms^{-1}) from the southern island (Figs. 5.1b, 6.1g and 6.2a). As a consequence, a convergence develops on the eastern side of the island consistently (hatched region in 6.2a). Downdrafts were barely detected on the lee side of the terrain. In contrast, as the southwesterly winds at low altitudes accelerate (*Fr* = 0.4 and *Fr* = 0.55), the low–level wind partly goes over the mountain generating a dry descending air (Figs. 5.2c–f, a white region in 5.13 and 6.1h), as similarly shown in 06P. It is revealed that the elliptical shaped terrain of Jeju Island generates wind convergence with absence of dry descending air on the lee side of the island, when the low–level wind is fairly weak to have low *Fr* of 0.2.

When the *Fr* is fairly low to be 0.2, the shape of the terrain seems to play an important role to generate wind convergence on the lee side of the terrain. With β of 0.8, the low–level southwesterly wind blows over the relatively gentle slope of the southeastern side of the island, consequently, the southwesterly upslope wind can arrive over the eastern slope where it converged with the weak westerly wind (Figs. 6.1g and 6.2a). Corresponding to this result, for 07P, the comparison of CNTL and NOTR runs indicates that the increase of the updraft is significant on the eastern slope of terrain, above 1.5 km ASL (Fig. 4.27a). Furthermore, the CNTL run conducts a local high–RH region (> 96 %) on the southeastern slope of the terrain where the southwesterly upslope wind prevails (Fig. 4.18), in contrast, NOTR run conduct that RH increased with decreasing latitude.

In the environment with further low β of 0.5 and low *Fr*, however the elliptical–shaped terrain generates the wind convergence of horizontally–rerouted wind out of the territory of the terrain and absence of the upslope wind (Fig. 6.1d; Smolarkiewicz and Rotunno, 1990). The comparison of results of this study and the previous studies (Smolarkiewicz and Rotunno, 1990; Petersen et al., 2005), the slightly low value of β ($0.5 < \beta < 1.0$) seems to be important factor to generate the low–level upslope wind on the southeastern side of the elliptical–shaped terrain and the convergence with the horizontally–rerouted wind on the lee side of the terrain. Thus the moist environment with β of 0.8, low *Fr* of 0.2, and the elliptical–shaped terrain (Jeju Island) generates a region of moist convergence on the lee side of terrain which is a favourable condition for inducing a rainfall enhancement. Through above discussions, what is stated below is become clearly.

1) An elliptical–shaped terrain (Jeju Island) generates the horizontal rerouting of the low–level southwesterly wind and the related moist convergence region on the lateral side in a moist environment with the relatively low $Fr \leq 0.55$.
2) When the *Fr* is fairly low, the shape of the terrain plays an important role to generate wind convergence on the lee side of the terrain.
   ✧ The southwesterly wind in low altitudes which is blowing over the southeastern slope of the

terrain ($\beta < 0.8$) is important to generate wind convergence on the lee side with weak westerly from northern side in environment of fairly–low *Fr* (0.2).

3) The accelerated low–level southwesterly wind with moderate *Fr* (*Fr* » 0.2) generates a region of dry descending air on the downwind side which weakens the wind convergence.

6.2. Effect of an isolated elliptic terrain on rainfall enhancement

In this section, considering the terrain effect on flow modification mentioned in section 6.1, the similar and dissimilar evolutionary features of a pre–existing rainfall system of two selected cases (06P and 07P) are compared and discussed with results of idealized experiments and previous studies to understand the effect of an isolated elliptical–shaped terrain on rainfall enhancement. The detailed comparison and discussion of the system evolutionary features have been done, dividing into three locations: (1) NW (northwestern) offshore of terrain, (2) N (north) lateral side of terrain, and (3) E (eastern) lee side of terrain.

6.2.1. NW offshore side of terrain

The system evolution off the northwestern shore of an isolated elliptical terrain (Jeju Island) is discussed in this section. Both the pre–existing rainfall systems of 06P and 07P moved eastward, but their arrival location on the island differed in that (1) the 07P landed on the northern side of the island, and (2) the 06P landed on the western side of the island. The evolution of the systems as they approached the island was also different: (1) The rainfall system (07P) approaching the northern side of the island travelled off the northwestern shore before landing on the island. As the distance between the system and the terrain decreased, the southwesterly wind at low altitudes accelerated in the space between the system and terrain, generating a local updraft; the interaction between the terrain and the system seemed to establish a wall. Therefore, rainfall was enhanced off

the northwestern shore of the island. (2) The rainfall system (06P) approaching the western side of the island did not enhance rainfall off the western shore of the island before it landed on the terrain. As the system approached the western shore, concentrated southwesterly winds at the low altitudes and the related updrafts were absent offshore.

In order to understand how the landing location of the eastward–moving rainfall system on the terrain affects the system's evolution as its approaches the terrain, two categories of system–passage regimes were conducted by the idealized experiments (BNW and BW; Fig. 1.5a and Table 2.3). The enhancement of rainfall systems prior to their arrival on a terrain was identified in the results of BNW runs but not in the results of BW runs. The rainfall systems in BNW runs passed off the northwestern shore of the island, while the rainfall systems in BW runs passed off the western shore of the island, shortly landing on the western side of the island.

In both the BNW2 and BNW4 runs, rainfall systems approached the northern side of the island and rainfall enhancement occurred on the northwestern shore of the island (Fig. 5.5 and 5.6). As the distance between a pre-existing rainfall system and Jeju Island decreased, low-level southwesterly winds became concentrated in the region between the rainfall system and the island, resulting in local updraft (Fig. 6.2b); this pattern was common to both the BNW2 and BNW4 runs. This result is consistent with that of results of 07P by dual-Doppler radar analyses (Fig. 4.6j–l) and numerical experiment (Fig. 4.20c–d). Furthermore, by numerical experimental analyses, it is revealed that the abundant vapour at sea surface supplied the interior of the convective cell of 07P by the locally generated updraft that developed between the system and the island (Fig. 4.23); most of hydrometeors thus increased from the surface to the region below the melting layer during the system approaches to the island (Figs. 4.28 and 4.29). The intensity of updraft in this region was relatively weak (less than 3×10^{-3} s^{-1}) compared to that shown on the lee side of the mountain, but higher value of water vapour (16–17 $g kg^{-1}$) was characterized over the sea surface. This explains the important role of large amount of water vapour off the northwestern shore of the island which

induced active warm rain process in enhancing the convective cell (Fig. 4.31a).

As the rainfall system approached the island, the accelerated southwesterly winds and related updraft region between the system and the island appeared to have been essential to the significant enhancement of the system in the coastal area. This result is consistent with the results of a previous study by Wang et al. (2005). In their study, southwesterly winds prevailed offshore of the isolated, elliptical mountainous island of Taiwan. The approach of the convective line toward northwestern shore of the island with *Fr* of 0.25 accelerated the southwesterly wind and generated a localized updraft region between the southern edge of the convective line and the high terrain of the island. As a result, the southern part of the convective line intensified significantly, particularly compared to the northern part. Though Jeju Island has relatively small horizontal scale compared to Taiwan, with a similar *Fr* (0.2), the acceleration of the southwesterly wind and the generation of an updraft region between the system and the terrain are common elements to both locations.

This pattern of enhancement seems strongly related to the shape of the terrain; Jeju Island is isolated elliptically shaped island (oriented east–west), and thus low–level southwesterly winds can flow parallel to the northwestern coastline (dark shaded arrows in Fig. 6.2b). In this condition, if an eastward–moving rainfall system approaches close to the coast, the warm and moist southwesterly wind becomes concentrated between the system and the island; in turn, the related local updraft triggers rainfall enhancement on shore (Fig. 6.2b). The identical condition was shown in Taiwan by Wang et al. (2005). Taiwan also is an elliptically shaped topography (oriented southwest–northeast), thus the terrain–modified southwesterly can flow parallel to the northwestern coastline, and accelerated between the approaching system and the terrain; in result, local updraft triggers the system enhancement on the shore.

This result accentuates the importance of the shape and orientation of a terrain with respect to prevailing low–level wind directions, and the approach–direction of a pre–existing rainfall system with respect to the terrain, on the evolution of a pre–existing rainfall system on the shore.

6.2.2. N lateral side of terrain

The system evolution on the northern side of an isolated elliptical terrain (Jeju Island) is focused in this section. As discussed in section 6.1.1, a local moist convergence region is characterized on the lateral side of the terrain. The isolated elliptically–shaped terrain of Jeju Island induces a horizontal rerouting of low–level winds with relatively low *Fr*, generating a local updraft region on the lateral side of the island (Fig. 6.1g–h and Fig. 6.2a).

Both pre–existing rainfall systems of 06P and 07P passed over the northern side of the island, and their evolution were similar in that rainfall is intensified on the northern lateral side of the island (Figs. 3.14 and 4.17). For the 06P, the rainfall system approached from the western offshore of the island, and passed on the northwestern side of the terrain showing a dramatic intensification; maximum rainfall amount was recorded on the northwestern slope of the island. For the 07P, the rainfall system approached from the northwestern off shore to the northern side of the island. Following its intensification in the northwestern coastal area of the island, the convective cell maintained its intensity as it moved along the northern lateral side of the island.

The rainfall enhancement on the lateral side of the island was identically shown in the results of idealized experiments (Figs. 5.4 and 5.9). The rainfall system which is passing on the northern lateral side of the island shows the further rainfall intensification than that passing over the northern offshore of the island (Fig. 5.4). The local updraft on the northern lateral side of the terrain (a hatched area in Fig. 6.2c), resulting from the convergence of horizontal–rerouting wind and predominant southwesterly wind (Fig. 6.2c), appears to play an important role in enhancing the rainfall system on the northern lateral side of the island (Fig. 6.2c). The southwesterly wind ($Fr \leq$ 0.5) in low altitudes rerouted its direction to go around the mountain, rather than to blow over it. The orographically–rerouted south–southwesterly wind converged with ambient southwesterly wind on the 4th quarter of the terrain; intense convergence (symbols of gray circles in Fig. 4.20a–b

and contours in Figs. 5.5f–j, 5.6f–h and 5.12f–h) distributed on the northwestern side of the island. In this distribution of convergence, with southwesterly wind, the relatively–high q_v decreased with increasing latitude and longitude to the northeast direction, in a range of 33.2–33.5°N and 126.0°E–126.5°E, at the height of 233 m (data not shown). Simultaneously, with the horizontal–rerouting of low–level wind on the western side of the terrain, a high–RH region (> 88 %; Fig. 5.1 and shaded area in Fig. 6.2a) develops in an arc shape surrounding the terrain. On the 4th quarter of the island, the q_v of 16–17 g kg^{-1} distributed. By the intense convergence on the northwestern side of the island (gray circles in Fig. 4.20a–b), the air with the high q_v in low altitude of 233 m seems to be lifted to higher altitude of 1 km. The lifted water vapour from low to higher altitudes was identified as the local high q_v (≥ 16 g kg^{-1}) on the northwestern side of the island at a height of 1 km (data not shown), where the intense convergence was identified. Simultaneously, toward the northwestern side of the island, the southwesterly wind continuously supplied air having the high q_v at the height of 233 m. In this condition, while the rainfall system locates on the northern lateral side of the island, the terrain–induced southwesterly winds are extended to the northern part of the island with relatively low Fr ($Fr \leq 0.55$). This extension maintains the supply of low–level moist air to convective cell. The generation of local updrafts by the convergence of the predominant southwesterly and horizontal–rerouting winds allows the rainfall system to intensify on the northern lateral side of terrain.

6.2.3. E lee side of terrain

The system evolution on the lee (eastern) side of an isolated elliptical terrain (Jeju Island) is discussed in this section. As discussed in section 6.1.2, the distinguished wind distribution is conducted on the lee side of the terrain with Fr = 0.2, 0.4 and 0.55 in identical moist environment. With a fairly–low Fr (0.2; Fig. 6.2d1), the horizontally–rerouted south–southwesterly wind on the northwestern side of the island arrives on the northeastern side of the island as a weak westerly,

converging with the relatively strong southwesterly from the southern island (Fig. 6.2a). As the low–level wind accelerated (*Fr* = 0.4 and *Fr* = 0.55; Fig. 6.2d2), the low–level wind partly goes over the mountain, generating a dry descending air on the northeastern downwind side.

Corresponding to the different wind distribution on the lee side with different low–level wind intensity (measured by *Fr*), the rainfall evolution of the 06P and 07P differed, from (1) rainfall dissipation on the northeastern side of the island in 06P (*Fr* = 0.55), to (2) rainfall enhancement on the eastern side of the island in 07P (*Fr* = 0.2).

The role of basic-state flow on the enhancement of rainfall systems on the lee side of the isolated elliptically–shaped terrain of Jeju Island has been confirmed by a series of idealized experiments, especially by the comparisons of the experimental results of runs BNW2 and BW5. The rainfall systems in both BNW2 and BW5 runs show similar path from the northern to the northeastern lee side of the island, but the evolution of the systems is distinct (Figs. 5.3a and 5.8c).

The most intense rainfall over the broadest region occurred in the BNW2 run, not only lateral to (A_{west} = 150 km^2, Table 5.2), but on the lee side of (A_{east} = 173 km^2) the island. The previously enhanced rainfall system moved further to the east, without dissipating on the northeastern downwind slope. As shown in the NB2 run, a weak dry descending air mass was generated near the crest of the mountain. The absence of dry descending air on the downstream side allowed the rainfall system to reach local updraft region on the lee side; therefore, rainfall was enhanced on the lee side. The enhanced rainfall was induced by the local updraft and the convergence (0.9×10^{-3} s^{-1}, Table 5.1) of the go-around northwesterly wind from the northern island with the southwesterly wind from the southern slope. The southwesterly wind from the southern island was relatively strong, which transported a plentiful supply of moist air to the updraft region on the eastern slope (Figs. 5.1a and 5.13). As explained in chapter 4.3 of numerical results of 07P, compared to those found in the NW offshore of the island, relatively intense convergence (greater than 3×10^{-3} s^{-1}) was identified on the E lee side, but with less amount of water vapour (15–16 g kg^{-1}) in low

altitudes as over the land. Even less amount of water vapour, intense convergence lifted the low–level vapour to further high altitudes above the freezing layer, thus enhancing cold hydrometeors (Figs. 4.17c and 4.31b).

In the BW5 run, very little rainfall occurred on the lee side of the island (A_{east} = 8 km^2, Table 5.2). This result is critically related to the intensification of dry descending air (D_{east} = –0.8 m s^{-1}, Table 5.1) in the downwind side of northeastern island. Because of the intensely dry descending air, the terrain-induced convergence shifted further downstream, as compared with the convergence in BNW2 (Fig. 5.2a and c). When the rainfall system moving eastward from the north to the northeast of the island encounters the intensely dry descending air, the rainfall rapidly dissipates before reaching local updraft on the lee side (C_{east} = 1.6 × 10^{-3} s^{-1}, Table 5.1). Thus, rainfall is absent on the lee side of the island in the BW5 run. This experimental result was similarly shown in result of case study of 06P, which reports both that terrain-generated dry descending air on the lee side and local updrafts on the lateral side of the island act to induce localized intense rainfall on the lateral side of the island when moist southwesterly winds prevail at low altitudes.

The comparison of the BW5 and BNW2 runs illustrates the important roles of both the absence of dry descending air and the presence of a moist updraft on the lee side of Jeju Island in generating rainfall enhancement (Figs. 5.13 and 6.2d1–d2, and Table 6.1). In a moist environment with prevailing southwesterly winds at low altitudes, the slightly different wind speeds at low altitudes (*Fr* = 0.2–0.55) become a crucial component determining the nature of system evolution on the lee side of the isolated elliptically shaped island; the patterns of rainfall enhancement and dissipation in the two systems result in a two-fold difference in the life-time of rainfall (D_{rain} of 150 min versus 70 min, Table 5.2).

As Akaeda et al. (1995) mentioned, the movement of a pre–existing rainfall system over a terrain has been dictated by the Froude number of the basic–state flow. Especially, within a narrow range of *Fr* from 0.2 to 0.55, the evolutionary characteristics and the related life–time of the

rainfall system are revealed to be distinguished by basic–state flow (measured by *Fr*) in a moist environment. Fairly weak southwesterly winds at low altitudes (*Fr*=0.2) drive rainfall enhancement on the lee side of the island, where a local updraft region and the absence of dry descending air are co–existing conditions. The absence of terrain–induced dry descending air on the northeastern downwind slope allows the rainfall system to reach the terrain–generated updraft region on the eastern side of the island. Then, the local updraft region on the eastern slope, which is generated by the go–around weak northwesterly flow from the northern island converges with the moist southwesterly winds from the southern island, which intensified the rainfall; thus, the rainfall system is relatively prolonged. As the southwesterly winds at low altitudes accelerate (*Fr* = 0.4 and *Fr* = 0.55), the low–level wind partly goes over the mountain. As a consequence, dry descending air which contributes to rapid rainfall dissipation strengthens on the northeastern downwind side of the terrain, which results in a relatively short life–time of the system. Through above discussions, the followings are become clearly.

(1) The shape and orientation of a terrain with respect to prevailing low–level wind directions, and the approach–direction of a pre–existing rainfall system with respect to the terrain, are important to determine the evolution of a pre–existing rainfall system on the shore.

(2) In a moist environment with low *Fr* (*Fr* ≤ 0.55), the terrain–modified south–southwesterly winds supply moist air to interior of the rainfall system on the northern lateral side of an elliptical–shaped terrain; it allows the rainfall system to intensify.

(3) The moist environment with fairly–low *Fr* (0.2) drives rainfall enhancement on the lee side of an elliptical–shaped terrain, where a local updraft region and the absence of dry descending air are co–existing conditions.

(4) The environment with the accelerated low–level wind (*Fr* = 0.4 and 0.55), a dry descending air which contributes to rapid rainfall dissipation strengthens on the northeastern downwind side of the terrain, which results in a relatively short life–time of the system.

7. Conclusions

Jeju Island, southern part of Korea has frequently suffered from flooding and landslides due to orographically–intensified rainfall systems during the rainy season. The island is an isolated terrain with an elliptical–shaped mountain extending east–to–west (width 35 km, length 78 km, height 1.95 km). In last 10 years (2003–2012), when the southwesterly wind prevails in low altitudes during June and July, the maximum rainfall amount of 3,805 mm was recorded locally on the northern slope of the mountain showing the relatively large rainfall (> 700 mm) on the northern and eastern side of the island, while rainfall less than 700 mm was accumulated on the western and southern sides of the island; the large regional–rainfall distinction was apparent on a mountainous region with a small horizontal scale. This study aims to reveal the effects of an isolated elliptical–shaped terrain on the flow modification and the related enhancement of rainfall system, especially on the northern side of the terrain, in a moist environment by both of data analyses and numerical simulations.

To achieve the aims, two intense rainfall systems occurred on 30 June 2006 and 6 July 2007 were selected. Both rainfall systems moved eastward and passed over the northern side of the island, showing the system enhancement on the northern side of the island. Four–dimensional structures of reflectivity and wind of convective cell within both systems were analyzed using S–band dual–Doppler radar dataset and a non–hydrostatic numerical model, CReSS. Comparison of enhancement mechanisms of two systems reveals that (1) moist environment and southwesterlies (β = 0.8) at low altitudes are favourable condition for the system enhancement, and (2) the isolated elliptical–shaped terrain of Jeju Island induces a horizontal rerouting of relatively–weak low–level southwesterly wind ($Fr \leq 0.55$) in low altitude, generating a local updraft region on the northwestern side of the island; in result, rainfall enhances on the northern lateral side of the island. Sensitivity experiments (with and without considering of terrain) reveals that (a) 30.6 % of rainfall

amount is induced by the steep topography of the island, and (b) abundant moisture content in low altitudes works for increasing rainfall; a reduction in the low–level RH of 2 % results in a 20.8 % reduction in rainfall amount.

Comparison of the two rainfall systems also shows some differences on the system evolution. In order to clarify the key parameter to induce the differences, a series of idealized experiments using CReSS were conducted. One key parameter is the arrival location of the eastward–moving system on the island. When the system travels off the northwestern shore of the island, further intensified system arrives on the island. As the distance between the system and terrain decreased, the southwesterlies blowing parallel to the coastline accelerates in the space between the system and terrain; thus updraft is locally generated. Subsequently, abundant vapour over sea surface is supplied to interior of the convective cell; thus warm rain process is mainly important to the system enhancement on the northwestern part of the island. Another key parameter is revealed to be intensity of low–level southwesterlies (measure be *Fr*). Fairly weak southwesterly wind ($Fr = 0.2$) at low altitudes allows enhancement of the system on the lee side of the island by generating the convergence of a relatively weak go–around northwesterly from the northern island and a relatively strong moist southwesterly from the southern island, thus producing a relatively long–lived rainfall system is resulted. With the strong southwesterly wind over the southeastern slope, the moist air is supplied to interior of the system to above the melting layer; thus both warm and cold rain processes are important in enhancing the convective cell on the eastern side of the island. As the low–level southwesterly winds strengthen at low altitudes ($Fr \gg 0.2$), a dry descending air mass intensified on the northeastern downwind side, which actively and rapidly dissipates rainfall system, resulting in a relatively short–lived rainfall system.

In this study, effect of an elliptical–shaped terrain (Jeju Island) on the enhancement of rainfall system in a moist environment is revealed. The result suggests us two meteorological elements for improving rainfall forecast over the mountainous region in a moist environment; (1) predominant

moist southwesterly wind has potential to bring out intense rainfall on the lateral (northern) side of the island, besides (2) the fairly–weak southwesterly wind has potential to induce intense rainfall, also on the lee (eastern) side of the island. Furthermore, in the identical environment, if the eastward–moving pre–existing rainfall system passes off the northwestern shore of the terrain, the system has potential to bring further intense rainfall on the lateral (northern) side of the terrain. These results suggest us key meteorological elements for rainfall enhancement which are applicable to a terrain with further complicated topographic feature in a moist environment so that it can help to improve the rainfall forecast over the mountainous region.

Acknowledgments

The author (Keunok LEE) is greatly indebted to her supervisor, Prof. Hiroshi Uyeda for his guidance for all years in Nagoya University, Japan. His thoughtful considerations, encouragement and supports have led her to concentrate on meteorology field and to know its sincere pleasure. Every wonderful discussion with him would be unforgotten in author's future research life.

Author wishes to acknowledge to Prof. Kazuhisa Tsuboki and Prof. Taro Shinoda of the laboratory of meteorology for their distinguished comments and suggestions. Regarding the helpful discussions and advices on numerical simulation, Mr. Atsushi Sakakibara of Chuden CTI Co., Ltd. and Mr. Masaya Kato of laboratory of meteorology are greatly acknowledged. Regarding the big helps in obtaining KMA radar dataset and providing fruitful advice on the radar analyses, Dr. Cheol-Hwan You of the laboratory of meteorology is also greatly acknowledged.

Author was fortunate to work with Dr. Shingo Shimizu of National Research Institute for Earth Science and Disaster Prevention (NIED) in Tsukuba, Japan. He has unconditionally shared his knowledge and deep experience with author. His enthusiasm for research and encouragement inspired author so that she could be absorbed in meso-scale meteorology field.

Prof. Masayuki Maki of Kagoshima University is greatly acknowledged for his every bright suggestion on research, and warm hospitality whenever author visited to NIED. Author would like to appreciate to Dr. Dong-Soon Kim of KMA for her sincere advice and encouragement.

Author would like to thank to Prof. Dong-In Lee of Pukyong National University, Korea for his steadfast support and elegant advices since 2005. Mr. S.-M. Jang, Mr. S.-H. Park, Mr. J.-H.Jeong and Ms. W.-S. Jung of Pukyong National University, are greatly appreciated for their radiant supports and warm encouragement.

Finally, author is grateful to her whole family for their spiritual support and devotion.

References

Akaeda, K., J. Reisner, and D. Parsons, 1995: The role of mesoscale and topographically induced circulations in initiating a flash flood observed during TAMEX project. *Mon. Wea. Rev*., **123**, 1720–1739.

Akiyama, T., 1975: Southerly transversal moisture flux into the extremely heavy rainfall zone in the Baiu season. *J. Meteor. Soc. Japan*, **53**, 304–316.

Akiyama, T., 1978: Mesoscale pulsation of convective rain in medium–scale disturbances developed in Baiu front. *J. Meteor. Soc. Japan*, **56**, 267–283.

Asselin, R., 1972: Frequency filter for time integrations. *Mon. Wea. Rev*., **100**, 487–490.

Baik, J.-J. and H.-Y. Chun, 1997: A dynamical model for urban heat islands. *Bound.–layer Meteor.*, **83**, 463–477.

Bernardet, L. R. and W. R. Cotton, 1998: Multiscale evolution of a derecho-producing mesoscale convective system. *Mon. Wea. Rev*., **126**, 2991–3015.

Bousquet, O. and B. F. Smull, 2003: Airflow and precipitation fields within deep Alpine valleys observed by airborne Doppler radar. *J. Appl. Meteor*., **42**, 1497–1513.

Byers, H. R. and R. R. Braham Jr., 1948: The thunderstorm structure and circulation. *J. Meteor*., **5**, 71–86.

Chen, G. T-J., and C. P. Chang, 1980: The structure and vorticity budget of an early summer monsoon trough (Mei-Yu) over southeastern China and Japan. *Mon. Wea. Rev*., **108**, 942–953.

Chen, G. T.-J., 1992: Mesoscale features observed in the Taiwan Mei-Yu season. *J. Meteor. Soc. Japan*, **70**, 497–516.

Chiao, S., and Y.-L. Lin, 2003: Numerical modeling of an orographically enhanced precipitation event associated with tropical storm Rachel over Taiwan. *Wea. Forecasting*, **18**, 325–344.

Chun, H.-Y. and J.-J. Baik, 1994: Weakly nonlinear response of a stably stratified atmosphere to diabatic forcing in a uniform flow. *J. Atmos. Sci.*, **51**, 3109–3121.

Cotton, W. R., G. J. Tripoli, R. M. Rauber, and E. A. Mulvihill, 1986: Numerical simulation of the effects of varying ice crystal nucleation rates and aggregation processes on orographic snowfall. *J. Climate Appl. Meteor*., **25**, 1658–1680.

Cotton, W. R. and R. A. Anthes, 1989: *Storm and cloud dynamics*. Academic press, 883 pp.

Cressman, G. P., 1959: An operational objective analysis system. *Mon. Wea. Rev*., **87**, 367–374.

Doviak R. J. and D. S. Zrnic, 1984: Doppler radar and weather observation. Dover publications, 562 pp.

Fritsch, J. M. and G. S. Forbes, 2001: Severe convective storms: Mesoscale convective systems. Amer. Meteor. Soc. Monograph, **28**, 323–357.

Galewsky, J. and A. Sobel, 2005: Moist dynamics and orographic precipitation in Northern and central California during the new year's flood of 1997. *Mon. Wea. Rev*., **133**, 1594–1612.

Gal-Chen, T., 1982: Errors in fixed and moving frame of references: Applications for conventional and Doppler radar analysis. *J. Atmos. Sci*., **39**, 2279–2300.

Gao, J., M. Xue, A. Shapiro, and K. K. Droegemeier, 1999: A variational method for the analysis of three-dimensional wind fields from two Doppler radars. *Mon. Wea. Rev*., **127**, 2128–2142.

Geng, B., H. Yamada, K. K. Reddy, H. Uyeda, and Y. Fujiyoshi, 2004: An observational study of the development of a rainband on a Meiyu front causing heavy rainfall in the downstream region of the Yangtze River. *J. Meteor. Soc. Japan*, **82**, 1095–1115.

Geng, B., H. Yamada, K. K. Reddy, H. Uyeda, and Y. Fujiyoshi, 2009: Mesoscale development and along-frontal variation of a Meiyu/Baiu front and precipitation observed in the downstream region of the Yangtze River. *J. Meteor. Soc. Japan*, **87**, 423–457.

Grossman, R. L. and D. R. Durran, 1984: Interaction of low-level flow with the western Ghat Mountains and offshore convection in the summer monsoon. *Mon. Wea. Rev*., **112**, 652–672.

Hobbs, P. V., R. A., Houze, Jr. and T. J. Matejka, 1975: The dynamical and microphysical structure of an occluded frontal system and its modification by orography. *J. Atmos. Sci*., **32**, 1542–1562.

Houze, R. A. Jr., 1993: *Cloud dynamics*. Academic press, 573pp.

Houze, R. A. Jr., 2012: Orographic effects on precipitating clouds. *Rev. Geophys*., **50**, RG1001.

Houze, R. A. Jr. and S. Medina, 2005: Turbulence as a mechanism for orographic precipitation enhancement. *J. Atmos. Sci*., **62**, 3599–3623.

Ikawa, M. and K. Saito, 1991: Description of a nonhydrostatic model developed at the Forecast Research Department of the MRI. MRI Tech. Rep. 28, Meteorological Research Institute, 238 pp. [Available online at http://www.mri-jma.go.jp/Publish/Technical/DATA/VOL_28/28_en.html.]

Jiang, Q., 2003: Moist dynamics and orographic precipitation. *Tellus*, **55A**, 301–316.

Jirak, I. L. and W. R. Cotton, 2007: Observational analysis of the predictability of mesoscale convective systems. *Wea. Forecasting*, **22**, 813–838.

Johnson, R. H., S. Chen, and J. J. Toth, 1989: Circulations associated with a mature-to-decaying midlatitude mesoscale convective system. Part Ⅰ: Surface features–heat bursts and mesolow development. *Mon. Wea. Rev*., **117**, 942–959.

Johnson, R. H., T. M. Rickenbach, S. A. Rutledge, P. E. Ciesielski, and W. H. Schubert, 1999: Trimodal characteristics of tropical convection. *J. Climate*, **12**, 2397–2418.

Kanada, S., H. Minda, B. Geng, and T. Takeda, 2000: Rainfall enhancement of band-shaped convective cloud system in the downwind side of an isolated island. *J. Meteor. Soc. Japan*, **78**, 47–67.

Kane, R. J. Jr., C. R. Chelius, and J. M. Fritsch, 1987: Precipitation characteristics of mesoscale convective weather systems. *J. Climate Appl. Meteorol*., **26**, 1323–1335.

Kato, K., 1985: On the abrupt change in the structure of the Baiu front over the China continent in late May of 1979. *J. Meteor. Soc. Japan*, **63**, 20–36.

Kato, T, 2005: Statistical study of band-shaped rainfall systems, the Koshikijima and Nagasaki lines, Observed around Kyushu Island, Japan. *J. Meteor. Soc. Japan*, **83**, 943–957.

Kato, T., M. Yoshizaki, K. Bessho, T. Inoue, Y. Sato, and X-BAIU-01 observation group, 2003: Reason for the failure of the simulation of heavy rainfall during X-BAIU-01-Importance of a vertical profile of water vapor for numerical simulations. *J. Meteor. Soc. Japan*, **81**, 993–1013.

Kirshbaum, D. J., G. H. Bryan, and R. Rotunno, 2007: The triggering of orographic rainbands by small-scale topography. *J. Atmos. Sci*., **64**, 1530–1549.

Klemp, J. B. and R. B. Wilhelmson, 1978: The simulation of three-dimensional convective storm dynamics. *J. Atmos. Sci*., **35**, 1070–1096.

Kondo, J., 1976: Heat balance of the China Sea during the air mass transformation experiment. *J. Meteor. Soc. Japan*, **54**, 382–398.

Kottek, M., J. Grieser, C. Beck and F. Rubel, 2006: World map of the Koppen–Geiger climate classification updated. *Meteorol. Z*., **15**, 259–263.

Kuo, Y.-H. and G. T.-J. Chen, 1990: The Taiwan area mesoscale experiment (TAMEX): An overview. *Bull. Amer. Meteor. Soc*., **71**, 488–503.

Li, J., Y.-L. Chen, and W.-C. Lee, 1997: Analysis of a heavy rainfall event during TAMEX. *Mon. Wea. Rev*., **125**, 1060–1082.

Lin, Y.-L., 1993: Orographic effects on airflow and mesoscale weather systems over Taiwan. *Terr. Atmos. Ocean Sci*., **4**, 381–420.

Lin, Y.-L., 2007: *Mesoscale dynamics*, Cambridge University Presss, 630 pp.

Lin, Y.-L., D. B. Ensley, S. Chiao, and C.-Y. Huang, 2002: Orographic influences on rainfall and track deflection associated with the passage of a tropical cyclone. *Mon. Wea. Rev.*, **130**, 2929–2950.

Lin, Y.-L., H. D. Reeves, S.-Y. Chen, and S. Chiao, 2005: Formation mechanisms for convection over the Ligurian Sea during MAP IOP-8. *Mon. Wea. Rev*., **133**, 2227–2245.

Lin, Y.-L., R. D. Farley, and H. D. Orville, 1983: Bulk parameterization of the snow field in a cloud model. *J. Climate Appl. Meteor*., **22**, 1065–1092.

Lin, Y.-L., S. Chiao, T.-A. Wang, M. L. Kaplan, and R. P. Weglarz, 2001: Some common ingredients for heavy orographic rainfall. *Wea. Forecasting*, **16**, 633–660.

Lin, Y.-L., T.-A. Wang, 1996: Flow regimes and transient dynamics of two-dimensional stratified flow over an isolated mountain ridge. J. Atmos. Sci., 53, 139-158.

Louis, J. F., M. Tiedtke and J. F. Geleyn, 1981: A short history of the operational PBL parameterization at ECMWF. *Proc. Workshop on Planetary Boundary Layer Parameterization*, Reading, United Kingdom, ECMWF 59–79.

Maddox, R. A., 1983: Large-scale meteorological conditions associated with midlatitude, mesoscale convective complexes. *J. Atmos. Sci*., **111**, 1475–1493.

Miles, J. W. and H. E. Huppert, 1969: Lee waves in a stratified flow. Part 4: Perturbation approximation. *J. Fluid Mech.*, **35**, 497–525.

Moteki, Q., H. Uyeda, T. Maesaka, T. Shinoda, M. Yoshizaki and T. Kato, 2004a: Structure and development of two merged rainbands observed over the East China Sea during X-Baiu-99 Part Ⅰ: Meso-β-scale structure and development processes. *J. Meteor. Soc. Japan*, **82**, 19–44.

Moteki, Q., H. Uyeda, T. Maesaka, T. Shinoda, M. Yoshizaki and T. Kato, 2004b: Structure and development of two merged rainbands observed over the East China Sea during X-Baiu-99 Part Ⅱ: Meso-α-scale structure and development processes. *J. Meteor. Soc. Japan*, **82**, 45–65.

Murakami, M., 1990: Numerical modeling of dynamical and microphysical evolution of an isolated convective cloud – The 19 July 1981 CCOPE cloud. *J. Meteor. Soc. Japan*, **68**, 107–128.

Murakami, M., T. L. Clark, and W. D. Hall, 1994: Numerical simulations of convective snow clouds over the Sea of Japan; Two-dimensional simulations of mixed layer development and convective snow cloud formation. *J. Meteor. Soc. Japan*, **72**, 43–62.

Ninomiya, K., 2001: Large Λ-shaped cloud zone formed around July 6, 1991 with pole-ward moisture transport from intense rainfall area in Meiyu-Baiu front. *J. Meteor. Soc. Japan*, **79**, 805–813.

Ninomiya, K. and H. Mizuno, 1987: Variations of Baiu precipitation over Japan in 1951–1980 and large-scale characteristics of wet and dry Baiu. *J. Meteor. Soc. Japan*, **65**, 115–127.

Ninomiya, K. and H. Muraki, 1986: Large-scale circulations over East Asia during Baiu period of 1979. *J. Meteor. Soc. Japan*, **64**, 409–429.

Ninomiya, K. and T. Akiyama, 1974: Band structure of mesoscale echo clusters associated with low-level jet stream. *J. Meteor. Soc. Japan*, **52**, 300–313.

Ninomiya, K. and T. Akiyama, 1992: Multi-scale features of Baiu, the summer monsoon over Japan and East Asia. *J. Meteor. Soc. Japan*, **70**, 467–495.

Olafsson, H., 2000: The impact of flow regimes on asymmetry of orographic drag at moderate and low Rossby numbers. *Tellus*, **52A**, 365–379.

Olafsson, H. and P. Bougeault, 1996: Nonlinear flow past an elliptic mountain ridge. *J. Atmos. Sci*., **53**, 2465–2489.

Orlanski, I., 1975: A rational subdivision of scales for atmospheric processes. *Bull. Amer. Meteor. Soc*., **56**, 527–530.

Olsson, P. Q., 1994: Evolution of balanced flow in a simulated mesoscale convective complex. Ph.D. dissertation, Colorado State University, Dept. of Atmospheric Sience, Fort Collins, CO 80523, 177 pp.

Pandya, R. E., and D. R. Durran, 1996: The influence of convectively generated thermal forcing on the mesoscale circulation around squall lines. *J. Atmos. Sci*., **53**, 2924–2951.

Petersen, G. N., H. Olafsson, and J. E. Kristjansson, 2003: Flow in the lee of idealized mountains and Greenland. *J. Atmos. Sci*., **60**, 2183–2195.

Petersen, G. N., J. E. Kristjansson and H. Olafsson, 2005: The effect of upstream wind direction on atmospheric flow in the vicinity of a large mountain. *Q. J. R. Meteorol. Soc*., **131**, 1113–1128.

Raymond, D. J. and H. Jiang, 1990: A theory for long-lived mesoscale convective systems. *J. Atmos. Sci*., **47**, 3067–3077.

Rotunno, R. and R. Ferretti, 2001: Mechanisms of intense Alpine rainfall. *J. Atmos. Sci*., **58**, 1732–1749.

Rotunno, R. and R. Ferretti, 2003: Orographic effects on rainfall in MAP cases IOP 2b and IOP 8. *Q. J. R. Meteorol. Soc*., **129**, 379–390.

Reeves, H. D. and Y.-L. Lin, 2007: The effect of a mountain on the propagation of a preexisting convective system for blocked and unblocked flow regimes. *J. Atmos. Sci*., **64**, 2401–2421.

Rowe, A. K., 2011: A polarimetric radar analysis of convection observed during NAME and TIMREX. Ph. D. Thesis, Colorado State University.

Schmidt, J. M. and W. R. Cotton, 1989: A high plains squall line associated with a derecho. *J. Atmos. Sci*., **46**, 281–302.

Segami, A., K. Kurihara, H. Nakamura, M. Ueno, I. Takano, and Y. Tatsumi, 1989: Operational mesoscale weather prediction with Japan spectral model. *J. Meteor. Soc. Japan*., **67**, 907–923.

Shimizu, S, 2007: Study on maintenance mechanism of convective cells in meso-scale convective system in humid subtropical region. Ph. D. Thesis, Nagoya University.

Shimizu, S. and T. Maesaka, 2006: Multiple Doppler radar analysis using variational technique to retrieve three-dimensional wind field. Technical Report 70, National Research Institute for Earth Science and Disaster Prevention, Japan, 1-8 (in Japanese).

Smith, R. B., 1980: Linear theory of stratified hydrostatic flow past an isolated mountain. *Tellus*, **32A**, 348–364.

Smith, R. B. and S. Gronas, 1993: Stagnation points and bifurcation in 3-D mountain airflow. *Tellus*, **45A**, 28–43.

Smolarkiewicz, P. K., R. M. Rasmussen, and T. L. Clark, 1988: On the dynamics of Hawaiian cloud bands: Island forcing. *J. Atmos. Sci*., **45**, 1872–1905.

Smolarkiewicz, P. K. and R. Rotunno, 1989: Low Froude number flow past three-dimensional obstacles. Part Ⅰ: Baroclinically generated lee vortices. *J. Atmos. Sci*., **46**, 1154–1164.

Smolarkiewicz, P. K. and R. Rotunno, 1990: Low Froude number flow past three-dimensional obstacles. Part Ⅱ: Upwind flow reversal zone. *J. Atmos. Sci*., **47**, 1498–1511.

Tatehira, R. and O. Suzuki, 1994: Accuracy in estimation of wind velocity from single Doppler radar. *Tenki*, **41**, 761–764 (*in Japanese*).

Trewartha, G. T. and L. H. Horn, 1980: *An introduction to climate*. Mc Graw Hill, 416 pp.

Tripoli, G. J. and W. R. Cotton, 1989a: Numerical study of an observed orogenic mesoscale convective system. Part 1: Simulated genesis and comparison with observations. *Mon. Wea. Rev*., **117**, 273–304.

Tripoli, G. J. and W. R. Cotton, 1989b: Numerical study of an observed orogenic mesoscale convective system. Part 2: Analysis of governing dynamics. *J. Atmos. Sci*., **117**, 305–328.

Tsuboki, K. and A. Sakakibara, 2001: CReSS User's Guide, 2nd edition, 210 pp. [available from http://www.rain.hyarc.nagoya-u.ac.jp/~tsuboki/cress_html/src_cress/CReSS2223_users_ guide _eng.pdf].

Tsuboki, K. and A. Sakakibara, 2002: Large-scale parallel computing of Cloud Resolving Storm Simulator. High Performance Computing: Proceedings of the Fourth International Symposium on High Performance Computing, H. P. Zima et al., Eds., Springer, 243–259.

Waldteufel, P. and H. Corbin, 1979: On the analysis of single-Doppler radar data. *J. Appl. Meteor*., **18**, 532–542.

Wang, C.-C., G. T.-J. Chen, T.-C. Chen, and K. Tsuboki, 2005: A numerical study on the effects of Taiwan topography on a convective line during the Mei-Yu season. *Mon. Wea. Rev*., **133**, 3217–3242.

Woods, C. P., M. T., Stoelinga, J. D. Locatelli, and P. V. Hobbs, 2005: Microphysical processes and synergistic interaction between frontal and orographic forcing of precipitation during the 13 December 2001 IMPROVE-2 event over the Oregon Cascades. *J. Atmos. Sci*., **62**, 3493–3519.

Xu, W., E. J. Zipser, Y.-L. Chen, C. Liu, Y.-C. Liou, W.-C. Lee, and B. J.-D. Jou, 2012: An orography–associated extreme rainfall event during TiMREX: Initiation, storm evolution, and maintenance. *Mon. Wea. Rev*., **140**, 2555–2574.

Yamada, H., B. Geng, K. K. Reddy, H. Uyeda, and Y. Fujiyoshi, 2003: Three-dimensional structure of a mesoscale convective system in a Baiu-frontal depression generated in the downstream region of the Yangtze River. *J. Meteor. Soc. Japan*, **81**, 1243–1271.

Yoshizaki, M., T. Kato, Y. Tanaka, H. Takayama, Y. Shoji, H. Seko, K. Arao, and K. Manabe, 2000: Analytical and numerical study of the 26 June 1998 orographic rainband observed in western Kyushu, Japan. *J. Meteor, Soc, Japan*, **78**, 835–856.

Yu, C.-K., D. P. Jorgensen, and F. Roux, 2007: Multiple precipitation mechanisms over mountains observed by airborne Doppler radar during MAP IOP5. *Mon. Wea. Rev*., **135**, 955–984.

Yuter, S. E. and R. A. Houze, Jr., 2003: Microphysical modes of precipitation growth determined by S-band vertically pointing radar in orographic precipitation during MAP. *Quart. J. Roy. Meteor. Soc*., **129**, 455–476.

Figures and Tables

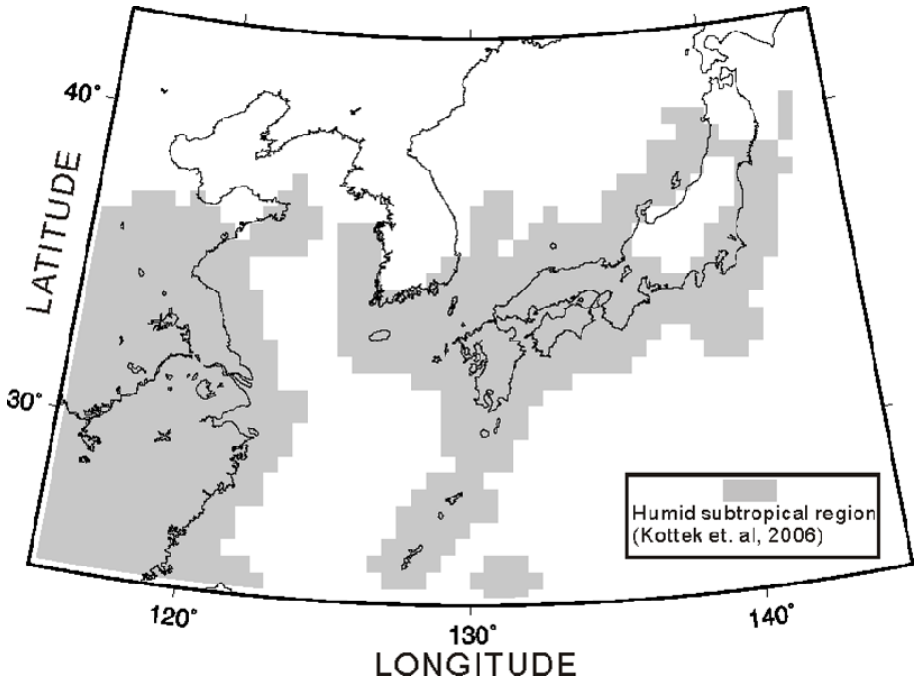

FIG.1.1. Climatological distribution of humid subtropical region (adopted from Fig.1.1 of Shimizu, 2007).

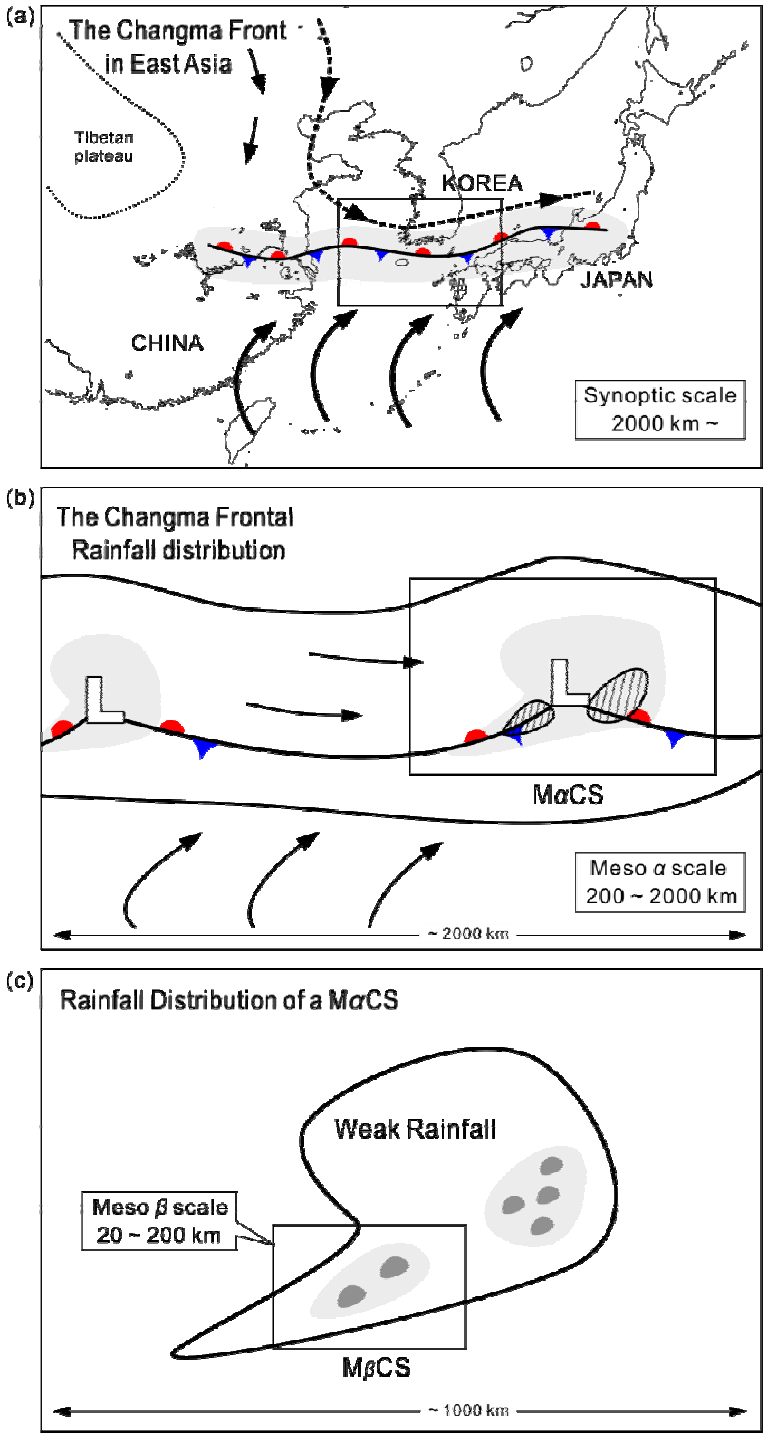

FIG.1.2. Schematic illustration of Hierarchical structures of precipitation system in Changma/Baiu/ Meiyu frontal region (adopted from Fig. 35 of Ninomiya and Akiyama, 1992). An inner domain in (a) and (b) is the domain of (b) and (c), respectively.

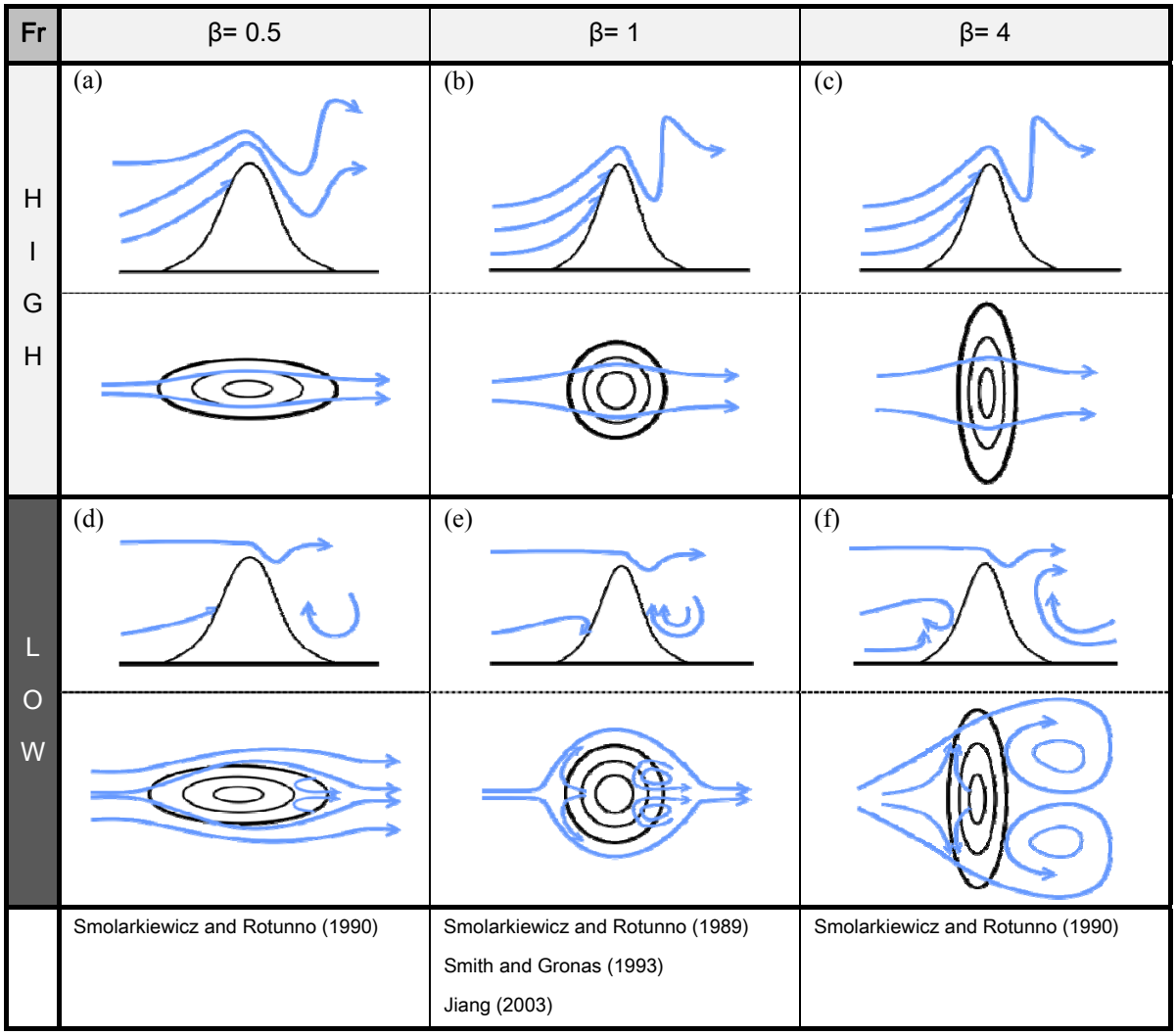

FIG.1.3. Schematic diagram of flow modification (blue arrows) adjacent to an isolated mountainous region (black solid lines) with a relatively–small horizontal scale: (a)–(c) high–*Fr* regime and (d)–(f) low–*Fr* regime. (a) and (d) are flow modifications around an elliptical shaped terrain in environment with β = 0.5, (b) and (e) are flow modifications around an bell shaped terrain in environment with β = 1.0, and (c) and (f) are flow modification around an elliptical shaped terrain in environment with β = 4.0.

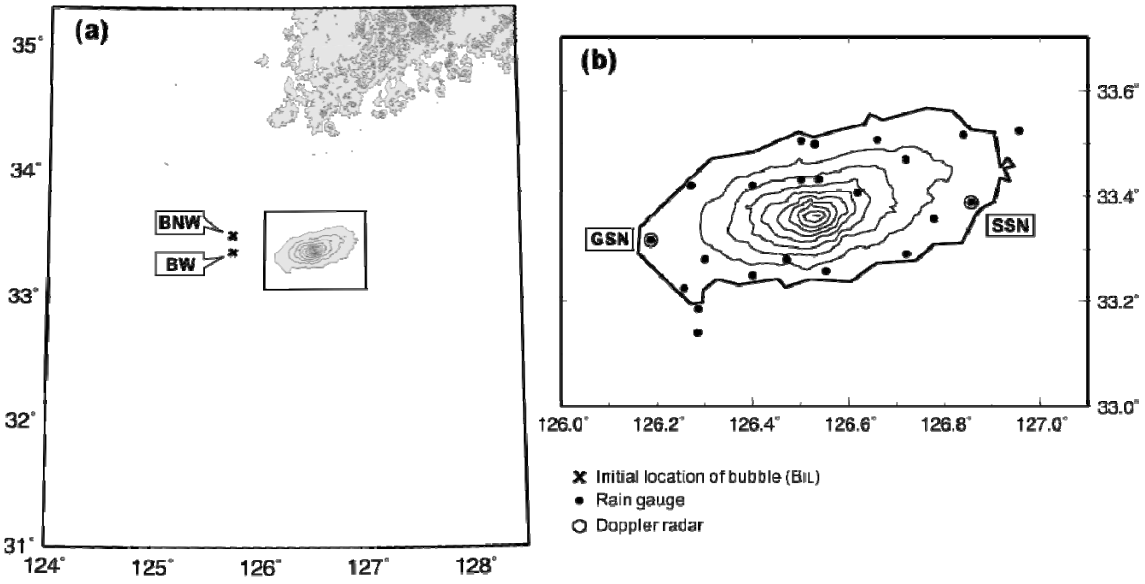

FIG.1.4. Location and elevation map of Jeju Island. Thin contour lines show topography (contour interval: 200 m). The centre locations of initial warm bubbles (BNW and BW) for the idealized numerical experiments are depicted by cross symbols in (a). The locations of 22 rain gauges are depicted by dots on Jeju Island in (b). The locations of the two radar sites (GSN and SSN) are indicated by small open circles in (b).

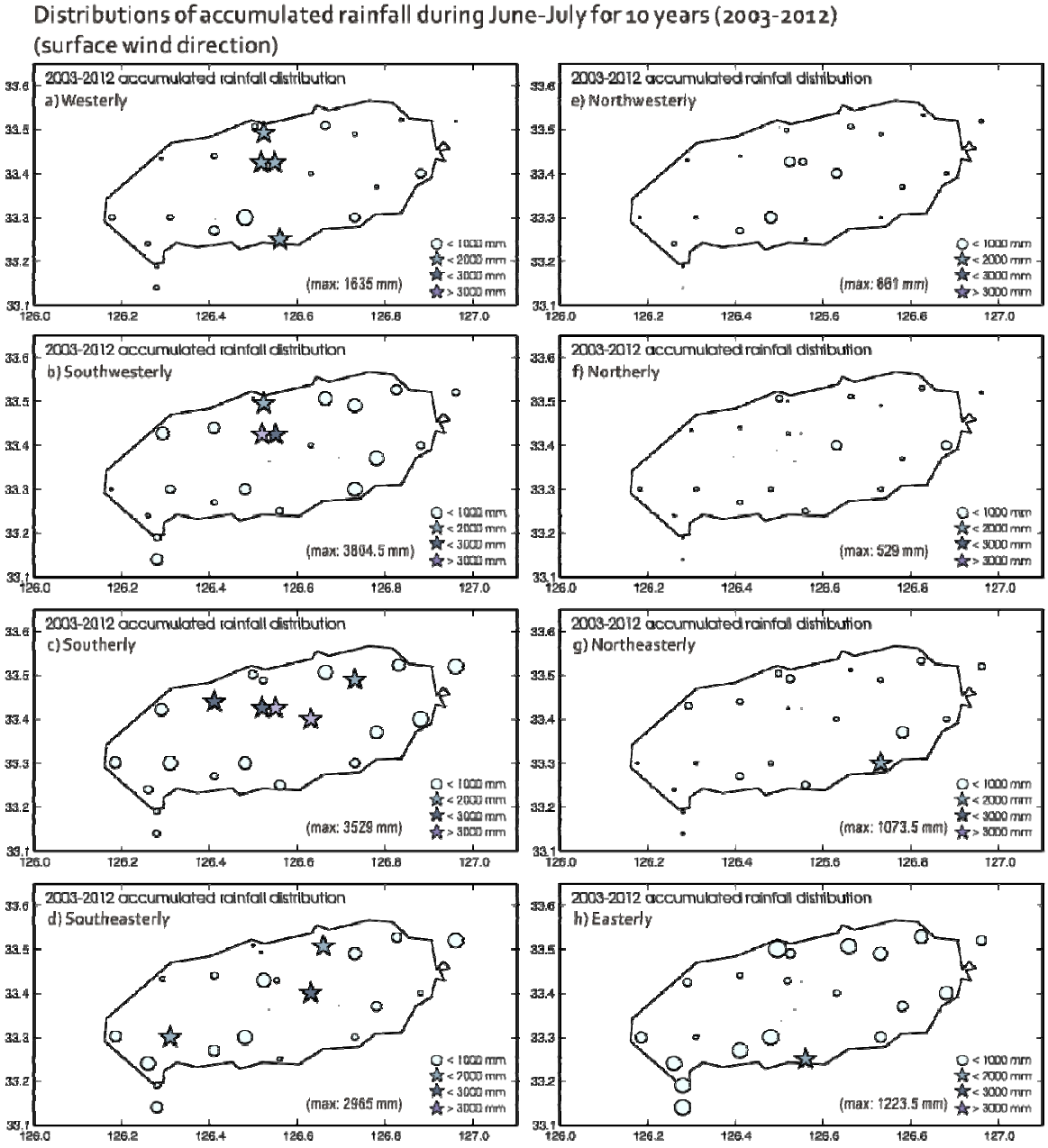

FIG.1.5. Distributions of accumulated rainfall amount during June-July for 10 years from 2003 to 2012 on Jeju Island, dividing by surface wind direction of (a) westerly, (b) southwesterly, (c) southerly, (d) southeasterly, (e) northwesterly, (f) northerly, (g) northeasterly, and (h) easterly wind. Locations of each symbol are the observation location of the 22 surface rain gauges (dots in Fig. 1.4b). The circle symbols indicate the accumulated rainfall amount less than 1000 mm, and the size is weighted to show the relative rainfall amount. The star symbols depict the accumulated rainfall amount less than 2000 mm, and 3000 mm, and larger than 3000 mm by light blue, blue, and violet shadings, respectively.

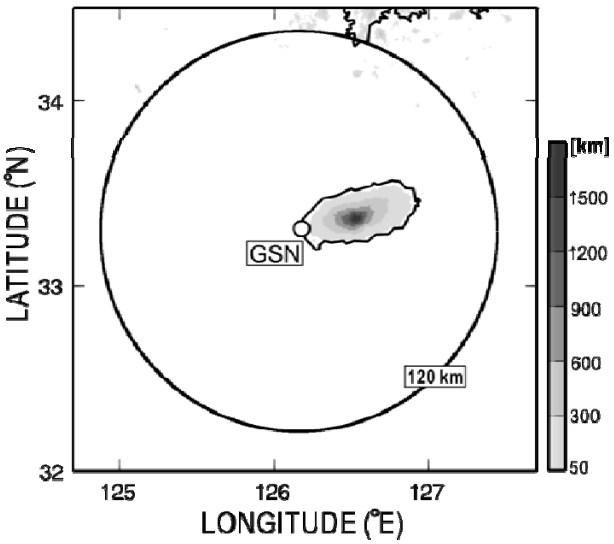

FIG.2.1. Elevation map of Jeju Island and observation range (120 km) of the S-band Doppler radar (large circle) installed at Gosan (GSN). Upper-air soundings were recorded at the radar site.

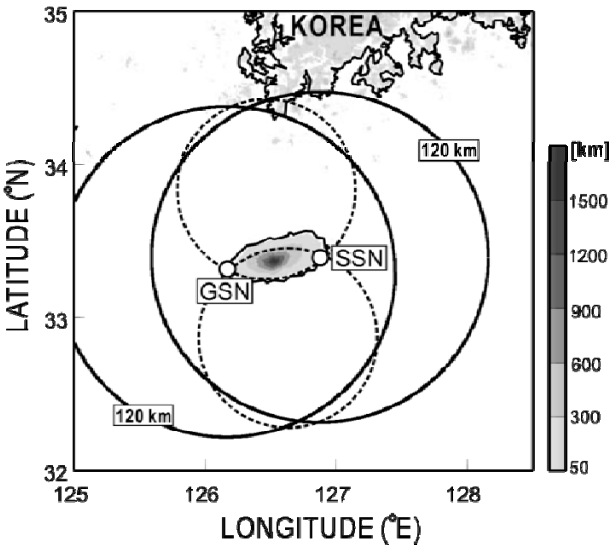

FIG.2.2. Elevation map of Jeju Island and observational range (120km; black circles) of the dual-Doppler radars installed at Gosan (GSN) and Seongsan (SSN). The GSN and SSN radar sites are indicated by small open circles. The upper-air sounding station is located at the GSN radar site. Dual-Doppler radar analysis is conducted within the two dashed circles, except for within the area of intersection (intersection angle less than 35°).

TABLE 2.1. Specifications of CReSS.

Model feature	Description
Basic equation	Quasi-compressible non-hydrostatic Navier–Stokes equations with a map factor
Projection	Lambert conformal conic
Vertical coordinate	Terrain-following
Grid	Staggered Arakawa C type in the horizontal and Lorenz type in the vertical
Advection scheme	Antiflux form with fourth-order central differential
Diffusion scheme	Fourth-order central differential method
Turbulent closure	1.5-order closure scheme
Time splitting	Horizontally explicit and vertically implicit for sound waves
Precipitation scheme	Bulk cold-rain scheme (predicting q_v, q_c, q_r, q_i, q_s, q_g, N_i, N_s, and N_g)
Surface layer	Bulk method similar to Segami et al. (1989)
Lower boundary	Rigid; temperature is forecast using a 30-layer one-dimensional model
Upper boundary	Rigid lid with absorbing layer
Lateral boundary	Radiative nesting boundary condition

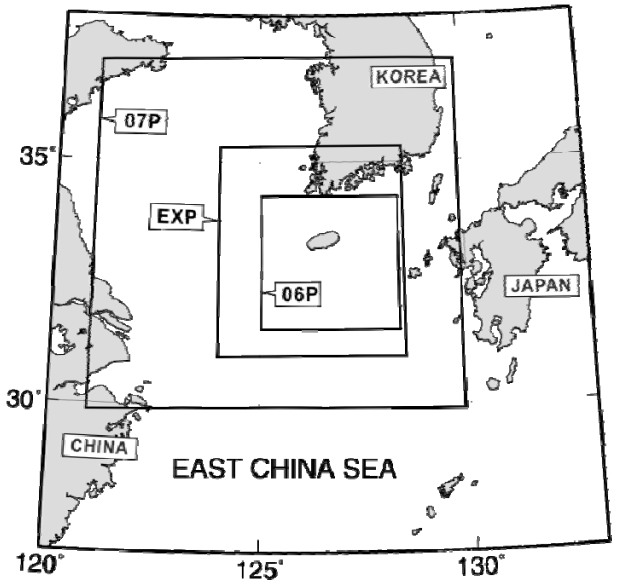

FIG.2.3. Domain considered in numerical simulations using CReSS. Inner domain named **06P**, and **07P**, is considered in numerical simulations for rainfall system on 30 June 2006 (shown in chapter 3.3) and 6 July 2007 (shown in chapter 4.3), respectively. An inner domain **EXP** is used for idealized experiments (shown in chapter 5).

TABLE.2.2. Vertical profiles of initial temperature (T) and relative humidity (RH) used in experiments.

HEIGHT (m)	T (K)	RH (%)
8000	259	50
7500	262	50
7000	265	60
6500	267	60
6000	270	60
5500	272	70
5000	273	70
4500	274	80
4000	277	80
3500	280	80
3000	284	85
2500	287	85
2000	290	90
1500	294	90
1000	294	90
500	299	90
150	299	90

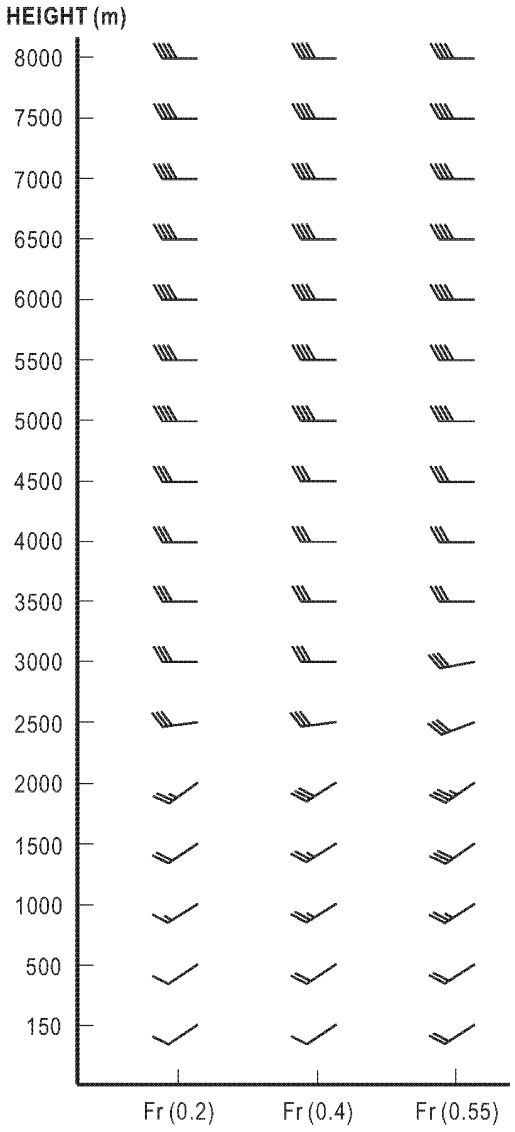

FIG.2.4. Vertical profile of the initial horizontal wind used in the experiments.

TABLE.2.3. List of idealized experiments.

Category	*Fr* (0.2)	*Fr* (0.4)	*Fr* (0.55)
No bubble (NB)	NB2	NB4	NB5
B_{IL} (BNW)	BNW2	BNW4	BNW5
B_{IL} (BW)	BW2	BW4	BW5

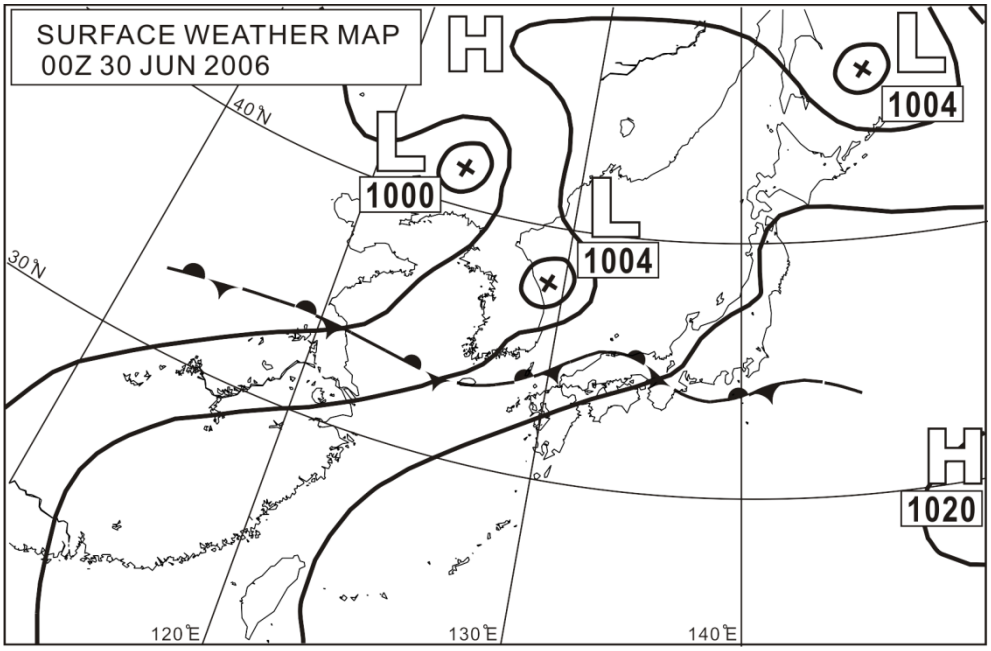

FIG.3.1. Surface weather map of East Asia at 0900 LST on 30 June 2006.

TABLE.3.1. Environmental parameters determined from upper-air sounding data. Lifting convection level (LCL), level of free convection (LFC), and surface relative humidity (RH) are shown. Calculated precipitable water (PW) from the surface to 300 hPa and convective available potential energy (CAPE), Brunt-Vaisala frequency (N), and Froude number (*Fr*) are shown.

Parameter	Value
LCL	951 hPa
LFC	724 hPa
RH (surface)	92 %
PW (below 700 hPa)	44.9 kg m^{-2}
CAPE	33.2 J kg^{-1}
N	1.3 10^{-2} s^{-1}
Fr	0.55

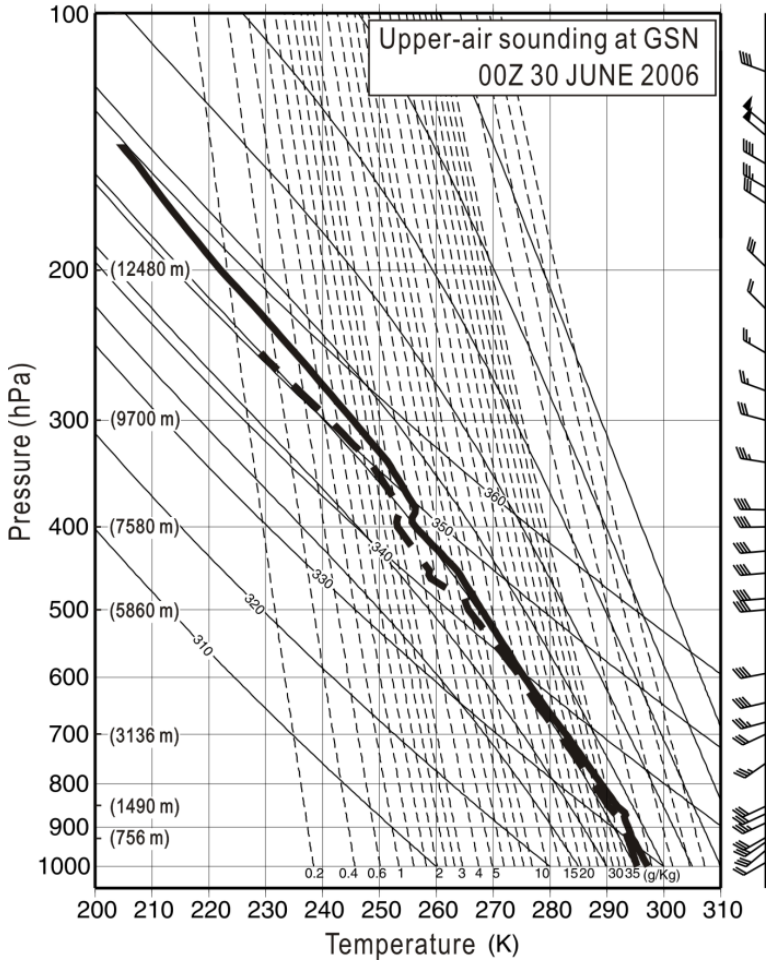

FIG.3.2. Vertical profiles of temperature (thick line), dew-point temperature (thick dashed line), and wind speed and direction (right side of the figure) on an emagram. Data are sounding data obtained at GSN at 0900 LST on 30 June 2006. One pennant, full barb, and half barb denote wind speeds of 25, 5, and 2.5 $m\,s^{-1}$, respectively.

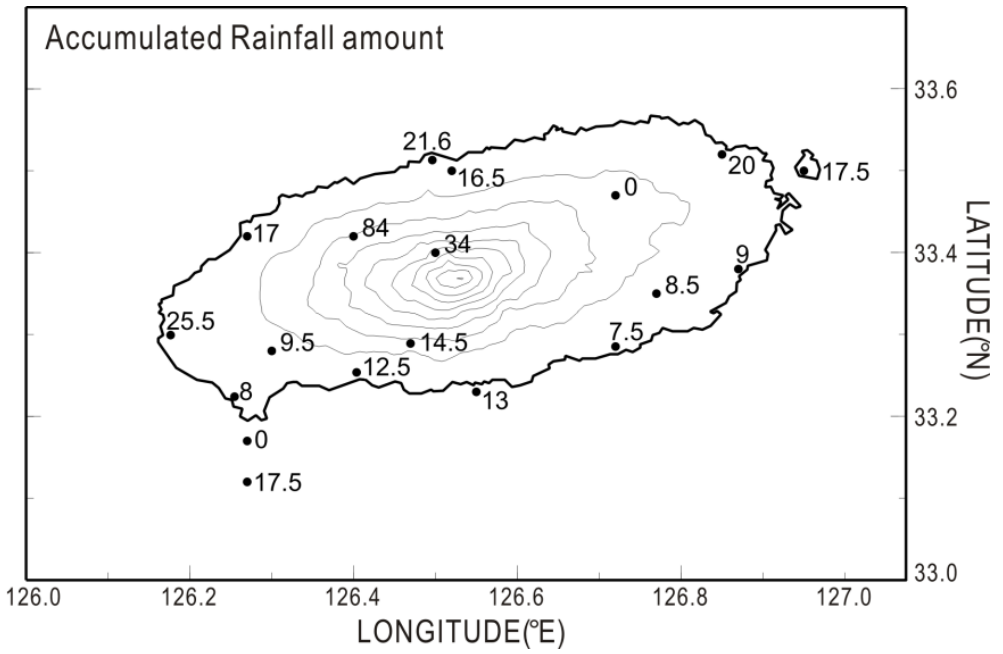

FIG.3.3. Accumulated rainfall amount recorded by 19 rain gauges (dots) adjacent to Jeju Island from 1320 to 1500 LST on 30 June 2006. Thin contour lines show topography (contour interval: 200 m).

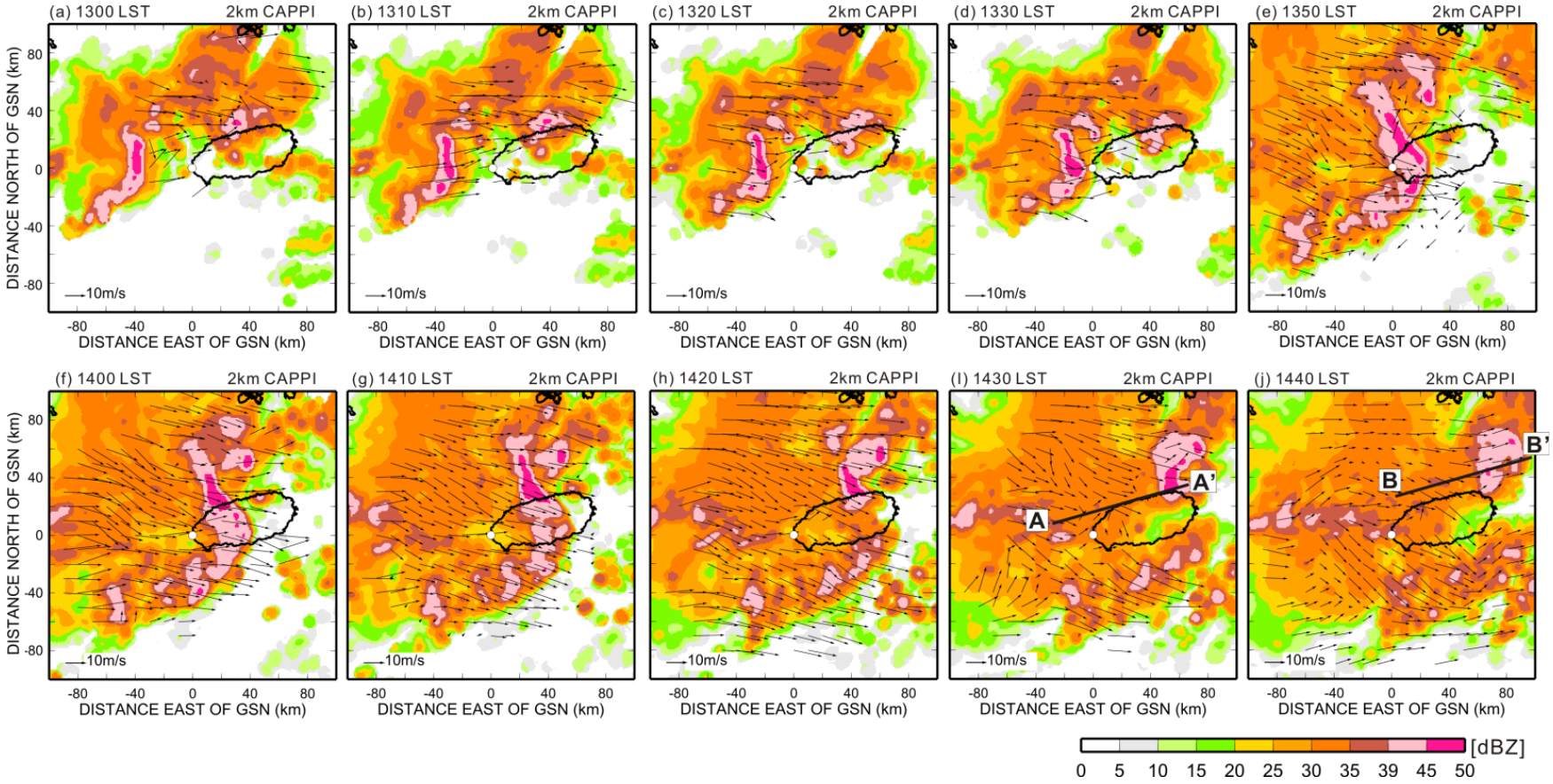

FIG.3.4. Horizontal distribution of reflectivity at 2 km ASL and low-level wind vectors for (a) 1300 LST, (b) 1310 LST, (c) 1320 LST, (d) 1330 LST, (e) 1350 LST, (f) 1400 LST (left bottom), (g) 1410 LST, (h) 1420 LST, (i) 1430 LST, and (j) 1440 LST on 30 June 2006. The lines A-A' in (i) and B-B' in (j) show the locations of the vertical cross-section of reflectivity shown in Fig. 3.5.

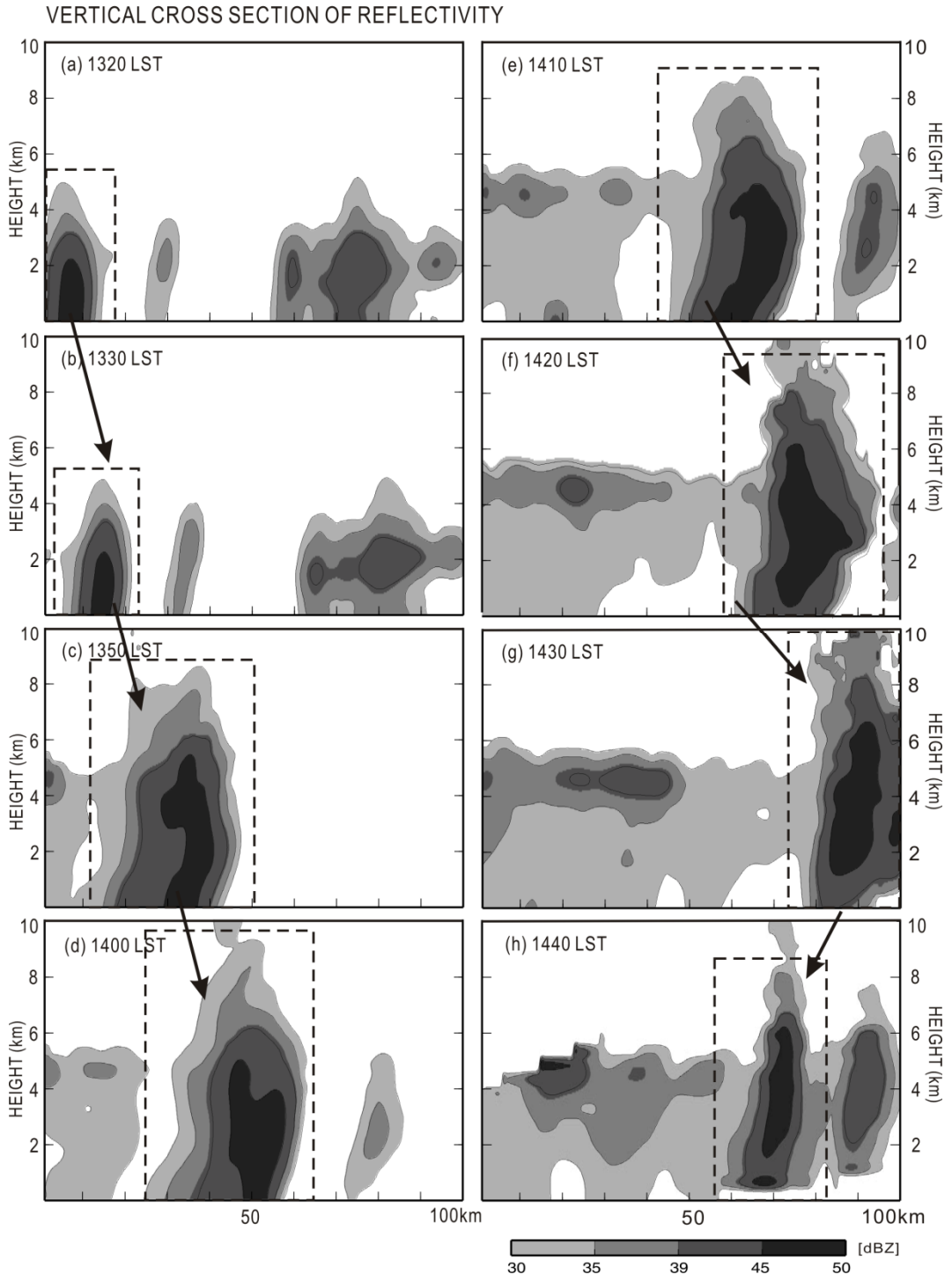

FIG.3.5. Vertical cross-sections of reflectivity (along A-A' in Fig. 3.4i) for (a) 1320 LST (left upper), (b) 1330 LST, (c) 1350 LST, (d) 1400 LST, (e) 1410 LST (right upper), (f) 1420 LST, (g) 1430 LST, and vertical cross-section (along B-B' in Fig. 3.4j) for (h) 1440 LST on 30 June 2006.

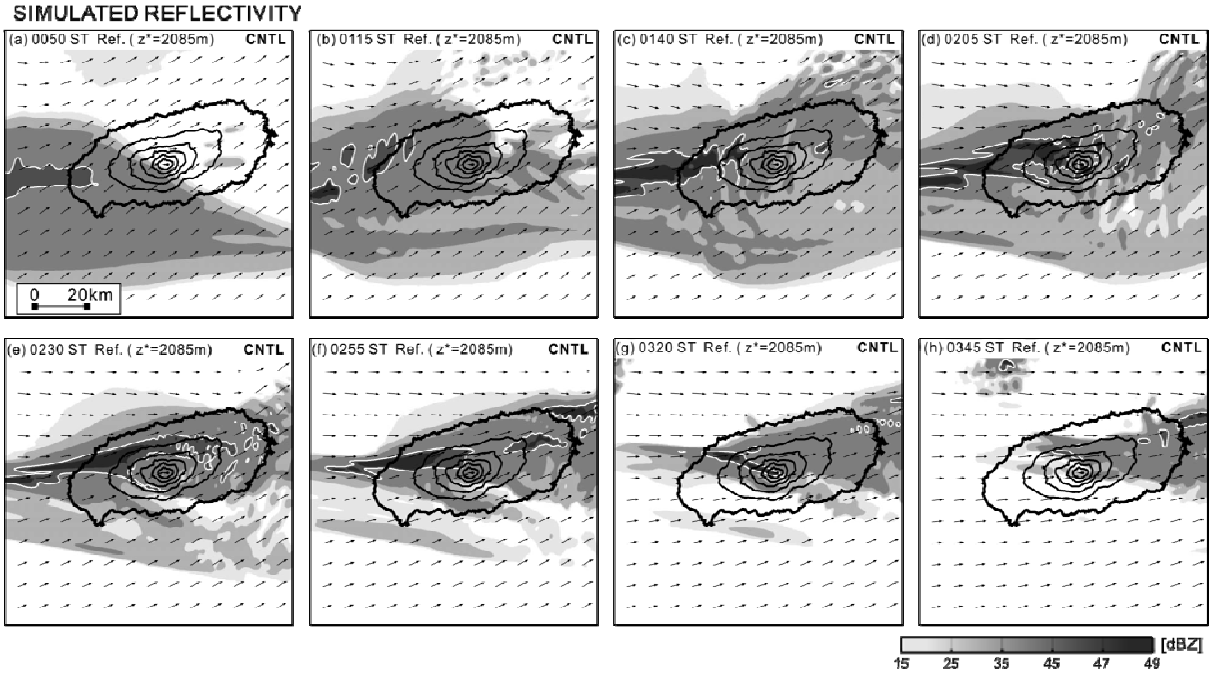

FIG.3.6. Distributions of simulated horizontal reflectivity (gray scale) and wind (vectors) within the convective system simulated by the CNTL experiment at a height of 2,085 m from 50 to 225 min running time (integration every 25 min). White contours show reflectivity of 45 dBZ.

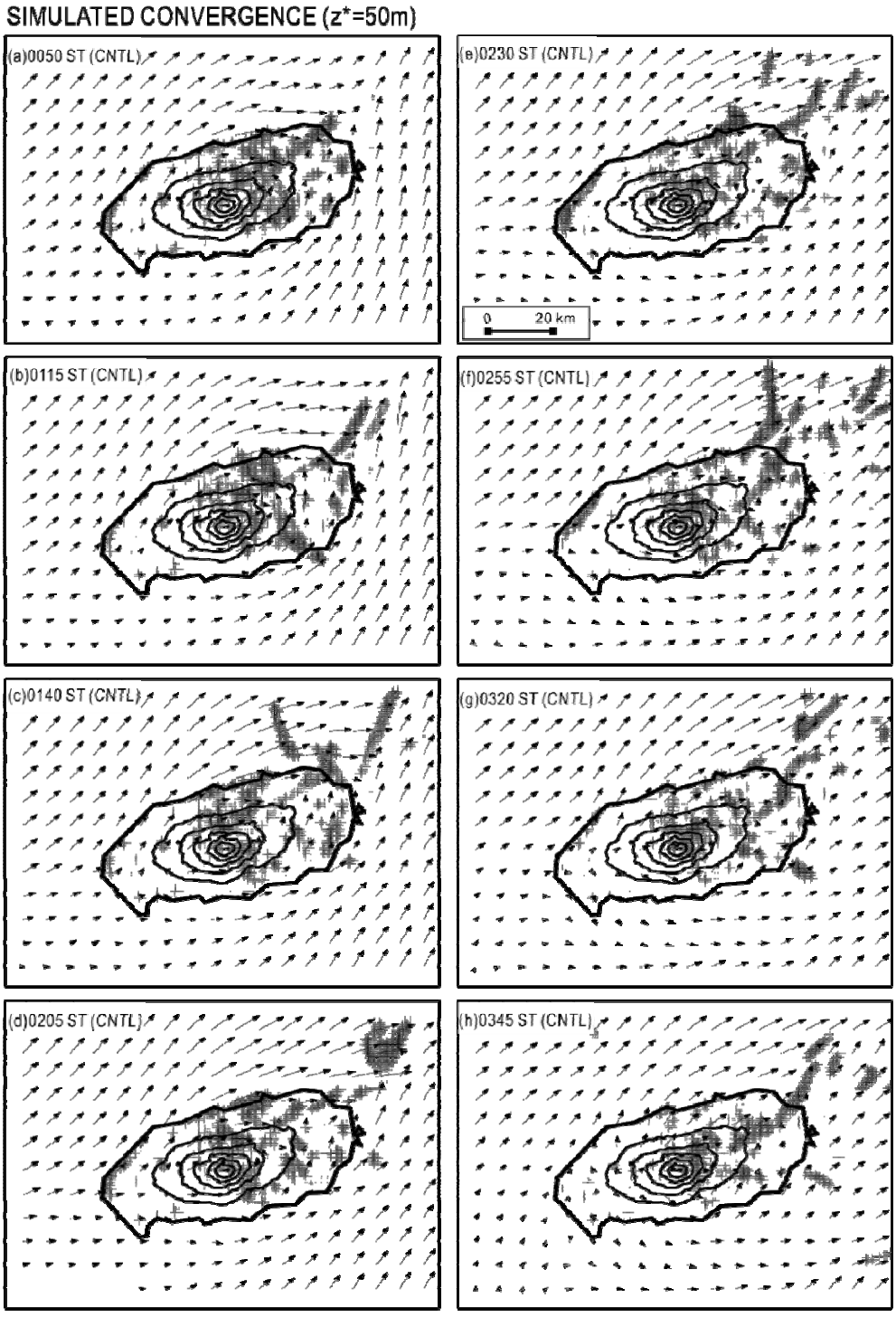

FIG.3.7. Distributions of horizontal wind (vectors) and wind convergence (shades) at a height of 50 m, as simulated by the CNTL experiment from 50 to 225 min running time at 25 min intervals. Gray shades indicate area where the convergence value was less than –0.001 s^{-1}.

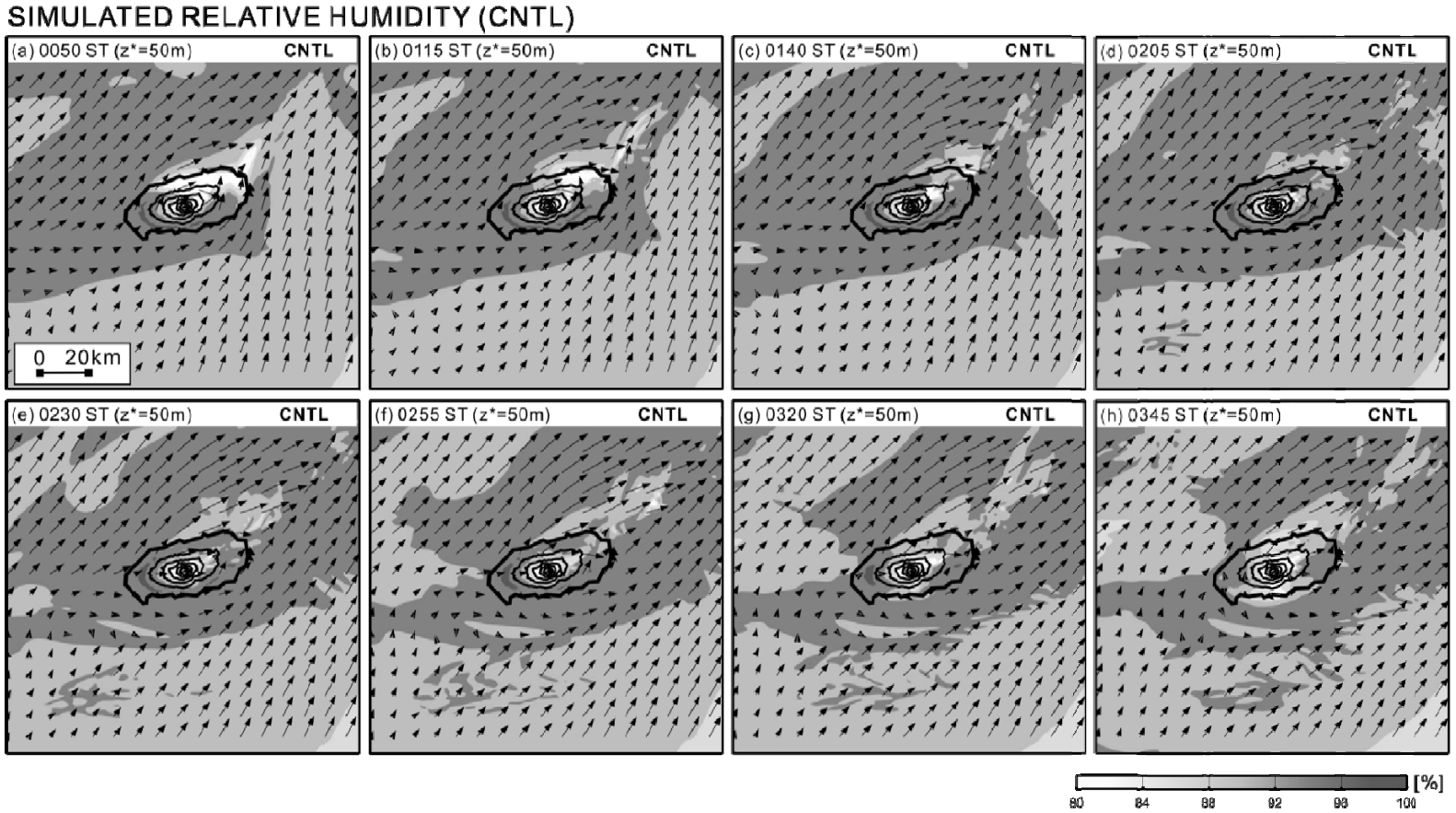

FIG.3.8. Distributions of horizontal wind (vectors) and relative humidity (gray scale) at a height of 50 m, as simulated by the CNTL experiment from 50 to 225 min running time at 25 min intervals.

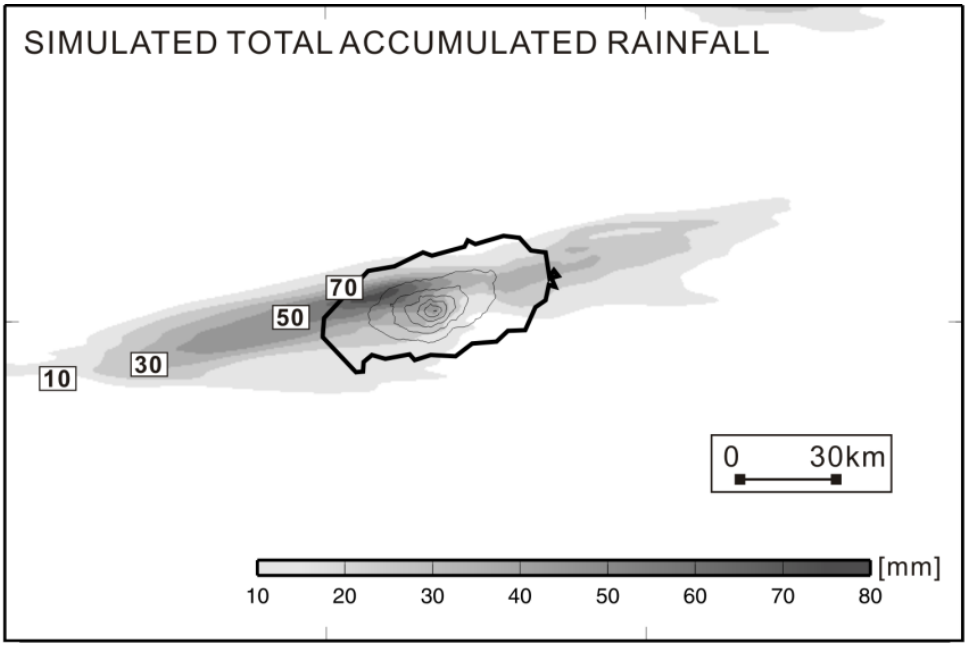

FIG.3.9. Simulated total accumulated rainfall amount (gray scale) at hours of running time in the CNTL experiment. Contour lines show the topography of Jeju Island (contour interval: 300 m).

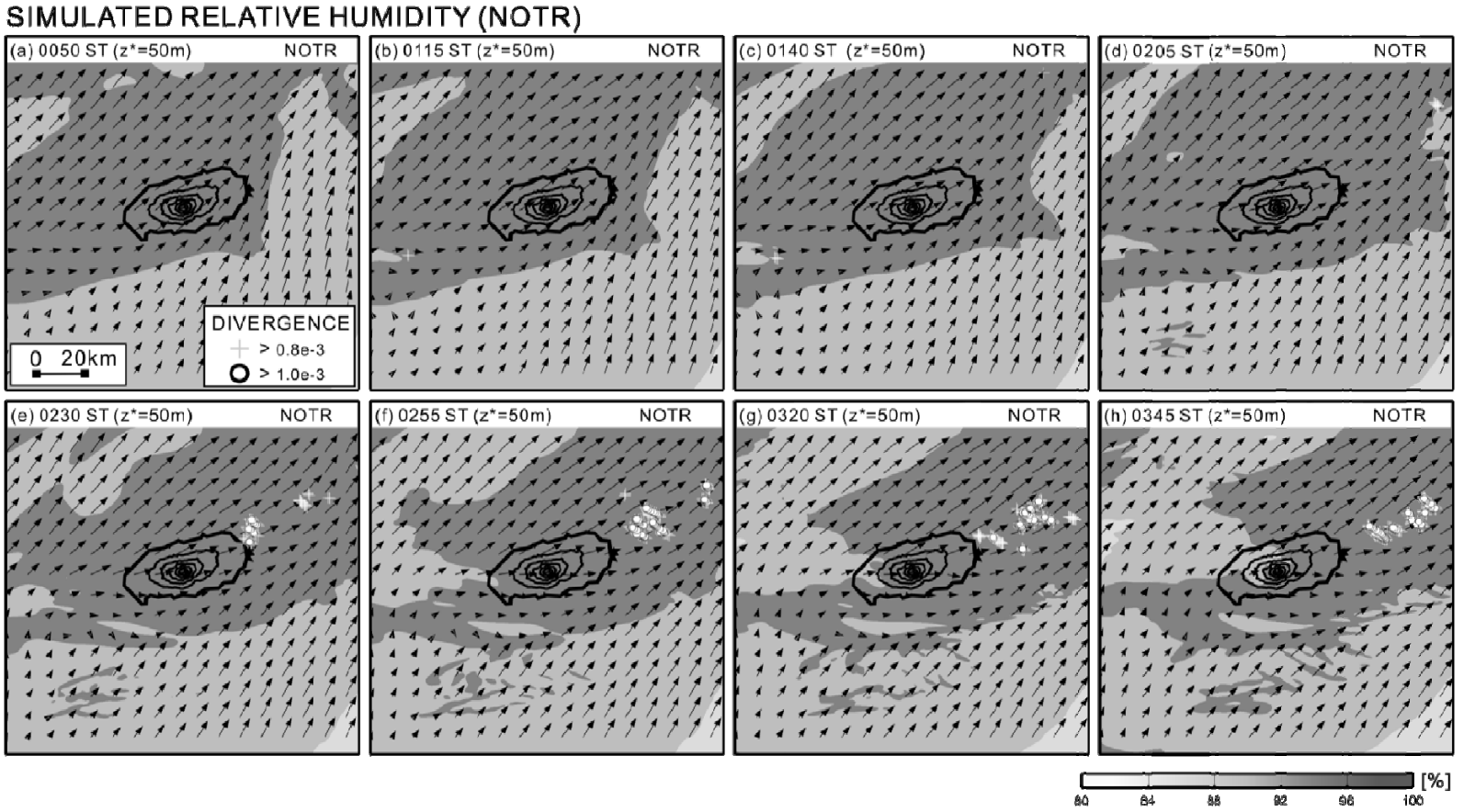

FIG.3.10. Distributions of horizontal wind (vectors), wind convergence (white crosses and circles), and relative humidity (RH; gray scale) at a height of 50 m, as simulated by the NOTR experiment from 50 to 225 min running time at 25 min intervals. White crosses and circles indicate points where the convergence value was between –0.001 and –0.0008 s^{-1}, and less than –0.001 s^{-1}, respectively.

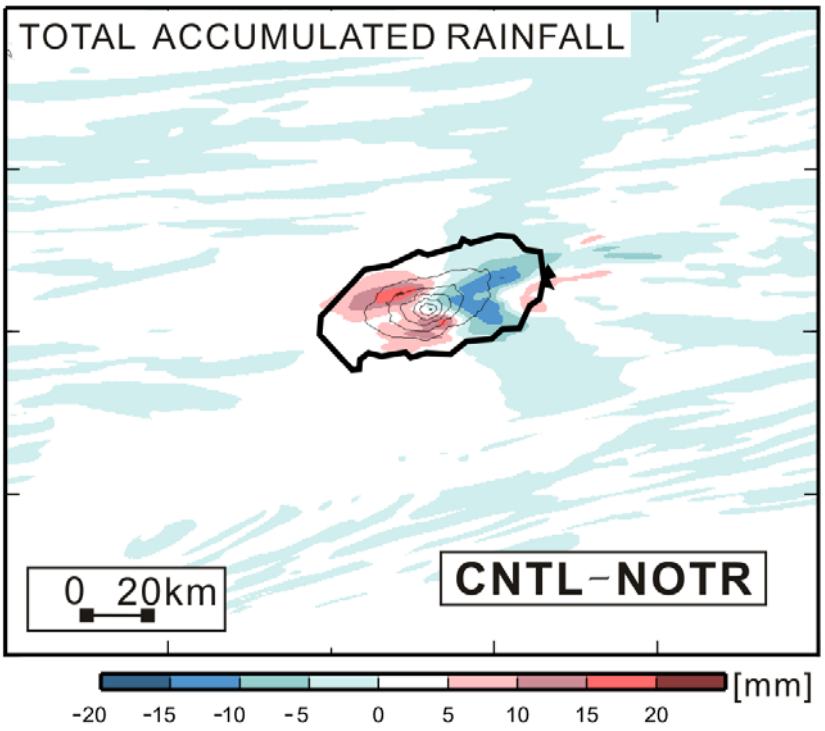

FIG.3.11. Distribution of the difference in total accumulated rainfall amount (color scale) between the CNTL and NOTR experiments (CNTL minus NOTR). Black contour lines show the topography of Jeju Island (contour interval: 300 m).

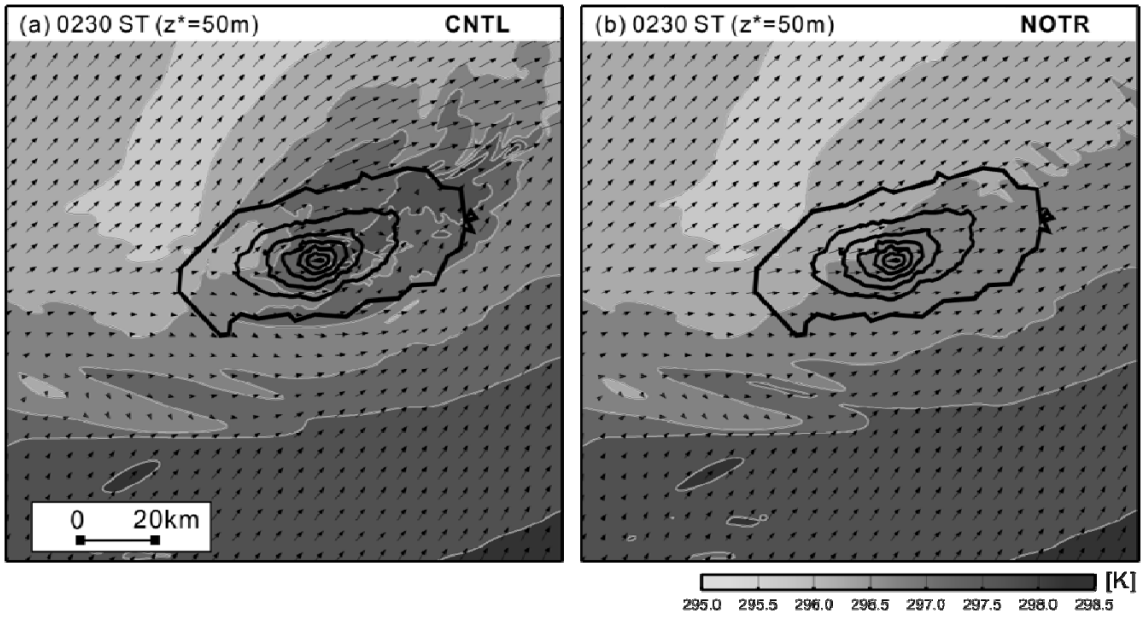

FIG.3.12. Distributions of horizontal equivalent potential temperature (gray scale) and wind (vectors) at 150 min of running time, as simulated by CNTL (a) and NOTR (b). Thick contour lines show the topography of Jeju Island; thin contour lines indicate potential temperature from 295 to 298.5 K (contour interval: 0.5 K).

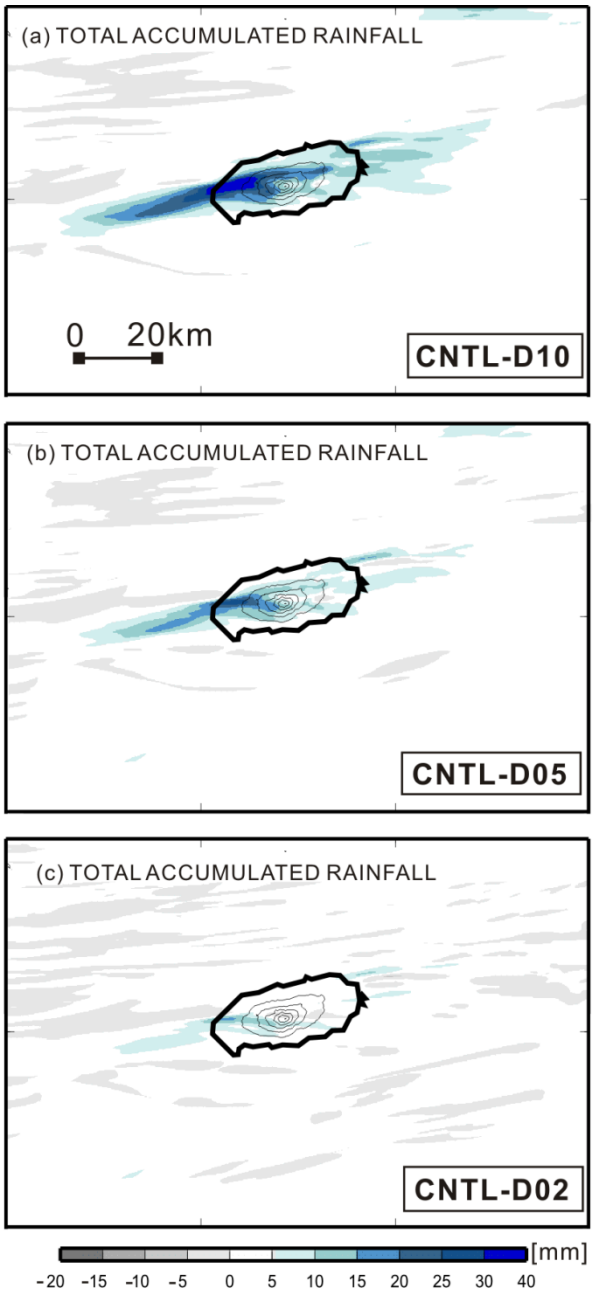

FIG.3.13. Distribution of the difference in total accumulated rainfall amount between CNTL and (a) D10, (b) D05, and (c) D02. Black contour lines show the topography of Jeju Island, and the color scale shows the rainfall difference.

TABLE.3.2. Summarized analysis results of case on 30 June 2006 (06P): the environmental parameters of surface humidity and temperature, wind direction, Froude number and stability, and the passage and evolution of each convective system.

	Parameter		06P
ENVIRONMENT	Surface Humidity		**MOIST** 92 %
	Surface Temperature		**WARM** 26°C
	Wind Direction	Mid Level	
		Low Level	
	Froude Number		**MODERATE** 0.55
	Stability		**STABLE** 1.4×10^{-2} s^{-1}
SYSTEM	Passage	Direction	Eastward
		Speed	~ 13 $m\,s^{-1}$
	Evolution 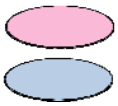	Enhancement Dissipation	

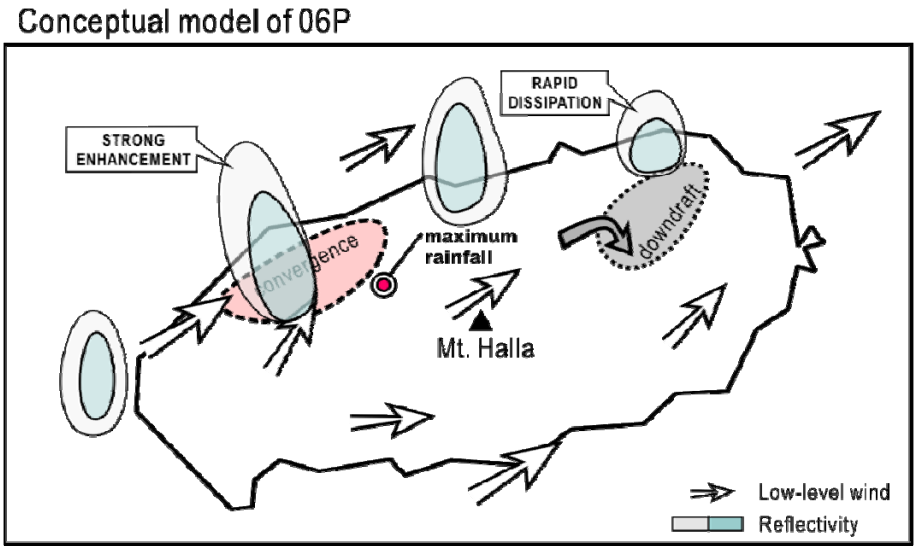

FIG.3.14. Horizontal schematic illustration of 30 June 2006 precipitation system (06P). A thick solid line is the coastline of Jeju Island. A shaded area by red and gray colour depicts the convergence region and downdraft region at low altitudes, respectively. The horizontal range of intense reflectivity greater than 40 and 45 dBZ at 2 km height is shaded by gray and blue colour, respectively, every 20 minutes. A white region with an inner red circle indicates a region of the maximum accumulated rainfall.

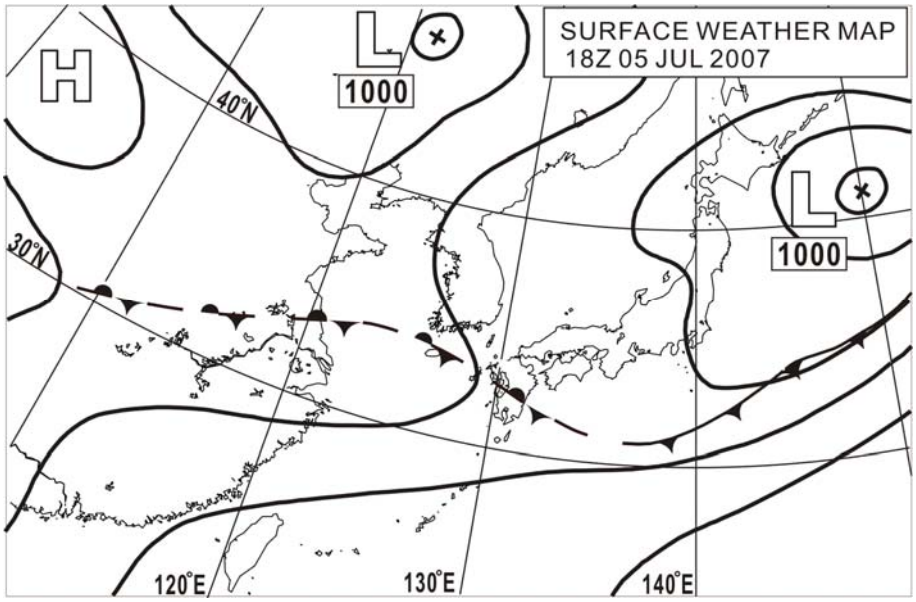

FIG.4.1. Surface weather map covering East Asia at 0300 LST on 6 July 2007.

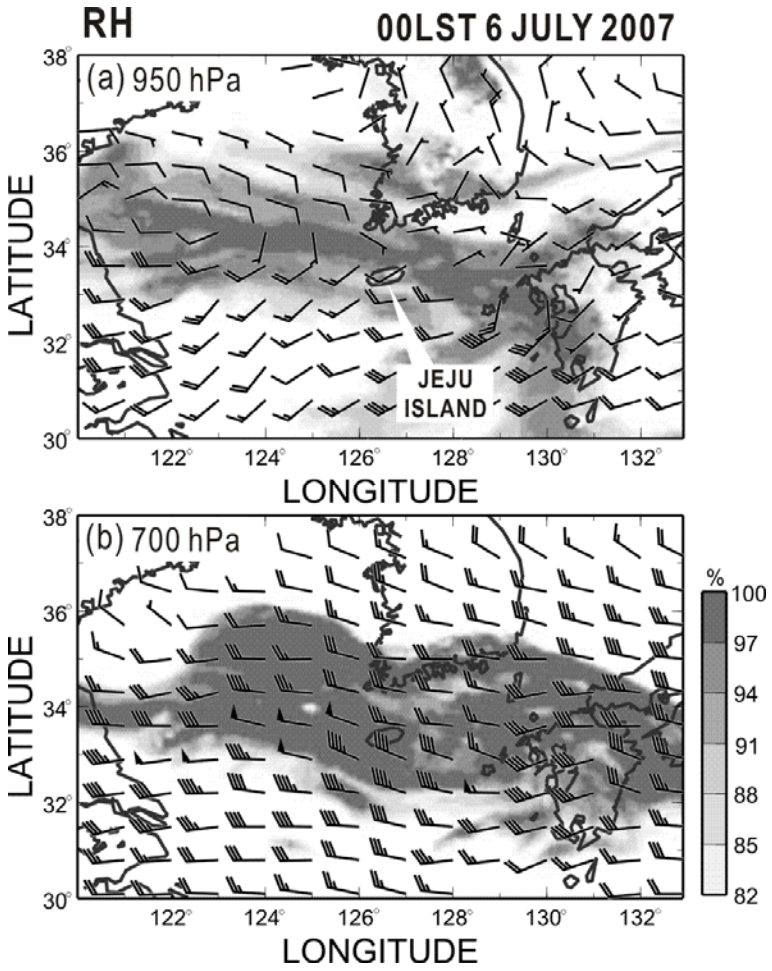

FIG.4.2. Distributions of relative humidity (RH) and horizontal wind at (a) 950 hPa and (b) 700 hPa at 0000 LST on 6 July 2007.

TABLE.4.1. Environmental parameters determined from upper–air sounding data obtained at GSN at 2100 LST on 5 July 2007: lifting condensation level (LCL), level of free convection (LFC), surface relative humidity (RH), calculated precipitable water (PW) from the surface to 700 hPa, Brunt–Väisälä frequency (N), and Froude number (*Fr*).

Parameter	Value
LCL	922.9 hPa
LFC	680 hPa
RH (surface)	94 %
PW (below 700 hPa)	41.7 kg m^{-2}
N	1.7×10^{-2} s^{-1}
Fr	0.2

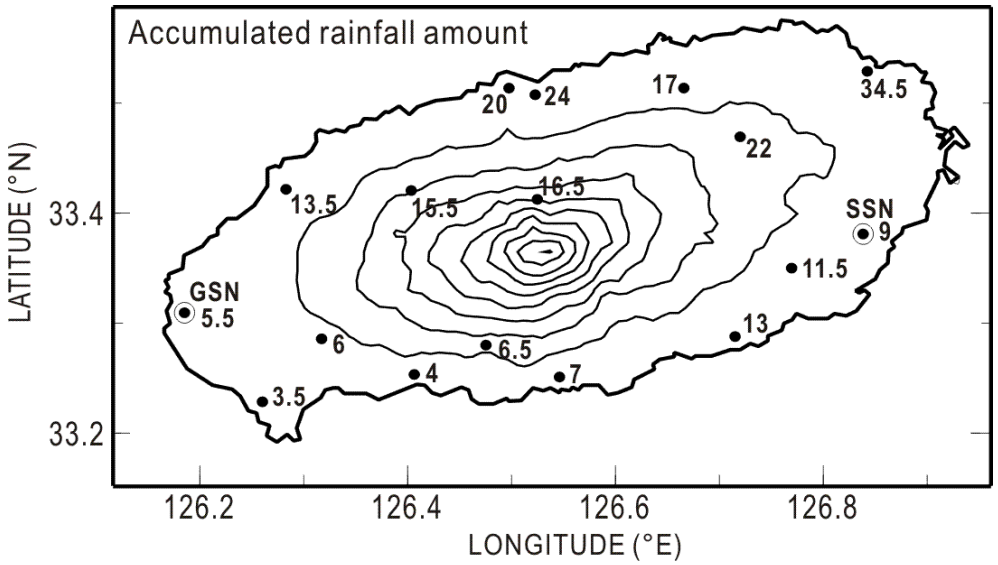

FIG.4.3. Accumulated rainfall amount recorded by 17 rain gauges (dots) on Jeju Island from 0000 to 0130 LST on 6 July 2007. Thin contour lines show topography (contour interval: 200m). The locations of the two radar sites (GSN and SSN) are indicated by small open circles.

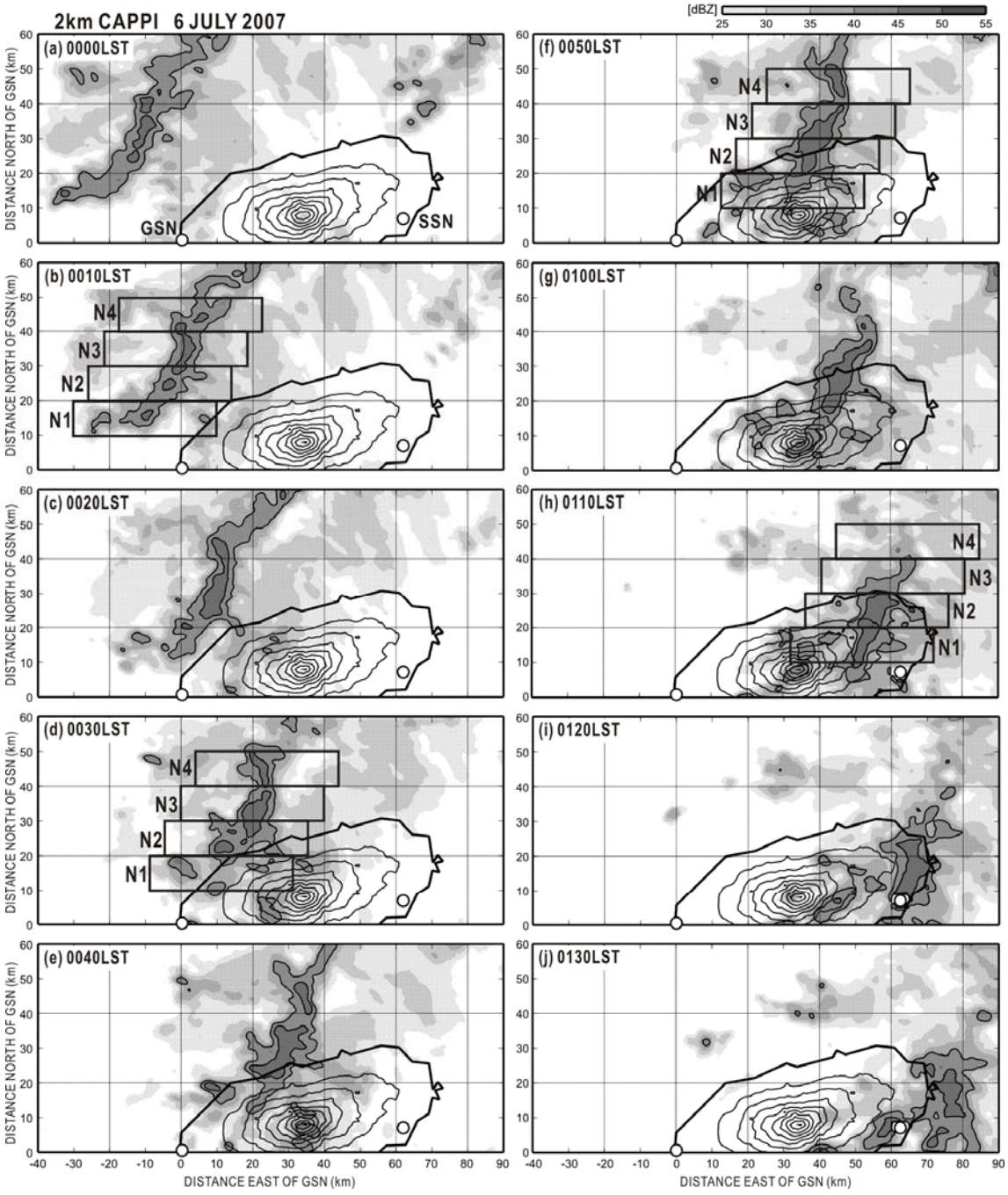

FIG.4.4. Horizontal distributions of radar reflectivity at 2 km ASL for (a) 0000 LST, (b) 0010 LST, (c) 0020 LST, (d) 0030 LST, (e) 0040 LST, (f) 0050 LST, (g) 0100 LST, (h) 0110 LST, (i) 0120 LST, and (j) 0130 LST on 6 July 2007. The reflectivity contour interval is 5 dBZ starting from 40 dBZ. The darkest shading represents the convective region, with radar reflectivity larger than 45 dBZ. The four rectangles (**N1**, **N2**, **N3**, and **N4**) demark the regions used for the detailed analysis of the convective region shown in Fig. 4.5 and Fig. 4.16. The locations of the radar stations (GSN and SSN) are indicated by small open circles. Reflectivity is from the GSN radar alone for 0000–0050 LST and from the SSN radar alone for 0100–0130 LST.

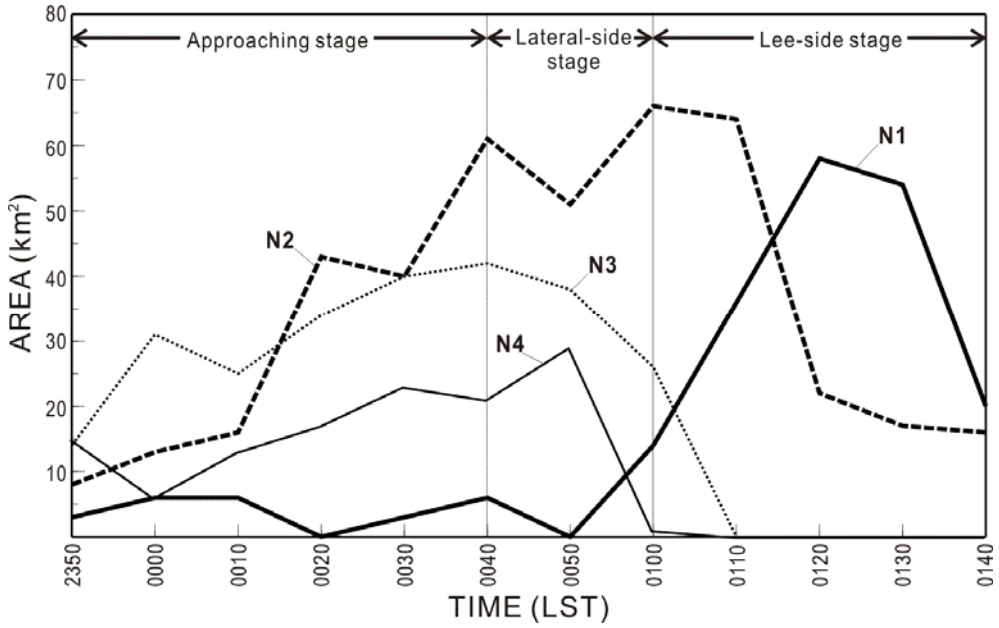

FIG.4.5. Time variations of the horizontal area of the convective region (reflectivity greater than 45 dBZ) at 2 km ASL within the **N1** (thick solid line), **N2** (thick dashed line), **N3** (thin dotted line), and **N4** (thin solid line) analysis domains. The boundaries of the analysis domains are shown in Fig. 4.4.

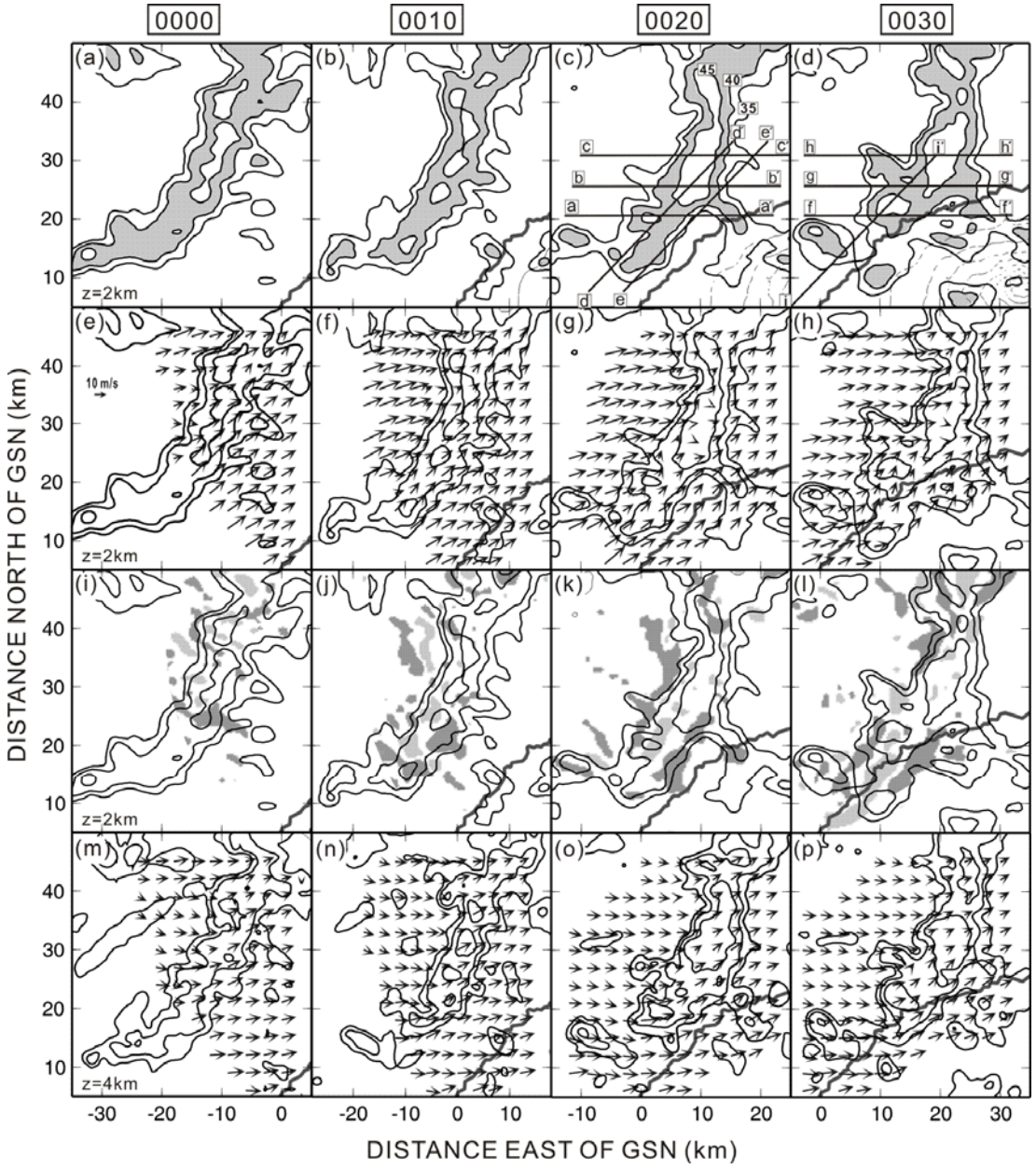

FIG.4.6. Horizontal distributions of reflectivity and system-relative wind fields during the approaching stage (0000–0030 LST). The first row (a)–(d) shows the radar–echo intensity at 2 km ASL. The reflectivity contours are drawn every 5 dBZ from 35 dBZ. Areas with reflectivity between 40 and 45 dBZ are shaded. The second row (e)–(h) and the fourth row (m)–(p) show horizontal wind vectors and reflectivity (contours as in the first row) at 2 km and 4 km ASL, respectively. The third row (i)–(l) shows vertical air velocity (shading) at 2 km ASL. Regions of updraft larger than 1.5 $m s^{-1}$ are shown as dark shading and regions of downdraft less than –1.5 $m s^{-1}$ are shown as light shading. The thick contour line in each panel represents the coastline of Jeju Island. The thin broken lines in (b)–(d) show the topography of Jeju Island (contour interval 200 m). The locations of the vertical cross-sections shown in Fig. 4.7 are indicated in (c), and the locations of those shown in Fig. 4.8 are indicated in (d).

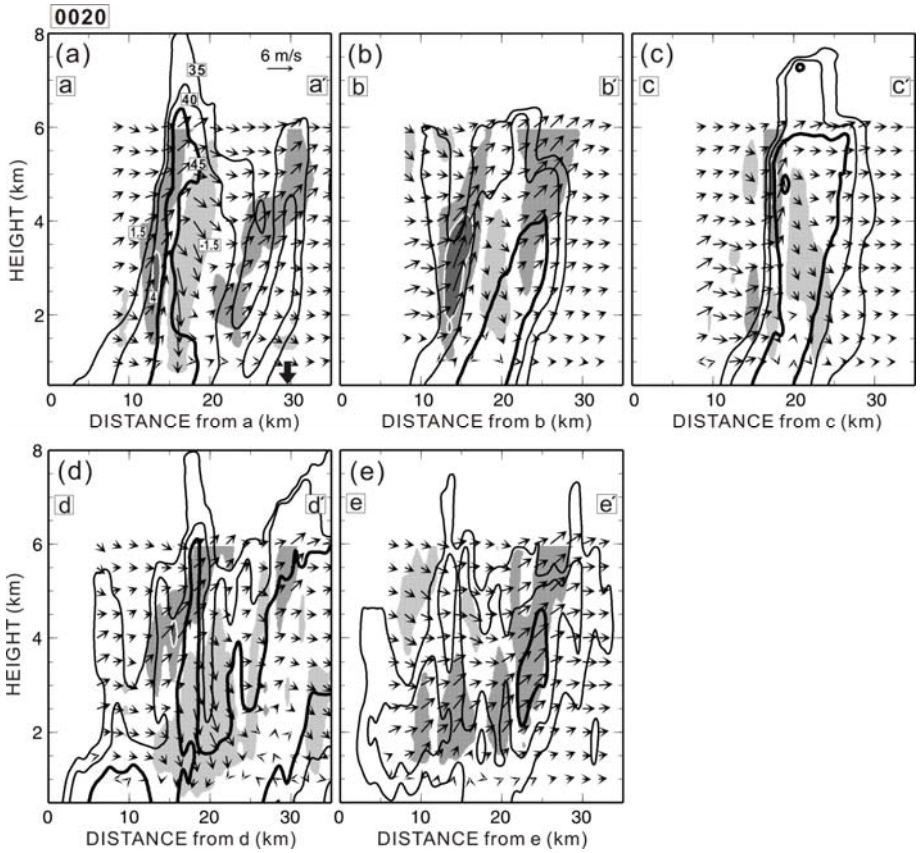

FIG.4.7. Vertical cross-sections of reflectivity and system-relative wind fields at 0020 LST. The locations of the transect lines are shown in Fig. 4.6c. Transects a–a' to c–c' are oriented parallel to the horizontal axis of Fig. 4.6c. Transects d–d' and e–e' are oriented parallel to the prevailing southwesterly wind. Regions of updrafts in excess of 1.5 ms^{-1} are shown as dark shading and regions of downdraft less than –1.5 ms^{-1} are shown as light shading. The regions of intense updrafts (greater than 4 ms^{-1}) are indicated by the darkest shading bounded by white contours. Thin contours indicate radar reflectivity from a minimum of 35 dBZ, with a contour interval of 5 dBZ. Thick contours indicate reflectivity in excess of 45 dBZ, with a contour interval of 5 dBZ. A thick downward arrow along the horizontal axis in (a) indicates the location of the Jeju Island coastline.

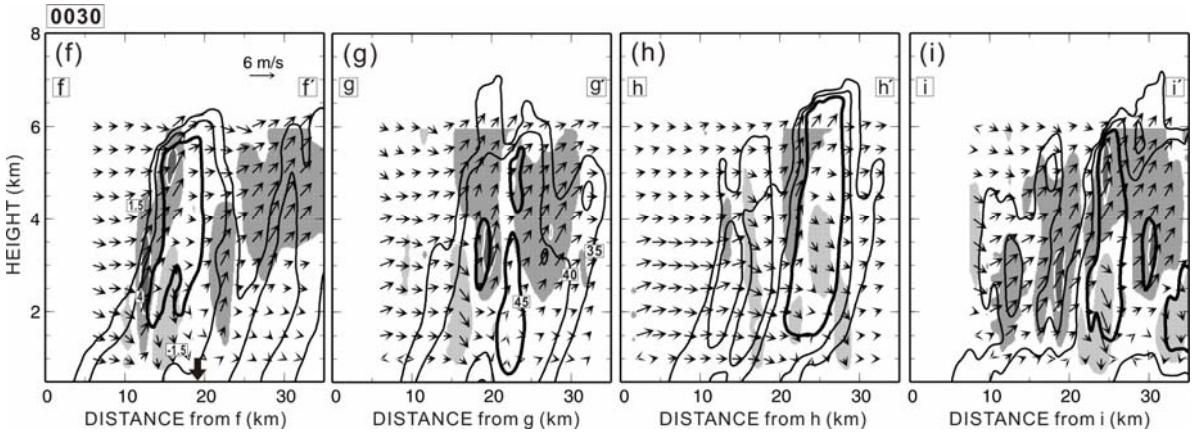

FIG.4.8. Vertical cross-sections of reflectivity and system-relative wind fields at 0030 LST. The locations of the transect lines are shown in Fig. 4.6d. Transects f–f' to h–h' are oriented parallel to the horizontal axis of Fig. 4.6d. Transect i–i' is oriented parallel to the southwesterly wind. Thin contours indicate radar reflectivity from a minimum of 35 dBZ, with a contour interval of 5 dBZ. Thick contours indicate reflectivity in excess of 45 dBZ, with a contour interval of 5 dBZ. The shaded regions and contours are as in Fig. 4.7. A thick downward arrow along the horizontal axis in (f) shows the location of the Jeju Island coastline.

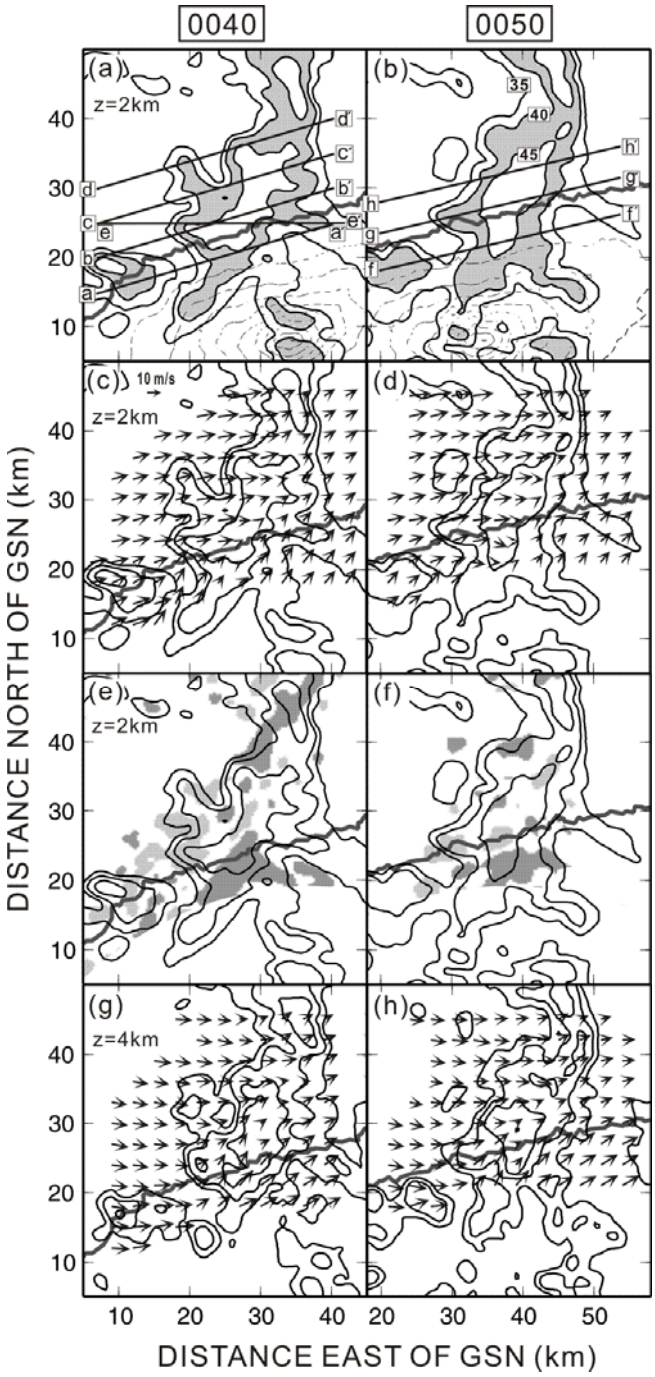

FIG.4.9. Horizontal distributions of reflectivity and system-relative wind fields during the lateral-side stage (0040–0050 LST). The reflectivity contours are drawn every 5 dBZ from 35 dBZ. The shaded regions and contours are as in Fig. 4.6. The locations of the vertical cross-sections shown in Fig. 4.10 are indicated in (a) and the locations of those shown in Fig. 4.11 are indicated in (b).

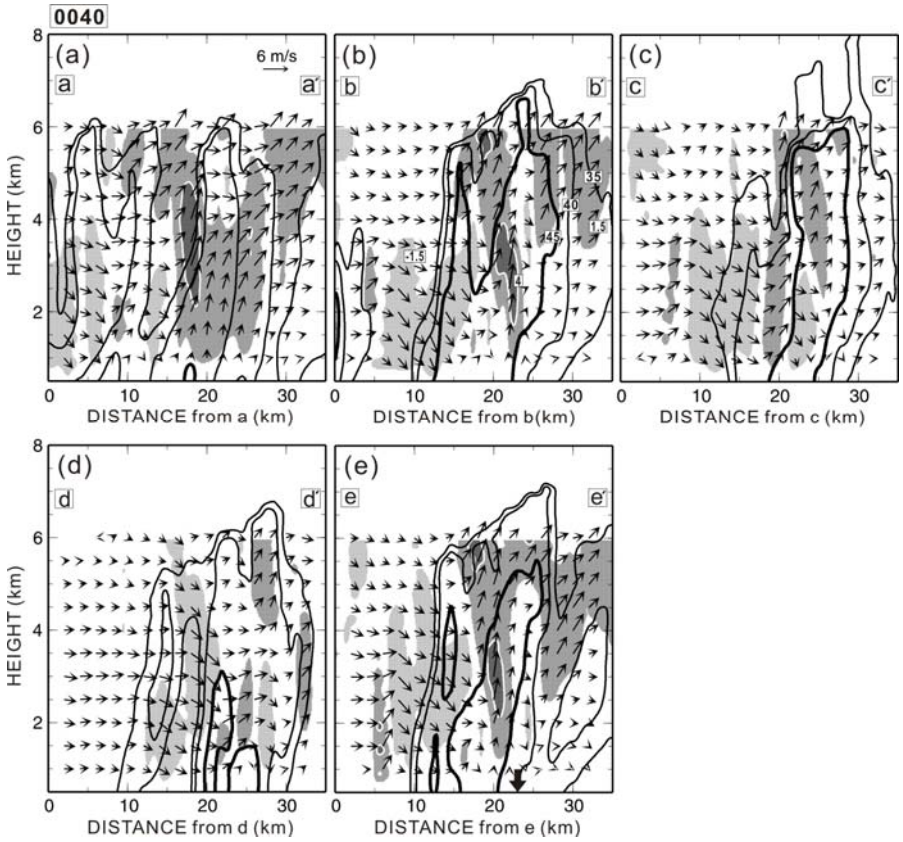

FIG.4.10. Vertical cross-sections of reflectivity and system-relative winds at 0040 LST. Locations of the transect lines are shown in Fig. 4.9a. Transects a–a', b–b', c–c', and d–d' are oriented parallel to the Jeju Island coastline. Transect e–e' is oriented parallel to the horizontal axis of Fig. 4.9a. Thin contours indicate radar reflectivity from a minimum of 35 dBZ, with a contour interval of 5 dBZ. Thick contours indicate reflectivity in excess of 45 dBZ, with a contour interval of 5 dBZ. The shaded regions and contours are as in Fig. 4.7. A thick downward arrow on the horizontal axis of (e) indicates the location of the coastline.

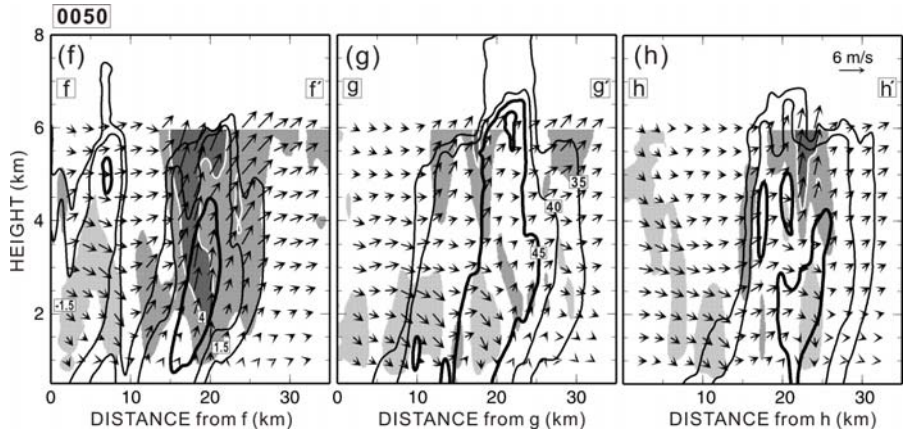

FIG.4.11. Vertical cross-sections of reflectivity and system-relative wind fields at 0050 LST. The locations of the transect lines are indicated in Fig. 4.9b. Transects f–f', g–g', and h–h' are oriented parallel to the Jeju Island coastline. Thin contours indicate radar reflectivity from a minimum of 35 dBZ, with a contour interval of 5 dBZ. Thick contours indicate reflectivity in excess of 45 dBZ, with a contour interval of 5 dBZ. The shaded regions and contours are as in Fig. 4.7.

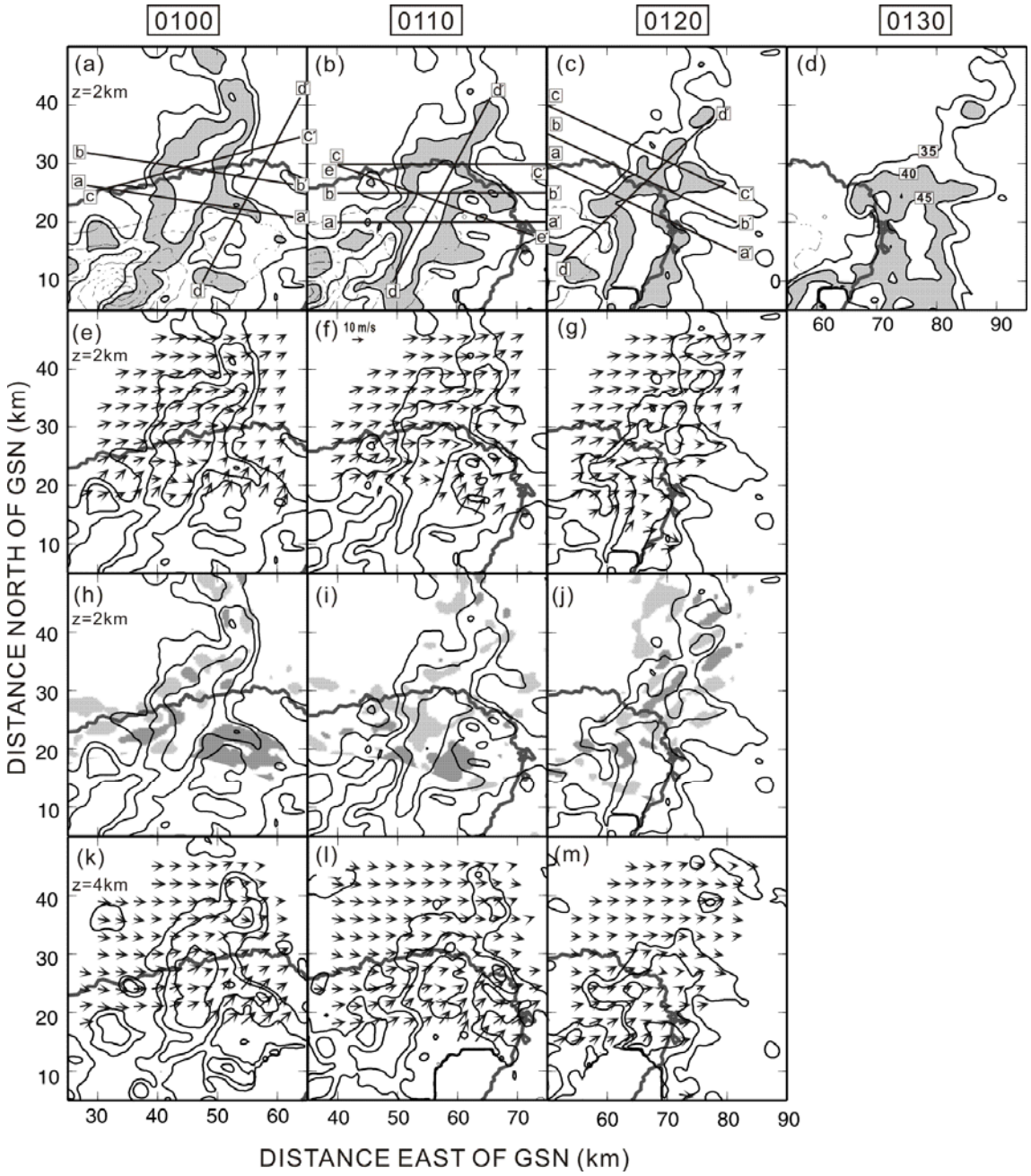

FIG.4.12. Horizontal distributions of reflectivity and system-relative wind fields during the lee-side stage (0100–0130 LST). The reflectivity contours are drawn every 5 dBZ from 35 dBZ. The shaded regions and contours are as in Fig. 4.6. The locations of the vertical cross-sections shown in Figs. 4.13, 4.14, and 4.15 are indicated in (a), (b), and (c), respectively.

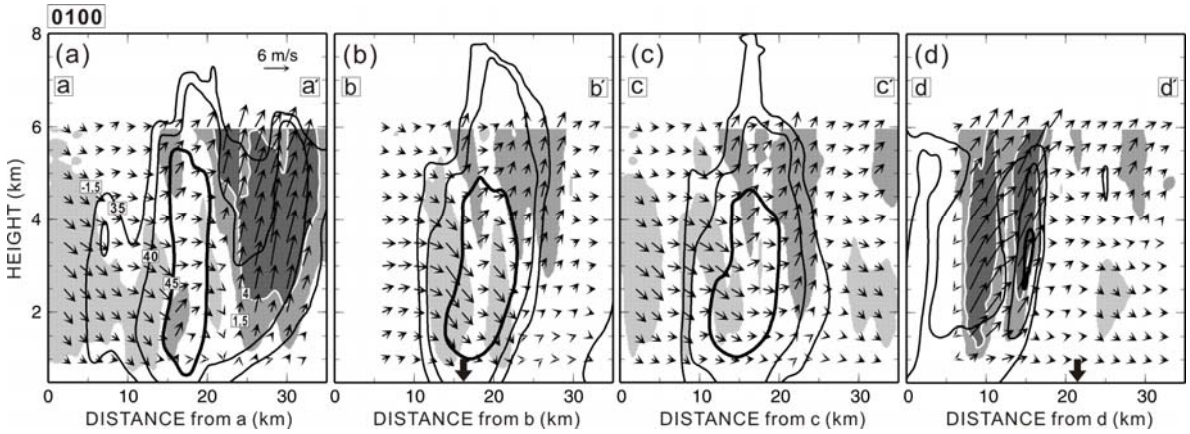

FIG.4.13. Vertical cross-sections of reflectivity and system-relative wind fields at 0100 LST. The locations of the transect lines are shown in Fig. 4.12a. Transects a–a' and b–b' are oriented perpendicular to the precipitation system. Transect c–c' is oriented parallel to the Jeju Island coastline. Transect d–d' is oriented parallel to the southwesterly wind. Thin contours indicate radar reflectivity from a minimum of 35 dBZ, with a contour interval of 5 dBZ. Thick contours indicate reflectivity in excess of 45 dBZ, with a contour interval of 5 dBZ. The shaded regions and contours are as in Fig. 4.6. Thick downward arrows on the horizontal axes in (b) and (d) indicate the locations of the coastline along these transects.

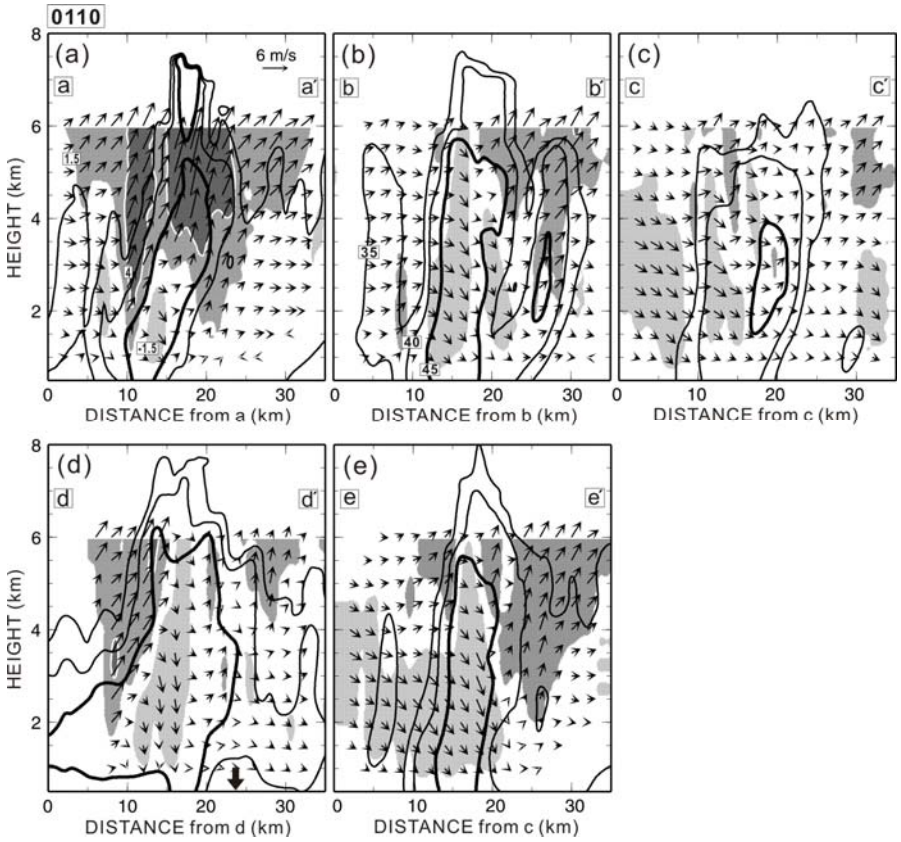

FIG.4.14. Vertical cross-sections of reflectivity and system-relative winds at 0110 LST. The locations of the transect lines are shown in Fig. 4.12b. Transects a–a', b–b', and c–c' are oriented parallel to the horizontal axis of Fig. 4.12b. Transect d–d' is oriented perpendicular to the southwesterly wind. Transect e–e' is oriented perpendicular to the precipitation system. Thin contours indicate radar reflectivity from a minimum of 35 dBZ, with a contour interval of 5 dBZ. Thick contours indicate reflectivity in excess of 45 dBZ, with a contour interval of 5 dBZ. The shaded regions and contours are as in Fig. 4.7. A thick downward arrow on the horizontal axis in (d) indicates the location of the Jeju Island coastline.

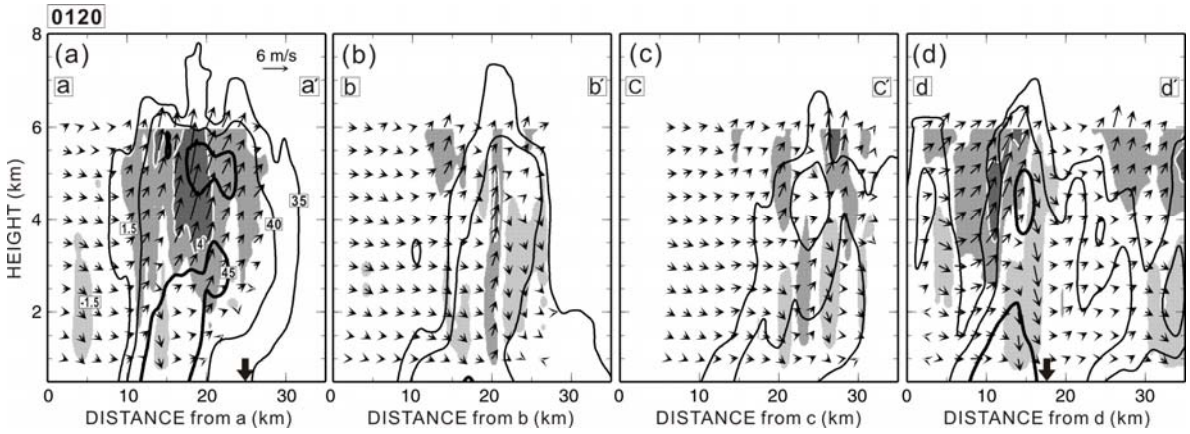

FIG.4.15. Vertical cross-sections of reflectivity and system-relative winds at 0120 LST. The locations of the transect lines are shown in Fig. 4.12c. Transects a–a', b–b', and c–c' are oriented parallel to the Jeju Island coastline. Transect d–d' is oriented parallel to the southwesterly wind. The shaded regions and contours are as in Fig. 4.7. Thin contours indicate radar reflectivity from a minimum of 35 dBZ, with a contour interval of 5 dBZ. Thick contours indicate reflectivity in excess of 45 dBZ, with a contour interval of 5 dBZ. The thick downward arrows on the horizontal axes in (a) and (d) indicate the location of the coastline.

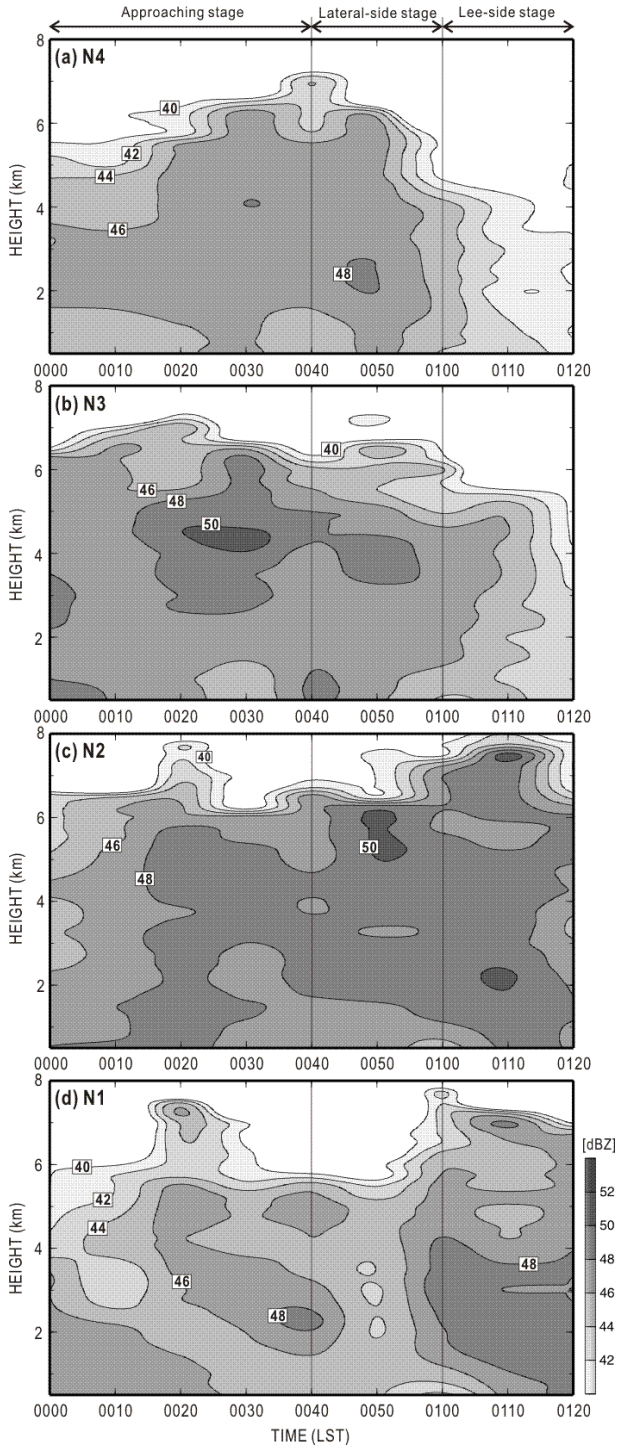

FIG.4.16. Time–height cross-section of maximum reflectivity from 0000 to 0120 LST in the analysis domains (a) **N1** (over land), (b) **N2** (coastal), (c) **N3** (offshore), and (d) **N4** (open sea). The boundaries of the analysis domains are depicted in Fig. 4.4. Contours and shading show reflectivity at intervals of 2 dBZ starting from 40 dBZ.

TABLE.4.2. Summarized analysis results of case on 6 July 2007 (07P): the environmental parameters of surface humidity and temperature, wind direction, Froude number and stability, and the passage and evolution of each convective system.

	Parameter		07P
ENVIRONMENT	Surface Humidity		**MOIST** 90 %
	Surface Temperature		**WARM** 24°C
	Wind Direction	Mid Level	
		Low Level	
	Froude Number		**MODERATE** 0.2
	Stability		**STABLE** 1.7×10^{-2} s^{-1}
SYSTEM	Passage	Direction	Eastward
		Speed	~ 11 $m\,s^{-1}$
	Evolution 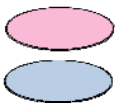 Enhancement Dissipation		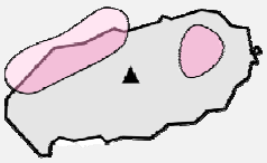

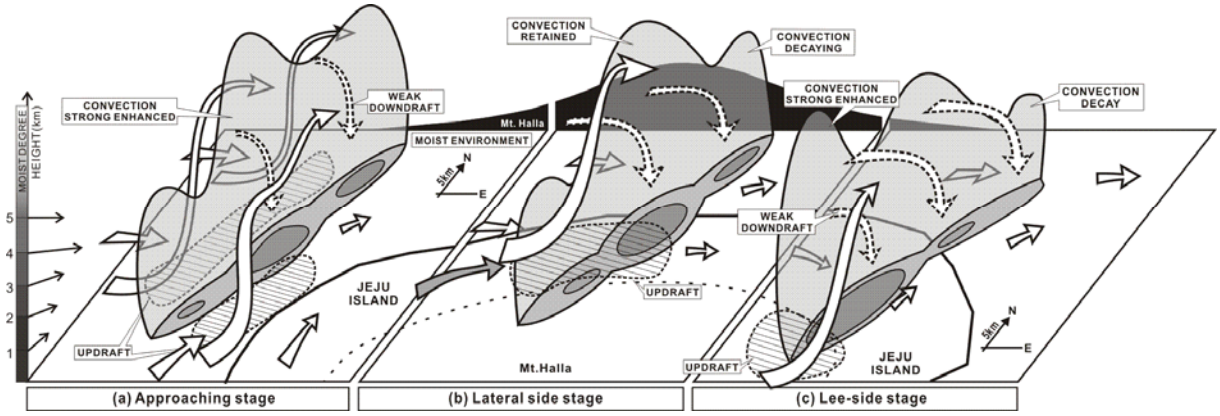

FIG.4.17. Three-dimensional schematic illustration of 6 July 2007 precipitation during (a) approaching stage, (b) lateral-side stage, and (c) lee-side stage. The three–dimensional distribution of precipitation is shown as gray shading. The darkest gray region indicates the location of the convective region at 2 km ASL. Upward white arrows with solid lines indicate updraft stream lines. Downward white arrows with broken lines indicate downdraft stream lines. Short white arrows indicate horizontal winds at 2 km ASL. Gray arrow indicates airflow around mountainous areas at 2 km ASL. The hatched area indicates the updraft region at 2 km ASL. The thick solid line in each panel indicates the Jeju Island coastline. The dotted line inside the thick solid line indicates the 500 m height contour. The height of Mt. Halla along the long axis is depicted on the horizontal axis behind the precipitation distribution. Shading on the vertical axis indicates the amount of moisture, with darker shading for greater moisture.

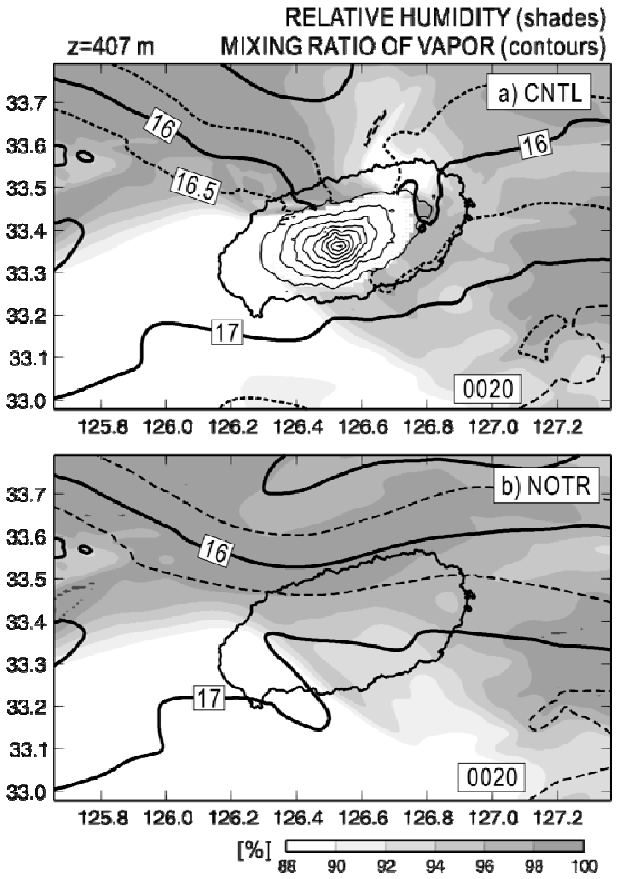

FIG.4.18. Distributions of the simulated relative humidity (%, gray) and mixing ratio of vapour (g kg^{-1}, contours) at a height of 407 m for (a) CNTL and (b) NOTR experiments at 0020 ST.

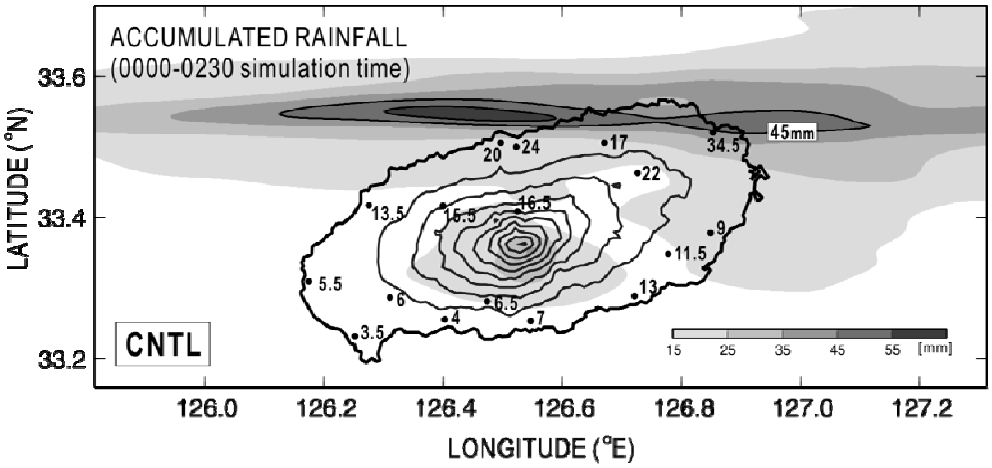

FIG.4.19. Rainfall amounts (mm) recorded by 17 rain gauges (dots) on Jeju Island between 0000 and 0130 LST on 6 July 2007. Rainfall amount simulated by CNTL over the whole calculation period (2.5 hours) is indicated by shading with thin contours of 45 mm and 55 mm. The contour lines show surface elevation (interval: 200 m).

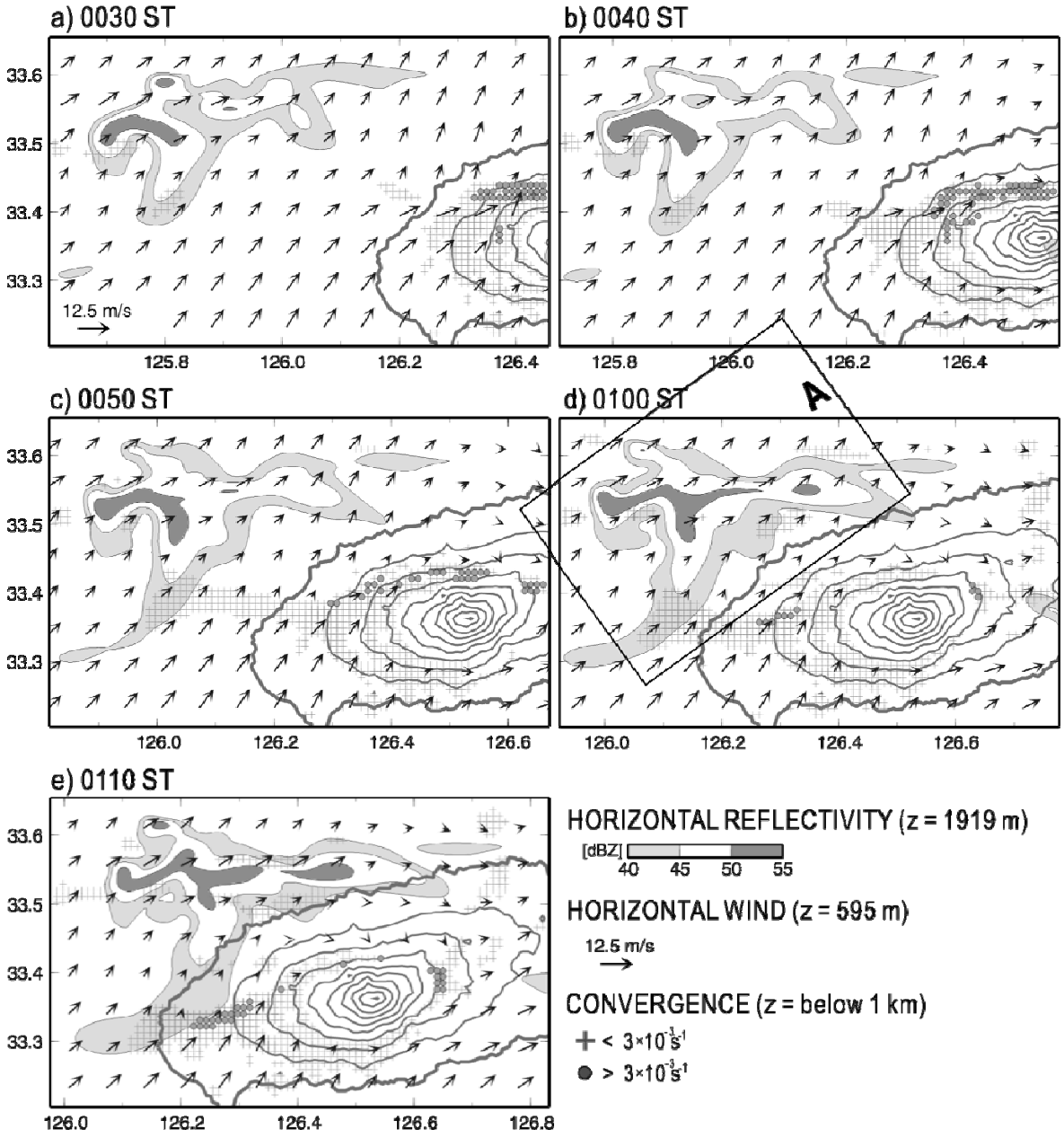

FIG.4.20. Horizontal distributions of the simulated wind (vectors) at a height of 595 m, reflectivity (shades) at a height of 1919 m, and convergence (symbols), simulated by the CNTL experiment for (a) 0030 ST, (b) 0040 ST, (c) 0050 ST, (d) 0100 ST, and (e) 0110 LST. The reflectivity contour interval is 5 dBZ, starting from 45 dBZ. Symbols indicate areas with maximum convergence weaker than 0.003 s^{-1} (cross) and stronger than 0.003 s^{-1} (circle) below 1 km. A rectangle in (d) indicates the regions used for detailed analysis shown in Figs 4.21, 4.22, 4.23, 4.28, and 4.29. Thick gray contour marks the coastline of Jeju Island and thin gray contour lines have an interval of 200 m.

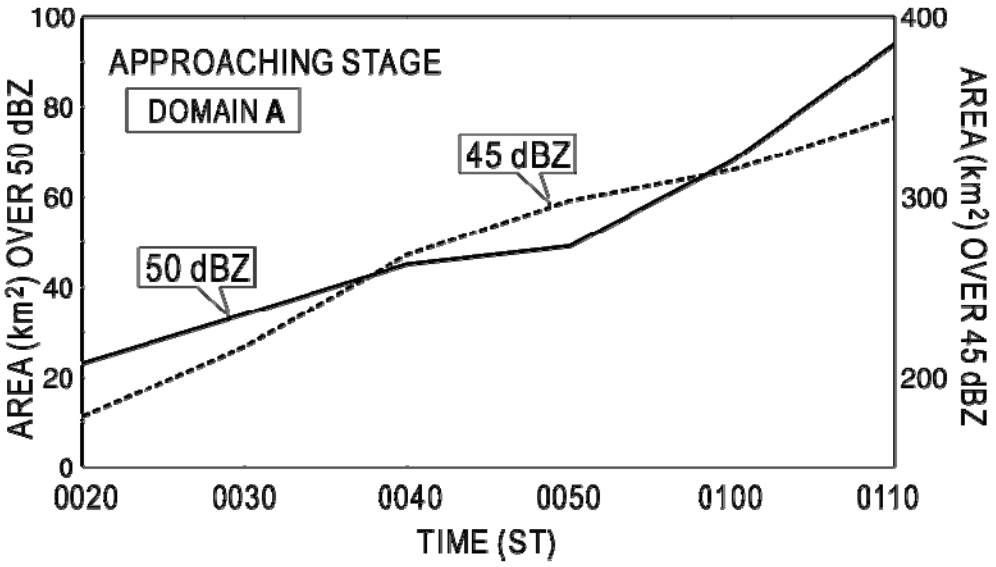

FIG.4.21. Temporal variations in the horizontal area of simulated reflectivity greater than 45 dBZ (broken line) and 50 dBZ (solid line) at a height of 1919 m from 0020 to 0110 ST. The analysis region **A** is shown in Fig. 4.20d by a rectangle.

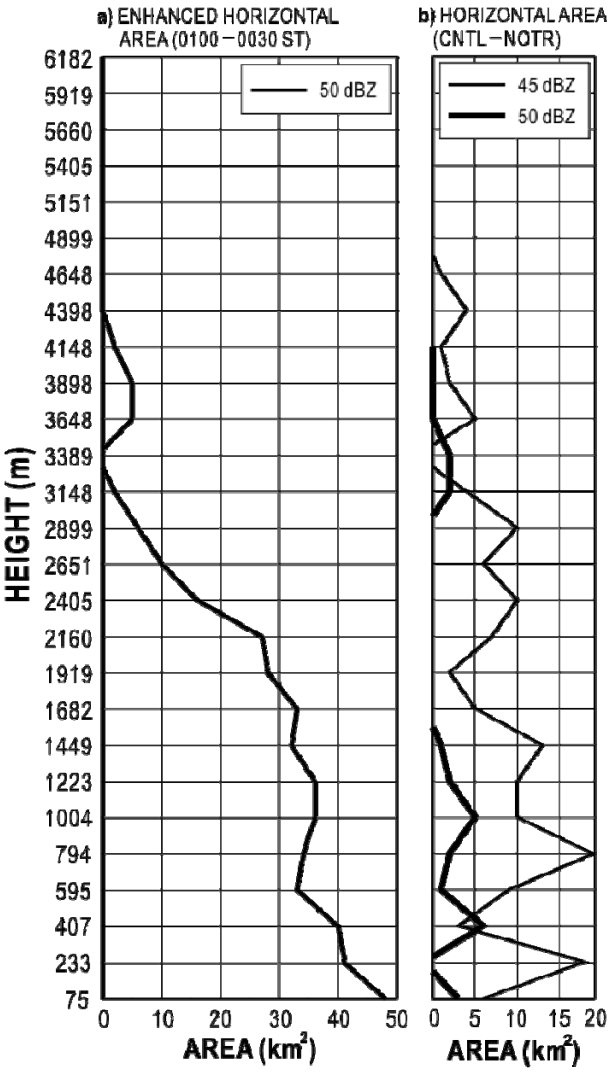

FIG.4.22. Vertical profiles of the expanded horizontal area during the approaching stage. (a) Enhanced horizontal area of reflectivity greater than 50 dBZ from 0030 to 0100 ST. (b) Differences in horizontal area of reflectivity greater than 45 dBZ (thin line) and 50 dBZ (thick line) between CNTL and NOTR experiments (CNTL minus NOTR) at 0100 ST.

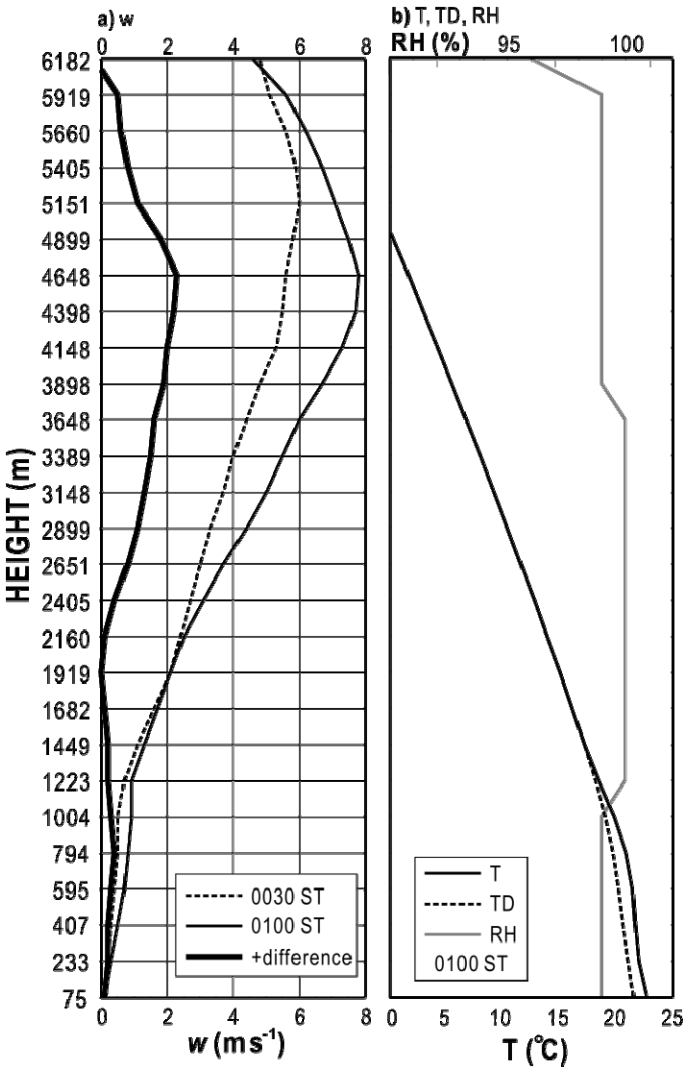

FIG.4.23. Vertical profiles of vertical wind (*w*), temperature (T), dew point temperature (TD), and relative humidity (RH) during the approaching stage. (a) Maximum vertical velocity at 0030 ST (thin broken line), 0100 ST (thin solid line), and the difference between 0030 and 0100 ST (thick solid line: 0100 minus 0030 ST). (b) T (black solid line), TD (broken line), and RH (gray solid line) at the point of maximum vertical wind at 0100 ST.

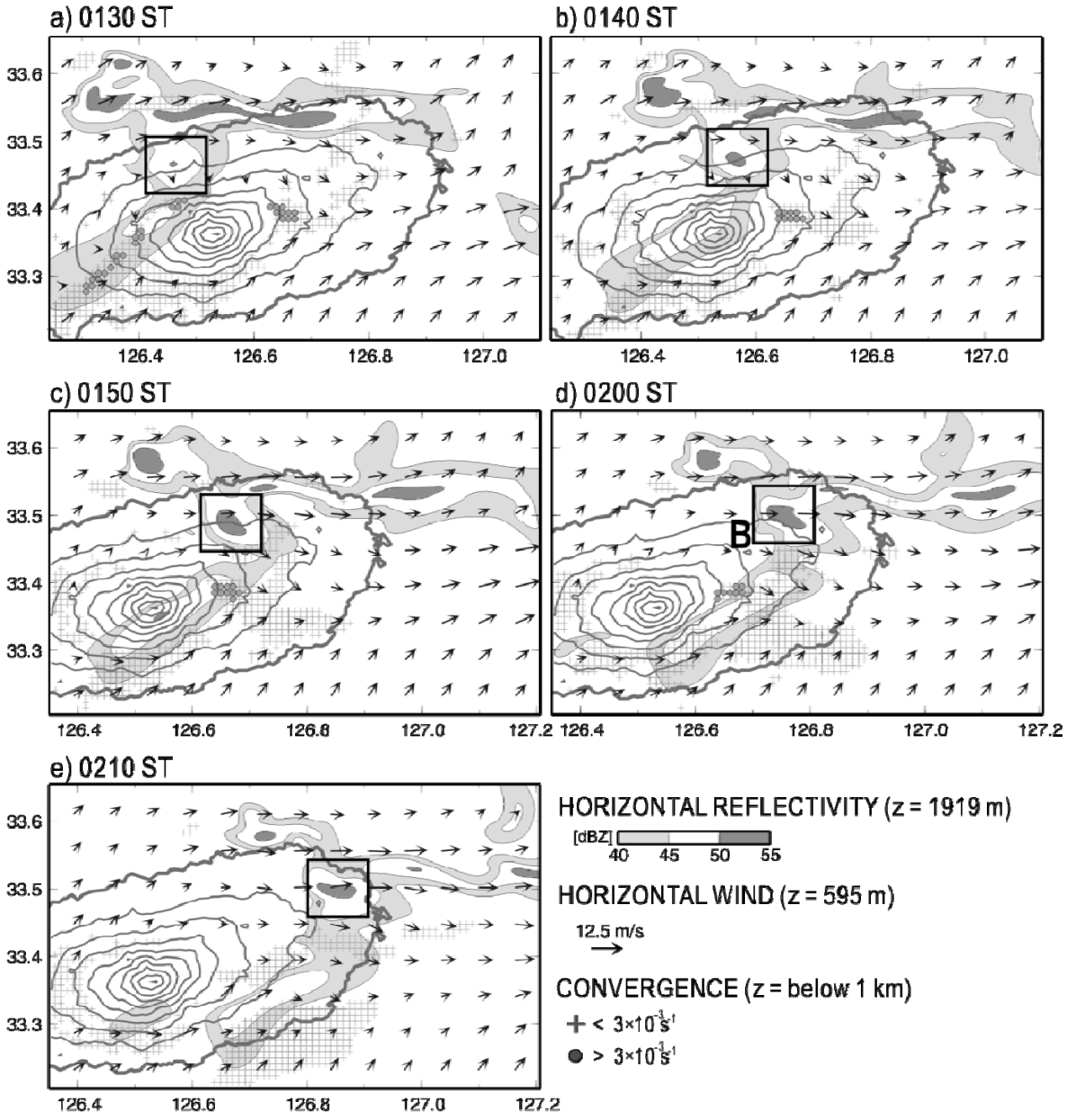

FIG.4.24. Horizontal distributions of wind (vectors) at a height of 595 m, estimated reflectivity (shades) at a height of 1919 m, and convergence (symbols), simulated by the CNTL experiment for (a) 0130 ST, (b) 0140 ST, (c) 0150 ST, (d) 0200 ST, and (e) 0210 ST. The shaded regions and contours are as in Fig. 4.20. Rectangles in each panel indicate the regions used for detailed analysis shown in Figs 4.25, 4.26, 4.27, 4.28, and 4.29.

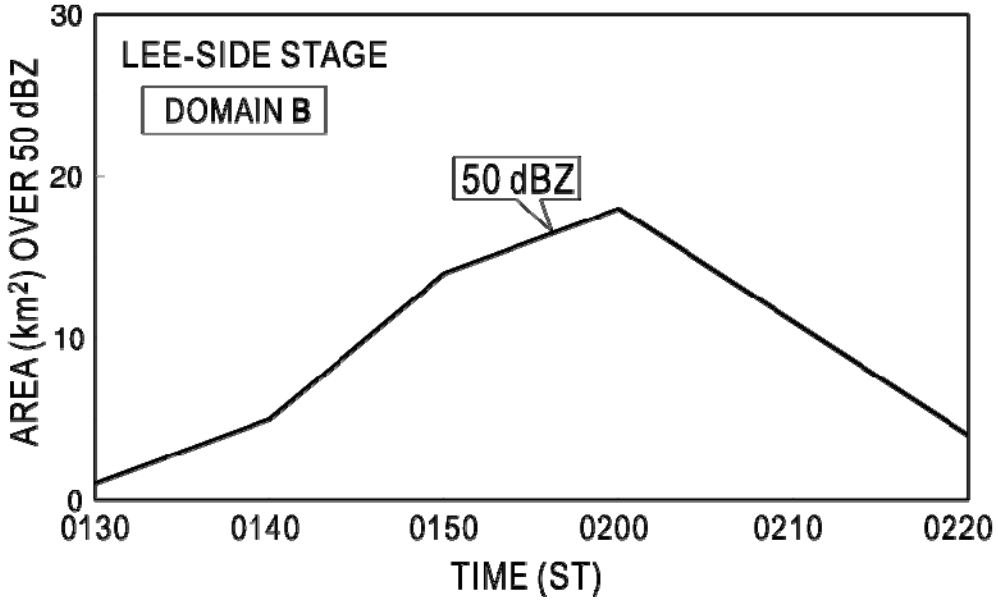

FIG.4.25. Temporal variations in the horizontal area of simulated reflectivity greater than 50 dBZ (solid line) at a height of 1919 m from 0130 to 0220 ST. The analysis region **B** is shown in Fig. 4.24 by rectangles.

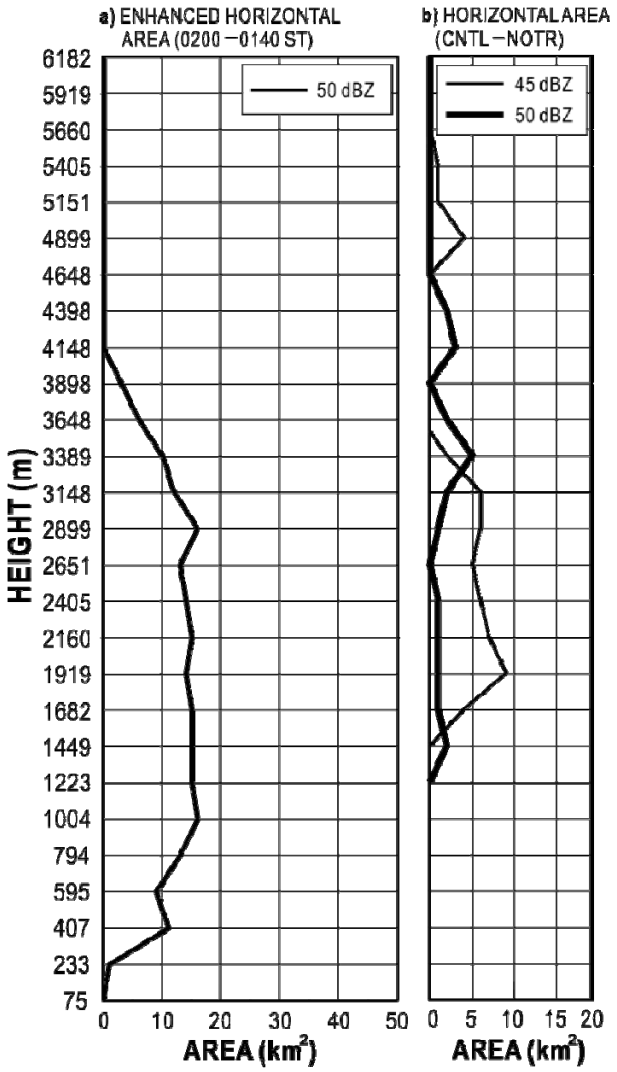

FIG.4.26. Vertical profiles of the expanded horizontal area during the lee–side stage. (a) Enhanced horizontal area of reflectivity greater than 50 dBZ from 0140 to 0200 ST. (b) Differences in horizontal area of reflectivity greater than 45 dBZ (thin line) and 50 dBZ (thick line) between CNTL and NOTR experiments (CNTL minus NOTR) at 0200 ST.

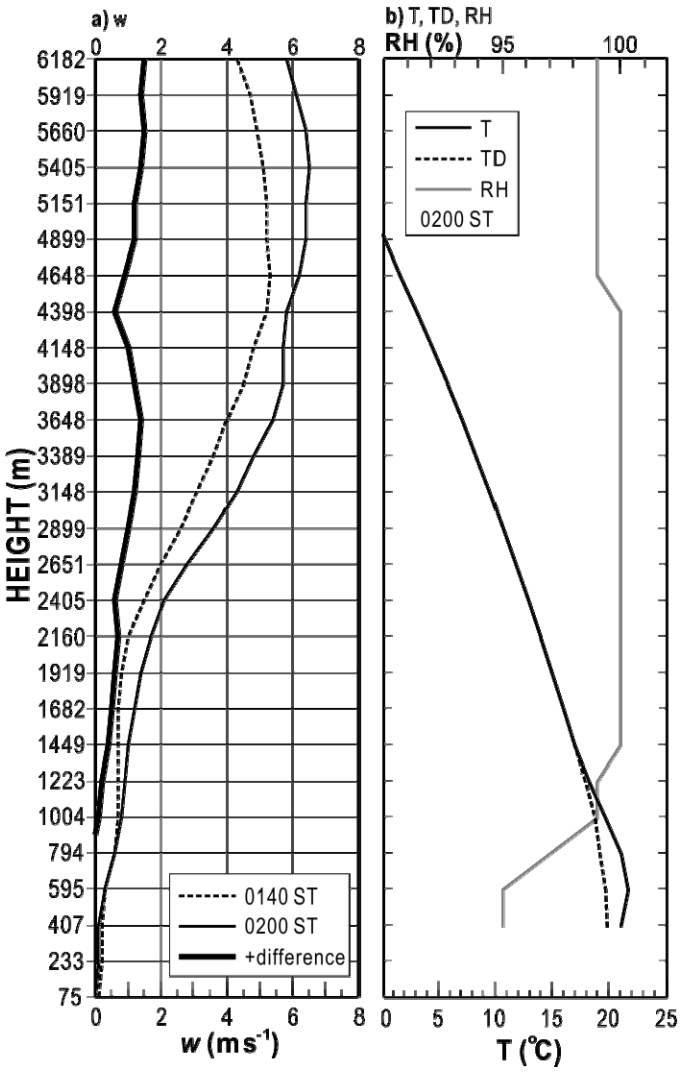

FIG.4.27. Vertical profiles of vertical wind (*w*), temperature (T), dew point temperature (TD), and relative humidity (RH) during the approaching stage. (a) Maximum vertical velocity at 0140 ST (thin broken line), 0200 ST (thin solid line), and the difference between 0140 and 0200 ST (thick solid line: 0200 minus 0140 ST). (b) T (black solid line), TD (broken line), and RH (gray solid line) at the point of maximum vertical wind at 0200 ST.

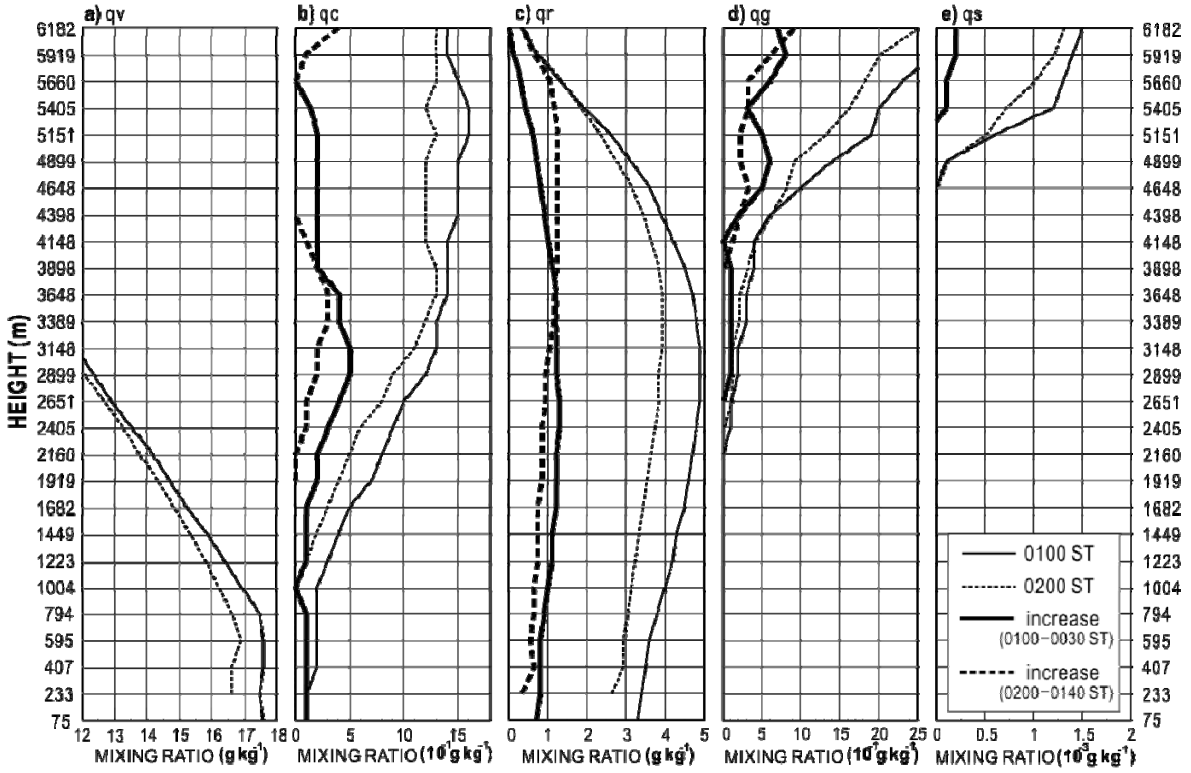

FIG.4.28. Vertical profiles of mixing ratios of (a) vapour (q_v, g kg^{-1}), (b) cloud water (q_c, 10^{-1} g kg^{-1}), (c) rain water (q_r, g kg^{-1}), (d) graupel (q_g, 10^{-1} g kg^{-1}), and (e) snow (q_s, 10^{-3} g kg^{-1}) at 0100 ST (thin broken line) and 0200 ST (thin solid line). Thick solid lines and thick broken lines in panels b–e indicate the increase in each mixing ratio during the approaching and lee-side stages, respectively.

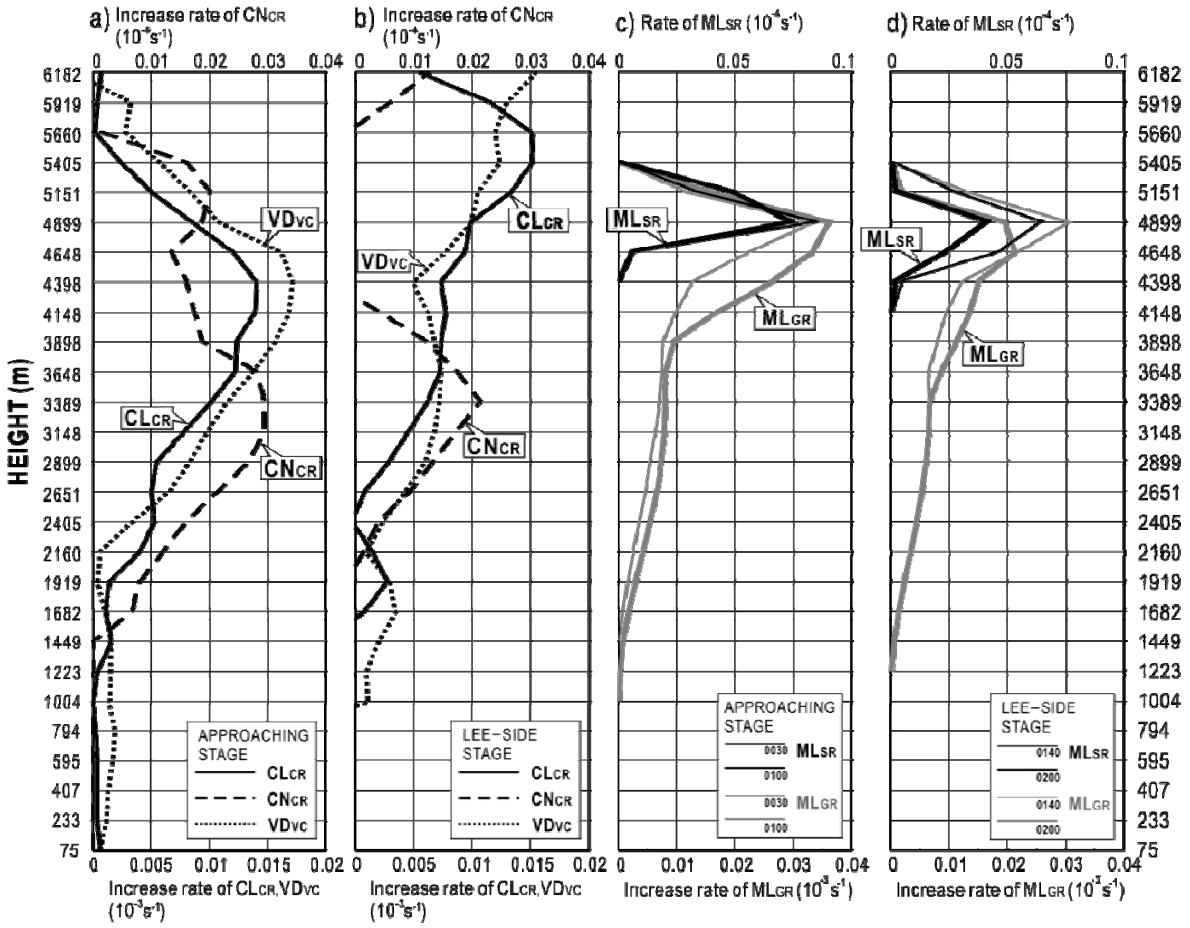

FIG.4.29. Vertical profiles of increase rates of microphysical parameters. (a) Increase rate of vapour deposition to cloud water (VD_{VC}, dotted line), collection from cloud water to rain water (CL_{CR}, solid line), and conversion from cloud water to rain water (CN_{CR}, broken line) during the approaching stage. (b) Increase rates of VD_{VC}, CL_{CR}, and CN_{CR} during the lee-side stage shown by the dotted, solid, and broken lines, respectively. (c) Maximum melting rates of graupel to rain water (ML_{GR}) at 0030 ST (gray thin solid line) and 0100 ST (gray thick solid line), and maximum melting rates of snow to rain water (ML_{SR}) at 0030 ST (black thin solid line) and 0100 ST (black thick solid line). (d) Maximum rates of ML_{GR} (gray lines) and ML_{SR} (black line) at 0140 ST (thin lines) and 0200 ST (thick lines).

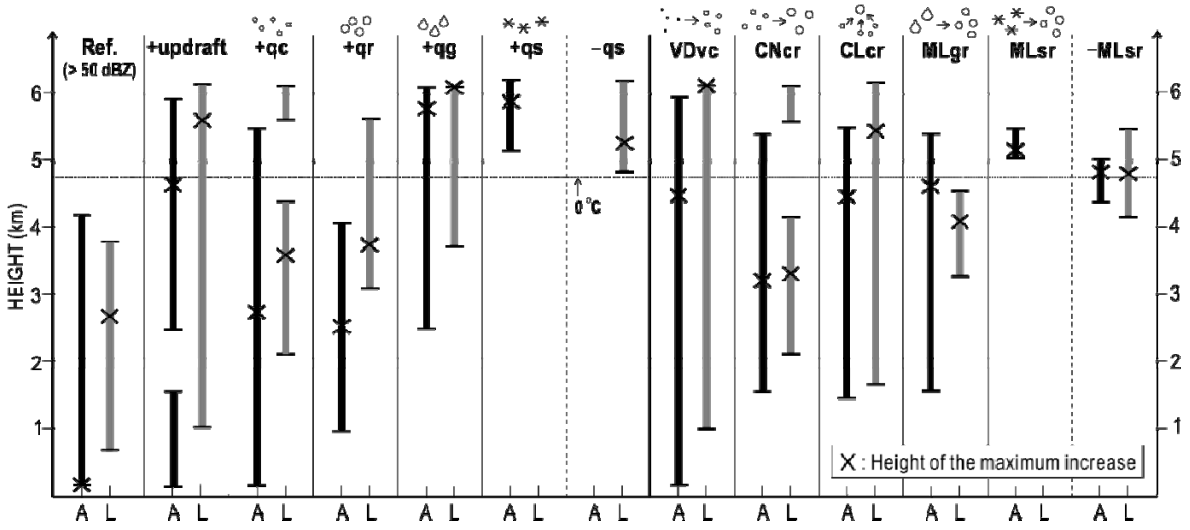

FIG.4.30. Height distributions of the increase of the convective region (reflectivity > 50 dBZ), updraft, mixing ratios of cloud water (q_c), rain water (q_r > 1 g kg^{-1}), graupel (q_g), snow (q_s), and the rates of vapour deposition to rain water (VD_{VC}), conversion from rain water to cloud water (CN_{CR}), collection from cloud water to rain water (CL_{CR}), graupel melting to rain water (ML_{GR}), and snow melting to rain water (ML_{SR}) during the approaching (**A**, black bars) and lee-side stages (**L**, gray bars). The black cross denotes the height of the maximum increase. The height of the 0°C level is indicated by the dotted line.

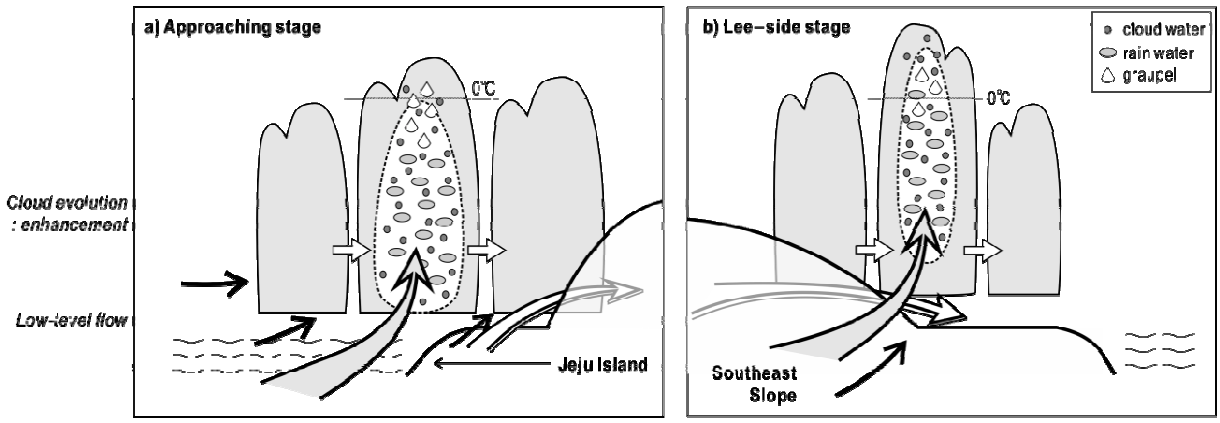

FIG.4.31. Schematic illustrations of the enhancements of the microphysical parameters in (a) the approaching stage, and (b) the lee-side stage of the 6 July 2007 precipitation system. Vertical cross-sections of the precipitation area are shown as gray shading. Black arrows indicate the low-level winds. Gray arrows depict local updraft in the vicinity of the terrain. White arrows indicate the terrain-induced circulatory winds at low altitudes. Symbols inside the precipitation area represent the increased hydrometeors. Dark gray circles and light gray ellipses indicate cloud water and rain water, respectively. White diamond indicates graupel. The height of the thick solid line in each panel shows the topography of Jeju Island.

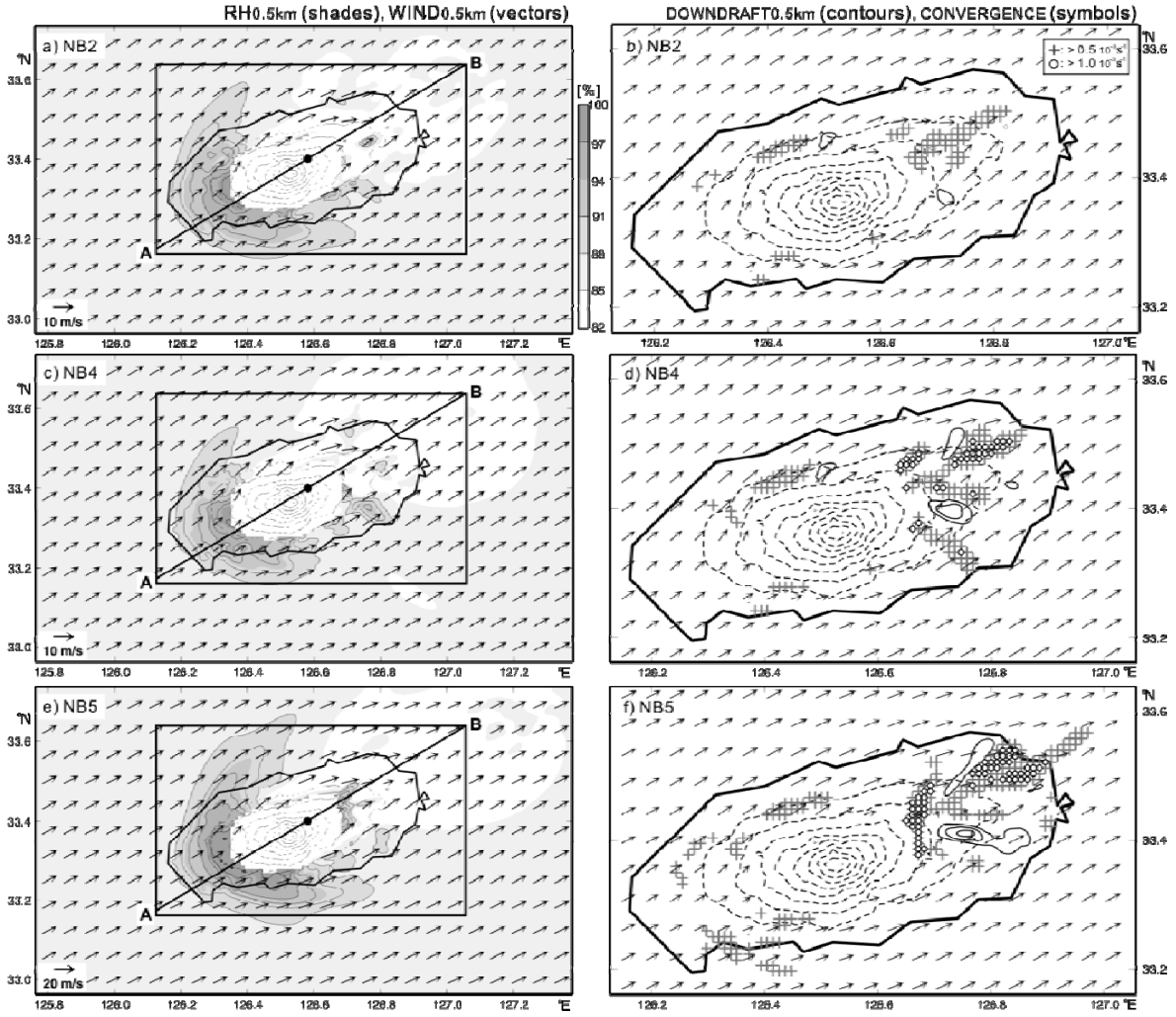

FIG.5.1. Horizontal distributions of horizontal wind, relative humidity (RH), convergence, and downdraft in the NB2, NB4, and NB5 runs. The thick solid line and thin dashed lines in each panel represent the coastline and topography, respectively, of Jeju Island (contour interval, 200 m). The left panels (a), (c), and (e) show the horizontal wind field (arrows) and RH (in gray scale) at a height of 500 m. The right panels (b), (d), and (f) show the horizontal wind (arrows), the downdraft (contour intervals of 0.2 $m\,s^{-1}$ from –0.3 $m\,s^{-1}$) and maximum convergence (gray crosses and open circles represent convergences between 0.5×10^{-3} s^{-1} and 1.0×10^{-3} s^{-1}, and greater than 1.0×10^{-3} s^{-1}, respectively). The locations of the vertical 100-km long cross–sections shown in Fig. 5.2 are indicated in (a), (c), and (e). Black dots on line A–B in (a), (c), and (e) are the midpoints (at 50 km) of the cross sections, and represent the locations of the downward pointing arrows in each panel of Fig. 5.2.

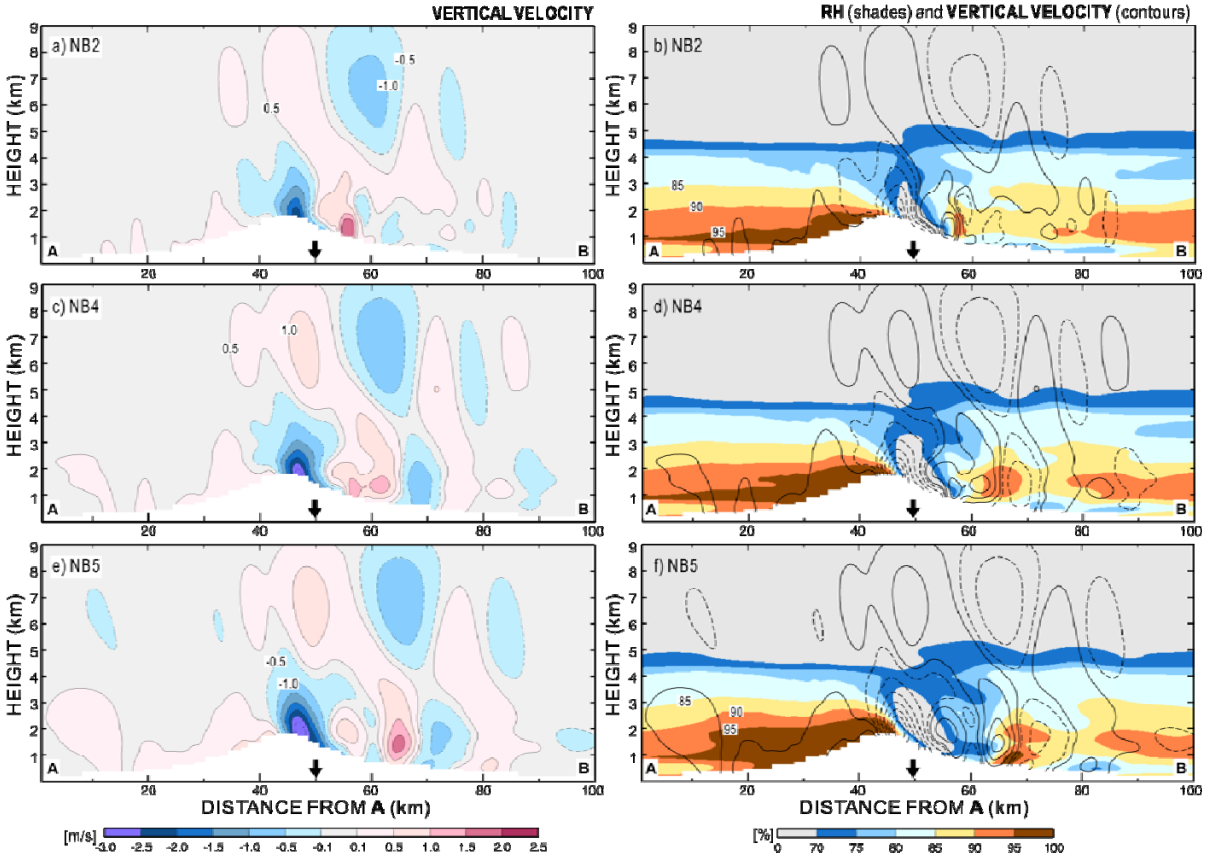

FIG.5.2. Vertical distributions of vertical velocity and relative humidity (RH) in the NB2, NB4, and NB5 runs. The locations of the cross sections are shown in Fig. 5.1a, c, and e. The left panels (a), (c), and (e) depict the updraft and downdraft in red and blue coloured scale, respectively. Regions of updraft stronger than 0.5 m s^{-1} and downdraft stronger than –0.5 m s^{-1} are contoured by solid lines and dashed lines, respectively, (contour interval, 0.5 m s^{-1}). The right panels (b), (d), and (f) indicate regions of RH >70% by shadings and the vertical velocity by contours (as in the left panel).

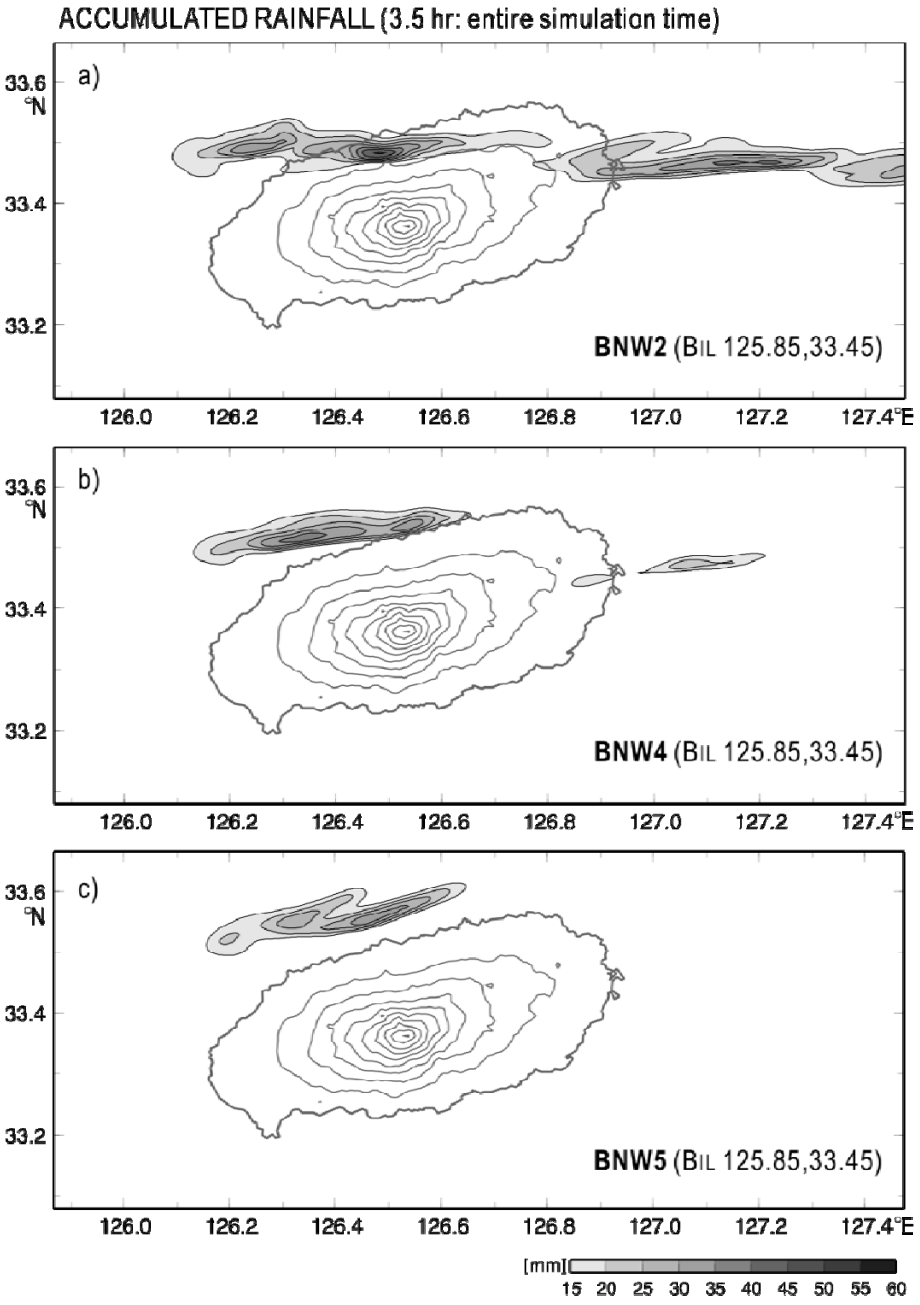

FIG.5.3. Accumulated rainfall during the 3.5-hr simulation in the (a) BNW2, (b) BNW4, and (c) BNW5 runs. Contour interval, 5 mm, starting from 15 mm. Thick and thin solid lines in each panel depict the topography of Jeju Island (contour interval, 200 m).

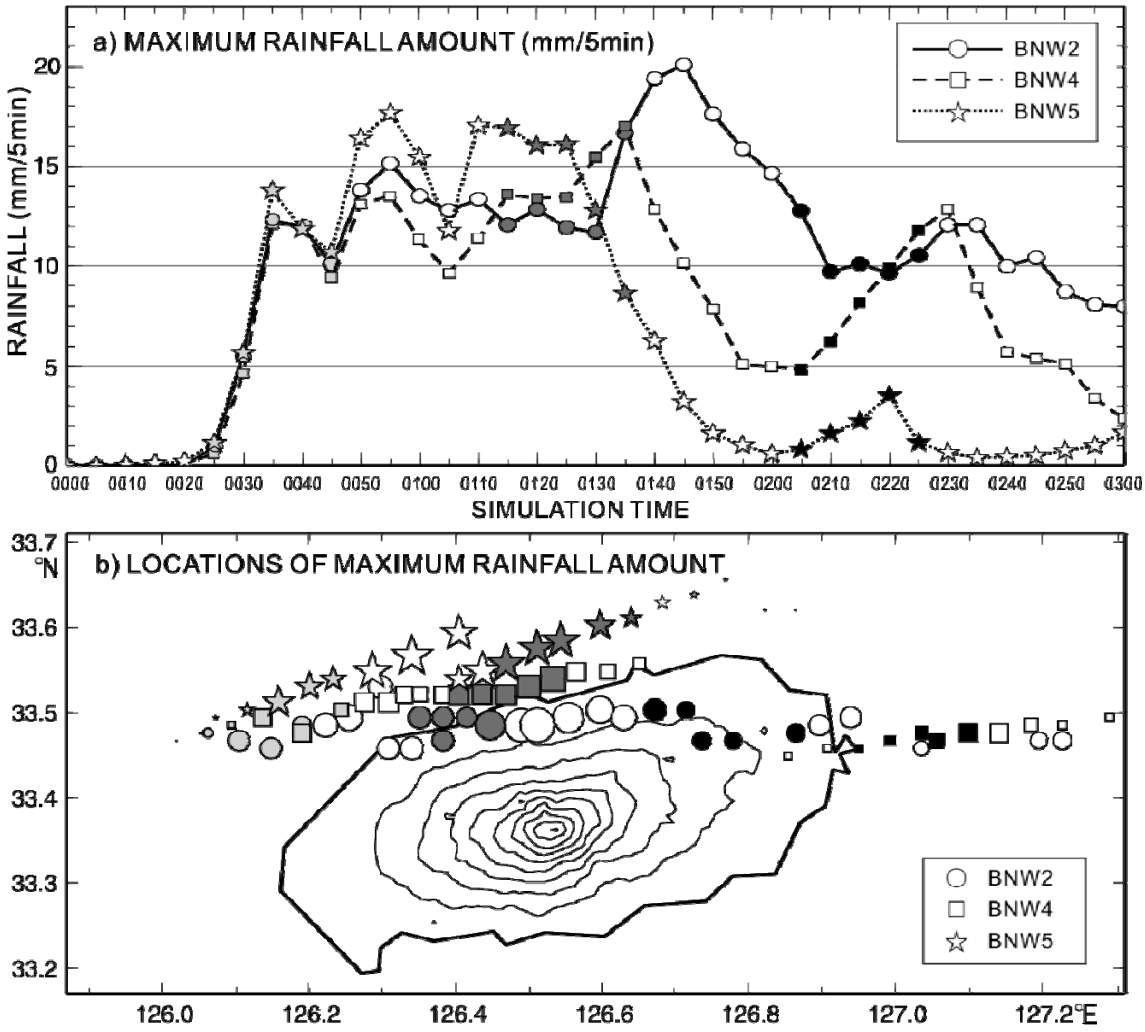

FIG.5.4. Temporal variations in rainfall intensity in the BNW2, BNW4, and BNW5 runs: (a) Time variation of the maximum rainfall intensity (rainfall per 5 min) for the BNW2, BNW4, and BNW5 runs are depicted with solid, dashed, and dotted lines, respectively. (b) The locations of maximum rainfall intensity for the BNW2, BNW4, and BNW5 runs are represented as shaded circles, squares, and stars, respectively. The gray shading of the symbols represents the time period and is changed every 25 min from 0025 ST; the size of each symbol is weighted to show the intensity relative to maximum values. Thick and thin solid lines in (b) depict the topography of Jeju Island (contour interval, 200 m).

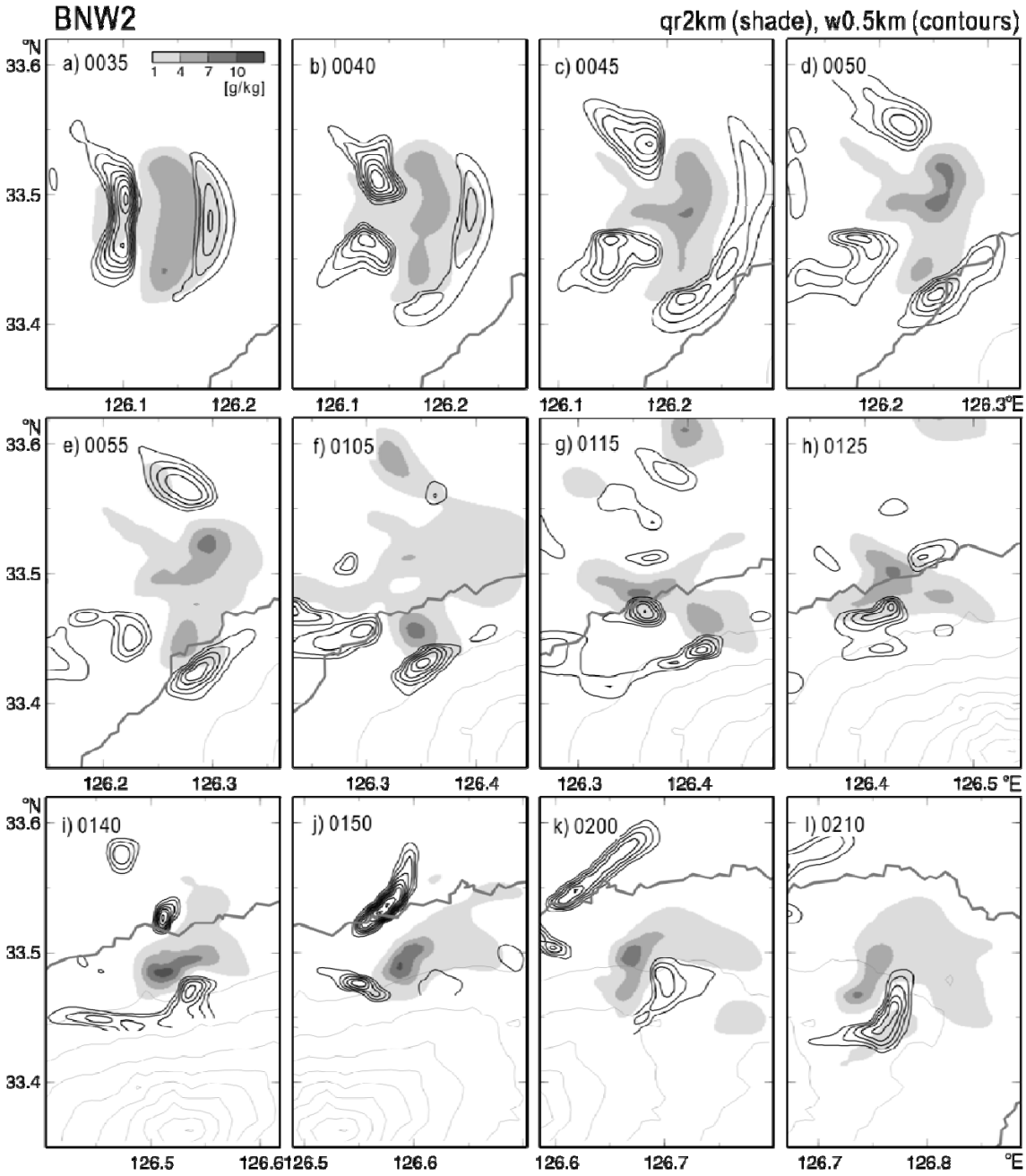

FIG.5.5. Horizontal distributions of the mixing ratio of rain water (q_r, in gray scale) at a height of 2 km and the updraft (w, contours) at a height of 500 m in the BNW2 run: (a)–(e) at 5-min intervals during the period 0035–0055 ST; (e)–(h) at 10-min intervals during the period 0055–0125 ST; and (i)–(l) at 10-min intervals during the period 0140–0210 ST. Regions of $w > 0.3$ m s^{-1} are contoured by solid lines (contour interval, 0.2 m s^{-1}). Regions of $q_r > 1$ g kg^{-1} are shaded in gray scale (shade interval, 3 g kg^{-1}). The thick and thin gray contour lines represent the coastline and the topography, respectively, of Jeju Island (contour interval, 200 m).

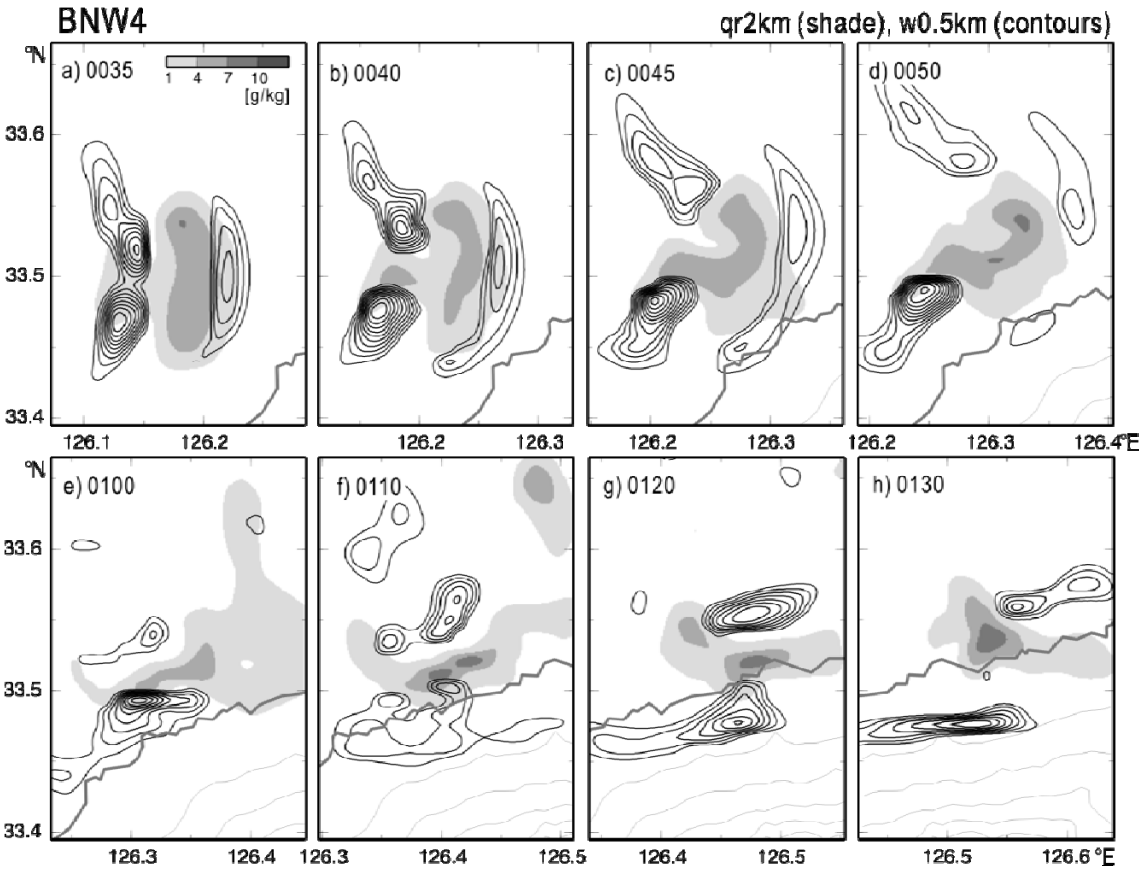

FIG.5.6. Horizontal distributions of the mixing ratio of rain water (q_r, in gray scale) at a height of 2 km and the updraft (w, contours) at a height of 500 m in the BNW4 run: (a)–(d) at 5-min intervals during the period 0035–0050 ST; and (d)–(h) at 10-min intervals during the period 0050–0130 ST. The shaded and contoured regions are as in Fig. 5.5.

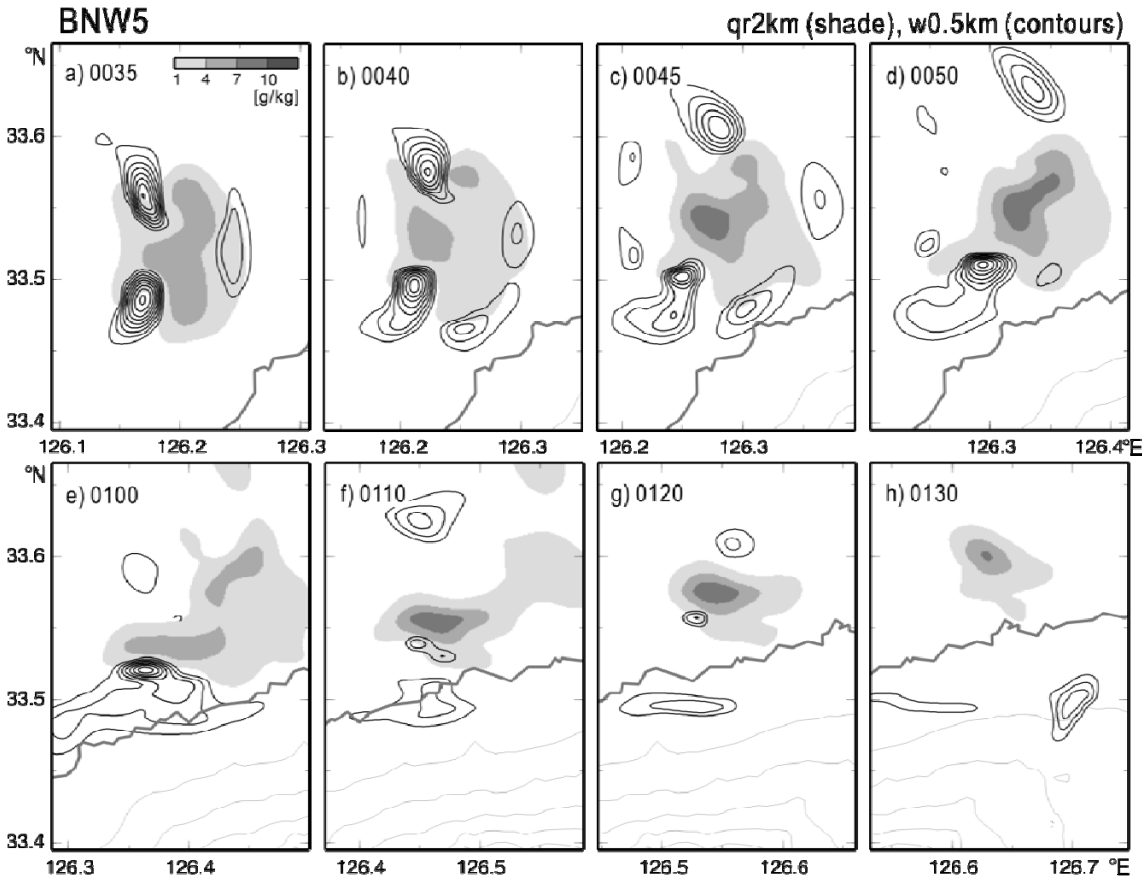

FIG.5.7. Horizontal distributions of the mixing ratio of rain water (q_r, in gray scale) at a height of 2 km and the updraft (w, contours) at a height of 500 m in the BNW5 run: (a)–(d) at 5-min intervals during the period 0035–0050 ST; and (d)–(h) at 10-min intervals during the period 0050–0130 ST. The shaded and contoured regions are as in Fig. 5.5.

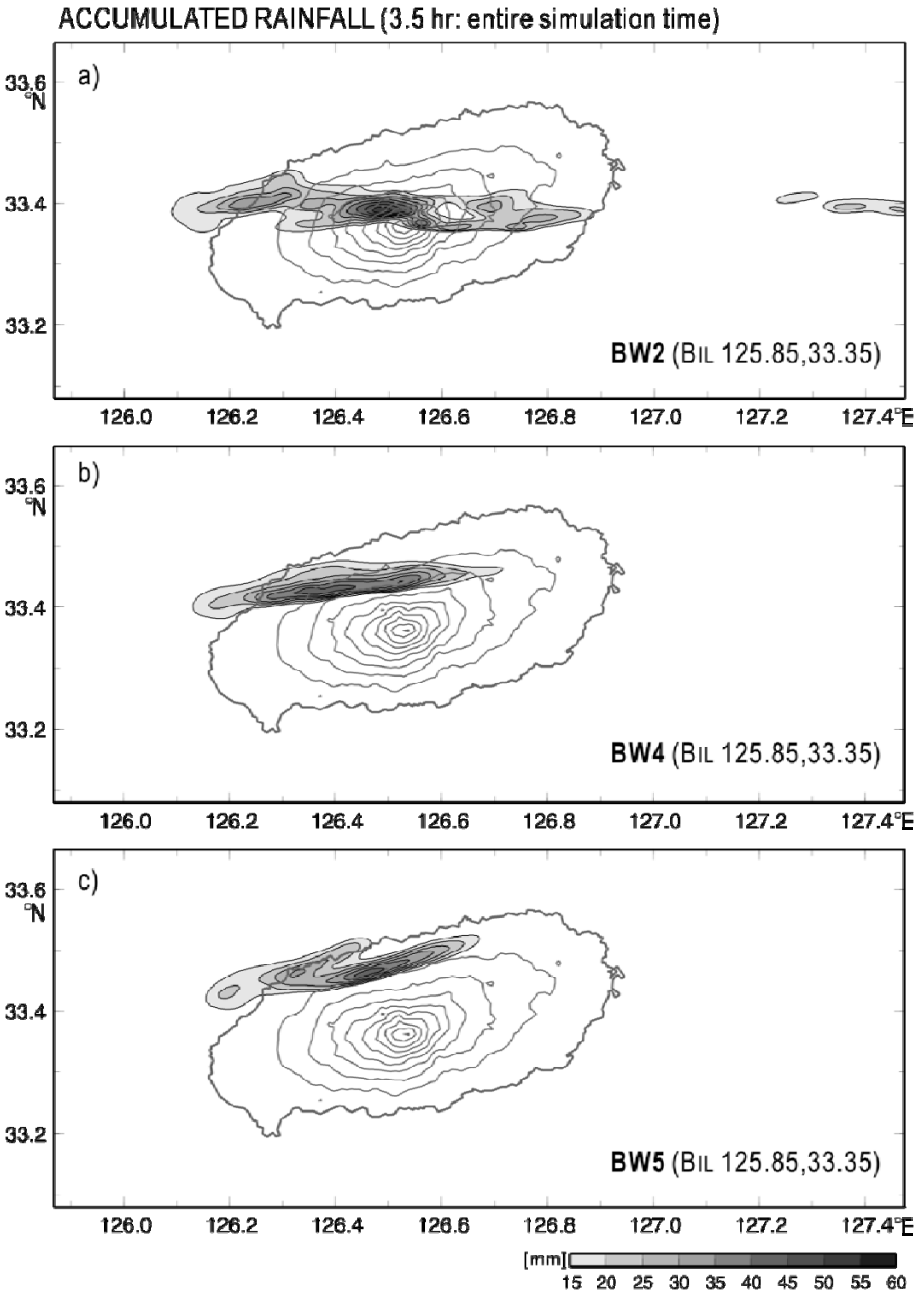

FIG.5.8. Accumulated rainfall amount for 3.5 hours of the entire simulation time in (a) BW2, (b) BW4, and (c) BW5 runs. Contour interval is 5 mm starting from 15 mm. Thick and thin solid lines in each panel depict the topography of Jeju Island (interval: 200 m).

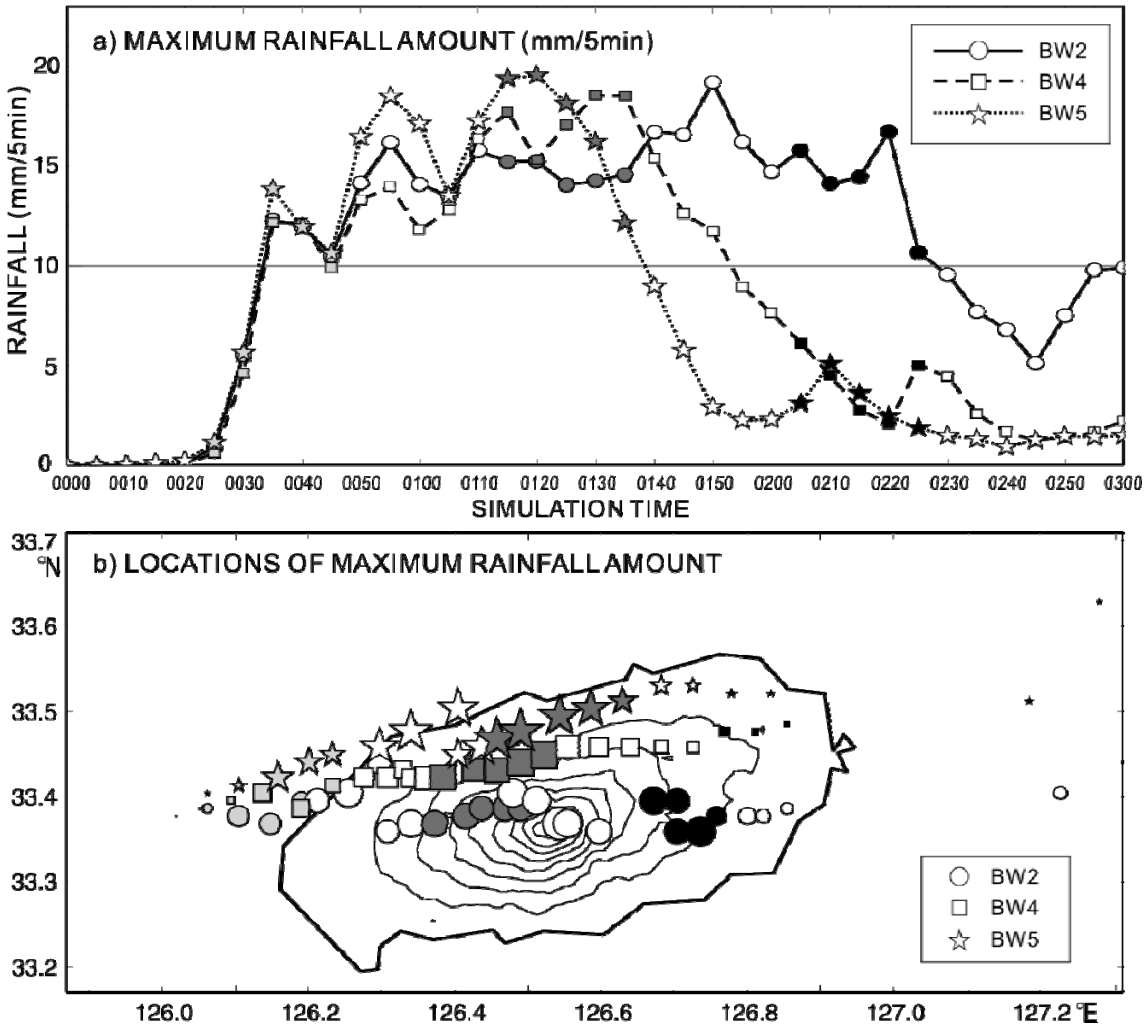

FIG.5.9. Temporal variations in rainfall intensity in the BW2, BW4, and BW5 runs: (a) Time variation of the maximum rainfall intensity (rainfall per 5 min) for the BW2, BW4, and BW5 runs are depicted with solid, dashed, and dotted lines, respectively. (b) The locations of maximum rainfall intensity for the BW2, BW4, and BW5 runs are represented as shaded circles, squares, and stars, respectively. The gray shading of the symbols represents the time period and is changed every 25 min from 0025 ST; the size of each symbol is weighted to show the intensity relative to maximum values. Thick and thin solid lines in (b) depict the topography of Jeju Island (contour interval, 200 m).

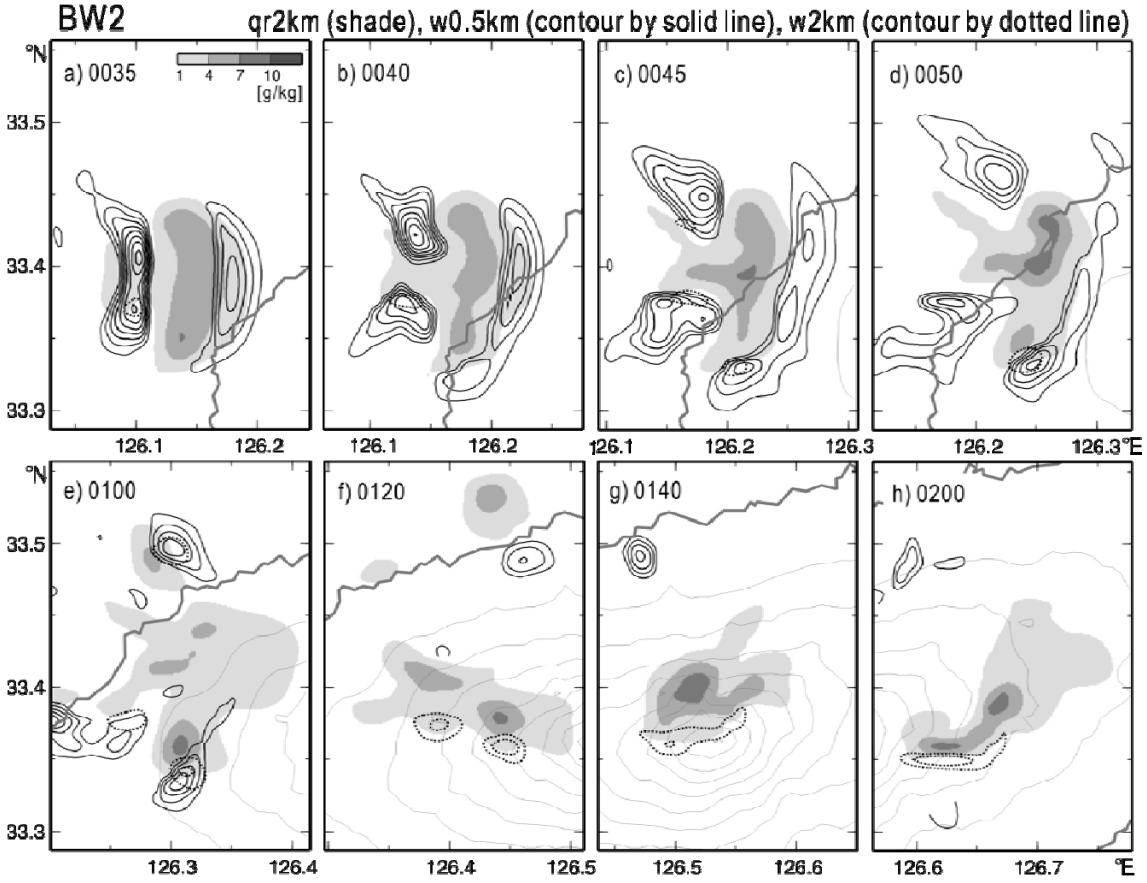

FIG.5.10. Horizontal distributions of the mixing ratio of rain water (q_r, in gray scale) and the updraft (w, contours) in the BW2 run: (a)–(d) at 5-min intervals during the period 0035–0050 ST; and (d)–(h) at 20-min intervals during the period 0050–0200 ST. Regions of $w > 0.3$ m s^{-1} at a height of 500 m are contoured by solid lines (contour interval, 0.2 m s^{-1}). Regions of $w > 4$ m s^{-1} at a height of 2 km are contoured by dotted lines (contour interval, 2 m s^{-1}). Regions of $q_r > 1$ g kg^{-1} are shaded in gray scale (shade interval, 3 g kg^{-1}). The thick and thin gray contour lines in each panel represent the coastline and topography, respectively, of Jeju Island (contour interval, 200 m).

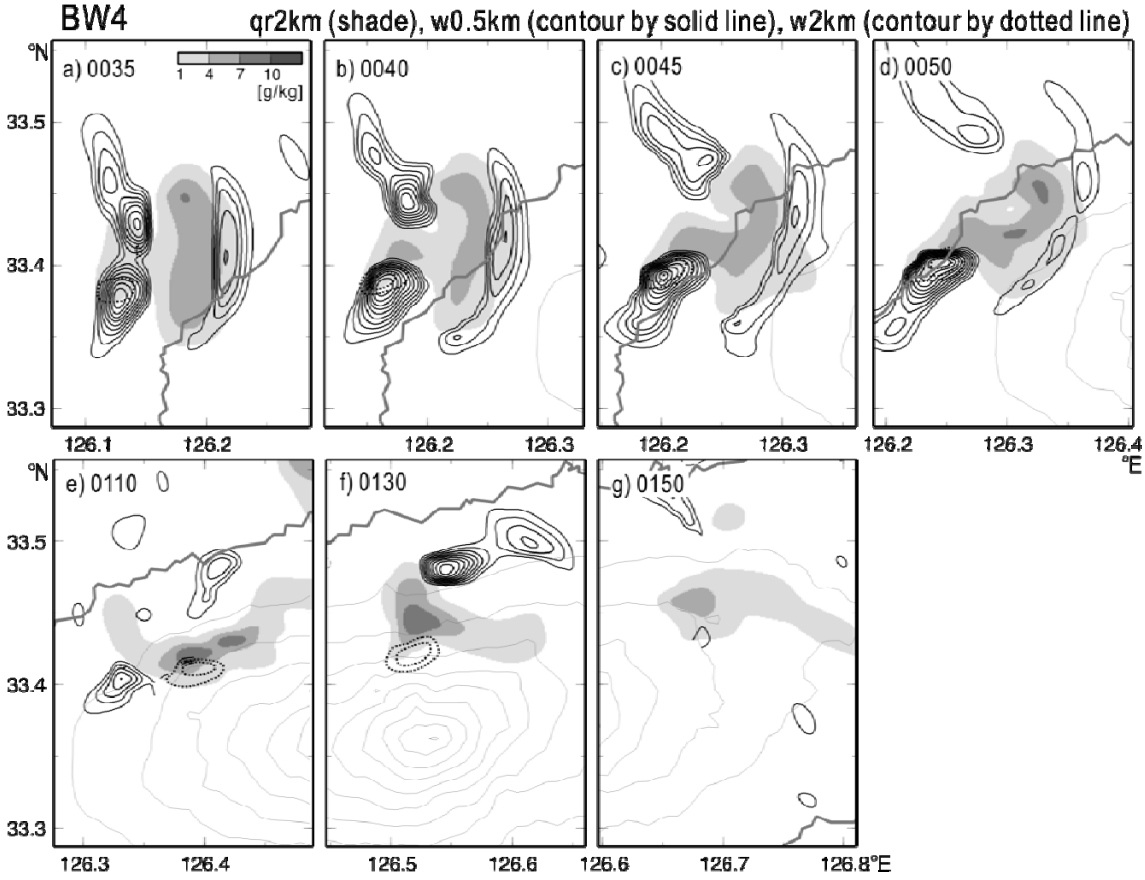

FIG.5.11. Horizontal distributions of the mixing ratio of rain water (q_r, in gray scale) at a height of 2 km and the updraft (w, contours) at a height of 500 m in the BW4 run: (a)–(d) at 5-min intervals during the period 0035–0050 ST; and (d)–(g) at 20-min intervals during the period 0050–0150 ST. The shaded and contoured regions are as in Fig. 5.10.

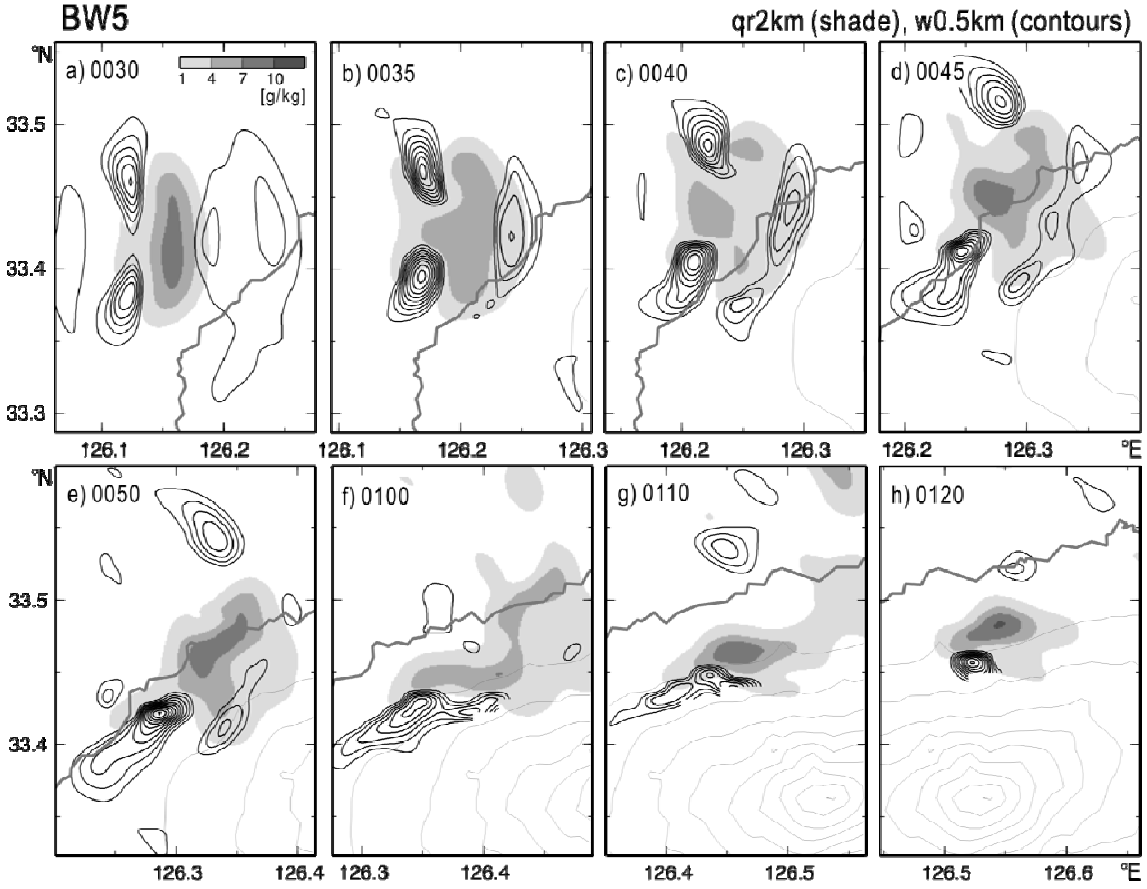

FIG.5.12. Horizontal distributions of the mixing ratio of rain water (q_r, in gray scale) at a height of 2 km and the updraft (w, contours) at a height of 500 m in the BW5 run: (a)–(d) at 5-min intervals during the period 0035–0050 ST; and (d)–(h) at 10-min intervals during the period 0050–0120 ST. The shaded and contoured regions are as in Fig. 5.5.

TABLE.5.1. Summarized results of experiments without bubble: inter-model comparisons. C_{west} and C_{east} are the maximum intensity of the convergence at a height of 500 m on the terrain in the western and the eastern sides, respectively, of longitude 126.6°E, respectively. D_{east} is the maximum intensity of downdraft at a height of 500 m on the terrain in the eastern side of longitude 126.6°E.

Experiment	C_{west} (10^{-3} s^{-1})	C_{east} (10^{-3} s^{-1})	D_{east} ($m\,s^{-1}$)
NB2	0.6	0.9	–0.3
NB4	0.7	1.7	–0.6
NB5	0.7	1.6	–0.8

TABLE.5.2. Summarized results of experiments with bubble: inter-model comparisons. P_{max} is the maximum rainfall intensity in 5 min, and L_{pmax} is the location of P_{max}. A_{west} and A_{east} is the horizontal area of accumulated rainfall exceeding 20 mm to the west and east, respectively, of longitude 126.6°E, respectively. D_{rain} is the duration of rainfall intensities exceeding 5 mm/5 min. OC_{west} and OC_{east} represent whether the rainfall system passes over the convergence zone on the western and eastern sides, respectively, of longitude 126.6°E.

Experiment	P_{max} (mm/5 min)	L_{pmax} (°N, °E)	A_{west} (km^2)	A_{east} (km^2)	D_{rain} (min)	OC_{west}	OC_{east}
BNW2	20.1	33.48, 126.5 (onshore)	150	173	150	Yes	Yes
BNW4	16.9	33.53, 126.5 (offshore)	141	13	80	No	Yes
BNW5	17.7	33.56, 126.3 (offshore)	110	1	70	No	No
BW2	19.2	33.36, 126.5 (crest)	241	49	130	No	No
BW4	18.6	33.44, 126.5 (onshore)	160	12	90	Yes	No
BW5	19.6	33.47, 126.5 (onshore)	138	8	70	Yes	No

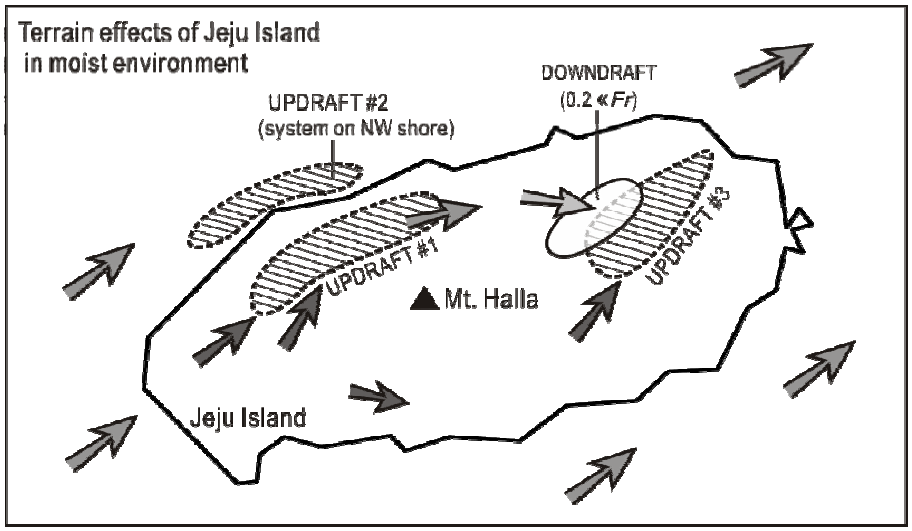

FIG.5.13. Schematic illustration of the terrain effect of Jeju Island in a moist environment with southwesterly winds ($Fr \leq 0.55$). The thick solid line is the coastline of Jeju Island. Gray shaded arrows represent horizontal winds around the island at low altitudes; the shading of each arrow indicates the amount of moisture (darker shading for greater moisture). The hatched area depicts the updraft region at low altitudes. The white region closed by a black line indicates a region of dry downdraft.

TABLE.6.1. Summary of 06P (Table 3.2) and 07P (Table 4.2): the environmental parameters of surface humidity and temperature, wind direction, Froude number and stability, and the passage and evolution of each convective system.

Parameter			(a) 06P	(b) 07P
ENVIRONMENT	Surface Humidity		**MOIST** 92 %	**MOIST** 90 %
	Surface Temperature		**WARM** 26°C	**WARM** 24°C
	Wind Direction	Mid Level		
		Low Level		
	Froude Number		**MODERATE** 0.55	**LOW** 0.2
	Stability		**STABLE** 1.4×10^{-2} s^{-1}	**STABLE** 1.7×10^{-2} s^{-1}
SYSTEM	Passage	Direction	Eastward	Eastward
		Speed	~ 13 m s^{-1}	~ 11 m s^{-1}
	Evolution 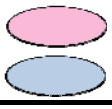 Enhancement Dissipation			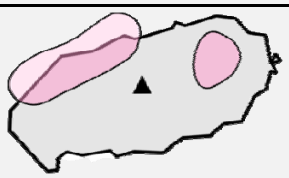

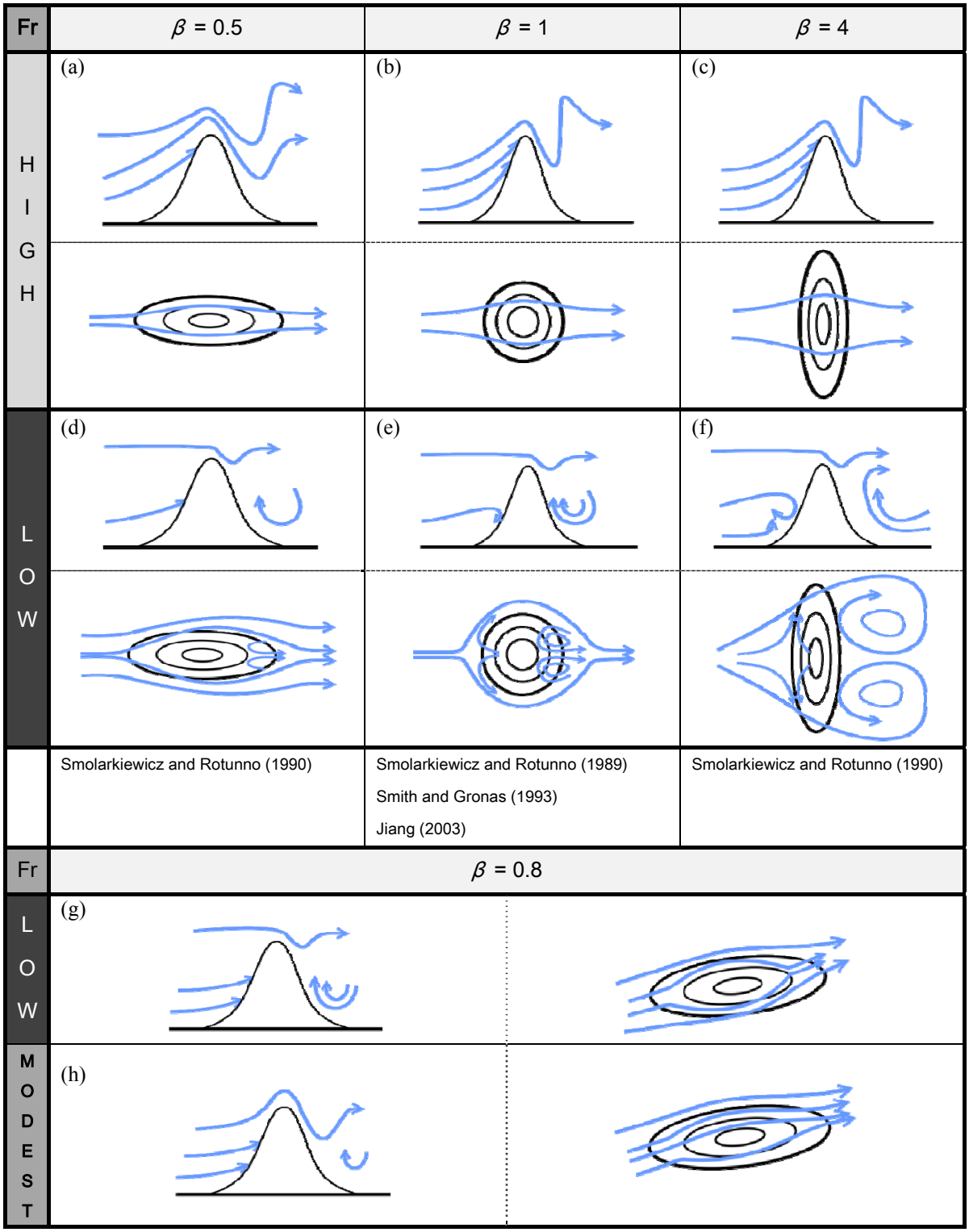

FIG.6.1. Schematic diagram of flow modification (blue arrows) by terrain (black solid lines): (a)–(f) is copy of Fig. 1.3, and the flow modification (blue arrows) by an isolated elliptical–shaped terrain (Jeju Island; black solid line) with southwesterly ($\beta = 0.8$) in (g) for low *Fr*, and in (h) for moderate *Fr*.

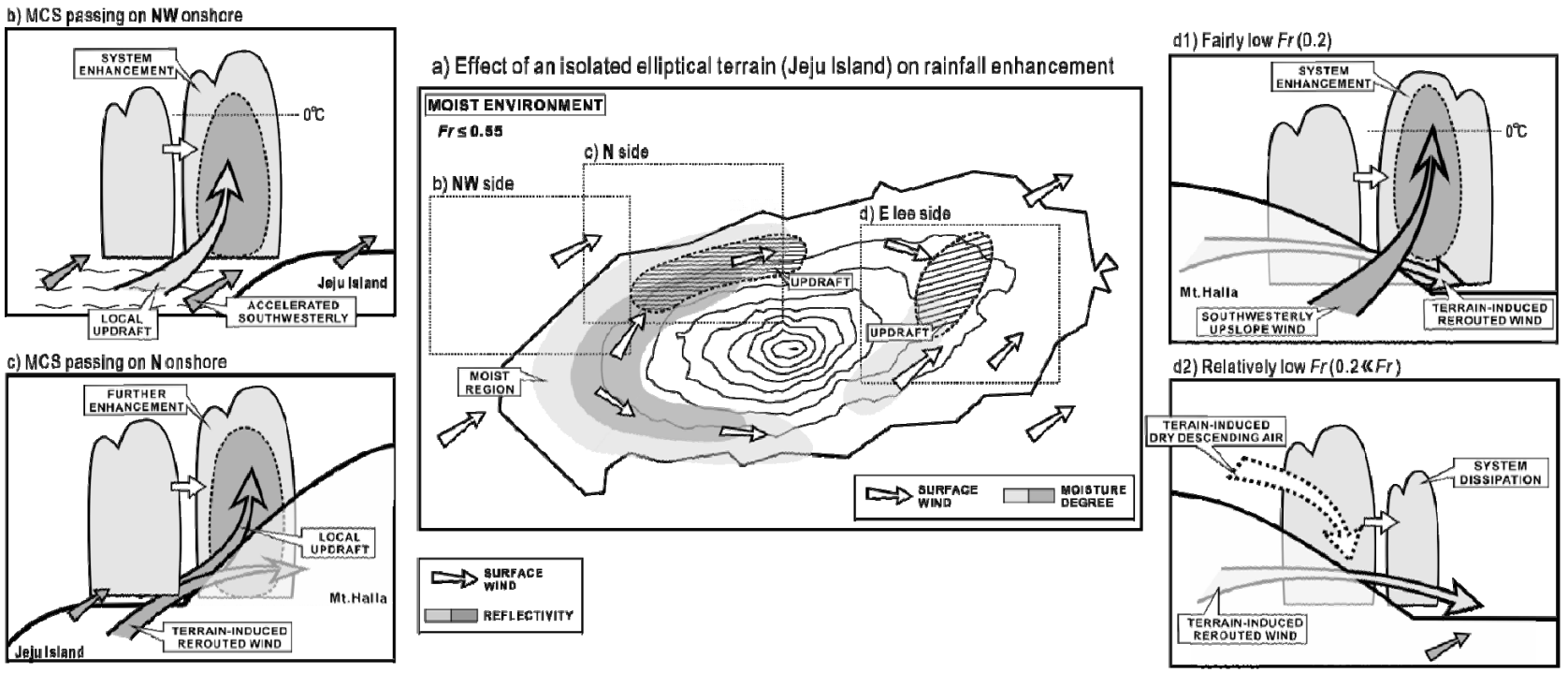

FIG.6.2. Schematic diagram of effect of an isolated elliptical shaped terrain on the distribution of surface moisture contents and evolution of rainfall system in the vicinities of the terrain: (a) distributions of surface wind (white arrows), moisture contents (shading), and updraft (hatched area), (b) is terrain–induced rainfall enhancement off the northwestern shore of terrain, (c) is terrain–induced rainfall enhancement on the northern lateral side of the terrain, (d1) is terrain–induced rainfall enhancement on the lee side of the terrain, and (d2) is terrain–induced rainfall dissipation on the lee side of the terrain. Thick solid line in each panel indicates topography of Jeju Island. The gray arrows in (b)–(d2) indicate the low–level wind.